DESIGN AND CHARACTERIZATION OF AEROSOL SHOCK TUBE METHODS FOR THE STUDY OF LONG-CHAIN HYDROCARBON FUELS

A Dissertation

by

JOSHUA WILLIAM HARGIS

Submitted to the Office of Graduate and Professional Studies of
Texas A&M University
in partial fulfillment of the requirements for the degree of

DOCTOR OF PHILOSOPHY

Chair of Committee,	Eric L. Petersen
Co-Chair of Committee,	Bing Guo
Committee Members,	Waruna D. Kulatilaka
	Adonios N. Karpetis
Head of Department,	Andreas A. Polycarpou

August 2020

Major Subject: Mechanical Engineering

ABSTRACT

A new shock-tube facility for the study of gas- and condensed-phase measurements has been developed for the investigation of various hydrocarbon species. At present, the shock-tube facility is intended for studying combustion properties of long-chain hydrocarbon fuel components and mixtures at realistic engine conditions. Equipped with an aerosol generation and entrainment apparatus, the facility also possesses an enlarged driver section and double-diaphragm interface between the driver and driven sections. The driver section diameter is 19.37 cm with a configurable length of 1-6 m. Additionally, the stainless-steel driven section has an mirror-finish internal diameter of 15.24 cm and is also configurable in length up to 5.18 m. As with most modern shock tubes, this shock tube is equipped for use with current methods of shock velocity detection, optical diagnostics, and other diagnostic techniques. In addition to the study of aerosolized liquids (fuels and non-fuels) related to combustion chemistry, reaction kinetics, evaporation studies, and particle-fluid interactions, the facility is capable of investigating traditional gas-phase mixtures like those previously undertaken in a similar facility in the Petersen Group Laboratory at the Texas A&M campus in College Station, TX. The operating limits of the facility include temperatures and pressures up to 4000 K and 100 atm, respectively. A basic characterization of all diagnostics, including the ignition delay results of lean methane mixtures, are presented in this study (T_5=1425-1825 K, P_5=1.5, 4 atm). Furthermore, the design and characterization of a novel aerosol introduction method for applications in shock tubes is presented. Lastly, the methods and procedures

implemented for conducting aerosol shock tube experiments are discussed and the results of various ignition delay studies in real fuel-air mixtures conducted over a modest range of temperatures and pressures are presented.

ACKNOWLEDGMENTS

I would like to thank my committee chair, Dr. Petersen, co-chair, Dr. Guo, and my committee members, Dr. Kulatilaka, and Dr. Karpetis for their guidance and support throughout this process. Both Dr. Petersen and Dr. Guo have been instrumental in the success achieved in this work, which has led to this project being rewarding and successful both personally and professionally. Further thanks go to Dr. Petersen for his unwavering commitment to his students. His standard of excellence for the work his students perform combined with his patience throughout the learning process are what make the Petersen Research Group such a great environment to be a part of.

Thanks also go to my friends and colleagues in the Petersen Research Group for making my time at Texas A&M University a great experience. Furthermore, your contributions to my education have multiplied my learning within the Petersen group immensely. Drs. Travis Sikes, Clayton Mulvihill, Anibal Morones, and Olivier Mathieu have been great colleagues, and better friends. You have all impacted me greatly and provided great encouragement in pursuing excellence in my professional and educational pursuits. Much thanks also goes to Sean Cooper for his assistance in the lab in Qatar.

Unseen by most, are the efforts and encouragements of my wonderful wife, Kaitlyn. She has provided great support to me during the course of my Ph.D. and has been a tremendous encouragement in the midst of the arduous work of completing my formal education. Your commitment to me has given me strength to face my greatest challenges.

Lastly, praise is due to God the Father for his innumerable blessings given throughout this process, including the birth of our daughter, Elizah Jeanne.

CONTRIBUTORS AND FUNDING SOURCES

Contributors

This work was supervised by a dissertation committee consisting of Professors Eric L. Petersen (Chair) and Waruna D. Kulatilaka of the Department of Mecahnical Engineering, Professor Bing Guo (co-Chair) of the Texas A&M Qatar Mechanical Engineering Department, and Professor Adonios N. Karpetis of the Department of Aerospace Engineering.

The development of the gas-phase laser absorption formulation of the fuel concentration using the Beer-Lambert relation in Appendix A was performed by the author in conjunction with Dr. Clayton Mulvihill (prior to completion of his Ph.D. at Texas A&M University).

Computational Fluid Dynamics (CFD) simulations discussed in Chapter 6 were performed in by Dr. Way Lee Chen during his time as a Postdoctoral Researcher at Texas A&M University Qatar.

All other work conducted for this dissertation was completed by the author independently.

Funding Sources

Graduate study was supported by an assistantship from the Texas Engineering Experiment Station Turbomachinery Laboratory Consortium, a fellowship from the Texas A&M University Mechanical Engineering Department, and a National Priorities Research Program (NPRP) research grant from the Qatar National Research Fund (QNRF), a

member of Qatar Foundation, under Grant Number NPRP 8-1358-2-579. The contents of this dissertation are solely the responsibility of the author and do not necessarily represent the official views of the Texas Engineering Experiment Station, Texas A&M University, the Qatar National Research Fund, or Qatar Foundation.

TABLE OF CONTENTS

Page

ABSTRACT....ii

ACKNOWLEDGMENTS....iv

CONTRIBUTORS AND FUNDING SOURCES....v

TABLE OF CONTENTS....vii

LIST OF FIGURES....x

LIST OF TABLES....xvi

1. INTRODUCTION....1

1.1. Motivation for the Study....2
1.1.1. Recent Combustion Studies of Real Fuels and Related Constituents....3
1.1.2. Challenges of Studying Real Fuels in Shock Tubes....12
1.2. The Working Principle of a Shock Tube: The Shock Wave....17
1.3. Shock-Tube Geometry and Operational Basics....20
1.4. Overview and Structure of the Dissertation....25

2. AEROSOL AND DROPLET THEORY WITH APPLICATIONS IN SHOCK TUBES....26

2.1. Governing Transport Mechanics of Droplets and Aerosols....27
2.1.1. Settling....28
2.1.2. Relaxation....30
2.2. Recent Studies of Aerosols in Shock Tubes....41
2.3. Guidelines for Conducting Kinetics Studies in Aerosol Shock Tubes....46
2.4. Methods of Aerosol Generation....49
2.5. Recent Kinetics Studies in Shock Tubes Using Nebulized Fuels....51

3. FACILITY DESIGN....60

3.1. Shock-Tube Development....60
3.1.1. Non-Idealities....60
3.1.2. Legacy Design Incorporations....64

3.2. Aerosol Generation and Handling....81
3.2.1. Design Considerations....82
3.2.2. Aerosol Transport Methods....85
3.2.3. Aerosol Entrainment Methods: Mass Loading and Uniformity....104
3.3. Shock-Tube and Aerosol-Generation Assembly Construction....121

4. CHARACTERIZATION AND EXPERIMENTAL CONSIDERATIONS....126

4.1. Shock Velocity Decay....126
4.1.1. Gaseous Velocity Decay....128
4.1.2. Impact of Aerosols and Changing Acoustic Impedance on Velocity Decay....129
4.2. Pressure Time Histories....134
4.2.1. Traditional Non-Idealities....134
4.2.2. Other Facility Effects on Pressure Time Histories....136
4.2.3. Effects of the U-Bend Driver Section....139
4.3. Gaseous Ignition Delay Times with Methane....144
4.4. Fuel Concentration Diagnostic and Thermodynamic Calculations....144
4.4.1. Thermodynamic Property Calculations....145
4.4.2. Fuel Concentration Measurement....149
4.5. Defining Ignition Delay Time and Sample Ignition Traces....156
4.6. Conclusions....159

5. IGNITION DELAY TIMES OF LIQUID FUELS IN THE AEROSOL SHOCK TUBE....162

5.1. Decane....163
5.2. DF-2....164
5.3. Jet-A....166
5.4. GTL Diesel....168
5.5. Discussion....170
5.5.1. Decane....172
5.5.2. Direct Comparison of Heated and Aerosol Shock....173
5.5.3. GTL Diesel....176
5.5.4. Evaporation and Uniformity Validation by Ignition Delay Time Data....177
5.5.5. Estimation of Experimental Temperature Uncertainty....186

6. CONCLUSIONS....188

6.1. Traditional and Aerosol Shock Tube Methods....188
6.2. Ignition Delay Time Results....190
6.3. Future Work....191
6.3.1. Aerosol Uniformity Measurement....192
6.3.2. Aerosol Introduction Scheme....193

6.3.3. Nonidealities....198
6.3.4. Negative Temperature Coefficient (NTC) and Low-Temperature Ignition Chemistry....200

REFERENCES....203

APPENDIX A PARAMETERS IN THE SPECTROSCOPIC FUEL ABSORPTION MEASUREMENT....216

A.1 Absorbance Formulation....216
A.2 Absorption Coefficients....222

APPENDIX B CALCULATION OF THERMODYNAMIC PROPERTIES IN SHOCK-INDUCED FLOWS WITH AEROSOLS....223

APPENDIX C LIST OF EXPERIMENTAL CONDITIONS AND IGNITION DELAY TIMES....229

LIST OF FIGURES

Page

Figure 1.1 An example shock-tube schematic diagram. 21

Figure 1.2 A distance versus time (x-t) diagram representing the spatial and temporal distributions of phenomena during a shock-tube experiment.....22

Figure 2.1 A diagram of the gate valve located within the driven section for constraining aerosol near the endwall.....27

Figure 2.2 Relaxation process of a shock wave propagating through a two-phase aerosol mixture in the shock-fixed coordinate frame 36

Figure 3.1 Diagram of post-reflected shock bifurcation. 63

Figure 3.2 View of driven tubing section. Ports are shown with spacing of 16". Grooves on each end accommodate the flanges. 65

Figure 3.3 Exploded view of driven tube joint with weldless flange couplings. 66

Figure 3.4 Driven-section flange coupling. a) External view, b) Section view. An o-ring is placed in a groove in one of the tube faces to provide a high-integrity seal.....67

Figure 3.5 Shock-tube experiment x-t diagram with driver gas utilizing backfilling compared to driver gas without backfilling (not to scale). Region 4 is filled with a helium-based mixture, as in a traditional experiment, while backfilling is performed to create region 4' with a low-sound-speed gas. 69

Figure 3.6 Picture of the driver tube in place prior to installation of the diaphragm breech mechanism assembly.....70

Figure 3.7 Section view of double-diaphragm breech loading section. 72

Figure 3.8 Diagram of shock tube setup showing inertial mass. The inertial mass also acts as a stand. Also shown is the new driver section and also the new gate valve located toward the right end of the driven section. 73

Figure 3.9 Views of the gate valve constructed for the aerosol shock tube. a) Isometric view; b) Isometric section view. The gate valve is in the open position. 75

Figure 3.10 Exploded view of gate valve components. The pneumatic piston is not pictured here. 77

Figure 3.11 External view of heated window ports near the endwall connection of the driven section. 79

Figure 3.12 Section view of the cylindrically shaped heated window port assemly mounted on the shock tube. 81

Figure 3.13 Image of 12-Disc ultrasonic nebulizer purchased from the House of Hydro. Image obtained from https://www.thehouseofhydro.com/store.html. Prior to operation with fuels, the water depth sensor had to be removed. 85

Figure 3.14 Difference between filling methods of the Gen. I aerosol shock tube of Davidson et al. and the Gen. II aerosol shock tube of Haylett et al. 87

Figure 3.15 Various stages of the filling process used to introduce aerosol into the test section of the shock tube between the gate valve and the endwall for an AGT and dump tank each of arbitrary size and position. Drawing not to scale. 91

Figure 3.16 Aerosol penetration through a straight tube with varying inner diameter and length of 0.50 m using DEPOSITION 2001a. Top) Inner diameter of 25 mm, Middle) Inner diameter of 15 mm, Bottom) Inner diameter of 38 mm. 98

Figure 3.17 Aerosol penetration through a straight tube with varying inner diameter and length of 0.50 m using DEPOSITION 2001a. Top) Inner diameter of 25 mm, Middle) Inner diameter of 15 mm, Bottom) Inner diameter of 38 mm. 99

Figure 3.18 Droplet penetration through a 0.50-m-long tube with two bends of 90 degrees. The inner diameter is 25 mm and curvature ratio is 4.0. a) 2 bends, b) 3 bends. 100

Figure 3.19 Aerosol penetration in straight tubes with inner diameter of 25 mm and varying lengths. a) Length=1.0 m, b) Length=2.0 m. 101

Figure 3.20 Diagram of aerosol filling scheme layout. The red dashed portion of tubing signifies the as-of-yet unspecified inlet design to pass aerosol from tubing into the shock tube. Not to scale. 103

Figure 3.21 Top view of Mie scattering laser diagnostic setup for measuring aerosol loading uniformity in the mock shock-tube test section. Length units are in cm. 108

Figure 3.22 Diagram of close-up view of aerosol inlet geometry (not to scale). a) Open-tube geometry; b) Injector head geometry (of an arbitrary configuration) whereby the injector is inserted into the shock tube during the filling process and removed prior to propagation of the shock wave. 112

Figure 3.23 Example injector head with showerhead configuration. The outer diameter of the injector is 1.5" and the overall length is approximately 5.00".....113

Figure 3.24 Cross-section representation of flow exiting aerosol injector. The flow energy is converted to dynamic pressure along the length of the injector. a) Exit velocities at holes near the end of the injector are greater than those at the base of the injector, b) Exit velocities are more even along the length of the injector with a conical internal insert. 114

Figure 3.25 Front and isometric views of final aerosol injector design in CAD software. The outlet holes have 12-mm diameter with 20-mm center-to-center spacing and beveled edges for easy passage over sealing o-rings. The top portion of the injector is curved to match the inner diameter of the shock tube when retracted and is made to mount to a custom port for attachment to the sidewall of the shock tube. 120

Figure 3.26 Results of aerosol loading and uniformity measurements from the Mie-scattering extinction diagnostic using the final two-holed injector geometry. Non-uniformity is measured at 5% at the completion of the filling process. Detector A corresponds to a Mie scattering measurement location near the aerosol test section outlet tube, and Detector D corresponds to a measurement location nearest to the injector, as shown in Figure 3.21. 121

Figure 3.27 Aerosol generation tank (AGT) assembled with mixing fan motor (blue power drill modified for remote operation). 123

Figure 3.28 View of the final construction of the shock-tube gate valve. a) Gate valve in closed position without aerosol test section attached; b) Gate valve assembled in the open position with aerosol test section and outlet tube connecting to the dump tank. 123

Figure 3.29 View of shock-tube assembly from driven endwall with optical table and associated laser diagnostics.....124

Figure 3.30 Aerosol injector attached to AGT and shock tube with accompanying pneumatic ball valve. 124

Figure 3.31 View from driver manifold looking toward the driven endwall. 125

Figure 3.32 Alternate view of the facility from endwall of driven section. 125

Figure 4.1 Velocity decay plot of a shock wave passing through the driven section in air. T_5=1013 K, P_5=7.04 atm. The extrapolated endwall velocity is 0.876 mm/μs. 129

Figure 4.2 Velocity decay plot for a shock wave in an aerosol experiment. The buffer gas is air and the aerosol is air with Jet-A fuel droplets. The mixture is a fuel-air mixture of Jet-A at ϕ=0.95 with T_5=1025 K, P_5=12.80 atm. Linear decay profiles are fit to the velocity data upstream and downstream of the gate valve, respectively, as well as all of the velocity data together. The fit through the downstream data results in V=0.932 mm/μs, whereas the fit thorugh all of the data results in 0.925 mm/μs, a difference of 0.6%, or a difference of approximately 7 K when calculating T_5. 131

Figure 4.3 Shock wave velocity decay with linear fit extrapolation for an experiment where aerosol was allowed to settle, showing that heaters have little or no effect on the velocity decay behavior of the shock wave near the endwall. T_5~1300 K. The sidewall window port heaters are approximately 5.5 cm from the endwall. 133

Figure 4.4 Pressure time history from endwall-mounted pressure transducer after passage of shock wave in an experiment using aerosol. Driven Buffer-air, Driven Aerosol- Jet-A in air, Driver gas-16% N_2/He , T_5=1025 K, P_5=12.8 atm, $\phi = 0.95$. 137

Figure 4.5 Pressure time history from endwall-mounted pressure transducer after passage of shock wave. Driven gas-N_2, Driver gas-16%N_2/He, T_5= 1086 K, P_5= 5.35 atm. 139

Figure 4.6 Shock-tube driven section pressure transducer spacings and arrangement prior to installation of gate valve. 140

Figure 4.7 Pressure time histories from pressure transducers as shown in Figure 4.6 with a shortened driver section without the U-bend. The Arrival of the incident shockwave occurs first at transducer T_1 and last at the endwall transducer T_5. Individual pressure traces are offset vertically for easier viewing. Experimental conditions: Driver gas-He, Driven gas-Ar, T_5=1785 K, P_5=2.02 atm. 142

Figure 4.8 Pressure time histories from pressure transducers with an elongated driver section including the U-bend. The Arrival of the incident shock wave occurs first at transducer T_1 and last at the endwall transducer T_5. Individual pressure traces are offset vertically for easier viewing. Experimental conditions: Driver gas-He, Driven gas-Ar, T_5=1879 K, P_5=3.77 atm. 143

Figure 4.9 Ignition delay time plots for methane in air with an equivalence ratio of ϕ = 0.5. a) Experimental pressure, P_5, normalized to 1.5 atm. The data from Petersen et al. were recorded for P_5 < 1 atm. b) Experimental pressure, P_5, normalized to 4 atm. Data from Bowman et al. used Ar instead of N_2 as a surrogate for air.....145

Figure 4.10 Laser diagnostic setup for verifying aerosol vaporization and subsequent measurement of fuel concentration using a Mie scattering and absorption spectroscopy diagnostic, respectively.....152

Figure 4.11 Evaporation and fuel concentration measurement of aerosols composed of fuel droplets in air after passage of the incident shock wave. The black trace represents scattering of the 650-nm laser by aerosol droplets, while the red line represents gas-phase absorption of the vaporized fuel at an IR wavelength of 3.39 microns. Time zero on the plots correspond to the arrival of the shock wave at the endwall of the driven section. The temperature of each experiment is around 1000 K and the pressure is in the range of 9.4-12.8 atm. a) Decane/Air, b) Jet-A/Air, c) DF-2/Air. 155

Figure 4.12 a) Schematic setup of example emission diagnostic configuration, b) Emission traces from sidewall and endwall detector locations with ignition delay time defined as the zero-intersection of the steepest slope of the endwall detector.....157

Figure 4.13 Pressure and emission time histories behind reflected shock waves for sidewall and endwall measurement diagnostics in the aerosol shock tube from various aerosol fuel experiments near 1000 K and 10 atm. a) Decane/Air, b) DF-2/Air, c) Jet-A/Air. 158

Figure 5.1 Ignition delay time data collected in the aerosol shock tube for mixtures of decane in air at ϕ=1.0 and P_5=11 atm and corrected using correlations from Olchanski and Burcat [131]. The data from the aerosol shock tube are compared to those of Shen et al. [9]. 163

Figure 5.2 Ignition delay times collected in the aerosol shock tube with DF-2/air mixtures compared to data from Alturaifi et al. [23] a) Stoichiometic equivalence ratio, b) lean equivalence ratio, also including data from

Haylett et al. [15]. All data are corrected using the DF-2 correlation from Alturaifi et al. 165

Figure 5.3 Ignition delay times collected in the aerosol shock tube with Jet-A/air mixtures compared to ignition delay time data from Alturaifi et al. [23]. a) Stoichiometric equivalence ratio, b) Lean equivalence ratio. All data are corrected using the Jet-A correlation from Alturaifi et al. 167

Figure 5.4 Ignition delay times collected in the aerosol shock tube with GTL-Diesel/air mixtures compared to DF-2 ignition delay time data from Alturaifi et al. [23], DF-2 ignition delay time data from this study, and DF-2 data from Haylett et al. [15], all at lean equivalence ratios. All data are corrected using the correlation from Alturaifi et al. 169

Figure 5.5 x-t diagram of the time experienced by a fluid element at an arbitrary location upstream from a sidewall measurement station compared to the time 180

Figure 5.6 Illustration of sources of discrepancy between Mie scattering uniformity diagnostic and fuel concentration diagnostic. The jet causes induced vorticity which disperses the aerosol. Once the jet is attenuated, however, the flow is slower and less likely to have regions of high vorticity where mixing happens. 184

Figure 6.1 Results of CFD simulations of the aerosol injection process in the aerosol test section. The total duration of the simulation is 3.5 s with steps of 0.5 s between each picture (simulation time steps are 0.01s). The top set of pictures displays velocity contours, and the bottom set of figures displays droplet mass concentration, each from a central horizontal slice coincident with the central axis of the shock tube. The injector geometry used is similar to that of the final design of the final aerosol injector geometry used in this study. 197

Figure A.1 Time-varying behavior of laser signals over the course of approximately 30 minutes. The (I_0-I) signal is offset by +1.0 V for easier comparison to the I_0 signal. 221

LIST OF TABLES

Page

Table 2.1 Calculated values of terminal settling velocity for water droplets in air. 30

Table 2.2 Droplet breakup regimes by Weber Number. 44

Table 3.1 List of flow path parameter configurations and their associated figure references. 96

1. INTRODUCTION

In a global economic environment where energy needs continue to grow and diversify, hydrocarbon consumption has continued to be the stalwart supply of much of the world's energy needs. Although new modes of power generation are coming to the forefront of public interest in the United States, the consumption of hydrocarbons has continued to increase over the past half-century [1]. In particular, the US transportation sector had an average petroleum-product consumption of roughly 14 million barrels per day in 2018, which is one of the highest-consumption years on record. Additionally, until the energy storage capabilities of alternative methods of power generation approach that of conventional petroleum-based methods, the transportation sector will likely continue to use hydrocarbons as its primary energy supply. While hydrocarbons will continue to be a significant contributor in satisfying energy demands in the near future, the ways in which they are used will continue to grow and develop.

From the inception of the combustion-driven engine, improved power output and efficiency have been desired improvements for new generations of engines. In the latter half of the 20th century, however, the desire for improved emissions performance was an added requirement in design considerations for engine manufacturers. Modern engines continue to develop with these three areas of emphasis as benchmarks for improvement: power generation, efficiency, and low emissions. One such engine which has gained significant notoriety in the early 21st century is the homogenous charge compression

ignition (HCCI) engine [2]. Like engines, fuels and the knowledge of them must also continue improving to comply with stricter power and emissions and requirements.

1.1. **Motivation for the Study**

When considering various lanes of interest in directing efforts towards improving engine performance, chemical pathways of fuel combustion must also be considered. In fact, with tens, hundreds, or even thousands of components in a conventional fuel, there is much to examine when investigating the combustion behavior of a given fuel. For example, there can be upwards of 100 component groups (such as various types of C_7-, C_8-, and C_9-benzenes, etc.) to consider when examining petroleum-based fuels with high energy density like diesel and jet fuels. Newer gas-to-liquid (GTL) fuels made using the Fisher-Tropsch process [3] have fewer components and component groupings than do conventional petroleum products derived from crude stock, yet they are still composed of a large number of components themselves [4]. Furthermore, with so many components in high-energy-density fuels, simulating the full fuel mixture during combustion in a chemical kinetics software package is not possible due to the high number of reactants and higher number of resultant intermediates and reactions. Thus, it is necessary to simulate the combustion environment of an engine with surrogate models which mimic both thermodynamic and combustion behaviors of the full fuel mixture [5]. Yet, with such complex fuels and mechanisms [6], significant experimentation is needed in the laboratory to validate these large mechanisms prior to implementing them in engine design. One instrument used to investigate the combustion properties of a fuel and validate mechanism behavior with data from the laboratory is a shock tube, which is a device that produces a

near-zero-dimensional environment in which various combustion properties of a fuel can be isolated and examined without interference from environmental factors such as fluid flow and pressure fluctuations. Many shock-tube studies investigating the combustion properties of real fuel-air mixtures have been conducted, mostly since the beginning of the 21st century.

1.1.1. Recent Combustion Studies of Real Fuels and Related Constituents

Although full simulation of a real fuel with hundreds or thousands of components is not yet possible, a shock tube is still a valuable tool with which the combustion properties of a given fuel mixture may be investigated for the purposes of model validation. Several combustion studies of real fuels, and their major components, have been undertaken over the past couple of decades. Of course, studies of larger hydrocarbons were undertaken several years and decades prior to the turn of the 21st century, but homogenous mixtures of real fuels in air had not been carried out until relatively recently by shock-tube experimentalists. In general, these studies were conducted with the intent of investigating the combustion behavior of real fuels and their constituents in high-temperature and -pressure environments, respectively, for the purpose of model validation.

When considering combustion-modeling calculations of a real fuel, modelers are interested in performing such calculations with a surrogate fuel mixture. Such a mixture mimics the overall combustion behavior of a real fuel, without the requirement of having hundreds or thousands of constituents like a real fuel. As computing power has increased in recent decades, modern combustion modelers have gained the capability of simulating the combustion behavior of surrogate fuels with a surrogate formulation consisting of

several components. However, even as recently as 10-15 years ago, the aim of surrogate formulation was to determine an appropriate surrogate from a single component due to limitations in computing power [7]. Thanks to continual advances in computing power, however, multi-component surrogate models have been developed, and various kinetics solvers have been formulated with which complex reaction mechanisms can be investigated and tuned using laboratory data.

When tuning chemical kinetic mechanisms, various types of data are used to validate different portions of the functionality of a given mechanism. Furthermore, different types of data can be collected in a shock tube which aid in mechanism validation. For the purposes of this work, and this review, however, the discussion of the studies herein will be focused primarily on ignition data collected in shock tubes. Such data are aimed at the global validation of the mechanism. Aside from ignition delay time measurements in shock tubes, some discussion will also be given on ignition data collected in rapid compression machines (RCMs) and other devices. In order to gain a more thorough picture of the state of current research involving liquid fuel combustion and the governing chemical kinetic phenomena, it is necessary to discuss ignition data from various types of facilities. This inclusivity is because the different types of facilities, while all intended for the collection of ignition data, investigate different temperature regimes (and by extension, different temporal regimes). In short, shock tubes are primarily intended for the investigation of high-temperature chemistry above temperatures of roughly 950 K, which generally tends to occur on time scales of tens of microseconds to several milliseconds in hydrocarbons. RCMs, and other types of flow reactors, on the other

hand, are intended for the investigation of low-temperature combustion chemistry below roughly 900 K. The time scales of these lower-temperature combustion events can last for a couple to tens of milliseconds in hydrocarbon mixtures. This regime of above roughly 950 K is generally referred to as the high-temperature region when considering ignition delay time behavior of hydrocarbons. The regime below roughly 950 K is referred to as the low-temperature region, and the temperature region in the middle of the two from roughly 900-1000 K (for liquid fuels) is referred to as the negative temperature coefficient (NTC) region. The significance of this is discussed in a separate section.

The aim of the various experimental studies reviewed herein can be separated into three main categories in terms of the fuel mixtures investigated: real fuels, single-component fuels, and multi-component fuels. From an experimental perspective, both single- and multi-component fuel data can be compared to real-fuel data for the purpose of surrogate formulation. If the ignition behavior of a surrogate aligns well with that of the real fuel, then the surrogate is a good candidate for formulation and validation of various combustion kinetics models. Additionally, single-component fuels can be studied for the purpose of direct comparison of ignition behavior between various components. For example, n-decane and n-dodecane can be studied independently to see which fuel is more reactive, providing information on which component may be more influential in the global behavior of pre-ignition chemistry. Similarly, mixtures of 2 components can also be investigated with various mixing ratios to study the parametric effect of component concentration on combustion behavior. An example of this type of study is the comparison

of mixtures with high alkane concentration versus high aromatic concentration, aimed at determining the effect of differing hydrocarbon groupings on global ignition behavior.

1.1.1.1. High-Temperature Ignition Chemistry

As previously mentioned, many studies have been conducted in which the ignition behavior of single-component hydrocarbons was investigated. In the work by Horning and coworkers [8], the ignition behavior of several n-alkanes was studied in a shock tube over a temperature range of 1300-1700 K. A correlation based on normal alkane chain length was formulated with a goodness-of-fit parameter (R^2) of 0.992. It was also observed that when the data were scaled to a normalized pressure and oxygen content, ignition behavior of the 4 n-alkanes (C_3, C_4, C_7, and C_{10}) decreased as the carbon number in the fuel increased. Thus, propane showed a longer ignition time than n-decane at equivalent experimental conditions. Furthermore, the longer-chain molecules displayed similar ignition behavior to one another than the shorter chains; this is evidenced in their empirically formulated ignition correlation, which has an ignition dependence on carbon number of $\tau \propto C^{-0.5}$. This correlation yields the ignition delay time of C_9 being closer to that of C_{10} than C_3 is to C_4 for identical experimental conditions. One observation from such a result is that the ratio in ignition time based on 2 carbon adjacent carbon numbers, C_n and C_{n+1}, approaches unity as n increases. Consequently, alkanes with similar carbon numbers, as n approaches roughly 10 and beyond, should exhibit similar ignition delay time behavior. Such behavior in alkanes was confirmed by the work of Dean et al. [7] who collected shock-tube ignition data of n-hexane, n-decane, and mixtures of the two. Shen et al. [9] also confirmed similar ignition behavior between n-alkanes when they

investigated the ignition behavior of 4 n-alkanes from n-heptane to n-tetradecane ($C_{7\text{-}14}$) in shock tubes. Further verification of this behavior in n-alkanes was given by Davidson et al. [10] when they investigated the full range of n-alkanes from $C_{4\text{-}10}$ (their carbon-number dependence for ignition was $\tau \propto C^{-0.39}$) and by Rotavera and Petersen [11] when they investigated n-nonane and n-undecane (both studies in shock tubes). From these studies, and the many others which investigated normal alkane combustion chemistry (the studies listed here are by no means an exhaustive list), it can be inferred that the combustion behavior of n-alkanes is roughly independent of carbon number in the high-temperature regime of ignition chemistry behavior.

Besides comparing ignition delay times of n-alkanes to one another in the high-temperature ignition regime, various investigators have studied the behavior of other components relative to that of n-alkanes. In addition to comparing ignition delay times of pure alkane components, Dean and coworkers [7] also compared ignition delay times of an aromatic species, benzene, to the n-alkane, n-decane. While the ignition behavior of the two was similar, the benzene ignition behavior was noticeably longer than that of n-decane. In addition to n-alkanes, Flora et al. [12] compared alkane isomer (iso-alkane) ignition behavior to that of aromatics. The iso-alkane ignition behaviors were similar to those of their n-alkane counterparts, but aromatic ignition behavior of m-xylene was again slower than either of the alkane groups, similar to the study by Dean et al.

Although kinetics models can be tuned against ignition data from single-component fuel mixtures, the ultimate goal of combustion simulation packages is to simulate real fuels. Thus, data from real fuels must be collected at realistic engine

conditions, similar to those of the single-component fuel ignition data discussed in the preceding paragraphs. Some of the authors of the aforementioned studies also investigated real liquid fuels to compare ignition behaviors to those of single-component fuels. In addition to collecting alkane ignition data, Dean et al. [7] also studied the kerosene-based fuel Jet-A over the range of 1000-1700 K and pressures near 8.5 atm. Other investigations of various types of jet, diesel, and/or rocket fuel were also conducted by a wide range of conditions by various groups (which overlap with some of the aforementioned ignition studies) including Vasu et al. [13], Wang and Oehlschlaeger [14], Haylett et al. [15], Gowdagiri et al. [16], Zhukov et al. [17], Zhang et al. [18], Zhu et al. [19], Davidson et al. [20], De Toni et al. [21], Flora et al. [12], Burden et al. [22], Alturaifi et al. [23], Mao et al. [24], and Wang et al. [25]. From the results of these studies, it can be observed that the ignition delay time behaviors of various types of jet, diesel, and rocket fuels are generally similar in nature. The reason for this is based on common components shared by all of these liquid fuels.

When investigating the ignition behavior of a fuel, the types of constituents of which the fuel is composed play a significant role in determining the combustion behavior of the fuel. In the case of jet, diesel, and rocket fuels, these fuels behave similarly with regard to their ignition behaviors in the high-temperature ignition regime. Furthermore, synthetic fuels derived from Fisher-Tropsch processes exhibit ignition behavior similar to their counterparts derived from crude stock [12, 14, 19, 26]. If so many various types of fuels, with different formulations and production methods display similar ignition behavior, then what are the commonalities among these fuels? As previously mentioned,

a given fuel may contain upwards of hundreds or thousands of different of hydrocarbons. Yet, during a combustion reaction, all of these different compounds are broken down into smaller compounds, including high-energy radical species, prior to recombining to form products. A sensitivity analysis of a modern reaction mechanism prior to ignition of a combustion reaction in the high-temperature ignition region (such as those conducted in the works of Zhang, Flora, Mao, Wang, and coworkers, respectively [12, 18, 24, 27]) reveals that the chemistry is most influenced by reactions involving these smaller radical species, and not larger species like the initial fuel molecules. This influence of the smaller species is confirmed by the behavior observed in works like that of Oehlschlaeger et al [28], which showed that iso-octane is somewhat more reactive than iso-cetane, for equivalent conditions, because iso-octane is broken apart into CH_3 radicals more quickly than iso-cetane. Additionally, before the ignition phenomenon is able to occur during combustion, the number of radicals must reach a minimum threshold prior to the occurrence of the high energy release commonly associated with ignition. For radicals to be formed, they must undergo abstraction from carbon bonds. This abstraction most easily occurs by oxidation of constituents (fuels and fuel fragments) with carbon numbers in the range of C_1-C_4, which play a prominent role in controlling the overall rate of the reaction compared to the larger fuel molecules. From the work of Flora et al. [12], it is observed that both light branching and alkane chain length does little to affect ignition behavior because the predominant reactions where radicals are formed come from the breakup of C_1-C_4 fuel fragments. By extension, fuel component groups such as aromatics and cyclo-alkanes are not as quickly broken into radicals because the carbon rings must first be

broken apart and, in the case of aromatics, C=C double-bonds must also be broken. In summary, although many fuel mixtures are composed of various types of fuel components, if they contain significant amounts of n- and iso-alkanes, they will display similar ignition behavior to one another in the high-temperature ignition regime because the reaction chemistry is controlled primarily by C_1-C_4 chemistry and in turn by radicals formed from these C_1-C_4 compounds and to a much lesser extent by the original composition of the fuel mixture themselves.

1.1.1.2. Low-Temperature Ignition Chemistry

Until recently, shock tubes have not been utilized to investigate low-temperature ignition behavior on a regular basis until relatively recently due to their inability to obtain test times longer than several milliseconds coupled with experimental non-idealities [29]. While most studies referenced in this review investigated some form of high-temperature ignition chemistry using shock tubes, several also investigated the NTC- and low-temperature regimes, respectively, which required the use of a reactor vessel different from a shock tube. Such a vessels include the rapid compression machine (RCM) and other types of flow reactors. Some studies employing these other devices to study NTC and low-temperature combustion of liquid fuels are those by Kumar and Sung [30], Dagaut et al. [26], De Toni et al. [21], and Burden et al. [22]. In addition to these other devices, shock tubes have also begun producing reliable results in the low-temperature and NTC regime within the last decade. For example, the Oehlschlaeger group at Rensselaer Polytechnic Institute have presented ignition data in shock tubes with test times up to 10 ms in their works by Wang and Oehlschlaeger [14] and Gowdagiri et al. [16]. These

studies were able to examine the full scope of the NTC ignition region, and some of the low-temperature ignition region at various pressure conditions in shock tubes for some common liquid fuels.

Harking back to the brief mention of negative-temperature-coefficient (NTC) and low-temperature ignition chemistry in a preceding section, the nature of these ignition regimes is now discussed in some more detail as follows. The reason for referring to different temperature regimes in characterizing the behavior of ignition chemistry is because different types of chemistry govern the overall behavior of the combustion reaction in each different temperature regime. In the high-temperature regime, the formation of small, high-energy radical species (H, O, OH, for example), which require the kinds of temperatures available in the high-temperature regime, govern the ignition behavior of the combustion reaction. In the NTC and low-temperature ignition regimes, however, many of the reactions that take place in the high-temperature regime are not able to take place because the average energy of the system is not high enough to form the radical compounds required for high-temperature ignition chemistry. As the initial temperature at which the combustion reaction occurs is raised, more high-temperature radicals are formed, and the reactions which are not accessible at lower temperatures become more prevalent. Thus, while smaller, high-energy radicals govern high-temperature ignition, larger radicals, including alkyl and alkylperoxy radicals, play a more significant role in the oxidation of fuels in the low-temperature and NTC regimes. Furthermore, the NTC regime serves as a transition, of sorts, between the high-temperature and low-temperature regimes. In the low- and high-temperature ignition

regions, respectively, increasing the initial temperature at which the reaction is initiated increases the overall rate of reaction (raise the temperature and the combustion event proceeds more quickly). However, in the NTC regime, as the initial temperature is raised, the overall reaction rate is decreased and ignition exhibits a negative temperature dependence, $\tau \propto T^{-n}$, which gives rise to the name describing this intermediate ignition region. More discussion on the nature of these combustion regions is given by Carrigan et al. [31].

1.1.2. Challenges of Studying Real Fuels in Shock Tubes

Because of the low volatility of common liquid fuels, the majority of the studies discussed in this brief review were conducted in facilities equipped with heating systems. A couple of studies investigated some fuels which are commonly gases at room temperature and therefore did not require heating (lower pressures and carbon numbers at or below C_7). One exception to the studies that investigated liquid fuels and required heating is the work conducted by Haylett et al. [15], which was conducted without a heating system and is discussed later. A heating system enables low-volatility liquids to be studied in the gas phase by raising their vapor pressures. Once the vapor pressure of the fuel is raised substantially enough, a gaseous mixture can then be prepared with a sufficient concentration for conducting medium-to-high-pressure shock-tube experiments. Gas-phase-shock-tube experiments involving larger hydrocarbons, however, traditionally use heating systems. Although such methods are intended to avoid issues with vapor condensation, they do not come without challenges as they introduce various complications into the experimental procedure.

One property of high-energy-density liquid fuels, which make them excellent candidates for use in transportation-focused engines also happens to cause difficulty when investigating their behavior in the laboratory. This property is the general tendency for the fuels to be composed of compounds with low to very-low vapor pressures. There are, of course, many factors influencing a fuel component's vapor pressure, but in general the larger the molecule, the greater the vapor pressure. Thus, these fuels and molecules will henceforth generally be referred to as "heavy" or "low-vapor-pressure" hydrocarbons. The low volatility of such molecules makes them very stable and relatively low risk for storing or transporting. However, when introducing such liquid molecules into a reactor vessel for the purpose of studying their behavior in a gas-phase chemical kinetics measurement, several challenges arise which impede the acquisition of reliable kinetics data.

The most obvious difficulty associated with using a low-vapor-pressure liquid fuel as a constituent in a room-temperature, gas-phase shock-tube experiment is the fact that the gas-phase mixture will likely not have a high enough fuel concentration to collect meaningful data. In general, shock-tube experiments conducted where the initial temperature before the experiment is near room temperature require the fuel portion of a given mixture to have a partial pressure in the range of 10-100 torr (for realistic fuel-air mixtures). This range enables the mixture to have a sufficiently high equivalence ratio for the intended application. Such room-temperature experiments can be conducted with relative ease for hydrocarbons with carbon numbers up to approximately C_7. Depending upon the conditions, alkanes with carbon number of C_8 and even C_{10} can be investigated in a shock tube at room temperature, but the maximum mass loading that can be achieved

is limited. Thus, to study the combustion properties of larger hydrocarbons in detail, another technique is required to provide sufficient mass loading for components with carbon numbers above approximately C_8.

One solution to introducing components with lower vapor pressure into a shock tube with the intention of achieving high mass loadings in such a system is to raise the temperature of the entire apparatus. Increasing the temperature of the liquid also increases the vapor pressure of the various components in the fuel mixture and helps to keep it suspended in the gas phase. This technique also ensures that a sufficiently high equivalence ratio can be achieved when investigating fuels with heavy hydrocarbons and is indeed the method which has often been employed when investigating fuels and other liquids with low vapor pressure [23]. When the temperature of a shock-tube facility is raised to accommodate components with low vapor pressures, the temperatures required are generally more than a few degrees above room temperature, however. Often, the entire shock-tube apparatus (plumbing, mixing tanks, pressure manometers) must be raised to temperatures of roughly 100-200° Celsius. Reaching this temperature range is no small feat when considering the amount of mass which is required to be heated. Such heating adds significant complexity from an operational standpoint as well. These operational complexities are due in part to thermal expansion of joints and tubing associated with the shock-tube setup. The tendency of the facility to leak is significantly increased, and leak rates of heated systems are rarely as low as those of unheated systems. Such an undertaking of heating the shock tube can also introduce new challenges which are not

present at room temperature in dealing with the behavior of the heavy hydrocarbons themselves.

Although heating a low-vapor-pressure fuel may increase its vapor pressure, such heating may activate other modes of instability in the fuel which are not present at common, laboratory room temperatures. Such instability is related to the molecules themselves and to the fuel mixing ratios. If insufficient heating is applied to the shock-tube apparatus such that the temperature is too low, there arises the potential for the fuel to become fractionally distilled. That is, some of the heavier components in the mixture will not remain in the gas phase and will condense, settling on the walls of the system. Additionally, if temperatures are too great or residence times (on the order of hours) are too long, fuel cracking or pyrolysis can occur. These added complexities associated with heated shock-tube experiments are not impossible to overcome, however, but must certainly be accounted for when taking precautions to correctly operate a heated shock-tube facility.

Heating a shock tube to vaporize fuel is an effective method of ensuring all or most of a given fuel mixture remains suspended in the gaseous phase. However, when considering the composition of fuels, there is a limit to how much heating can be applied in an attempt to vaporize all of the constituents. The heaviest constituents are not able to be fully vaporized for heating temperatures under 200°C. This limitation can be a significant problem if the mixture contains substantial amounts of such components. Based on the work of Assad et al. [32], it would seem that hexadecane, and similar such C_{16} fuels, should be considered as the approximate upper limit in regards to how large a

given constituent can be for a viable-heated shock-tube experiment. Thus, if C_{16} is an upper limit regarding the rough size of a molecule when considering heavy hydrocarbon combustion, the question arises as to how heavier hydrocarbons should be investigated. What methods, then, should be used if heating is no longer a viable option for investigating molecules with greater than C_{16} carbon numbers? This dilemma is especially concerning considering that both diesel and jet fuels are composed of many components with carbon numbers of C_{16} and greater. Further, how can a kineticist go about examining renewable fuels, which are often produced from bio-derived feedstocks, since they too are composed of large hydrocarbons, the majority of which tend to be larger in size at C_{16} and beyond [33]? It may seem like the answer is to proceed further beyond the room-temperature condition and heat the fuels above the range of 100-200 C. This path is not a wise endeavor, however, as additional stresses associated with further heating and resultant degradation of physical properties make the desired experimental pressures relevant to engine conditions unsafe when conducting experiments in most modern shock tubes. The solution to proceeding towards experimentation of larger fuels with higher carbon number without continuing to higher temperatures is to not heat the fuel at all but rather to suspend it in droplet form directly within the shock tube itself.

Although heated shock tubes provide advantages in increasing the vapor pressure of many low-vapor-pressure fuels such that they can be easily vaporized when compared to conventional shock tubes, they nonetheless have limitations in regard to the maximum heating temperature and molecular carbon number that can be utilized effectively. Thus, the solution to these limitations is to bring the shock tube back to room temperature and

introduce the fuel directly into the shock tube as an aerosol prior to the experiment. When a shock-tube experiment is initiated, the aerosol is evaporated and the experiment continues in the same manner as a traditional gas-phase experiment. Such a technique for investigating liquid combustion behavior for hydrocarbon mixtures in shock tubes was developed and refined in the works of Davidson et al. [34] and Haylett et al. [35], respectively. This process avoids the potential of fuel cracking or partial distillation in that the process of droplet evaporation behind a shock wave effectively decouples the heat transfer process of evaporation from chemical-kinetic processes. These works of Davidson et al. and Haylett et al. are, of course, not the first studies of aerosols and/or droplets in shock tubes (to be examined further in a subsequent section), but they are the first to successfully develop methods for studying homogeneous mixtures of fuel in aerosolized form in shock tubes in a highly controlled manner. Prior to describing this aerosol process further, however, it is necessary to provide an overview of the basics of shock-tube operation.

1.2. **The Working Principle of a Shock Tube: The Shock Wave**

When considering the various types of instruments used to study combustion in the laboratory, the first device that may come to mind for those not familiar with the field of combustion science is a flame burner. While this apparatus is of course a valuable instrument used for studying combustion, scientists will employ various types of reactor vessels for the purpose of investigating the combustion properties of a fuel. Among these are plug flow reactors, well-stirred reactors, and constant-volume reactors. More information on some of the different forms of combustion flow reactors is given in various

texts, including those by Turns [36] and Law [37]. Although it can be used in other ways, a shock tube will be used as a constant-volume reactor for the purposes of this work.

A shock tube, as indicated by its name, is a device which generates shock waves in gases for the purposes of investigating fluid mechanic and thermodynamic phenomena. A shock wave, unlike a pressure wave, is a positive discontinuity in thermodynamic properties (variables temperature, pressure, density, velocity, etc., increase across a shock wave), through which information about such properties cannot propagate. This phenomenon is because a shock wave is created by the acceleration of a series of pressure waves, which travel at the speed of sound, until eventually all the pressure waves coalesce at a final speed greater than the speed of sound in the given gaseous medium into which they are propagating. Thus, since a shock wave is traveling at a speed greater than or equal to the speed of sound in the medium, thermodynamic information in the form of either fluid flow or, primarily, pressure disturbances, which are transmitted at the speed of sound, cannot cross the discontinuity of the shock wave. This property of shock waves, in addition to being nearly planar in shape, in a shock tube, is advantageous for chemical kinetics experiments in multiple ways.

Since the shock acts as a thermodynamic discontinuity for the gases which it passes through, there is no long period of relaxation, or delay, during which the properties of the shock-processed gases relax to the conditions behind the shock wave; their thermodynamic properties are near-instantaneously altered as the shock passes through them with respect to the time scales of one might consider in flow reactors (that is, within microseconds). Such an instantaneous increase in properties results in the chemical kinetic

reaction process being de-coupled from any heating process. In a flame burner for example, the gas is heated over a period of time until it begins to burn (this time is relatively short to a human observer, but it is quite long relative to kinetic time scales). This temporal heating links the kinetic processes to the heat transfer processes. In a shock tube, however, since the gas is heated instantaneously, the heat transfer process does not influence the temporal behavior of the kinetics, and the time-dependent chemical kinetics can be examined without influence from heat transfer effects.

Another advantage of using shock waves to examine chemical-kinetic behavior is that they are roughly constant in velocity and nearly planar in geometry, which means that the shock processes the gas through which it propagates in a uniform manner. Thus, if the properties of the region into which the shock propagates are spatially uniform then the region behind the shock wave will also be uniform in its thermodynamic properties (or nearly so) in directions both parallel to the shock front and perpendicular to it as well. Furthermore, when a shock wave reflects off of a flat surface which is oriented perpendicular to the direction of shock propagation, the region behind the shock wave reflection will be stagnant or have no mean velocity. This region behind a reflected shock wave can also be referred to as zero-dimensional, in which the properties are constant with respect to the 3 spatial dimensions. Take again the example of the flame burner. Such a device uses flow to produce a steady flame, but the gas in the flame is not in a steady state, in fact. The gases are moving and the flame itself has spatial temperature and pressure gradients. These gradients greatly affect the way in which the gas in the various parts of the flame burn. But in zero-dimensional environments, the environment is uniform

spatially which prevents any temperature or pressure gradients from affecting the bulk of the flow behind the reflected shock wave and influencing the kinetics. Thus, the kinetics are decoupled from spatial effects and non-stagnant flows.

As briefly discussed above, a shock tube takes advantage of the nature of shock waves to instantaneously increase the temperature, pressure, and density of gases. More detail on the formation of shock waves and other gas-dynamic phenomena can be found in the foundational text of Gaydon and Hurle [38]. Next, a brief overview of the basic geometry and operation of a shock tube is presented.

1.3. **Shock-Tube Geometry and Operational Basics**

In general, shock tubes are vessels used for the study of thermodynamic, fluid mechanic, and chemical kinetic phenomena involving high-temperature gases (~ 600-4000 Kelvins). The basic geometry of a shock tube, as the name indicates, is tubular in form and can have varying length and diameter depending upon the applications of interest. An example diagram of a shock tube is shown in Figure 1.1. The tube is portioned into two separate sections referred to as the driver and the driven sections, respectively. Between these sections is an interface of either plastic or metal material (typically), which is known as the diaphragm. Prior to the initiation of a shock wave, the diaphragm is inserted between the 2 sections, and the tube is sealed from the lab environment. The driven section is then filled with a test gas of interest at an initial pressure of the experimenter's choosing. Similarly, the driver section is filled to a high pressure until the

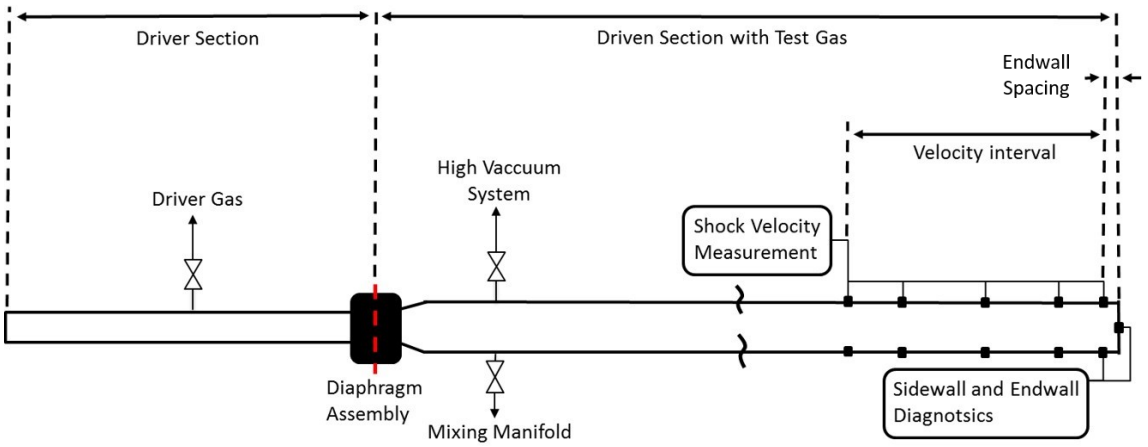

Figure 1.1 An example shock-tube schematic diagram.

diaphragm ruptures. Diaphragm-rupture pressures depend upon both the thickness and strength of the diaphragm material. This pressure in the driver section at the time of diaphragm rupture is what determines the strength of the shock wave. In general, since shock waves travel at a speed greater than or equal to the speed of sound, it is often convenient to use the convention of Mach number as a measure of the strength of the shock wave, and not driver pressure. After diaphragm rupture, the experiment is considered to have been initiated.

A shock-tube experiment for the purposes of this work is generally intended to provide a steady-state environment in which a chemical kinetics experiment can be performed. The process of shock wave generation and propagation in a shock tube, however, is an inherently unsteady process, and different gas-dynamic phenomena related to the shock wave are present in the shock tube at a given time during the experiment. It is convenient to diagrammatically separate these different processes into regions in both space and time. Such a diagram which is convenient for use with shock tubes is the x-t

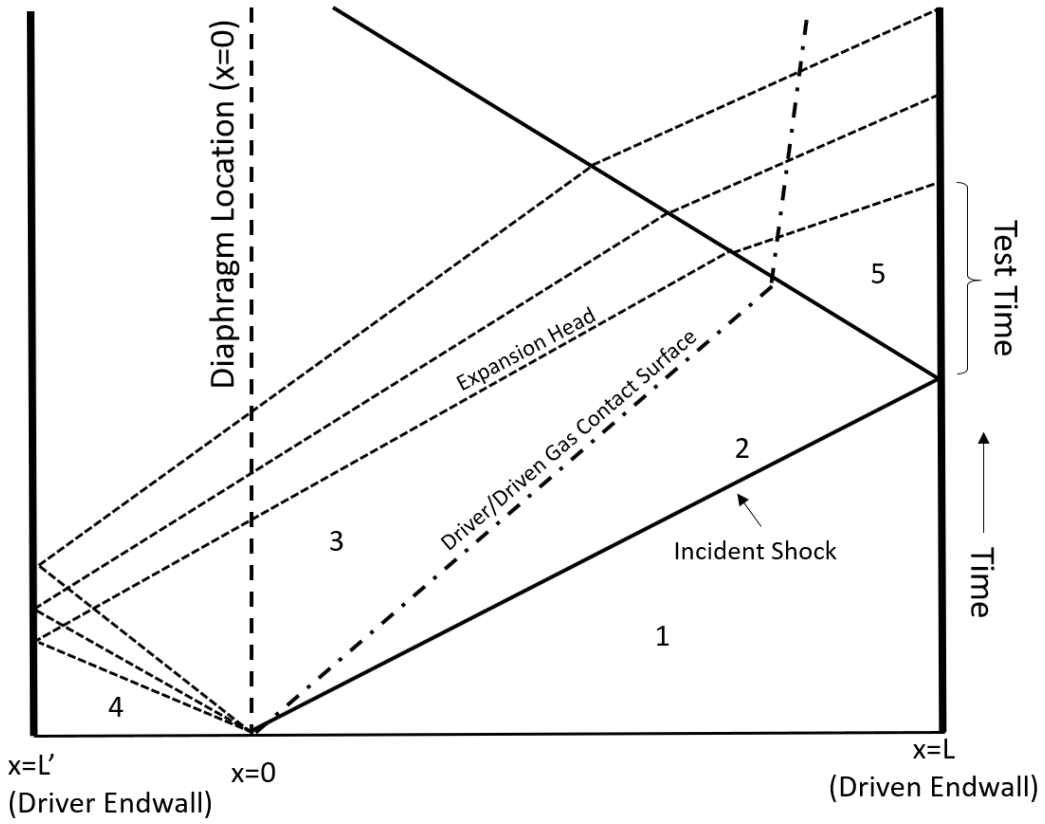

Figure 1.2 A distance versus time (x-t) diagram representing the spatial and temporal distributions of phenomena during a shock-tube experiment

diagram. The process of a shock-tube experiment is shown on a typical x-t diagram in Figure 1.2. At time t=0, the experiment has yet to begin (diaphragm is unruptured and no shock is formed) and the driven section and driver section each have distinct pressures. When the diaphragm ruptures, a shock wave is formed and propagates towards the driven endwall of the tube. To maintain conservation of mass and energy, an expansion wave travels in the opposite direction towards the endwall of the driver section of the tube. The regions into which the shock and expansion waves travel are referred to as region 1 (driven section) and region 4 (driver), respectively. Thus, region 1 and region 4 during the

experiment are at the initial conditions of the tube just prior to the start of the experiment and these are the regions into which the shock and expansion head initially propagate.

As the shock wave travels through the gas in region 1, it increases the temperature and pressure of the gas and also imparts momentum to the gas such that the gas then follows after the shock in the same direction, albeit at a slower speed than the shock itself. This time/space region of shock-processed gases is canonically referred to as region 2. By its name, the gases in region 4 are at a high pressure and they provide the energy to drive the shock wave forward. As is intuitively expected, the gas in the driver rushes into the driven section after rupture of the diaphragm. The driver gases are thus in contact with the gases in region 2. This interface is called the contact surface, and the region formed in the center (axially) of the tube between the contact surface and the expansion head is referred to as region 3. After the shock wave reaches the endwall of the driven section, it is reflected back towards the diaphragm, simultaneously and further heating, pressurizing, and stagnating the gas in region 2. This newly formed region between the now-reflected shock and the driven endwall is referred to as region 5. For the purposes of this work, the region of interest for experimentation is region 5.

As mentioned previously, when the diaphragm ruptures, an expansion wave travels towards the driver endwall. This expansion then reflects and travels back towards the diaphragm and continues toward the driven endwall, lowering the pressure and temperature of the shocked gases as it travels through them. Eventually, this expansion wave envelopes the entire shock tube and reaches the driven endwall. When this event occurs, then the experiment is considered to be completed. As can be inferred from the

explanation of a shock experiment, the length of time in which region 5 exists during a shock experiment is quite short, on the order of 1-10 milliseconds. This time for existence of region 5 conditions, however, is plenty of time in which to conduct a chemical kinetics experiment since the time scales of high-temperature and -pressure chemistry are often in the range of tens of microseconds to milliseconds. Additionally, the conditions in the various regions are considered to be uniform within a given region. For example, the conditions in region 2 are uniform, yet distinct from the conditions in region 5. Measurements of post-incident and post-reflected shock conditions are difficult to make directly, but by using diagnostics and the known initial conditions, the conditions behind shock waves can be calculated.

Modern shock tubes are equipped with various diagnostics. These measurements range from shock velocity and pressure diagnostics, to optical diagnostics for light emission and absorption measurements. As shown in Figure 1.1, a shock tube equipped to study combustion chemistry is fit with a series of pressure transducers near the driven endwall. These transducers are used to track the position of the shock wave as a function of time and back out the velocity of the shock as it makes its way towards the endwall. By knowing the initial conditions prior to passage of the shock wave and measuring the velocity over a region near to the driven endwall, the step increase in thermodynamic conditions imparted to the gases from the shock can be calculated iteratively by using the normal-shock-wave versions of the thermodynamic conservation laws [38]. Time histories of pressure can also be recorded using the same pressure transducers used to measure shock velocity. These sensors are typically mounted at the driven endwall and at a sidewall

location close to the driven endwall [39]. Light emission time histories can also be measured by mounting window ports at sidewall and endwall locations and recorded via optical detectors. Lastly, an ever-expanding suite of laser diagnostics are available to experimenters for the detailed measurement of species time histories [40].

1.4. **Overview and Structure of the Dissertation**

This dissertation is organized into six different chapters. The first chapter provides motivation for the work from both an application and an experimental standpoint. The second chapter provides a brief overview of the governing phenomena controlling the behavior of aerosols in atmospheric flows and shock-tube flows with an eye towards shock-tube experimentation. Chapter three provides all design considerations for both the shock tube and aerosol-generation facilities and gives an overview of the operation of the aerosol shock tube. In Chapter Four, the characterization of the aerosol shock tube is discussed, and non-ideal facility affects are outlined. All experimental ignition delay time data are displayed and discussed in Chapter Five, and the conclusions are drawn in Chapter Six. This dissertation also includes three appendices. The first appendix discusses spectroscopic parameters of the fuels used in this study; the second gives an overview of the method of measuring and calculating thermodynamic properties behind shock waves when an aerosol is part of the pre-shock mixture; and the third and final appendix contains the machine drawings for the facility.

2. AEROSOL AND DROPLET THEORY WITH APPLICATIONS IN SHOCK TUBES

Traditionally, the study of low-vapor pressure fuels in shock tubes has been conducted using the heated shock-tube method, such as in previous works by Rotavera and Petersen [11, 41], Horning et al. [8], Davidson et al. [20], and Shen et al. [9], to name a few. This kind of experiment is due to the low vapor pressures of heavy hydrocarbons; they are unable to be mixed reliably as a gaseous component at standard atmospheric temperatures and pressures using traditional shock-tube mixing methods. Instead, such fuels must either be heated so as to be held in the gas phase, or physically suspended as an aerosol while being introduced into a shock-tube mixture [34, 35, 42]. For the work discussed in this thesis, the heavy hydrocarbons were suspended in a carrier gas as an aerosolized mixture and constrained to a region near the endwall of the shock tube prior to shock wave passage. A diagram of the gate valve setup is shown in Figure 2.1. Prior to detailing the design of the current facility, however, a brief overview of studies from the literature which investigate aerosol mechanics and aerosol-related combustion behaviors is necessary.

In addition to outlining the behavior of small particles and particle-laden mixtures, it also necessary to define precisely the definition of an aerosol. For the purposes of this work, an aerosol is defined as a suspension of solid or liquid particles in a gas [43]. Thus, when liquid droplets are formed and suspended in a gas, the mixture of the two phases is what constitutes an aerosol, not only the droplets themselves. This detail is perhaps not a

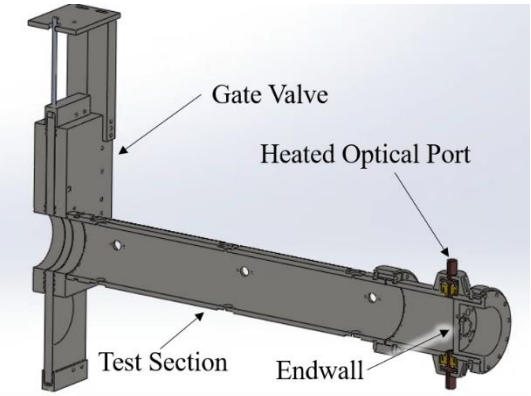

Figure 2.1 A diagram of the gate valve located within the driven section for constraining aerosol near the endwall.

critical distinction but does provide clarity for the purposes of discussion. Further definitions of the varieties and types of aerosols are also given by Hinds [43].

2.1. **Governing Transport Mechanics of Droplets and Aerosols**

When considering the phenomena which govern the transport of droplets in atmospheric settings, few physical effects are coupled due to the relatively low temperatures involved. In flow regimes associated with shock tubes, however, the governing mechanics affecting the behavior of the droplets are significantly more complex due to coupling of various phenomena. Such flow involves high velocities but also high temperatures, activating a coupling between momentum and energy transfer where the droplets are not only changing positions as a function of time, but also temperature and size due to heating and evaporation, respectively. This coupling in the energy equation makes rigorous analysis quite difficult, making coupled analysis of this nature beyond the scope of this work. A general analysis and discussion of the various governing phenomena

is nevertheless necessary to gain understanding of the appropriate methods for handling aerosols intended for use in shock tubes.

Consideration is given here to two types of processes specific to shock tubes which utilize particle-laden flows and the phenomena associated therein; filling the driven section volume of the shock tube with aerosol, and the flow resultant from the propagation of a shock wave through an aerosol. First, when an aerosol is entrained in a flow while filling the shock tube, two general phenomena are considered: 1) velocity and/or momentum relaxation effects, and 2) settling. While introducing aerosols into a shock tube, the general intention when entraining droplets in a gaseous flow is for the droplets to track the streamlines of the flow to be transferred easily between various volumes (from the location of the aerosol generator to the shock-tube driven section). Second, for the flow of aerosols involving shock waves, the ideal behavior of the droplets is to evaporate instantaneously and then diffuse immediately into the carrier gas surrounding the droplets. Such an idealized case is, of course, not completely in line with reality but gives a reference point for what the desired behavior of an aerosol should be in an application such as this.

2.1.1. Settling

An oft-mentioned property of solid particles or liquid droplets is their terminal settling velocity. The terminal settling velocity is a critical parameter because it provides an approximate time scale for how long a particle of a given size will remain suspended in a gas. Such an estimate is critical when considering the time between the completion of an aerosol filling process and the initiation of a shock wave during a shock-tube

experiment which is intended for studying aerosols. If the particles are too large, then the settling time is short and the droplets in the shock tube will have nearly all settled to the bottom of the tube before the shock wave is initiated. Obviously, were this a systematic occurrence, it would be a critical failure for any shock-tube design intended for investigating aerosols behind shock waves. Because settling implies that droplets are effectively in free-fall, this requires that there be no (or relatively little) bulk flow around the droplet itself. Such flow around the droplet can be modeled as Stokes flow where the Reynold number is less than 1 (Re < 1). The Reynolds number is defined as the ratio of inertial forces to viscous forces and is given by Eq. (2.1). The variables of the gas surrounding the droplet are density, ρ, velocity, u, and viscosity, μ, respectively, and D is the diameter of the droplet.

$$Re = \frac{\rho u D}{\mu} \tag{2.1}$$

Setting the drag force equivalent to the gravitational force yields the simple result in Eq. (2.2) where ρ_p is droplet density, d is droplet diameter, g is gravitational acceleration, and μ is viscosity, and C_c is a slip correction factor accounting for differences in pressure, respectively[43].

$$V_{TS} = \frac{\rho_p d^2 g C_c}{18\mu} \tag{2.2}$$

This result, although limited in terms of its rigor for flows with values of Re < 1, yields useful results in considering the relative impact of differing droplet sizes on the terminal settling velocity. Such results can aid in the selection of appropriate droplet sizes

Table 2.1 Calculated values of terminal settling velocity for water droplets in air.

Particle Diameter (μm)	V_{TS} at the Indicated Pressure (m/s)		
	0.1 atm	1.0 atm	10.0 atm
0.001	6.9×10^{-8}	6.9×10^{-9}	6.9×10^{-10}
0.01	6.9×10^{-7}	7.0×10^{-8}	8.7×10^{-9}
0.1	7.0×10^{-6}	8.8×10^{-7}	3.5×10^{-7}
1	8.8×10^{-5}	3.5×10^{-5}	3.1×10^{-5}
10	3.5×10^{-3}	3.1×10^{-3}	2.9×10^{-3}
100	0.29	0.25	0.17

for maximizing settling time. Representative values of terminal settling velocities in air for water droplets of varying diameters are shown in Table 2.1.

It can be seen from the values in the table that there is significant variation in terminal settling velocity as a function of diameter. One noteworthy difference is seen between the 1-micron and 10-micron diameter droplets. At 1 atm of pressure, the 1-micron droplets settle roughly 100 times more slowly than the 10-micron droplets. This difference is due primarily to the fact that the slip correction factor has a value near unity for these droplet sizes, and the mass-to-volume ratio is much greater for 10-micron droplets than for the 1-micron droplets. Thus, it is observed from these values that choosing the appropriate particle size plays a significant role in minimizing settling of an aerosol.

2.1.2. Relaxation

For the purposes of this work, the concept of relaxation is discussed in relation to two separate events involving aerosols. The first event is related to the response of droplets in an aerosol to a change in the direction of streamlines in a flow (like those resulting from

a bend in a pipe or tube). The second type of relaxation process discussed here is relaxation of the aerosol to an equilibrium state after being processed by the shock wave during an experiment. This thermodynamic relaxation affects not only the properties behind the incident shock wave (Region 2), but also behind the reflected shock wave. In particular, the presence of particles or droplets can lead to a significant temperature decrease in Region 5 which is the region of interest for experiments related to aerosol combustion in this work. Petersen and Smith discuss this in their work on the effects of solid particles in shock tubes [44]. They showed significant deviation from ideal, gaseous shock-induced flow behavior as particle concentration was increased. Thus, if particle relaxation effects are not considered, this can lead to an increased uncertainty in thermodynamic calculations in a region where minimizing uncertainty is critical for correct interpretation of recorded data.

2.1.2.1. Relaxation in Sub-Sonic Curvilinear Flows

The process of introducing an aerosol into the shock tube is a relatively slow process compared to that of conducting an experiment with shock waves. That is, the flow velocities associated with aerosol filling prior to passage of the shock wave are significantly slower than those induced by shock passage. In general, the flow velocity of the aerosol during filling is such that the bulk gas can be considered as incompressible since the flow velocity is low relative to the speed of sound in the gas. Additionally, the flow used to transport aerosol into the shock tube may generally be considered as laminar. Furthermore, defining various non-dimensional parameters related to the flow and the droplets aid in understanding the nature of flows with droplets or particles. One such

parameter is the Stokes number. Although the Stokes number may be defined differently depending upon the type of application, it is generally described as a ratio of particle response time to the characteristic time of a flow and it serves as a general measure of the ability of a particle to respond to a change in flow conditions. The Stokes number can similarly be described as a measure of how well a particle tracks the path of a streamline as the streamline changes direction. In general, the Stokes number is defined as shown in Eq. (2.3).

$$Stk = \frac{t_0 u_0}{l_0} \tag{2.3}$$

The Stokes number is defined as a ratio of a characteristic stopping distance (characteristic deceleration time multiplied by characteristic deceleration velocity) to a characteristic length dimension of an obstacle. It can be seen from the definition that if the characteristic stopping distance is equal to the characteristic length, then the value of Stk is unity. This value corresponds to the ability of the particle to avoid collision with the obstacle. An alternate definition is given in Eq. (2.4) for particles in an impactor in terms of particle density, ρ_p, particle diameter, d_p, flow velocity, U, jet diameter or maximum bend diameter, D_j, dynamic viscosity, η, and a slip correction factor, C_c, respectively.

$$Stk = \frac{\rho_p d_p^2 U C_c}{9\eta D_j} \tag{2.4}$$

From the definition given in Eq. (2.4) we can observe the Stokes number is a function of critical diameter, or radius, of the bend in the flow leaving the nozzle. Similar such definitions can be given for flows in tubes as well where the critical dimension is the tube diameter or bend radius of a bend in the tubes. In these flows, the Stokes number

relates to the likelihood that a particle with a given diameter will pass through the tube or bend without contacting the impactor plate or being lost to the tube wall. A further application of the Stokes number is to determine a critical droplet diameter whereby a majority of particles with diameters larger than the critical diameter will not pass through the system. Such analysis can give guidance in selecting the maximum size of particles to be used in a given flow scheme, or in selecting the appropriate size of tubing for a given particle size to maximize the penetration of particles and/or droplets through the system. Given that a relationship exists between droplet diameter and various parameters of the flow system for aerosol introduction into the shock tube, it is apparent that optimization of flow parameters will play a critical role in the design of any method of introducing aerosol into the shock tube.

2.1.2.2. Relaxation Processes in Shock-Induced Flows

Another form of relaxation of aerosol droplets related to shock tubes in this study is the thermodynamic relaxation of the droplets and the surrounding carrier gas in the flow induced by a shock wave. In particular, the aerosol is in equilibrium prior to propagation of the shock wave (in Region 1). After the shock wave passes and the highly transient change of thermodynamic conditions across the shock occurs, however, a period of equilibration follows where the properties of the droplets and carrier gas come to a new state of thermodynamic equilibrium after an impulsive change in conditions. As mentioned previously, the ideal process for this relaxation would be for the droplets to evaporate and diffuse within the surrounding gas in a uniform manner almost instantaneously, thereby creating a homogenous gaseous mixture in place of what was a

two-phase aerosol. Such a process would nearly occur instantaneously if the droplets were extremely small (sub-micron) with tremendously high number densities (very small inter-droplet spacing). However, although aerosol droplets are indeed small with diameters on the order of less than one to hundreds of microns, they are not small enough to evaporate instantaneously relative to the time scales of shock propagation. For example, in an environment of air at atmospheric pressure and 650 K, a water droplet with a 1-micron diameter in evaporates in less than 50 microseconds. A 100-micron droplet, on the other hand, requires over 300ms in order to evaporate completely (although droplet breakup is likely to be more significant for 100-micron droplets compared to 1-micron droplets). Thus, these droplet relaxation processes behind shock waves must be understood to optimize the process of generating a homogenous, single-phase gaseous mixture from a two-phase aerosol mixture of fuel and oxidizer.

In traditional gas-phase shock-tube experiments, the primary source of relaxation after passage of the incident shock wave is vibrational relaxation of any di-, tri-, or polyatomic species, respectively, which are included in the mixture. This is because collisional energy transfer to vibrational degrees of freedom is significantly slower than any other type of molecular collisional interaction. After being excited translationally and rotationally by the step change in temperature and pressure across the shock wave, the molecules can take hundreds to thousands of microseconds to relax back to thermodynamic equilibrium while the vibrational energy levels repopulate [45-48]. In general, however, this is not a concern when interpreting thermodynamic conditions behind the incident and reflected shock waves. Of greater concern is the relaxation of the

aerosol mixture to its new thermodynamic equilibrium. As previously mentioned, the end goal of using the aerosol is to shock-heat it such that the droplets evaporate quickly and a homogeneous gaseous mixture results from this heating and subsequent diffusion. However, such a mixture is only fully created after the relaxation process is completed.

In pre-shock conditions, the liquid droplets in the aerosol are in thermodynamic equilibrium with the surrounding carrier gas. Once a shock wave passes through the mixture, however, the resultant step change in conditions affects the liquid droplets and surrounding gas in different ways. As in traditional gaseous shock-tube experiments, the gas molecules are accelerated, heated, and compressed. The droplets also experience this acceleration, heating, and compression. They do not respond immediately, however, because unlike the gas molecules, they have masses which are significantly larger than that of the surrounding molecules and they are larger than the mean free path of the collisions occurring between the gas molecules. Thus, the momentum inertia and thermal inertia of the liquid droplets are much greater than that of the gas and they cannot respond within a few molecular collisions like the gas molecules can. This response to a change in conditions in turn requires longer time scales for the droplets to come into thermodynamic equilibrium with the gas. The process of relaxation is visualized in Figure 2.2 from a shock-fixed reference frame. Additionally, this graphic and the discussions in this chapter include the general assumption that any aerosol droplet has a perfectly spherical geometry. This spherical shape can be proved via various minimum energy laws in the context of surface tension. Such discussions are beyond the scope of this work, however.

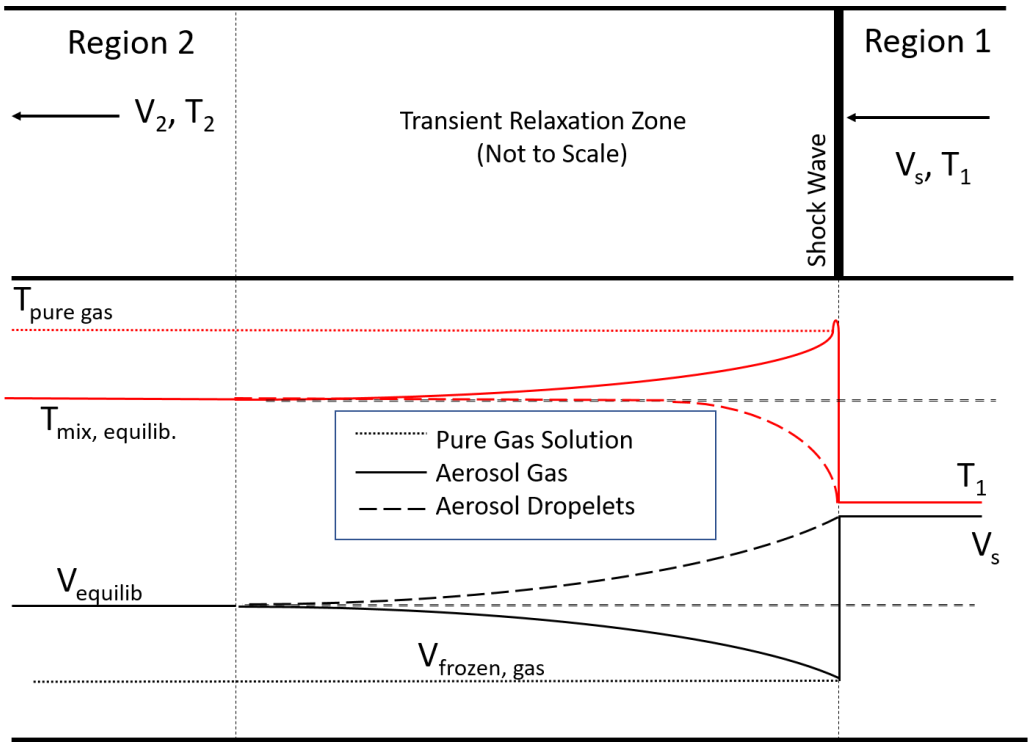

Figure 2.2 Relaxation process of a shock wave propagating through a two-phase aerosol mixture in the shock-fixed coordinate frame

2.1.2.2.1. Velocity Relaxation

The qualitative analysis for the case of a single droplet will now be considered during the event of momentum transfer to the droplet in the relaxation zone after being processed by the incident shock wave. Such an analysis is also applicable to hard spheres. As can be seen from Figure 2.2, the velocity of the droplet and gas in the aerosol are the same when on the upstream side of the shock wave. Once they cross the shock boundary, however, the gas is instantly accelerated to the value of the pure-gas solution to the shock jump equations. This post-shock condition is referred to as the frozen solution (where the energy transfer by momentum or heating to the droplet is temporarily frozen). In the

unfrozen solution, however, the droplet remains stationary only for the first few microseconds after passage of the shock wave. In the shock-fixed coordinate frame, a stationary object enters and exits the shock at the same velocity, which is shown as the droplets having the same velocity just downstream of the shock as they do upstream. As the shock moves away from the droplet, the velocity of the droplet increases as momentum from the surrounding gases is imparted to the droplet. The gas behind the shock moves in the same direction as the shock, but with a lower velocity. In the transformation to shock-fixed coordinates, this is described as a gas velocity lower than the velocity of the droplet relative to the shock front (i.e. the shock moves away from the droplet more quickly than it does the gas which is trailing behind it). As is shown in Figure 2.2, the resultant velocity after relaxation of the aerosol mixture in the shock-fixed frame is greater than that of the frozen (purely gaseous) solution because the gas must impart momentum to the droplet, which has roughly two orders of magnitude more mass than an equivalent volume of gas.

In the case of a solid sphere, the sphere would experience only heating and momentum change during this relaxation process. For a liquid droplet, however, it also experiences evaporation due to this heating. Thus, while momentum is of course transferred to the droplet, the droplet itself changes phase and evaporates during the momentum exchange process, revealing that the processes are coupled. A side note is that the momentum and heat transfer relaxation zones may not be the same temporal or physical length from Figure 2.2, and the figure is not to scale but merely a reference for the purposes of discussion. Since the droplet is shrinking as it is heated, the momentum transfer process quickens as the droplet shrinks due to the loss of mass from evaporation.

2.1.2.2.2. Droplet Breakup

Another phenomenon associated with the relaxation process of a droplet reacting to the flow behind a shock wave is droplet breakup. The high velocity flowing around the droplet and the dynamic pressure of the flowing gas acting on the upstream side of the stationary droplet combine to exert significant force on the droplet surface which leads to droplet deformation and eventually the breakup of the droplet. There are several factors influencing the nature of droplet breakup which makes rigorous analysis complex. A parameter can be defined, however, which elucidates some behavior of the mechanics of droplet breakup, combined with empirical results. The Weber number is a term combining the droplet surface tension, gas density and velocity, and droplet size, respectively. It is defined as a ratio comparing the gaseous inertial forces to the surface tension forces of the droplet. The Weber number is defined in Eq. (2.5).

$$We = \frac{\rho v^2 l}{\sigma} \tag{2.5}$$

Intuitively, as the initial velocity impinging on the surface of a droplet increases, this will likely lead to a faster and/or more violent droplet breakup process. Another non-dimensional number which considers the additional effect of droplet viscosity is the Ohnesorge number, which relates viscous forces of the gas to the inertial forces acting on the droplet and the surface tension forces of the droplet. This non-dimensional parameter is a function of the Weber number and the Reynolds number and accounts for gas viscosity. The definition is shown in Eq. (2.6).

$$Oh = \frac{\sqrt{We}}{Re} \tag{2.6}$$

As can be observed in the definition of Weber number, as velocity of the gas increases, the Weber number increases. This effect of velocity shows that higher Weber numbers are associated with faster and/or more catastrophic droplet breakup events. Such a dependence is in line with results of experiments, such as those referenced by Gelfand et al. [49] and Pilch and Erdman [50]. While the Weber and Ohnesorge numbers provide insight into the likelihood and/or time scales of droplet breakup, such behavior may vary considerably depending upon the size and flow properties of a given aerosol experiment. Similar to the intuitive results that stronger shock waves (higher shock speeds) lead to faster droplet acceleration and breakup is the presumption that stronger shocks lead to quicker rates of evaporation.

2.1.2.2.3. Droplet Heating and Evaporation

The final mechanism for droplet relaxation processes of aerosols behind shock waves is droplet heating, which results in droplet evaporation and diffusion. The combination of heating, evaporation, and diffusion is, of course, not one single process, but rather three distinct processes. These processes do not occur independently from one another in time, though, so they will be combined for the purposes of the analysis discussed here. In a typical shock-tube experiment involving aerosols for the purposes of studying combustion phenomena of hydrocarbons, droplets are first exposed to temperatures in the range of 400-750 K. This increase in temperature occurs in the region immediately behind the incident shock wave. After shock passage, the droplets and gas are not immediately at equivalent temperatures, however. The gas is at a temperature

greater than what will eventually be the equilibrium temperature, and the droplets are at a temperature lower than what will eventually be the equilibrium temperature. This temperature difference is shown in Figure 2.2. First, the gas rises to the temperature of the pure-gas solution, or the frozen condition. Heat transfer between the gas and the droplets then begins to take place and the temperature relaxation process between gas and droplets begins. This heating causes the droplets to increase in temperature by way of convection from the surrounding gas transferring heat to the liquid droplets, which lowers the temperature of the gas.

Once the droplets rise to their boiling point temperature, evaporation begins to occur, further cooling the gas. As the liquid changes phase, the freshly evaporated gas at the surface of the droplet diffuses into the surrounding carrier gas. Once evaporation of the droplets (fuel, in this case) is complete, diffusion continues until the gaseous fuel-oxidizer mixture is uniform in concentration throughout the volume. This scenario of a final, uniformly diffused mixture of gaseous fuel and oxidizer is the planned course of events intended for the purposes of this work. In practice, however, the largest droplets may not evaporate completely prior to the arrival of the reflected shock wave if they are near the endwall. Such non-ideal breakup could cause some issues related to interpretation of the thermodynamic conditions behind the incident and reflected shock waves. Thus, it is necessary to examine the literature for previous studies investigating the nature of droplet-related phenomena in shock tubes to determine best practices and challenges that may arise when conducting shock-tube experiments with such mixtures.

2.2. **Recent Studies of Aerosols in Shock Tubes**

A brief review of shock-droplet and shock-aerosol interactions is necessary for the purposes of better understanding the various governing phenomena of aerosol droplets as they pertain to applications in shock tubes. Such studies are quite abundant, and a thorough review of all prior works is not presented here. Several recent studies are cited, however, which provide insight into the current state of research investigating droplet mechanics in shock-induced flows. These works will aid in elucidating the relative significance of both the various phenomena and the important considerations upon which a successful aerosol shock-tube facility should be based. Many noteworthy studies of aerosols and droplets conducted prior to the turn of the 21st century in shock-tube flows have been reviewed in detail in works by Petersen [51] and Nettleton [52]. Sources of information about the more generalized theory of aerosols are given by Huimin [53], and that previously mentioned by Hinds [43]. Although the works cited by Petersen and Nettleton are generally exploratory in regard to their application, they provide critical insight into the phenomenological nature of aerosol and droplet interactions with shock waves. Furthermore, even though the review by Petersen is wide-ranging in scope, it is nonetheless roughly two decades old at the time of this writing. Hence, many significant contributions to the study of droplets and aerosols have been made in that time frame and warrant consideration.

It has been discussed previously that the presence of an aerosol during a shock tube experiment can affect local thermodynamic properties of the post-shocked fluid. In addition to local effects, aerosols can also influence the global behavior within the shock

tube as the shock wave interacts with the aerosol contact surface. It has been shown in both experimental and numerical studies that aerosol clouds can impact shock wave propagation. Experimental work by Jourdan et al. [54] showed significant dependence of the attenuation of pressure ratio across the shock wave as a function of droplet size and mass loading during shock propagation. This work was a novel study which did not investigate the de-coupling of mass loading and droplet size independently, but still provided valuable insight into the nature of shock propagation into uniform aerosol loading conditions. Effects of droplet size and mass loading have been investigated separately in numerical studies, however, such as those by Chang and Kailasanath [55], Kersey et al. [56], Gai et al. [57], and some references therein. Chang and Kailasanath showed significant attenuation of shock Mach number as a function of particle size for constant mass loading. The Mach number behavior displayed an inverse dependence on the particle size; shocks were attenuated more quickly for smaller particles than large particles at a given mass loading. However, it was also shown that smaller particles led to less variation in the ideal post-incident shock pressure behavior as the shock propagated through the mixture when compared to a mixture with no droplets. This behavior of varying particle/droplet size and subsequent shock Mach number attenuation and pressure variation was also confirmed in the numerical calculations of Kersey et al. [56].

Similar to the case of varying particle size, it was shown by Gai et al. in their simulations that increasing droplet volume fraction (in parts per million by volume, PPMV) resulted in a significant impact on the pressure behavior behind the incident shock wave. The increased volume fraction of aerosol results in the aerosol behaving as a semi-

permeable wall which sends back small shock reflections. As the volume fractions increase, this effect is increased as well. This numerical result of shock reflection from droplets agrees with the experimental results of the experimental study of Jourdan et al. which recorded the presence of reflected shock waves in post-incident-shock pressure traces. This shock reflection, however, when considered purely as a function of droplet volume fraction (or mass fraction) is strongly dependent on the amount of droplet loading. For droplet loadings of roughly 100 PPMV, however, the simulations of Gai et al. revealed a minor change in the pressure behind the incident shock due to the presence of a uniform field of 10-μm droplets for a shock Mach number of 1.1 at an initial pressure of 1 atm. Furthermore, with higher incident shock Mach numbers and lower pressures (as in typical combustion applications for shock tubes), the effect of high droplet loadings is expected to be minimal (provided the majority of droplets are near 10 μm in diameter or smaller). Lastly, in addition to pressure effects from the presence of droplets, post-incident and reflected temperatures were also shown to be affected by the presence of droplets in the work of Kersey et al., with higher mass loadings lessening the temperature increase of the mixture behind the shock waves.

In addition to the study of bulk shock-aerosol interactions, investigations intent on studying more localized phenomena have also furthered the understanding of shock-droplet and shock-particle interactions. These studies, in general, focus on the interaction of a shock wave with a single droplet, or several droplets, with the purpose of investigating droplet acceleration, deformation, and breakup phenomena. As was previously mentioned, the breakup of droplets has been categorized by past researchers into various regimes

based on the Weber number of the droplet. These modes are separated into six different ranges of Weber number. Subsequent works have simplified the breakup regimes into 3 regions [58, 59]. These regimes are loosely defined in Table 2.2.

Table 2.2 Droplet breakup regimes by Weber Number.

Breakup Type	Weber Number Range
Rayleigh-Lamb-Taylor Instability	10-40
Sheet Stripping and Boundary Layer Instability	40-10^3
Catastrophic Breakup	10^3-10^5

An experimental study by Kobiera et al. studied interactions of hexane droplets with the flow behind incident shock waves. In general, their efforts were focused on droplets in the catastrophic breakup regime and found the results of their experiments agreed well with droplet breakup models. A lower range of Weber numbers was studied in the first and second regimes by Kim and Hermanson [60] who examined breakup in Weber numbers up to 300 using a supersonic wind tunnel. With the continued improvement of numerical solvers, empirical droplet breakup studies can be aided by supplementing the experimental work with computational fluid dynamics (CFD) simulations. Examples of such CFD-aided studies are given by Yeom and Chang [61], Meng and Colonius [62], and Poplavski et al. [63]. In particular, the study by Poplavski et

al. provides great detail on the droplet deformation and breakup behavior for times shortly after passage of a shock wave over a wide variety of Weber numbers. Their modeled results have excellent agreement with experimental shadowgraphs in regard to not only the shape of droplets as they form, but also with the rates of deformation. Thus, the study by Poplavski et al. not only provides detail on the governing mechanics of droplet breakup, but also accurate interpretation of the time scales of droplet breakup as a function of Weber number; a critical consideration when examining the governing dynamics of droplet interactions with shock waves in shock-tube flows.

Experimental evaporation studies have not been a significant focus of aerosol investigations in shock-tube research over the last one to two decades, primarily because much work was conducted in examining the nature of evaporation of droplets behind shock waves prior to the 21st century. Multiple recent experimental studies associated with evaporation exist, of course. They are not emphasized here, however, because they are focused on fluid-mechanic instabilities and related effects of evaporation and are not within the scope of this work. Some examples are those given by Paudel et al. [64] and Middlebrooks et al. [65]. As mentioned previously, a thorough review by Petersen [51] discusses some of the landmark studies on aerosol evaporation rates behind shock waves [66-73]. A more recent paper by Hanson et al. [74] also provides updated modeling for the evaporation behavior of micron-sized aerosols behind shock waves, however. Their work focused on droplets ranging in size from roughly 1-15 μm in diameter and found that significant non-continuum effects caused the overprediction of evaporation rates for droplets with diameters of roughly 5-10 μm and below.

2.3. **Guidelines for Conducting Kinetics Studies in Aerosol Shock Tubes**

The preceding literature review, while not exhaustive, outlines recent work investigating the physical phenomena involved in shock wave interactions with aerosols. An analysis concerning the nature of the governing behavioral aspects of aerosols in shock-induced flows has not yet been conducted, however. Such an analysis requires answers to questions which are more application-specific, unlike the generalized phenomenological investigations and theory. The present application of aerosol entrainment and vaporization behind shock waves for the purposes of combustion in shock tubes has been an active area of research since the beginning of the 21st century. Earlier attempts at investigating droplet and aerosol combustion in a homogenous fashion in shock tubes were primarily limited to spray combustion studies [51, 75]. The work of Hanson et al. [74], however, aimed at producing spatially uniform aerosols which could be introduced into the driven section of the shock tube prior to passage of the incident shock wave. Such a method was further discussed in the work of Davidson and coworkers [34] and is provided in more detail in a following section. In their paper, Davison et al. outlined three primary areas of emphasis for conducting experiments with aerosols in shock tubes. These areas offer a framework around which a method for introducing aerosol into the driven section may be conceptualized. The first emphasis is related to droplet diameter.

As discussed previously, there exists a relaxation zone behind the incident shock wave when it passes through an aerosol mixture of fuel and oxidizer. This relaxation zone can obfuscate the interpretation of droplet evaporation if the properties of the droplets are

not favorable. In essence, if the droplets are not small enough, and if their size distribution is too large, then the evaporation event will not occur quickly and calculations of thermodynamic conditions behind the incident and reflected shock waves, respectively, will have increased uncertainty. Reducing uncertainty in experimental conditions is of paramount importance in conducting shock-tube experiments, and significant additions of uncertainty from relaxation must be minimized. Minimizing this uncertainty can be achieved by producing a large number of droplets with small diameters such that the evaporation process behind the incident shock wave is much quicker than the droplet breakup process. For example, in the work of Poplavski et al. [63], it can be seen that the fastest breakup occurs for large droplets with high Weber numbers. However, such droplets would likely be too large to remain suspended for long periods of time (tens of seconds) for applications in a shock tube. Thus, smaller droplets must be used to avoid settling, which also means that the Weber numbers associated with smaller droplets are such that the breakup time scales are significantly longer than evaporation time scales for the experimental conditions of interest to heavy hydrocarbon combustion in shock tubes.

In addition to producing small droplets, the lognormal size distribution of the droplets [43] must be somewhat narrow such that the majority of the particles behave similarly in regard to acceleration and evaporation behind the incident shock wave. Lastly, although the size of the droplets should be small to allow for quick evaporation, they must also be large enough to accommodate high fuel mass loadings, which are required for high-pressure experiments.

Another area of emphasis given by Davidson et al. [34] is that of spatial loading uniformity of the aerosol. The primary challenge associated with generating homogenous aerosol mixtures in shock tubes is twofold. The first challenge is the lack of spatial droplet loading uniformity in the pre-shock mixture. The second challenge is the settling of droplets prior to passage of the shock wave through the mixture. This second challenge is why sprays were most commonly employed in studies of heavier hydrocarbons; the fuel liquid could be sprayed into the driven section of the tube shortly before passage of the shock wave (on the order of 1-2 milliseconds) or directly after passage of the reflected shock wave near the endwall, not allowing the aerosol sufficient time to settle. These practices, however, eliminated the ability of researchers to have control over the homogeneity of the resulting aerosol cloud produced by the spray, such as the kind used by Rotavera and Petersen [76]. Control of the spatial uniformity of the dispersed liquid droplets is difficult, if not impossible, when using spray techniques for combustion studies in shock tubes.

Moreover, the reason that spatial loading uniformity is critical for chemical kinetics or combustion-related studies, respectively, in shock tubes is that a non-uniform concentration of fuel (which is usually in the form of aerosolized droplets in these applications) will introduce added uncertainty as to the precise value of the fuel-oxidizer equivalence ratio in the experimental region of the shock tube. Furthermore, uncertainties in mass loading uniformity can lead to localized regions of extremely high or low fuel concentrations. Thus, in undiluted real-fuel air mixtures in which fuel-rich conditions produce faster ignition events, pockets of high fuel concentration will ignite earlier than

the bulk of the mixture and cast doubt on the accuracy of the ignition delay time results. In addition to providing correct interpretation of spatial fuel concentrations, spatial uniformity of the aerosol is also important in providing a uniform flow field through which the shock wave propagates. If significant concentration gradients exist in the aerosol, the shock wave will not pass through the mixture in a uniform manner, adding uncertainty to thermodynamic calculations.

The final area of emphasis by Davidson et al. [34] is that of the method of aerosol generation. Since mixtures of liquid fuels are known to have numerous components [77], the method of aerosol generation must generate droplets in such a way so as to ensure that the composition of the nebulized liquid is the same as that of the original bath. Otherwise, the composition of the droplets will not be known with high accuracy, leading to an increase in the experimental uncertainty.

2.4. **Methods of Aerosol Generation**

Prior to discussing specific studies which have investigated homogenous fuel-oxidizer aerosols for combustion in shock tubes, it is necessary to discuss in brief some of the methods of aerosol generation and the devices which produce aerosols. These devices, while easily overlooked in studies related to aerosol combustion, are critical in establishing the most influential property of the aerosol itself; the droplet size distribution. This size distribution is a crucial parameter governing both the design and operation of an aerosol shock-tube system. Thus, the device used in controlling the parameters of the size distribution cannot be overlooked.

Many methods for generating liquid droplets are available for experimenters to use when producing an aerosol. One of the most common methods of producing droplets is air blast atomization. This method is the technique used in many industrial applications such as the application of various spray coatings and the injection of fuel via a fuel injector in modern combustion engines. Atomization occurs by the violent shearing of the liquid as it is release from a high-pressure orifice into a gas. In general, the average size of the droplets produced by air blast atomization can vary widely [78, 79], although newer generations of modern fuel injectors are generating smaller droplets as supply pressures within the injector are increased.

Another method of atomization is effervescent atomization. This method is similar to air blast atomization in that a liquid is sprayed into a gas. Prior to exiting the nozzle orifice, however, the liquid is mixed with a high-pressure gas to form bubbles within the nozzle of the injector, aiding the breakup process upon exiting the nozzle. Like air blast atomization, the size range of droplets which are produced can vary significantly. Some examples of effervescent atomization are given by Sovani et al. [80] and an alternative approach is given by Mesherichter [81]. Some additional examples of liquid atomization include electrostatic atomization [82] and centrifugal atomization [83]. More information regarding droplet production is given by Hinds [43].

The final method of droplet creation discussed here is ultrasonic nebulization. Ultrasonic nebulization takes advantage of piezoelectric materials which expand and contract under the influence of an alternating current [84]. These current oscillations can be very rapid (on the order of Megahertz) which result in high-frequency oscillations of

the piezoelectric material. When the oscillating piezoelectric material is submerged in a liquid bath, the oscillations of the material will result in the formation of small, undulating waves at the surface of the liquid. As the waves oscillate, small droplets are broken off at the surface of the wavelets and are propelled upwards above the surface of the liquid. Additionally, the high-frequency oscillations of the piezoelectric material controls the size range of the droplets, resulting in very small diameters on the order of microns. This size range of droplets is advantageous for suspending the droplets for significant periods time in a gas. Furthermore, such ultrasonic nebulizers can produce high mass loadings required to fill larger volumes such as those found in shock tubes.

2.5. **Recent Kinetics Studies in Shock Tubes Using Nebulized Fuels**

Until relatively recently, combustion studies investigating spatially homogenous mixtures of low-vapor-pressure hydrocarbons and oxidizer in shock tubes had been conducted with heated shock-tube facilities. As the desire to investigate progressively larger fuel molecules found in real fuel mixtures has grown, however, the need for novel methods of introducing the liquid fuel into the shock tube has become apparent due to the upper limit on safety factors when heating a high-pressure shock-tube facility. Such novel methods require that the shock-tube facility not be heated, yet also provide a means by which the fuel can be introduced into the shock-tube driven section in a uniform manner prior to passage of the incident shock wave. These requirements are met by the aerosol shock tube and techniques associated thereof. Care must be taken to select the appropriate size distribution of aerosol droplets, however, such that uncertainties due to settling and droplet relaxation processes are minimized while still allowing high mass loadings.

Additionally, the method of entrainment by which the aerosol is introduced into the shock-tube driven section must also be strategically designed to minimize non-uniformities. These requirements necessitate empirical investigation (i.e. experimentation) to optimize the various parameters and methods necessary for the collection of quality kinetics data using aerosols in shock tubes.

The work of Hanson and coworkers [74] is the first study known to the author in which a non-spray technique was used in attempting to introduce a uniformly spaced aerosol into a shock tube for the ultimate purposes of hydrocarbon combustion. In their study, Hanson et al. generated nebulized fuel droplets via an ultrasonic nebulizer. Such a nebulizer is not only able to generate a small mean droplet size with a tight droplet distribution but is also able to generate high-mass loadings required for undiluted high-pressure experiments at realistic equivalence ratios. In their paper, Hanson et al. characterized the size distribution of the aerosol from the ultrasonic nebulizer and found it had a mass-mean diameter using water of around 4-5 μm and a geometric standard deviation of roughly 1.5. They also introduced a novel technique for introducing the aerosol into the shock tube. A nebulizer was housed in a shallow bath of liquid over which a carrier gas flow traveled, creating an aerosol. The aerosol was then sent to a pre-mixing chamber which was attached to the endwall of the shock tube with a custom mount that doubled as the shock-tube endwall. This modified endwall contained 4 valves which were similar in geometry to that of an intake/exhaust valve in a piston-driven engine. The mixing chamber was continuously purged with the aerosol mixture and the valves were opened. Additionally, an exit port connected to a vacuum pump was opened near the

diaphragm in the shock-tube driven section, and the aerosol was continuously introduced into the shock tube for roughly 50 seconds. This continuous flow-through technique provided values of non-uniformity of 5-8% RMS using water droplets when measured using a light sheet and image analysis technique.

From the methods used by Hanson et al., Davidson and coworkers [34] expanded the use of the aerosol shock tube to the combustion of hydrocarbons behind reflected shock waves. In their work, they analyzed the characteristic evaporation times of dodecane droplets in air behind incident shock waves and found the typical time scale of evaporation for their experiments to be roughly 150-300 μs. Although they were not able to measure the diffusion rates of the evaporated fuel into the carrier gas, they did perform calculations to approximate the diffusion time scales for droplets of 1-10 μm in size. For 10-μm droplets, the maximum diffusion time scales were on the order of 50-100 μs. Thus, they concluded that the mixture behind the incident shock wave could be considered a homogenous mixture of fuel and oxidizer roughly 200-400 μs after passage of the incident shock wave. This finding also led to the determination that droplets ranging from 1-10 μm in diameter relax quickly enough behind incident shock waves to enable accurate gas-phase thermodynamic calculations but are also large enough to provide sufficient mass loadings using the ultrasonic nebulizer as the method of aerosol generation.

Furthermore, it can be assumed that droplets nearest to the endwall do not evaporate prior to arrival of the reflected shock wave. However, it can also be assumed that they evaporate and diffuse much more quickly than the initial aerosol due to the higher temperatures and pressures behind the reflected shock wave. Additionally, although

Davidson et al. did not discuss the pre-shock aerosol loading uniformity, they did record uncertainty in fuel concentration behind the incident shock wave of roughly 1.7%. The facility used by Hanson et al. and Davidson et al. was then employed in measuring the ignition delay times of diesel fuels behind reflected shock waves by Haylett et al. [85].

Another flow-through technique to introduce aerosols into a shock tube was developed by Rotavera et al. [42]. Their method of aerosol generation did not employ an ultrasonic nebulizer but instead used a form of air blast atomization coupled with a cyclonic flow size selector which tailored off larger droplets by using a critical value of the Stokes number to determine which droplets to allow into the shock tube. The method of aerosol introduction was similar to that of Hanson et al. [74] and used a continuous flow-through technique by way of a vacuum pump to introduce the aerosol into the shock tube.

The aforementioned studies [34, 42, 74] employing continuous flow-through techniques of aerosol introduction marked a landmark period in the use of aerosols in shock tubes. For the first time, homogenous mixtures using liquid hydrocarbons could be generated and their combustion behavior studied reliably without the use of a heated shock-tube facility. The key contribution of these studies was that they combined the experience of previous researchers into a single facility capable of using the advantages afforded by aerosols to study liquid hydrocarbon combustion. Although these facilities successfully demonstrated the capabilities of aerosol shock tubes, they still required improvement. In particular, the flow-through techniques developed in these studies suffered either from limited aerosol mass loading capabilities, as was the case for Rotavera

et al. [42], or an increased degree of uncertainty in ignition delay time relative to those recorded using heated shock-tube facilities. Thus, further work was required to refine the aerosol shock-tube technique.

One significant drawback with the method of introducing aerosol into the entire length of the driven section of the first-generation (Gen. I) shock tube of Davidson et al. [74] using the flow-through setup is that the aerosol droplets had the tendency to settle after they move a significant distance away from the fill ports. According to Haylett and coworkers [35], the aerosol in the Gen. I tube would settle after the initial turbulence from the filling valves had dissipated as the aerosol moved towards the exit port. This settling caused a significant amount of non-uniformity of the aerosol within the tube, and Haylett et al. determined that the aerosol needed to be more uniform over the region nearest to the endwall of the driven section.

With this need in mind, they designed a gate valve for a second-generation (Gen. II) aerosol shock tube. The gate valve coupled to the shock tube itself and allowed for the driven section to be partitioned into two isolated sections. Thus, the valve could be closed for aerosol filling such that the aerosol was constrained to roughly the last meter of the shock tube and then opened after filling to allow passage of the shock wave. Such a technique was another landmark development in the progress of aerosol shock tubes. This refinement led to improvements in droplet loading techniques and in the prevention of settling since fill times could be shorter. Furthermore, the gate valve also enabled the refinement of a concept known as a constrained reaction volume (CRV) shock tube [86, 87].

In addition to modifying the way in which the aerosol was constrained within the shock-tube driven section, Haylett et al. [35] also modified the manner in which the aerosol was drawn into the shock tube. Instead of using a pre-filling chamber like in the Gen. I aerosol shock tube, the Gen. II facility made use of a second gate valve located at the end of the driven section so as to double as the shock-tube endwall. Additionally, the pre-filling chamber was replaced with a larger tank housing the ultrasonic nebulizer known as the aerosol generation tank (AGT). In the Gen. II aerosol shock-tube filling procedure, both of the gate valves were initially closed, and the nebulizer was turned on in the AGT. After a sufficient amount of time, the nebulizer was switched off and the endwall gate valve was opened.

A different flow technique was also used in the Gen. II version of the aerosol shock tube. Instead of a continuous-flow technique, a transient filling method was used. In this technique, an evacuated dump tank was used to draw the aerosol from the AGT towards the upstream gate valve by placing an exhaust port near the upstream gate valve which was connected to the dump tank. A valve on the dump tank was opened which allowed the gas upstream of the AGT to be drawn into the dump tank and in turn draw the aerosol into the driven section of the shock tube until the pressures equilibrated. This filling procedure represented a significant improvement in aerosol loading uniformity relative to that of the Gen. I aerosol shock tube. Furthermore, the subsequent ignition delay time data in the Gen. II facility exhibited significantly lower scatter than the data in the Gen. I aerosol shock-tube facility, while displaying generally similar ignition delay time behaviors [35].

The data from both the Gen. I and Gen. II aerosol shock-tube facilities from the Hanson group at Stanford which are presented here are comparable in their quality. However, a question arises regarding the source of the difference in ignition delay time behavior between the two facilities. What is the source of difference between the facilities concerning their differing, albeit similar, ignition delay time behavior for equivalent conditions and mixtures? The answer is multifaceted and lies in both the methods of measuring aerosol loading uniformity and the aerosol filling techniques.

Pre-shock aerosol loading uniformities presented by Hanson et al. [74] in the Gen. I facility were measured using a light sheet and image analysis. The non-uniformities were found to be nominally 5-8% prior to passage of the incident shock wave. Additionally, the quoted post-incident gas-phase fuel non-uniformity (measured using a 3.39-μm HeNe laser) from Davidson et al. [34] was approximately 1.7%. Furthermore, the uncertainty in post-incident gas-phase fuel absorption for the Gen. II facility presented by Haylett et al. was generally 0.5% or less. When comparing ignition data presented by Haylett et al. from the Gen. I and Gen. II facilities for dodecane, a substantial difference is observed between both the scatter of the data and the overall ignition behavior itself (the Gen. I facility has noticeably longer ignition delay times). This difference in ignition delay time behavior is likely not due solely to greater uncertainty in the measured fuel concentrations between the two facilities, however. After all, the offset seen in the ignition delay time comparison between the two facilities resembles a change in equivalence ratio of 20% or more, and not merely a few percent.

An uncertainty of 1.7% in the Gen. I fuel concentration measurement would lead one to think that the initial aerosol loading uniformity in the axial direction of the Gen. I shock tube was reasonably good (post-incident fuel absorption measurements were made in non-stationary flow, effectively measuring fuel concentrations at different pre-shock positions). The uncertainties in gas-phase fuel concentration behind the incident shock only tell part of the story, however. When Haylett et al. measured their aerosol loading uniformity while characterizing their filling method, they used a different diagnostic than the Gen. I light sheet method of Hanson et al. and Davidson et al., respectively. The Gen. II method for measuring pre-shock aerosol loading uniformity employed a Mie scattering diagnostic using the relative signal attenuation from droplet light scattering at 3 different locations along the axis of the aerosol-filled portion of the shock tube (more detail is given in the work by Haylett et al. [35]). This Mie scattering diagnostic revealed that the pre-shock loading non-uniformity in the Gen. II facility was better than 2%, while the non-uniformity measured in the Gen. I facility was as high as 16% using the Mie scattering diagnostic, as quoted by the doctoral thesis of Haylett [88].

From this investigation, two conclusions can be drawn. First, it can be concluded that the light sheet method was not an adequate diagnostic method for determining aerosol loading non-uniformities. Second, the measurement in uncertainty of gas-phase fuel absorption behind the incident shock wave is somewhat useful in determining pre-shock aerosol loading uniformity, but like the light sheet method, it should not be relied upon to accurately determine the pre-shock aerosol loading non-uniformity. Furthermore, the Mie scattering diagnostic served as a quality diagnostic for the Gen. II facility developed at

Stanford, and such a diagnostic may be considered when designing and characterizing other aerosol shock-tube facilities. Finally, it can be concluded that while effective as a first iteration, the flow-through technique used to introduce aerosol into the entirety of the shock-tube driven section without the addition of an isolating gate valve is not reliable in generating sufficiently homogenous aerosols in the shock-tube driven section.

Now that the state-of-the-art aerosol shock-tube facilities have been discussed in some detail, it is important to recognize that the most-recent aerosol shock-tube facility by Haylett et al. [35] provides a guide for future aerosol shock-tube designs. In particular, the incorporation of a gate valve to segregate the aerosol to a region near the endwall of the shock tube should be strongly considered for any design of an aerosol shock tube. Additionally, the aerosol loading non-uniformity should, at a minimum, be characterized using some type of Mie scattering diagnostic since it proved more accurate than other methods of diagnosing aerosol loading non-uniformities. With these guidelines in mind, the design of the new aerosol shock tube and aerosol-generation facility at Texas A&M University in College Station, employed in this study and subsequently constructed at Texas A&M University's Qatar campus, is examined in detail in the following chapters.

3. FACILITY DESIGN

A new shock tube and aerosol generation facility intended for the purposes of studying long-chain hydrocarbon mixtures was designed at the College Station campus in Texas and constructed at the Qatar Campus of Texas A&M University in Doha, Qatar. This chapter discusses the motivation behind various aspects of the shock-tube and aerosol-generation facility design, as well as some of the theory used as a framework for the design, and introduces novel aerosol shock-tube techniques unique to this facility.

3.1. Shock-Tube Development

The shock-tube facility constructed for this study incorporates design aspects of other similar facilities with an eye towards minimizing non-idealities. The design also integrated some of the latest hardware updates for aerosol shock tubes.

3.1.1. Non-Idealities

Although shock tubes are intended to provide an idealized environment to study zero-dimensional chemistry and interpret kinetic parameters, they are nonetheless operated in the real world and therefore exhibit non-ideal behaviors themselves. Furthermore, these non-idealities generally tend to worsen as the pre-shock specific heat ratio of the driven test gas is decreased. Thus, diatomic gases like nitrogen exhibit more significant non-ideal behaviors than do monatomic gases like argon.

3.1.1.1. Heat Transfer

The first non-ideal effect to be considered is the heat transfer of the hot gases behind the incident and reflected shock waves to the surrounding walls. The temperatures produced behind the reflected shock wave can reach several thousands of Kelvins during

an experiment and thus, the resultant temperature gradients between the walls of the shock tube and the hot gases can be extremely high. These gradients result in the transfer of energy from the shock-heated gases to the walls and can affect the quality of the test by increasing the uncertainty of the post-reflected-shock conditions. Because a typical shock-tube experiment is on the order of a few milliseconds, however, this is not sufficient time for significant energy transfer to the shock-tube walls to take place, provided that the thermal boundary layer is significantly smaller than the inner diameter of the tube itself. At longer experimental times, though, this energy loss must be accounted for [89]. The experiments in this work are not anticipated to last beyond 3 milliseconds, however, so this effect was not considered for this work.

3.1.1.2. Non-Ideal Pressure Rise: dP*/dt

The two remaining non-idealities to be discussed are the result of the formation of a boundary layer in the flow behind the incident shock wave. All shock tubes will exhibit boundary-layer growth from the flow induced by the incident shock wave. As a result of the boundary layer, small pressure perturbations are sent forward towards the shock wave relative to the flowing gases. These perturbations are displayed in the form small pressure increases. The flow behind the incident shock wave experiences a miniscule global pressure rise as a result of these perturbations, though. Behind the incident shock wave (which acts in a multiplying fashion of any perturbations), these pressure perturbations are multiplied and present themselves as a gradual increase in the post-reflected-shock pressure trace. This resultant, gradual rise in pressure exhibits itself in a near-linear fashion as a function of time behind the reflected shock, and it can thus be treated as nearly linear

[90-94]. Because of the near linearity of the non-ideal pressure rise, it is easy to describe with a single term and is defined as a normalized pressure change with respect to time, or dP*/dt, which is in units of percent per millisecond. As mentioned before, this pressure rise can be more pronounced if the driven bath gas is a diatomic or polyatomic molecule as compared to the more ideal argon.

For studies of real fuel-air mixtures, however, the driven bath gas is composed of diatomics with lower specific heats than argon, and thus the dP*/dt behavior will be significant compared to argon. The primary problem with dP*/dt is not actually the pressure increase, however. Pressure changes of several percent to even 10 percent over the course of a given experiment are shown to have little effect on the overall ignition delay time behavior in real fuel-air mixtures. The more important effect of dP*/dt is the change in temperature. If the dP*/dt can be said to occur in an isentropic environment (which is the general treatment for calculations related to dP*/dt), then the resulting temperature change takes the form in Eq. (3.1) where T_0 is the initial temperature in Kelvins, γ is the specific heat ratio of the gas and P/P_0 is ratio of the pressure at the end of the time interval, dt, to the initial post-reflected-shock pressure.

$$\frac{dT_{isen}}{dt} = 0.01\, T_0 \frac{dP^*_{isen}}{dt}\left(\frac{\gamma - 1}{\gamma}\right)\left(\frac{P}{P_0}\right)^{1/\gamma} \tag{3.1}$$

This resultant temperature rise can be several Kelvins, such as in argon-diluted mixtures, or it can be several tens of Kelvins if the mixture has a low enough specific heat ratio. Minimizing the effect of dP*/dt is therefore critical to minimizing the non-ideal temperature rise and accompanying contribution to the overall experimental uncertainty.

3.1.1.3. Reflected-Shock Bifurcation

Another significant non-ideal behavior in shock tubes due to boundary-layer growth in the post-incident shock flow is the formation of a bifurcation at the base of the reflected shock wave. A bifurcation forms when the boundary layer in the post-incident-

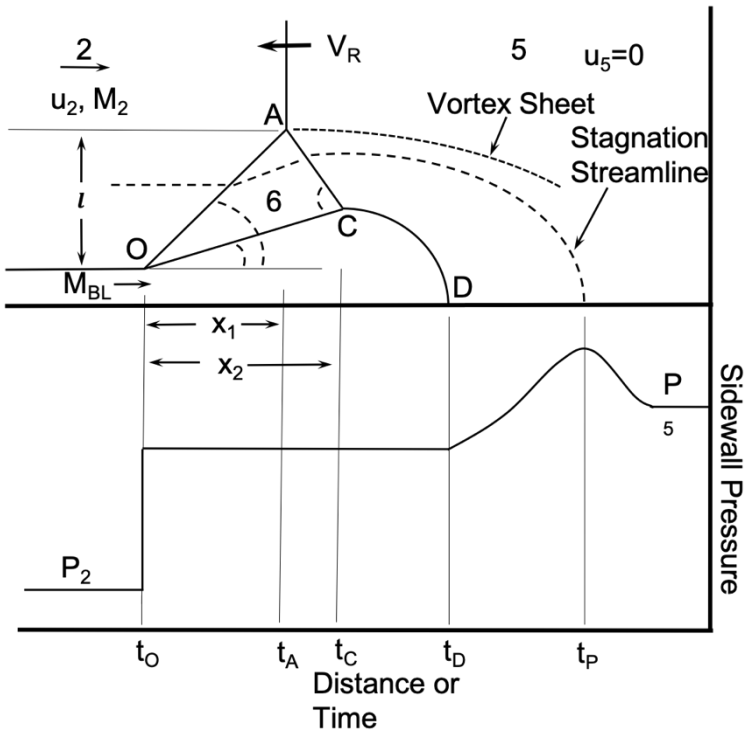

Figure 3.1 Diagram of post-reflected shock bifurcation.

shock flow lacks sufficient momentum to pass through the reflected shock wave [95]. This momentum deficit causes the base of the shock wave at the wall to form a λ-shaped structure, which is shown in more detail in Figure 3.1. The presence of the bifurcation feature is a strong function of the specific heat ratio of the mixture in Region 1. Thus, this

phenomenon generally does not occur in the more-idealized environment of experiments conducted in highly dilute mixtures of argon. When conducting experiments in real fuel-air mixtures, though, Ar is not used. The bifurcated foot of the shock wave forms near the endwall of the driven section and grows as the shock wave propagates back towards the diaphragm interface between the driver and driven sections. Such a feature undoubtedly causes flow in a region which is traditionally treated as ideally quiescent.

However, the presence of bifurcation has been shown not to cause a severe effect in the collection of ignition data in shock tubes, and it is generally ignored if the effect is minimal. Furthermore, the bulk flow in the central portion of the shock tube where ignition occurs is thought to be mostly quiescent in shocks displaying the presence of bifurcation [96]. More information regarding bifurcation is available in the references section of this document [95, 97-113]. Although the presence of the non-idealities listed herein can certainly affect the results of a shock-tube experiment, the design of the shock-tube facility plays a critical role in the extent to which these effects impede the collection of reliable ignition data.

3.1.2. Legacy Design Incorporations

In the previous section, various non-idealities which arise in shock-tube experiments were briefly discussed. For the experiments conducted in this dissertation, the boundary-layer non-idealities in particular will play a role in affecting the experimental results if they are unaccounted for. However, with appropriate consideration of these non-idealities in the design process, their effects can be somewhat mitigated. The primary way to mitigate effects related to boundary-layer growth from a design perspective is to use an

Figure 3.2 View of driven tubing section. Ports are shown with spacing of 16". Grooves on each end accommodate the flanges.

enlarged diameter in the driven section of the shock tube such that the resultant boundary-layer height is small compared to the overall diameter of the shock tube. This attention to the diameter has been done in the current facility by incorporating design characteristics of similar facilities from previous experiences of other researchers in the Petersen Research Group shock-tube laboratory at the Turbomachinery Laboratory on the main campus of Texas A&M University in College Station, TX [114-116].

Figure 3.2 shows a diagram of a length of driven section tubing. The inner diameter of the driven section of the shock tube is 6.00" (15.24 cm) with a configurable length up to 5.2 m. Several port locations are spaced 16" apart over the last 2 meters of the tube for diagnostic access. These ports are used to house pressure transducers or windows for *in-situ* laser experiments and light emission measurements. Additionally, the various tube

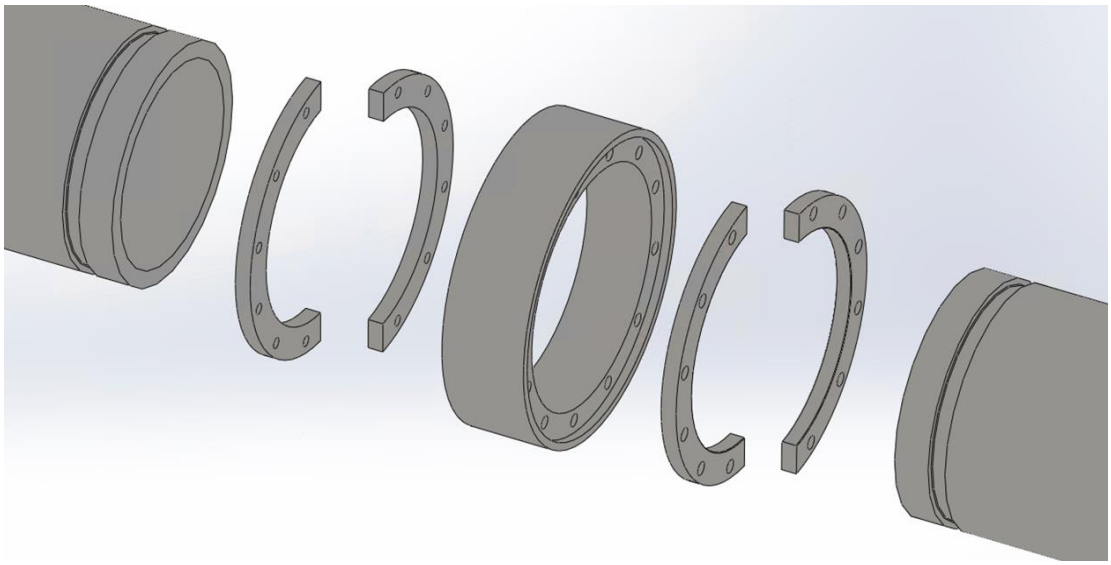

Figure 3.3 Exploded view of driven tube joint with weldless flange couplings.

sections are mated together using a weldless flange design such that the bolts can be removed and replaced should an overpressure event occur as opposed to a welded flange design which may require a replacement of an entire tube section should a flange be deformed during such an event. Views of the weldless flange are shown in Figure 3.3 and in Figure 3.4. In addition to a large inner diameter to mitigate boundary-layer effects during an experiment, the inner sidewalls of the shock tube are honed to a 6 μ-in RMS mirror finish to minimize turbulent boundary-layer formation.

In addition to the driven-section geometry being similar to that of previous shock tubes used in the Petersen group, the shock tube is also equipped with a high-vacuum section, a high-pressure mixing tank, and a gas-handling manifold for the creation of mixtures using the partial pressure mixing method. This apparatus results in the ability to

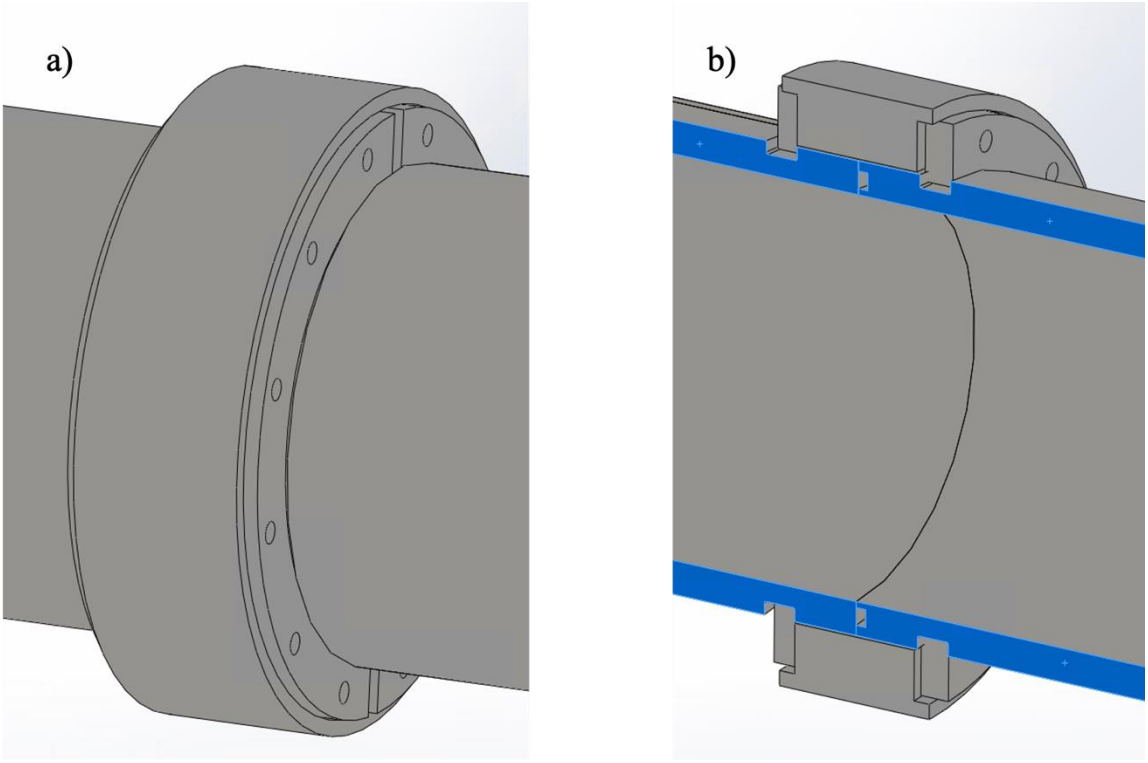

Figure 3.4 Driven-section flange coupling. a) External view, b) Section view. An o-ring is placed in a groove in one of the tube faces to provide a high-integrity seal.

create high-purity gaseous mixtures with compositional uncertainties of well under 1% or less.

3.1.2.1. Design Updates

Although the current facility has many shared features of other facilities utilized by the Petersen group at Texas A&M University [114-116], it also incorporates various design modifications. These modifications allow for the shock tube to be coupled to a new aerosol-generation and entrainment facility and operated as an aerosol shock tube. Furthermore, the shock tube can now be operated as a constrained reaction volume shock

tube [86] and has also been equipped with an enlarged driver section to enable extended test times.

3.1.2.1.1. Driver Section

Typical shock-tube test times are most often on the order of a couple to several milliseconds. Recently, however, a push has been made to study colder temperatures that require longer test times [29]. The shock tubes utilized in the Texas A&M Turbomachinery Laboratory have generally used driver-tube diameters which are smaller than that of the driven tube [114]. These two tubes are mated together using a diverging nozzle between the two sections of tube. In addition to the College Station shock tubes having diverging nozzle geometries, the driver tubes used in those facilities are used in configurations of 2-4 meters in length. Such a configuration is more than adequate to provide the test times needed for most shock-tube studies, especially those conducted in more idealized environments with Ar as a bath gas. However, when attempting to study ignition delay time behavior in the NTC- and low-temperature ignition regions, respectively, a different approach is necessary.

The new shock tube constructed for this work has been outfitted with a modified driver section compared to that of the shock tubes used in the College Station location of the Petersen group. With a modular design, the tube is configurable in length from one to six meters. Additionally, the driver-section inner diameter is made from ASME-certified pipe with Sch. 80 walls and an inner diameter of 7.63”. The driver section is mated to a converging nozzle at the diaphragm breech section. The enlarged driver diameter will aid in the extension of test times, as will the elongated length compared to the driver sections

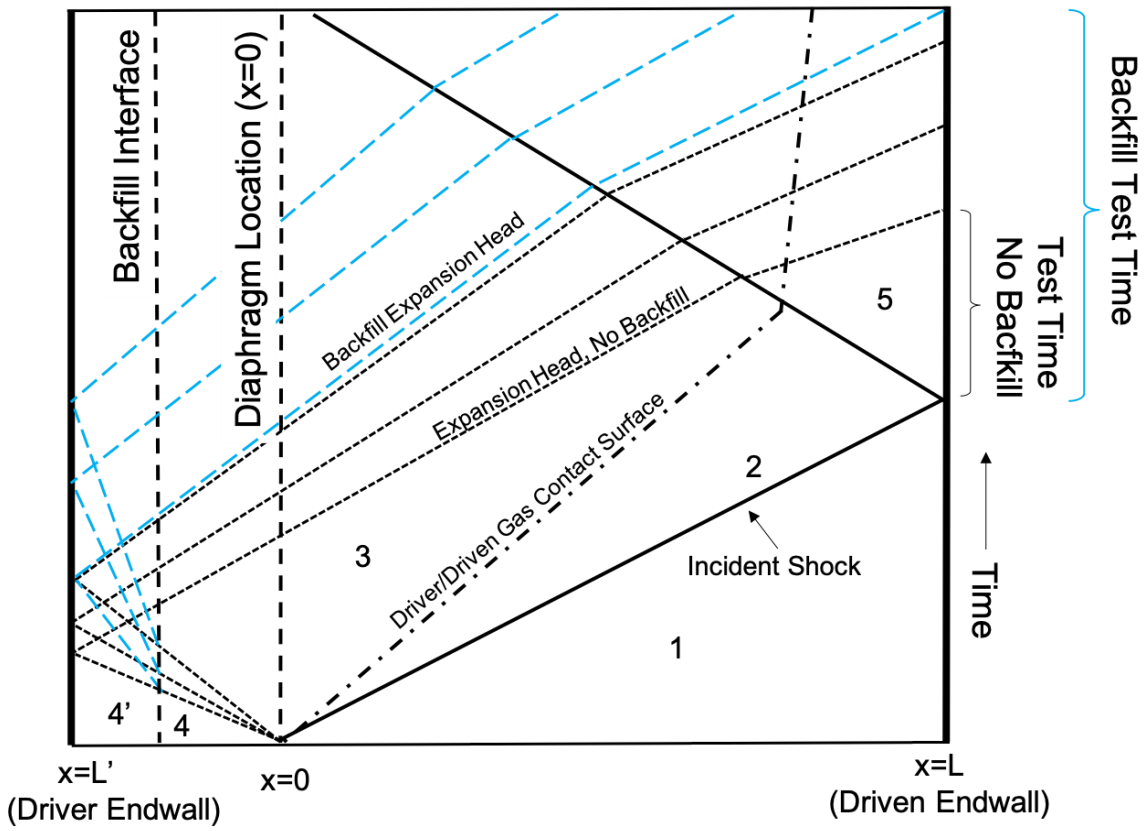

Figure 3.5 Shock-tube experiment x-t diagram with driver gas utilizing backfilling compared to driver gas without backfilling (not to scale). Region 4 is filled with a helium-based mixture, as in a traditional experiment, while backfilling is performed to create region 4' with a low-sound-speed gas.

of shock tubes at the College Station laboratory. A technique discussed by Campbell et al. for test time extensions in shock tubes is that of driver gas backfilling [29]. For such a technique, the driver fill port is required to be near the driver endwall. This method of backfilling enables the helium to be filled first to achieve high-strength (high Mach number) shock waves with a light, high-specific-heat gas near the diaphragm, while also lengthening test times with low-sound-speed gases near the driver endwall. Such a lengthening of test times occurs because although the sound travels quickly in He (~1000

m/s at room temperature), the backfill gas can be selected with a low sound speed. Thus, after diaphragm rupture, the expansion fan travels through the helium gas and once it arrives at the backfill gas its speed dramatically decreases, taking longer to travel through the tube than in an experiment using an all-helium driver gas. A schematic of this concept is shown on an x-t diagram in Figure 3.5.

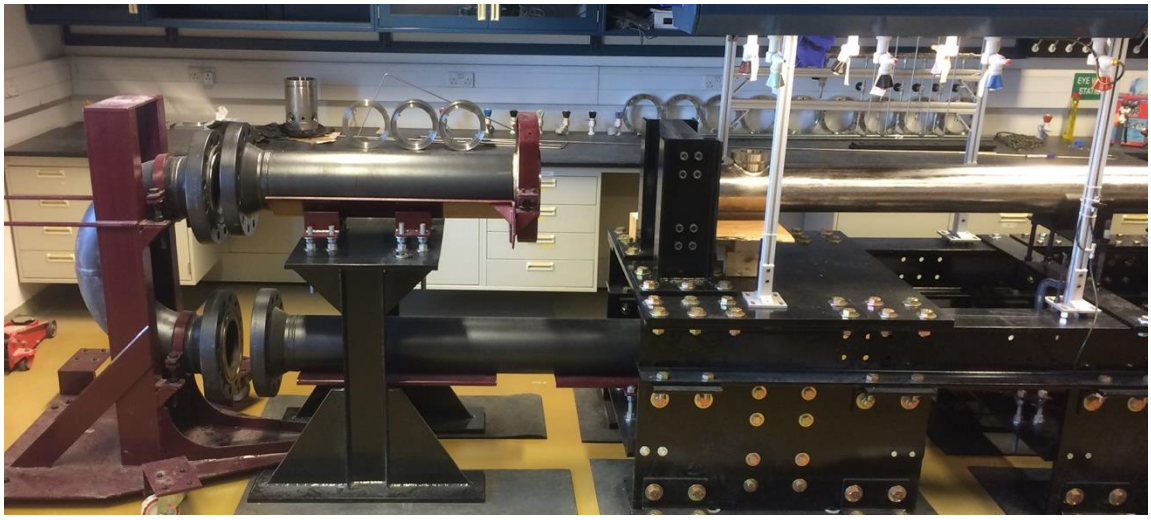

Figure 3.6 Picture of the driver tube in place prior to installation of the diaphragm breech mechanism assembly.

To enable such a backfill technique in the current shock tube, a fill port has been placed near the end of each length of driver tubing, enabling driver-gas backfilling to be performed in any configuration. A picture of the driver section of the shock tube is shown in Figure 3.6. The driver section is painted black and is shown on the left side of the picture with the stainless steel driven section shown on the right. The diaphragm cannister and breech-loading mechanism are not shown. One noticeable aspect of the driver section is that the geometry is not a straight piece of tubing, but instead is U-shaped. This geometry

was used to conserve space in the laboratory. Such a geometry was used by other researchers and is believed to show minimal effect on the post-reflected-shock pressure behavior [117]. More discussion is provided regarding the U-bend geometry of the driver tube in a following chapter.

A consequence of enlarging the driver-tube diameter for the current facility is the need for enlarged diaphragms and thus, an enlarged diaphragm loading breech cannister compared to the 3” inner diameter driver of the College Station shock tubes. With the opportunity to incorporate an enlarged diaphragm loading mechanism, the diaphragm cannister mechanism was also equipped with the ability to operate with a double-diaphragm section. In double-diaphragm operation, the timing with which the diaphragm ruptures can be precisely controlled, and by extension the pressure acting on the diaphragm when it breaks is also precisely controlled. This time control provides experimenters greater test-to-test control of the T_5 and P_5 conditions during a test campaign. A section view of the double-diaphragm configuration of the diaphragm breech loading mechanism is shown in Figure 3.7. When operating the shock tube at pressures below approximately 15 atm, the diaphragms used are made from polycarbonate. Polycarbonate is selected because of its high strength and the tendency to burst without stretching significantly. As it is a plastic, however, it can still deform somewhat prior to breaking and so a cutter is used to break the diaphragms in a repeatable fashion. For experiments at higher pressures of 20 atm and beyond, pre-scored metal diaphragms are used.

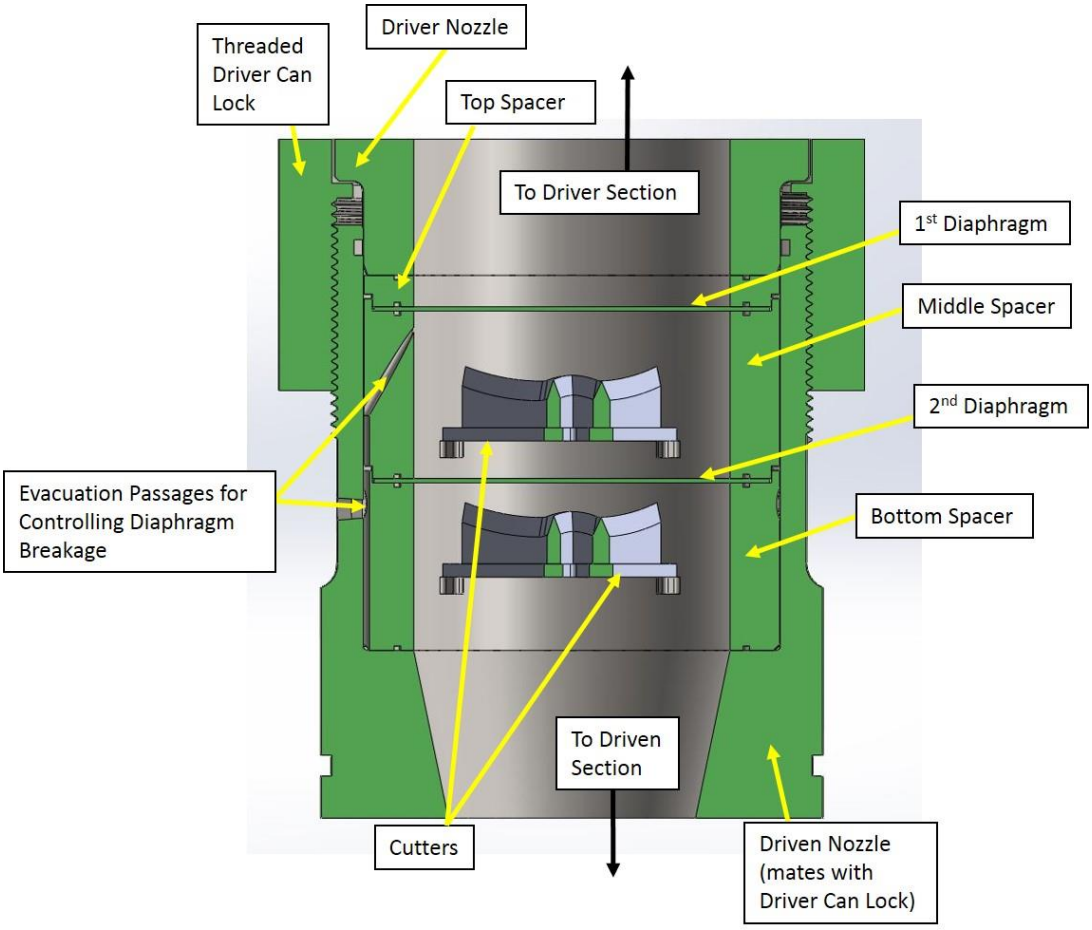

Figure 3.7 Section view of double-diaphragm breech loading section.

3.1.2.1.2. Inertial Mass

As stated previously, the pressure limit of this facility for experimental conditions behind the reflected shock wave is 100 atm. This pressure equates to roughly a 50,000-pound (~225 kN) impulse load applied to the driven endwall. Such an impulse will cause the facility to experience significant motion if it is not secured in some fashion. To offset the force from such an impulse, the shock-tube facility is equipped with a 7-tonne inertial mass. The inertial mass also doubles as the stands for the facility and is partially shown in Figure 3.6. It is constructed from 1" thick steel plates and I-beams. The shock tube is

mounted to an adapter plate which is attached to the inertial mass near the diaphragm interface. This mounting channels the force resultant from the impact of the shock wave at the driven endwall into the inertial mass in a horizontal direction, causing the mass to effectively behave as a sled. A 3-D rendering of the shock tube with the inertial mass shown in the center is displayed in Figure 3.8.

3.1.2.1.3. Driven Section

Although much of the geometry and length of the driven section of the new shock-tube facility is taken from previous designs in the Petersen Group shock-tube lab at Texas A&M [114-116], some additions and alterations have been incorporated into the present facility. These differences were incorporated primarily for use with the aerosol operation of the shock tube but will also facilitate other uses for the facility.

The first and most-significant difference between the driven-tube section of this shock-tube facility, pictured in Figure 3.8, and the shock-tube facilities in College Station is the addition of a gate valve placed approximately 1.25 m upstream of the driven endwall. The gate valve is also shown in Figure 3.8 towards the right end of the shock tube. The

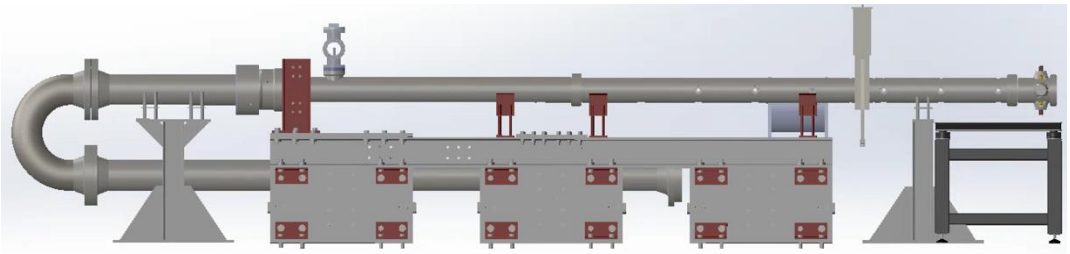

Figure 3.8 Diagram of shock tube setup showing inertial mass. The inertial mass also acts as a stand. Also shown is the new driver section and also the new gate valve located toward the right end of the driven section.

purpose of the gate valve is to aid in the process of introducing the aerosol into the shock tube. The concept of a gate valve technique for aerosol filling in shock tubes was introduced by Haylett and coworkers [35] in their second generation aerosol shock tube in an effort to improve the spatial loading uniformity of the aerosol within the shock tube compared to their first generation aerosol shock tube [34, 85]. In addition to being used with the aerosol capabilities, the gate valve may also be used to enable the shock tube to operate as a constrained reaction volume (CRV) shock tube [86, 87]. The purpose of a CRV shock tube is primarily to avoid the occurrence of remote ignition at locations far from the endwall and minimize the deviation of the constant-pressure and internal energy assumption due to reacting chemistry prior to ignition in non-dilute environments. Although it is a useful tool, the CRV shock-tube concept is not discussed in further detail herein, but the construction of the gate valve is instead examined more closely.

The geometry of the gate valve was modeled after that given by Campbell and coworkers [86] and is shown in Figure 3.9. There are three primary plates that perform the main functions of the gate valve, each with a central 6.00” hole for mating to the internal bore diameter of the driven section of the shock tube. A sliding gate is mounted between two face plates. Each face plate attaches to the shock tube in a similar fashion to that of the weldless flanges used to connect the driven tubing sections of the shock tube. Ports have been drilled into both the upstream and downstream face plates to allow for evacuation and purging of the internal gate valve volume before and after each experiment. Grooves have been machined on the internal faces of the gate valve face plates to

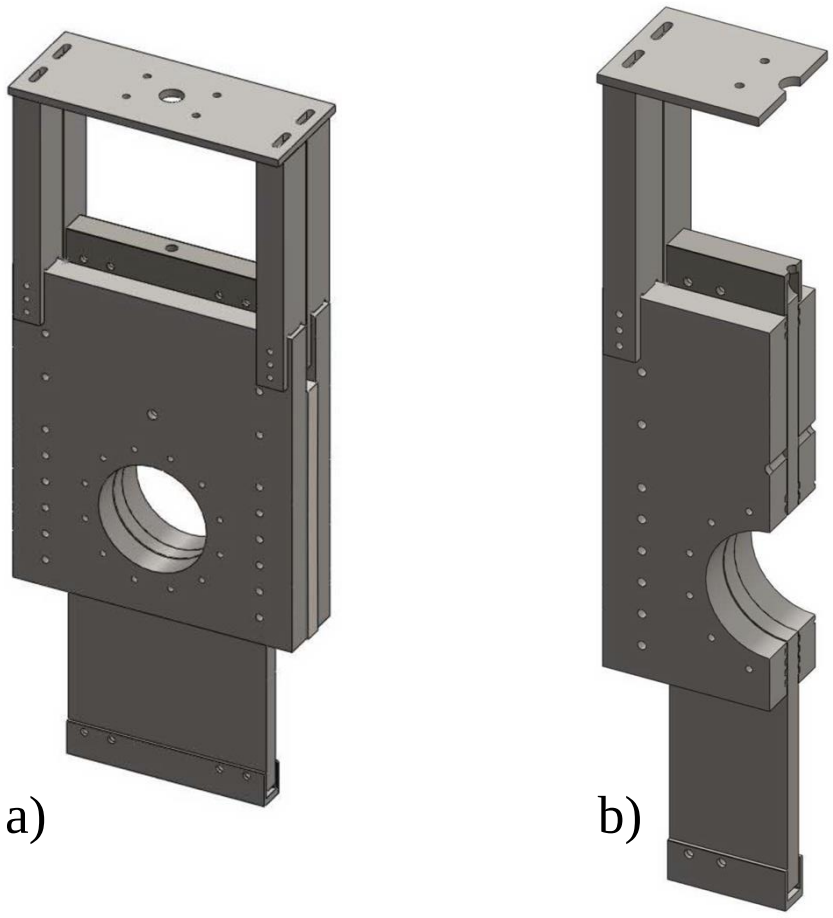

Figure 3.9 Views of the gate valve constructed for the aerosol shock tube. a) Isometric view; b) Isometric section view. The gate valve is in the open position.

accommodate o-rings which form a seal against the sliding gate. These seals form a cavity within the gate valve which is sealed from the shock tube as well as from the lab environment. The central sliding gate is approximately 1" thick and was machined to roughly a 16 μ-in RMS surface finish to enable the gate to slide smoothly.

It should be noted that for construction of such a sliding piece, a roughness no greater than approximately 16 μ-in. RMS is desired. This constraint is because the roughness on the surface allows grease to flow within the micro-imperfections in the

surface and maintain lubrication against the o-rings. A mirror finish would not be easily lubricated due to the surface not being able to hold much vacuum grease (no imperfections for grease to flow in to), and the o-rings would need to be replaced frequently. Furthermore, the central hole in the sliding gate which matches the bore of the shock tube is beveled so as to allow passage over the face plate o-rings without tearing them. Such a bevel has not been shown to cause significant perturbation of the shock wave or of the flow behind the incident shock wave in pressure traces (discussed more in the following chapter). To ensure that the spacing between the slider plate and the face plates remains consistent, spacers were placed between the face plates such that spacing on either side of the slider plate is approximately 0.030” and can be fine-tuned using shims. A pneumatic piston with a stroke of 8” is used to actuate the gate valve. An exploded view of the gate valve components is shown in Figure 3.10.

The second major hardware modification to the driven section of the aerosol shock tube is the addition of heated window ports placed at sidewall port locations near the driven endwall for laser diagnostic measurements associated with fuel aerosols. Locations of sidewall-mounted windows are near the endwall in shock tubes used for combustion kinetics because the primary region of interest for the experiment is the region that the reflected shock wave passes through first. This region is nearest to the driven endwall. Additionally, the fuel concentration diagnostic used to measure gaseous concentrations of evaporated fuel droplets is used not behind the reflected shock wave, but the incident shock wave. This location is because the region behind the reflected shock wave begins to undergo chemical changes immediately after the reflected shock wave passes, and the

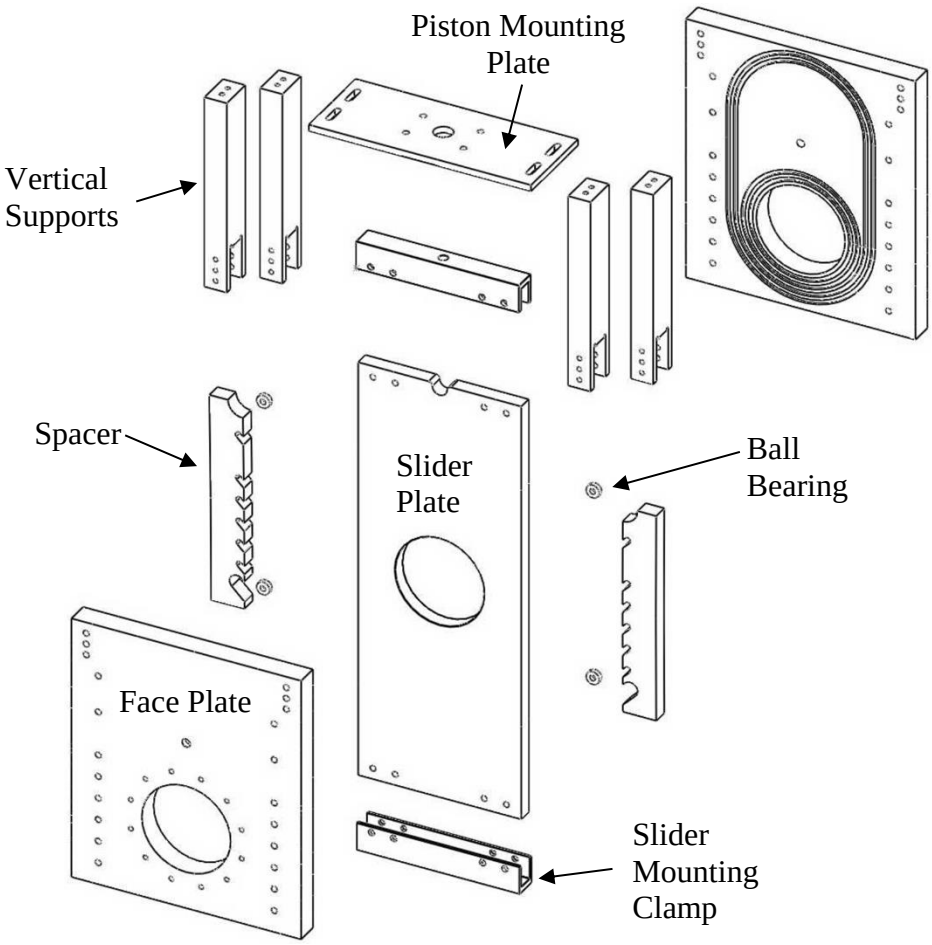

Figure 3.10 Exploded view of gate valve components. The pneumatic piston is not pictured here.

fuel concentration may not be constant for a long enough period to record an accurate reading prior to the occurrence of significant decomposition. Conversely, a sidewall window location placed a sufficient distance from the endwall provides an adequate period of time over which to collect spectroscopic laser absorption data for measuring the fuel concentration behind the incident shock wave.

Such a technique using heated window ports in an aerosol shock tube was first used by Davidson and coworkers in their first-generation aerosol shock tube while measuring evaporated fuel concentrations from nebulized fuels behind incident shock waves [34]. Although the liquid fuels in an aerosol shock tube are suspended in a carrier gas, they may still come into contact with the sidewalls of the shock tube during the filling process. Intuition may lead an experimenter to reason that although the droplets stick to the window prior to passage of the shock wave, the high temperatures behind the shock wave should evaporate the droplets on the windows. Evaporation of liquid droplets behind the incident shock wave certainly takes place in the region of the shock tube away from the walls, assuming the droplet distribution is similar to that of Davidson et al. However, near the walls of the shock tube the thermal boundary layer prevents the mixture from reaching the same temperature as the bulk of the flow in the center of the tube. This result is because the walls of the shock tube are at room temperature, several hundred K below that of the post-incident-shock gases, and act as a heat sink which extracts energy from the flow. Because of the relatively short duration of a shock-tube experiment, this heat sink action is generally not significant enough to interfere with the global behavior of the shock wave or the properties of the shocked gases, but it does keep the walls and windows of the shock tube near room temperature. Furthermore, the droplets on the windows will certainly evaporate behind the reflected shock wave.

However, the measurement of fuel concentration does not occur behind the reflected shock in Region 5 but instead is taken behind the incident shock wave in Region 2 where the pressure and temperature are significantly lower than Region 5. A lower

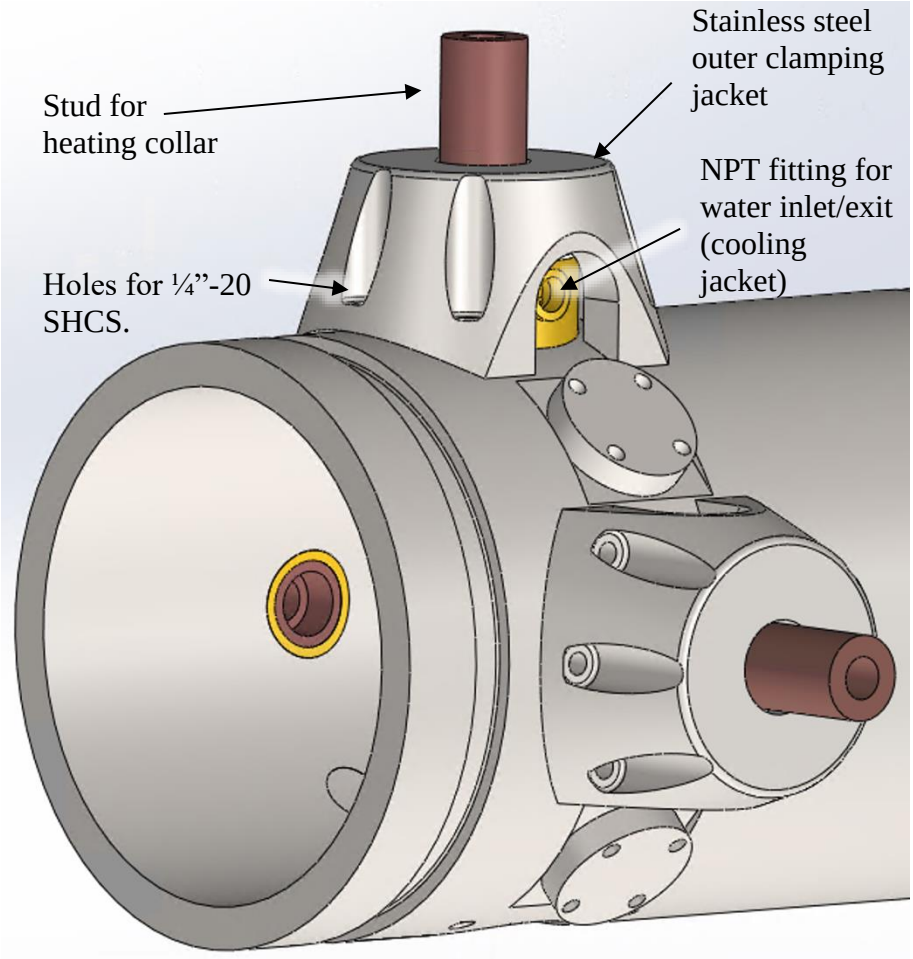

Figure 3.11 External view of heated window ports near the endwall connection of the driven section.

Region 2 temperature and pressure means a longer droplet evaporation time compared to Region 5 conditions. Combined with the effect of a cold wall, any droplets on the window will not evaporate quickly. Unevaporated droplets which are stuck to the windows will in turn interfere with the measurement of the fuel concentration behind the incident shock wave and bias the results. In fact, the droplets on the windows will likely grow behind the incident shock wave as the pressure increases due to an increase in fuel vapor partial

pressure in Region 2 compared to Region 1. Thus, it is critical for the windows to be heated for accurate measurement of fuel concentration behind the incident shock wave. A 3-D model rendering of the heated window port assembly is shown mounted to the shock tube in Figure 3.11.

Although heated windows are required to avoid fuel condensation and droplet fouling during a spectroscopic fuel concentration measurement, care must be taken to heat only the window itself and minimize heat transfer to the shock-tube walls immediately surrounding the window. To this end, a window port has been designed with a copper window port, brass cooling jacket, and insulated fittings to prevent significant conduction to the shock tube walls. The through hole is a half inch wide, providing ample room for laser beams to pass through.

A section-view of the port is shown in Figure 3.12. At first, the insulating spacers shown in white were made from alumina material. However, the task of installing such washers without cracking them was found to be extremely difficult. After some trial and error, it was found that washers made from polycarbonate performed well. Because the windows were heated to a maximum temperature of 100°C, the polycarbonate was able to withstand the force from shock waves while also withstanding the heat from the ports. This is because the glass transition temperature of polycarbonate is near 120°C and the material maintains much of its strength up to this transition temperature. Additionally, the washers were only subject to a compression force and not tension and shearing forces experienced by other materials in the shock-tube setup.

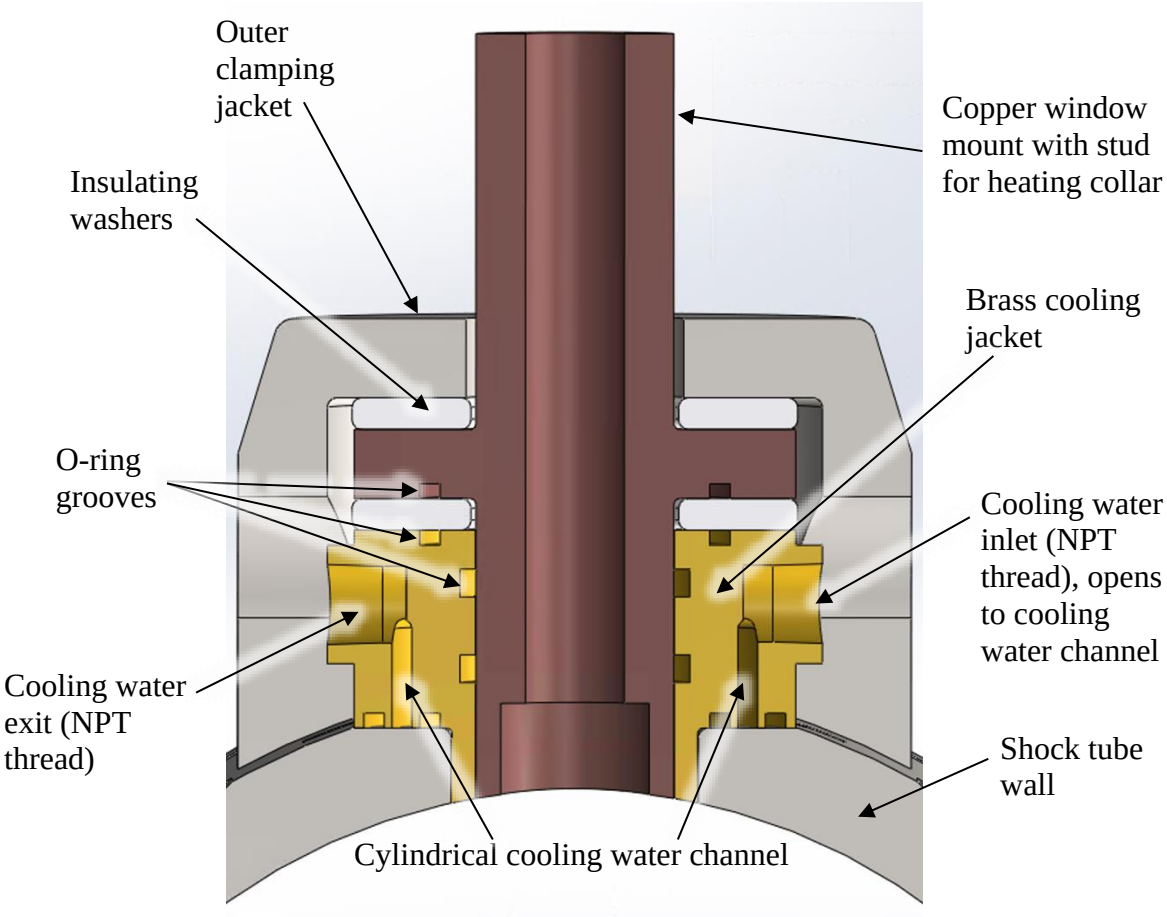

Figure 3.12 Section view of the cylindrically shaped heated window port assemly mounted on the shock tube.

3.2. **Aerosol Generation and Handling**

Although this project entailed the design and construction of a new shock tube, this was not the primary source of experimental innovation. In fact, the majority of the shock-tube design itself incorporated experiences gained by other researchers [29, 34, 35, 114, 115] and required little effort from a design perspective. The other major aspect of this new facility, however, required a thorough design process and rigorous characterization to evaluate the utility and applicability of the facility. All aspects of the

design of a new aerosol generation and entrainment facility utilized in this work is discussed in detail in this section.

3.2.1. Design Considerations

When designing the new aerosol-generation facility, several aspects of previously constructed facilities were taken into account during the design process [34, 35, 42]. The first, and perhaps most critical, aspect of the shock-tube design to consider was the impact of droplet size on the various processes associated with the aerosol shock tube.

3.2.1.1. Post-Incident-Shock Aerosol Transport Considerations

One of the processes involving aerosols which was influential in the design of this facility was that of droplet relaxation behind the incident shock wave. An appropriately sized droplet distribution provides experimenters confidence that droplets will accelerate and evaporate quickly behind the incident shock wave. However, a balance must be struck between relaxation behavior of the droplets and the total mass loading attainable in the shock tube. Mass loading will also be dependent on the droplet introduction method, but this is discussed in a following section. Large droplets will provide high mass loadings but may not be able to evaporate in a sufficiently fast time frame and thereby interfering with the calculation of post-shock properties. On the other hand, a grouping of extremely small droplets will accelerate and evaporate quickly behind the incident shock wave but may not provide sufficient mass loadings needed for real fuel-air mixtures at high experimental pressures. Thus, striking a balance between relaxation and mass loading is critical in selecting the appropriate size of aerosol droplets.

3.2.1.2. Droplet Generation

One of the primary reasons a tradeoff exists between droplet loading and relative size distribution lies in the technology available to generate droplets. Furthermore, the challenge in generating high mass loadings is due to the fact that droplet mass is proportional to the cube of the diameter. Thus, a droplet with a 1- μm diameter is a factor of 1000 smaller in volume and mass than a droplet with a diameter of 10 μm. Coupling this geometric tradeoff with the challenges associated with relaxation effects in larger droplets, the need to achieve an appropriately sized droplet distribution cannot be over-emphasized.

Fortunately, previous aerosol shock-tube researchers were able to settle on a mean droplet diameter and size distribution which accommodated high mass loadings while still enabling rapid evaporation behind the incident shock wave. Hanson and coworkers [74] used a droplet distribution with a mass mean near 4.9 μm and a lognormal spread parameter of 1.50, as did Davidson et al. [34] and Haylett et al. [35].

At present, various methods exist for generating extremely small droplets. Few methods, however, are able to generate high number densities of droplets with an adequately small mean diameter in a relatively short amount of time. The most common industrial method used to generate a large volume of droplets quickly is in the form of a high-pressure flow of liquid forced through a small orifice into a carrier gas, such as in the operation of fuel injector for an internal combustion engine. Historically, high-pressure fuel injectors have been able to generate the mass loadings required for use in shock tubes, like those used by Rotavera et al. [76] and Cadman et al. [75], among others. However,

the droplet distributions of typical automobile injectors are generally too large for applications to aerosol shock tubes when pre-shock dispersion and settling must be considered.

More promising results have been shown somewhat recently where a newer automobile fuel injector was used to generate droplets near 10 μm in diameter. The work of Jiang et al. [78] showed that fuels can be generated with Sauter mean diameters near 10 μm. Since the Sauter mean diameter is significantly smaller than the mass mean diameter for a given lognormal size distribution [43], however, this means that the mass mean diameter of the droplets was significantly larger than 10 μm. Compared to the mass mean diameters achieved by previously mentioned aerosol shock-tube researchers (4.5 μm), the smallest mass mean diameters from the fuel injector of Jiang et al. are not comparable to those generated using ultrasonic nebulizers when desiring to minimize droplet size yet also achieve high mass loadings.

Thus, for the work performed herein, the best device to generate a satisfactory volume of small droplets for use with a shock tube is the ultrasonic nebulizer. The ultrasonic nebulizer is generally available in two operating frequencies: 1.7 MHz and 2.4 MHz. Nebulizers operating at frequencies of 2.4 MHz generally produce droplets with a mass mean of 1-2 μm, and those operating near 1.7 MHz produce droplets with an average mass mean around 5 μm in diameter, as in the works previously mentioned in this section. The nebulizer was purchased from the House of Hydro [118] and is pictured in Figure 3.13.

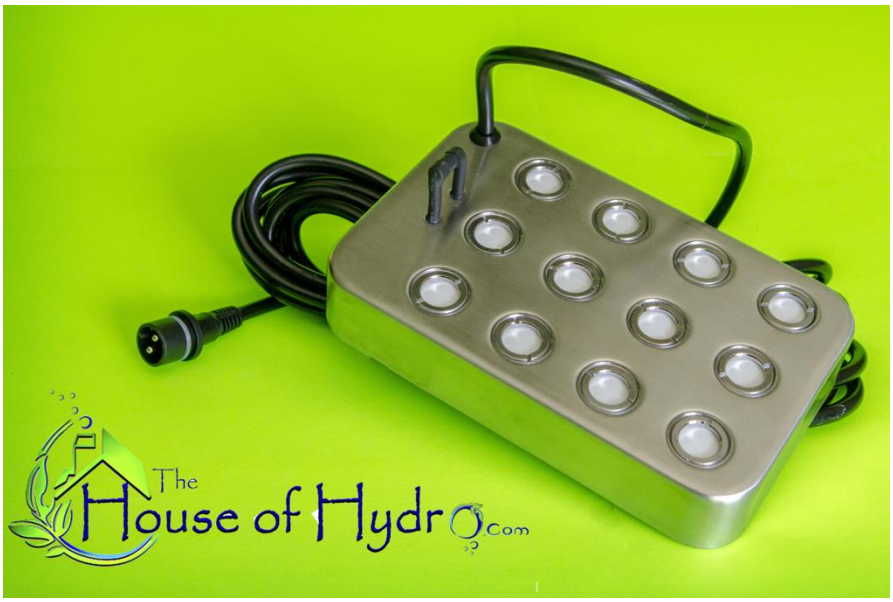

Figure 3.13 Image of 12-Disc ultrasonic nebulizer purchased from the House of Hydro. Image obtained from https://www.thehouseofhydro.com/store.html. Prior to operation with fuels, the water depth sensor had to be removed.

3.2.2. Aerosol Transport Methods

In addition to droplet relaxation being a critical process to consider when designing an aerosol shock tube, the aerosol entrainment method used to bring the aerosol into the shock tube is equally critical and requires significant analysis during the design process. Although the droplet-generation method for two of the most recent aerosol shock tubes was the same, the methods of aerosol introduction and entrainment between the two were significantly different [34, 35]. As discussed in a Chapter 2, the Gen. II facility developed by Haylett et al. displayed significantly better levels of aerosol loading uniformity than the Gen. I aerosol shock-tube facility of Davidson et al.

The reason for this difference was the method of aerosol dispersion and introduction into the shock tube itself. In their Gen. I facility, Davidson et al. generated

aerosol and brought it into the shock tube in a continuous manner: a constant flow of carrier gas was flowed from an external tank over a nebulizer to form an aerosol. The aerosol then passed through a pre-mixing chamber and finally into the shock tube itself, filling the entire driven section volume. After a length of time where the shock tube was determined to be adequately filled, all fill ports were closed and the nebulizer was turned off. In their Gen. II facility, Haylett et al. isolated approximately the last 1.2 m of the driven section near the endwall of the shock tube using a gate valve to restrict aerosol to this region. They also used an external holding tank mounted to the shock tube to generate a fixed volume of aerosol. The tank and isolated section of the shock tube were separated by a second gate valve which doubled as the shock tube endwall. With both gate valves closed, the aerosol was generated in the holding tank and then transferred into the shock tube by opening the endwall gate valve and a ball valve near the upstream gate valve connected to an evacuated dump tank, resulting in a plug flow within the driven section.

A diagram depicting the two differing processes is shown in Figure 3.14. As discussed by Haylett et al., the Gen. II aerosol shock tube displayed significantly better uniformity compared to the Gen. I aerosol shock tube. Although the plug-flow method of filling contributes to the improved uniformity in the Gen. II aerosol shock tube, it eliminates any possibility of utilizing endwall diagnostics. Furthermore, it is likely not only the plug flow which provides the high degree of aerosol loading uniformity displayed by this facility, but also the fact that only a relatively small portion of the driven shock-tube volume is filled with aerosol. This smaller active volume allows the filling process to occur over a shorter time scale than the Gen. I method and prevents the plug flow

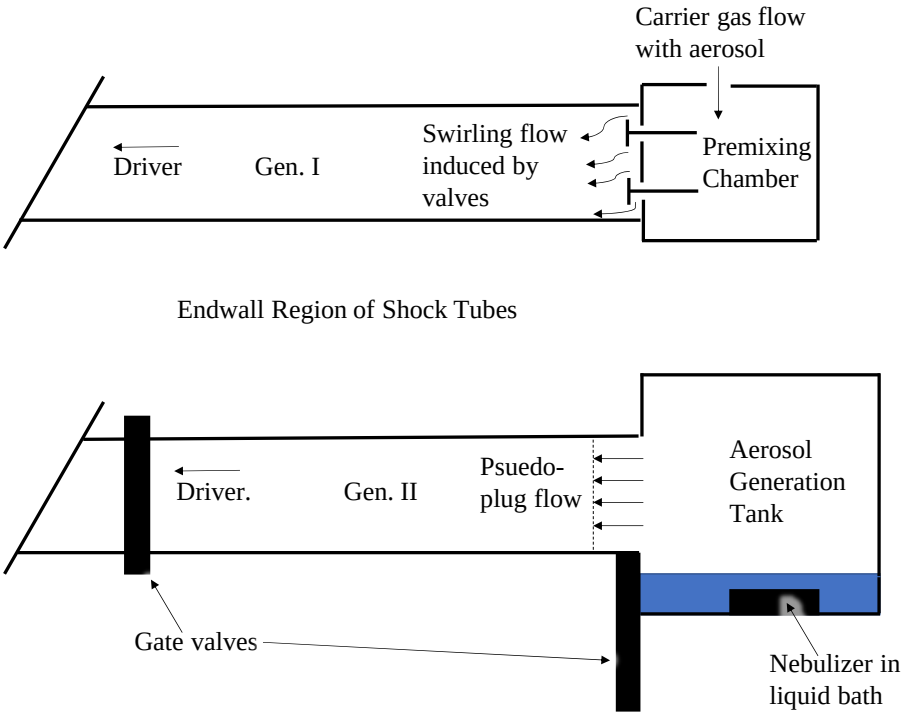

Figure 3.14 Difference between filling methods of the Gen. I aerosol shock tube of Davidson et al. and the Gen. II aerosol shock tube of Haylett et al.

interface from becoming distorted like it would over a longer distance. Additionally, if the plug flow filling method is used to fill only a small portion of the driven tube near the endwall then this requires the use of an upstream gate valve (unless, that is, an overly large aerosol generation tank were used to fill the entire driven section with a plug flow).

Thus, although a single upstream gate valve was considered critical for any aerosol shock tube from the recommendation at the end of Chapter 2, a second gate valve doubling as the endwall may not be equally as essential. Due to the lack of diagnostic access at the endwall of the driven section with an endwall gate valve, only a single gate valve was used in this thesis. Consequently, the plug flow method of Haylett et al. was not used to fill the

shock tube, and a new filling method which is somewhat of a combination of the filling methods from the Gen. I and Gen. II shock tubes was developed.

3.2.2.1. Filling Procedure and General Setup

Considering the case of an aerosol filling method, two general approaches have been used to create homogenous mixtures in shock tubes, as discussed previously [34, 35, 42]. Because the Gen. I filling method of Davidson et al. was shown to result in lower droplet loading uniformity in the shock tube as compared to the transient Gen. II method of Haylett et al., a similar transient approach to the Gen. II method was used in this work. Furthermore, a steady-state flow method of introducing the aerosol would have also required significant intricacies compared to a transient flow setup. In particular, control over the final pressure of the shock-tube setup at the completion of a filling event is more easily achieved with a transient method; when two separate tanks with different pressures are allowed to relax to an equilibrium pressure, this final pressure is easily calculable. Because of the desire to maintain endwall diagnostic access, however, the AGT could not be placed at the endwall and sealed via a gate valve that doubled as the endwall, as was the case with the Gen. II filling method. Thus, the final design of the aerosol generation and filling scheme required a combination of the Gen. I method which disbursed the aerosol in a more-turbulent manner than that of the plug flow method whilst still using the transient flow calculations of the Gen. II filling scheme.

For a transient flow scheme in which an aerosol is generated externally to the shock tube and then transferred into the driven section, two distinct volumes are required in addition to the shock tube test section between the gate valve and driven endwall: an

aerosol generation tank (AGT) and an evacuated dump tank. Additionally, the duration of the flow during the aerosol filling process will play a significant role in dispersing the aerosol within the test section volume. This flow duration can also be conceptualized from another perspective. In the work of Haylett et al. [35], a variable was defined that governed the number of times the plug flow filled the aerosol test section. Such a method insured that the aerosol contact surface (which was originally at the endwall gate valve prior to filling) passed through the outlet in the aerosol test section and into the dump tank and thus filling the test section with aerosol. This variable, termed here as the fill ratio (number of test section volumes filled), provides a more straightforward method of defining flow duration than a complex analysis of total flow time and was subsequently utilized in defining the flow duration of the filling process for this work.

Furthermore, such a method is relatively straightforward compared to defining a total time of flow duration because the fill ratio is defined only by total volumes and pressures, and not also by the flow coefficients of valves, tubing, and joints within the flow system. Using an isentropic assumption for the expansion of gases into the dump tanks, and the known volumes, fill ratio, and desired final pressure (the final post-fill pressure is also the pre-shock P_1), the pre-fill pressures in all volumes can be calculated. They are given by Eq. (3.2)-Eq. (3.4). In these equations, the subscript D corresponds to the dump tank, the subscript TS for the aerosol test section between the gate valve and endwall, and AGT for the aerosol generation tank. The fill ratio is defined by Eq. (3.4), where V' is the total volume to be filled by the aerosol in addition to the AGT volume. That is, the final volume occupied by the aerosol after the completion of the filling process

is equal to (V_{AGT} + V'). It should also be mentioned here that the concept of fill ratio is more easily visualized with a plug flow because the plug flow interface is more well-defined. However, this concept is still useful for filling methods where the aerosol is mixed within the driven section since the measured non-uniformity can be related to the fill ratio in an empirical sense.

$$P_D = \left[\frac{V_D - V'}{V_D}\right]^{\gamma} P_1 \tag{3.2}$$

$$P_{AGT+TS} = \frac{P_{initial}(V_{AGT+TS} - V_D) - P_D V_D}{V_{AGT+TS}} \tag{3.3}$$

$$X = \frac{V'}{V_{TS}} \tag{3.4}$$

Using the work of Haylett et al. as a framework, the length from the gate valve for this facility to the driven endwall was set at 1.30 m (adjustable by $\pm$0.05 m). This length in the driven section, along with the diameter, defines the volume of the aerosol test section at roughly 23.7 L. Additionally, the corresponding volumes of the AGT and dump tank were set such that the fill ratio could be selected with up to a maximum value of around 3.1. The dump tank volume was selected around roughly 125 L and the AGT at a volume of 27 L. With these parameters selected, a generalized filling process could be conceptualized. The process is as follows: 1) Evacuate all volumes then fill them to the appropriate pressures to achieve the desired fill ratio and final pressure, P_1 (the AGT and aerosol test section can remain open to one another because their initial pressures are the same); 2) run nebulizer and mixing fan within the AGT for desired length of time to achieve desired final aerosol loading; and, 3) open the ball valve between the aerosol test

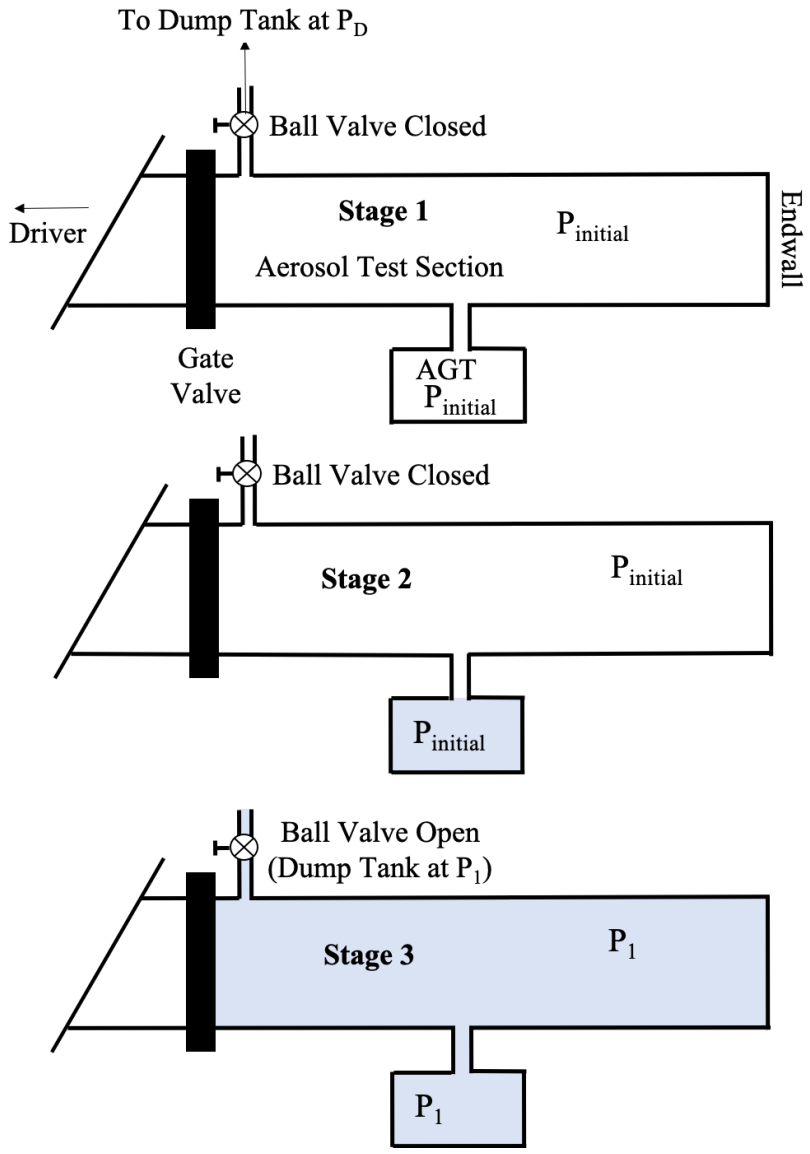

Figure 3.15 Various stages of the filling process used to introduce aerosol into the test section of the shock tube between the gate valve and the endwall for an AGT and dump tank each of arbitrary size and position. Drawing not to scale.

section and the dump tanks. A stepwise diagram of this process is shown in Figure 3.15. With this framework in mind, the design process by which the aerosol was introduced into the shock tube from the AGT was undertaken. The first phase of the design was that of the flow path between the AGT and the shock-tube aerosol test section.

3.2.2.2. Flow Path Considerations

When considering the orientation of the AGT relative to the shock tube, it was decided that the AGT could not be mounted directly to the endwall portion of the shock tube and had to instead be mounted in another location. This upstream location allowed access to endwall diagnostics to be preserved. Furthermore, the type of flow generated in the shock tube could no longer be a plug flow if the AGT were not mounted directly on the endwall of the shock tube. Given that the Gen. I aerosol shock tube of Davidson et al. displayed worse uniformity than the Gen. II version of Haylett et al., it was considered that perhaps only a plug-flow technique was able to achieve the uniformity necessary for the collection of quality kinetics data in an aerosol shock tube. Various imperfections in the handling of aerosols were present in the Gen. I filling method, however, which were likely unaccounted for in that design.

Thus, an effort was made here to generate a uniform aerosol within a standalone AGT and introduce it into the shock tube via a network of tubing as opposed to using the plug flow method with an AGT mounted to the shock tube itself. The final location of the mixing tank could not be arbitrary however, because both the orientation of the tank itself relative to the shock tube played a significant role in the flow of the aerosol during the filling process.

Various questions arise when considering the best methods to minimize aerosol losses during filling of the shock tube via an AGT. Where should the AGT be positioned? In what manner should it be connected to the shock tube? Of course, some type of plumbing must be utilized to maintain a vacuum-tight seal in the system. What diameters

and lengths of tubing should be used, and in what configurations? The answers to these and similar such questions which arose during the design and construction phase of the aerosol generation assembly required considerable analysis and iteration to answer satisfactorily.

When attempting to maximize the droplet penetration through a network of pipes, emphasis is often placed on the size of the droplets. In the case of the droplet distribution provided by an ultrasonic nebulizer operating at 1.7 MHz, it was shown by Hanson et al. [74] and Davidson et al. [34] that such droplets can pass through intricate flow pathways in sufficient quantities to perform aerosol shock-tube experiments. In fact, droplets with diameters in the range of 1-10 μm are generally quite robust as their small size often results in low Stokes numbers. However, the works of Hanson et al. and Davidson et al. which used the Gen. I aerosol filling method were benefitted by a continuous flow of aerosol, which made any losses in the tubing and pre-chamber less critical than in a transient flow scheme.

In a transient scheme, aerosol is not generated constantly until a desired loading is achieved, but is instead finite. Thus, the need to minimize losses in a transient filling scheme is more significant. In addition to the robustness of the aerosol in resisting the effects of losses based on droplet diameter, the geometry of the flow path itself also plays a critical role. Furthermore, since the droplet distribution was fixed at a range of roughly 1-10 μm by using an ultrasonic nebulizer, the only remaining method by which droplet losses could be mitigated was the design of the flow path architecture through which the aerosol would flow.

During the process of designing an aerosol introduction scheme, the geometry of the flow path was revealed to play a critical role in curtailing droplet mass losses to the walls of the aerosol transport system. In general, high accelerations and/or velocities resultant from narrow passageways and tight turns provide ideal opportunities for droplets to be lost to the wall in a transport system. When considering the flow path design, however, it is best not to work in generalities, and a more rigorous analysis for the purposes of design is necessary. One avenue available to experimenters for design of fluid-flow systems is computational fluid dynamics (CFD). Although complex analysis of aerosol processes in flows using CFD is possible, and is in fact the desired tool for rigorous analysis with which to investigate penetration of droplets through complex geometries, it is beyond the scope of this work.

Other, simpler analytical tools are available to experimenters for designing aerosol tubing systems, though. A program developed at Texas A&M University which calculates the penetration of droplets or particles through a network of pipes and/or tubes was made available to perform such calculations. The program is called DEPOSITION [119] and was developed in the Aerosol Technology Laboratory at Texas A&M University's Mechanical Engineering Department. An updated in-house version of the program was released shortly after the turn of the last century and is called DEPOSITION 2001a. Programs like DEPOSITION, and others like that given by von der Weiden [120] (and references therein), use empirically derived correlations for particle penetration in tubing networks. Because these correlations are specific to particular sets of flow conditions, they are not applicable to a wide-ranging variety of flow paths and geometries. However, they

can be applied to simple, generalized geometries (a network of simple unions and/or turns with contractions/expansions, etc.) and provide insight into the relative magnitudes of deposition when comparing the behavior of different tubing networks.

Such an analysis was performed for the tubing network designed for this work between the AGT and the shock-tube driven section. The full range of this analysis is not presented here as it was performed in somewhat of an empirical fashion: define roughly 10-20, or more, geometries and run various flow conditions through each one. Such an effort also lends itself to parametric design studies, which could be considered in a future analysis. Presented here are sample calculations and results using DEPOSITION 2001a to provide relative magnitudes of droplet penetration within sample sets of tubing. This can provide an intuitive feel for how deposition losses are accumulated within various components.

In the analysis that follows, three primary parameters related to tubing geometry were modified in a simplified tubing system to show the change of droplet penetration. Tube diameter, tube path shape, and tube length were modified to show the relative effects that these variables have on droplet penetration. A tube with an inner diameter of 25 mm and length of 0.50 m was set as the control case to which all variations were compared. Additionally, the flow rate within the system was set such that it equated to a velocity within the shock-tube test section of 45 cm/s. The value of 45 cm/s is the value found by Haylett et al. to be the optimum speed within the shock-tube test section for the Gen. II aerosol shock-tube filling method for an example pre-experiment pressure, P_1 of interest [35]. The various parameters in this simplified parametric study using DEPOSITION

Table 3.1 List of flow path parameter configurations and their associated figure references.

Length (m)	Inner Dia. (mm)	Number of Bends	Bend Curvature Ratio	Figure Ref.
0.50	25	0	∞	Figure 3.16
0.50	15	0	∞	Figure 3.16
0.50	38	0	∞	Figure 3.16
0.50	25	1	2	Figure 3.17
0.50	25	1	4	Figure 3.17
0.50	25	1	8	Figure 3.17
0.50	25	2	4	Figure 3.18
0.50	25	3	4	Figure 3.18
1.00	25	0	∞	Figure 3.19
2.00	25	0	∞	Figure 3.19

2001a are shown in Table 3.1. Each combination of parameters is referenced in the table and has a corresponding reference to a figure showing the percentage of penetration through the given tubing network as a function of droplet size over the range of 1-10 μm. This range of droplet diameters was selected since that is the approximate range of droplet sizes produced by the ultrasonic nebulizer used for this study.

The first parameter to be investigated for comparing different configurations is the change of tube diameter. Aerosol penetration through a straight tube of 0.5 m length and internal diameter of 25 mm was calculated and is shown in Figure 3.16. This case is also the baseline to which all other geometries are compared. Next, the length is kept constant while the inner diameter is changed to 15 mm. The penetration results of the 15-mm inner diameter tube are also shown in Figure 3.16. Comparing the results from the 25-mm tube

and the 15-mm tube, it can be seen that a significant loss of aerosol is observed for most of the droplets over the given range of droplet diameters. More than half of the original mass of droplets will not pass through the tubing network at the given flow condition if a 15-mm tube were used as opposed to a 25-mm tube, which has roughly 90% total penetration through the tube. Considering a larger tube diameter than the 25-mm tube, the results of calculations using a 38-mm inner diameter tube are also shown in Figure 3.16. Comparing this result to the 25-mm diameter tubing shows that a 38-mm diameter tube experiences negligible mass loss through a 0.50m-length section of tubing. The conclusion to be drawn from the comparison of various tube sizes is that maximizing tube diameter will aid in minimizing droplet losses in the tubing. Next, tubes with bends are examined in the calculation results.

The first tube with a bend to be examined is a tube with a total length of 0.50 m (including the bend) and a 90-degree bend of curvature ratio 2.0 at the exit. The curvature ratio is the ratio of the radius of the bend to the radius of the tubing's circular profile. The results of the calculation using a single bend of curvature ratio 2.0 are shown in Figure 3.17. Calculations for a single bend with curvature ratios of 4.0 and 8.0, respectively, were also performed, with respective results shown Figure 3.17 as well. A general observation from these results with a curved bend prior to the tube outlet is that although a bend does cause some loss of larger droplets, the curvature ratio seems to have little effect on the penetration of aerosol through the tube for values above 2.0 when considering the given flow parameters defined for this system. A single bend loses more mass than no bend at all, but as the bend length is changed and total tube length kept constant, little change in

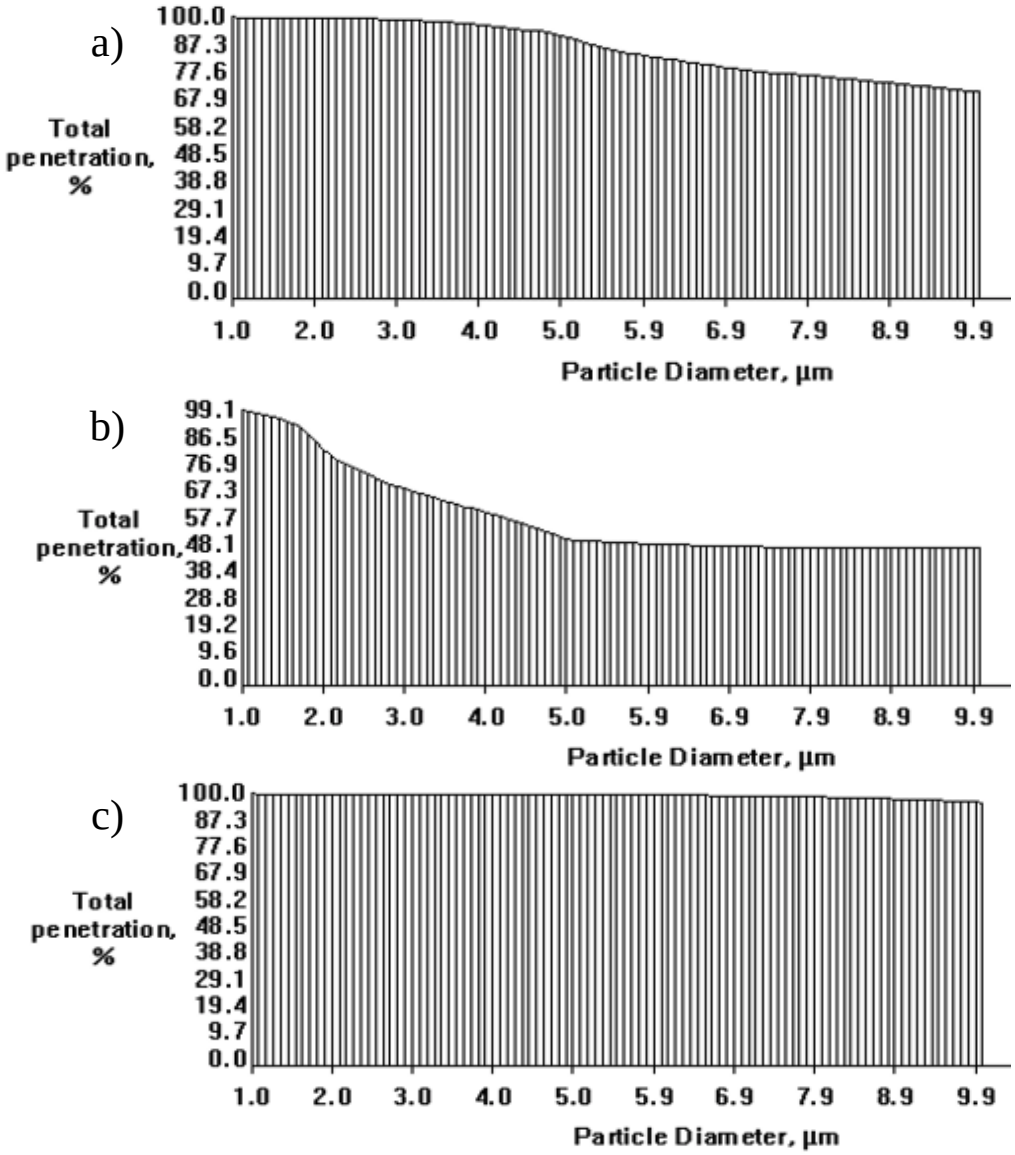

Figure 3.16 Aerosol penetration through a straight tube with varying inner diameter and length of 0.50 m using DEPOSITION 2001a. Top) Inner diameter of 25 mm, Middle) Inner diameter of 15 mm, Bottom) Inner diameter of 38 mm.

penetration is seen. It is likely that a sharp, 90-degree elbow with curvature ratio well below 2.0 would have significant effects on the amount of aerosol able to penetrate the system. Such a geometry is not available in the software of DEPOSITION 2001a, however, and was therefore not investigated.

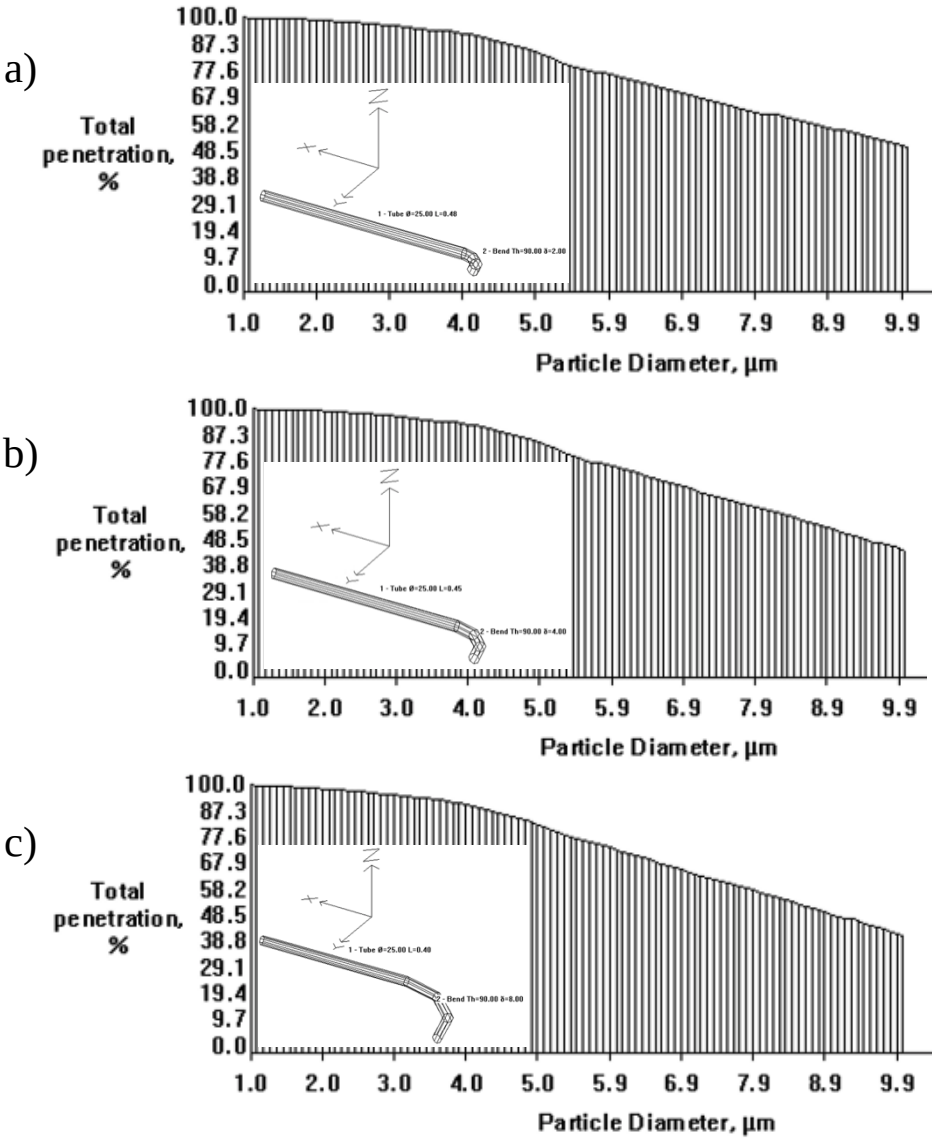

Figure 3.17 Aerosol penetration through a straight tube with varying inner diameter and length of 0.50 m using DEPOSITION 2001a. Top) Inner diameter of 25 mm, Middle) Inner diameter of 15 mm, Bottom) Inner diameter of 38 mm.

In addition to a single bend in the tube, calculations for tubes with two and three bends, respectively, were performed. The results of these calculations are shown in Figure 3.18. From the results of the calculations for the tubes with more than a single bend, the

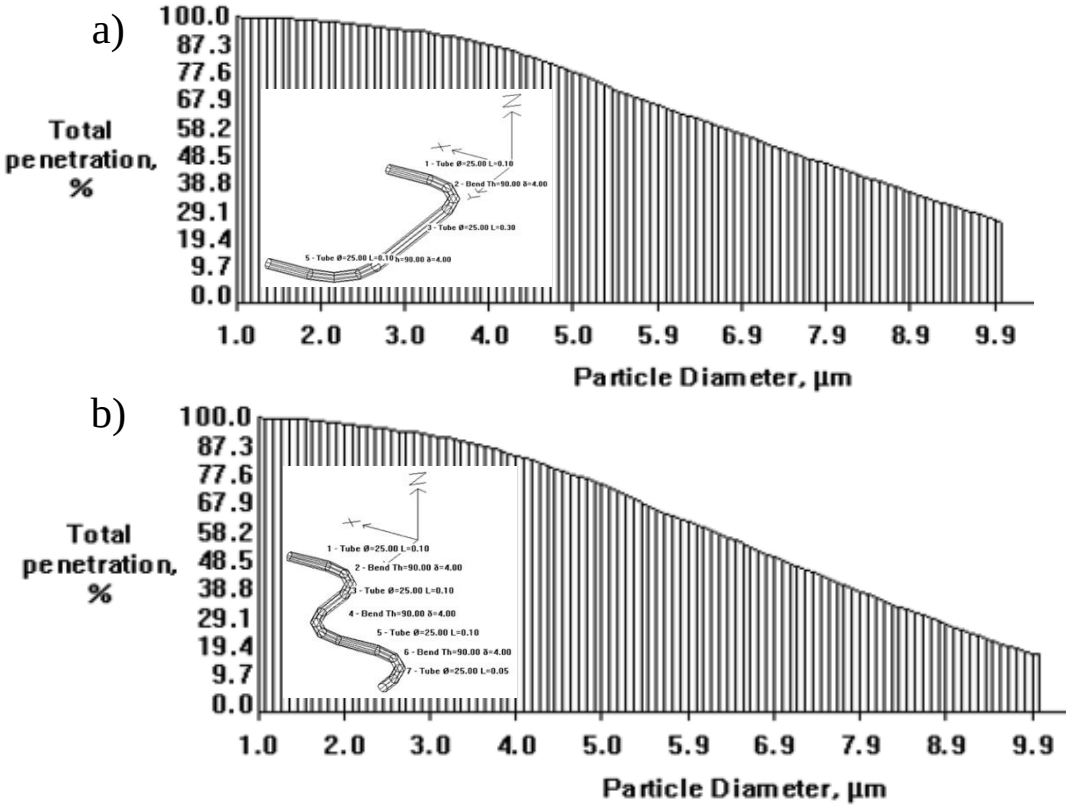

Figure 3.18 Droplet penetration through a 0.50-m-long tube with two bends of 90 degrees. The inner diameter is 25 mm and curvature ratio is 4.0. a) 2 bends, b) 3 bends.

amount of aerosol loss increases as the number of bends increases—an intuitive result. This analysis, however, shows that while some aerosol is able to penetrate a tube system with multiple bends, a majority of the larger droplets above approximately 5 microns for this flow rate configuration will be lost as the number of bends increases above 1. Thus, an important aspect of the design of the tubing network is that although some bends may be necessary, they should be generally avoided if possible. Furthermore, small tubing with multiple bends is not a good combination of geometries to use when maximized droplet penetration is desired through a network of tubes. This result is likely not a novel

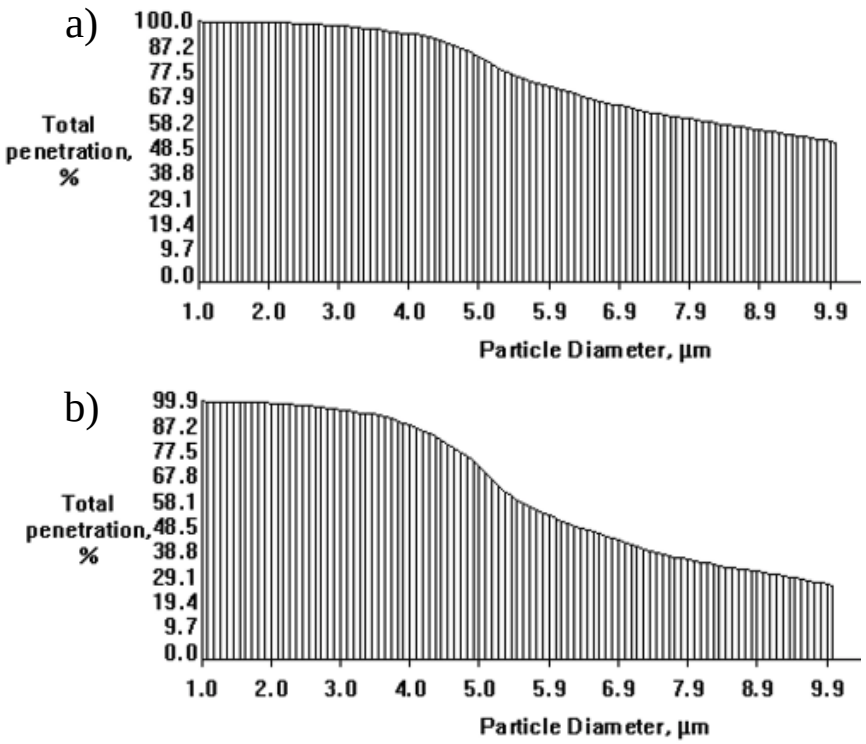

Figure 3.19 Aerosol penetration in straight tubes with inner diameter of 25 mm and varying lengths. a) Length=1.0 m, b) Length=2.0 m.

revelation, however it should provide experimenters with a framework of do's and don'ts to consider when designing aerosol transport methods where maximized droplet penetration is desirable. Finally, tube-length variations were input into the model and aerosol penetration calculated, with results shown in Figure 3.19.

At the completion of this simplified analysis, it should be re-emphasized that a change in flow properties (specifically, the flow rate) will alter the results of the calculations significantly. The overall conclusions of the relative magnitudes of the variation of each parameter will likely hold, however. Additionally, it is observed from the various droplet penetration plots in Figure 3.16-Figure 3.19 that an inflection point

may be seen to occur over a specific range of droplet sizes. This inflection point is related to the critical Stokes number for the given system (combination of velocities and particle sizes).

To conclude, the major takeaways from this analysis cemented the assumptions that minimizing the number of features in the tubing between the AGT and shock tube was critical. Furthermore, it was also confirmed that to best minimize losses, the tubing diameter should be maximized. The primary effect of modifying the tubing diameter was to reduce the velocity of the flow and prevent significant turbulent behavior from developing, making the penetration efficiency of the enlarged tube greater than the control tube diameter of 25 mm. Prior to conducting the analysis, it was theorized that perhaps a network of tubes could be designed such that certain sizes of droplets were tailored off in a controlled manner by way of a critical Stokes number. This idea proved to be unsuccessful, however, because the effectiveness of a simple tubing network at tailoring a droplet distribution is quite low compared to a precisely designed impactor [43].

Additionally, because the droplets are so narrowly distributed (1-10 μm is quite narrow for high-mass-output droplet generators), the level of control needed to tailor the distribution at a given flow condition would likely make the optimum design unusable at a different flow condition. That is, since the pre-shock pressure within the shock tube, and consequently the final pressure after completion of the filling process, is varied to modify the experimental temperature and pressure condition behind the reflected shock wave, it was not practical to create such a generalized device. Although more analysis can certainly be conducted to design a more generally applicable droplet size tailoring mechanism

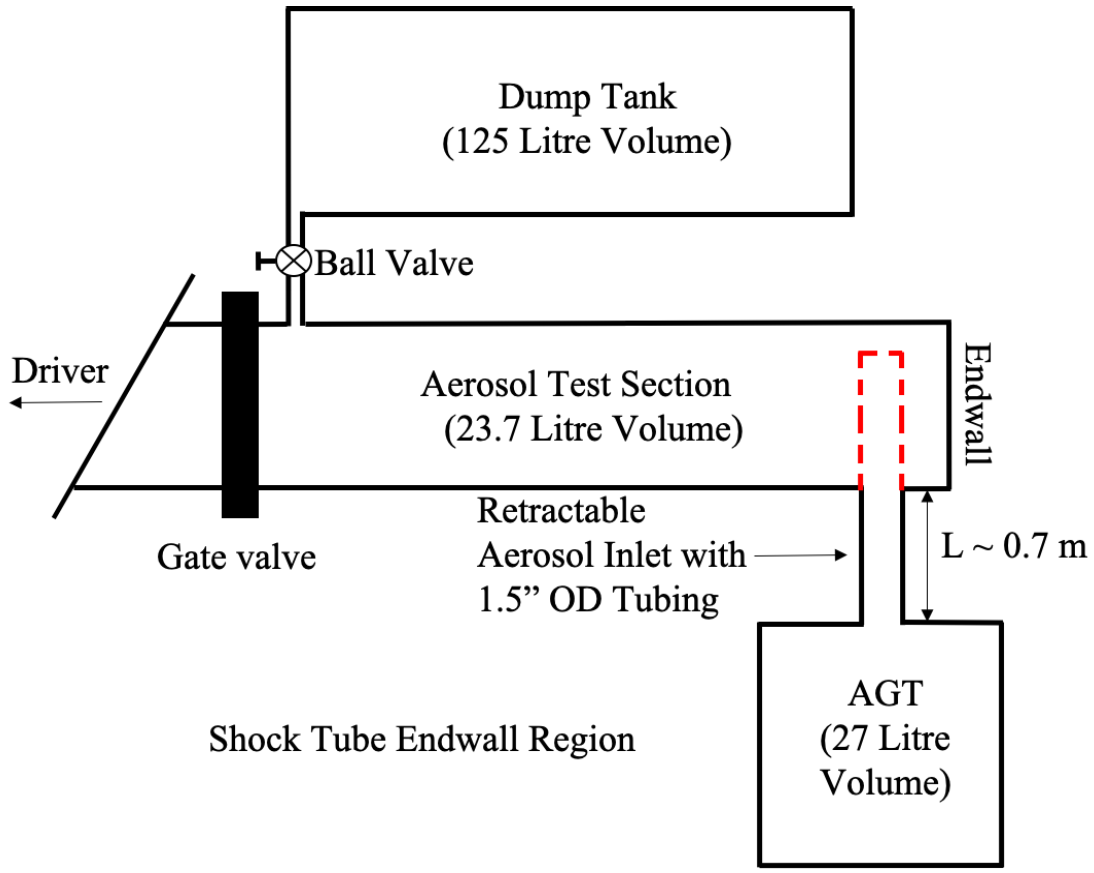

Figure 3.20 Diagram of aerosol filling scheme layout. The red dashed portion of tubing signifies the as-of-yet unspecified inlet design to pass aerosol from tubing into the shock tube. Not to scale.

where the droplet distribution is modified with greater control, it was decided that such an effort should not be conducted here, but rather as part of a future design iteration.

Thus, the simplest tubing geometry that enabled the shock tube to be filled with the maximum amount of aerosol from an externally mounted AGT was found to be a straight tube connected to the shock tube from the aerosol generation tank. Also, the maximum allowable diameter of the tubing (1.5", ASTM A213/A269) was selected such that the resultant velocity in the transport tube could be minimized while still being able

to easily couple to the shock tube. Finally, the AGT was mounted such that any transport tubing had its central axis in the same horizontal plane as the shock-tube central axis in an attempt to minimize gravitational effects. A diagram of the setup is shown in Figure 3.20.

Once the design of the tubing flow path between the AGT and shock tube came into focus by gaining a more intuitive feel for the droplet loss in various tubing components, attention was turned to the flow of aerosol out of the tubing and into the shock tube itself. Although the primary purpose of the design of the tubing between the AGT and shock tube was to minimize droplet losses, the purpose of the aerosol inlet in the shock tube was a more-challenging design problem with competing phenomena.

3.2.3. Aerosol Entrainment Methods: Mass Loading and Uniformity

While introducing aerosol into the shock tube during a filling process, it is desirable to minimize droplet losses to the walls of the shock tube. However, to achieve spatial loading uniformity of the droplets without the use of a plug flow, like that given by Haylett et al. [35], some form of mixing must be used to disperse the aerosol such that droplets are not concentrated in a region around the inlet. Otherwise, the introduction of the aerosol would result in poor droplet spatial uniformity. However, these two requirements of minimal loss and sufficient mixing are, in fact, competing processes which make the task of designing the aerosol inlet significantly more challenging than the flow path between the shock tube and the AGT.

Perhaps the most complicated portion of the aerosol-handling design process was the task of properly designing the outlet through which the aerosol passed from the tubing which connected the shock tube to the AGT and into the shock tube. At first, it may appear

that little can be done, or needs to be done, to control the process of aerosol passing from the inlet tubing and into the shock tube. On the contrary, a lack of focus on designing this inlet would lead to an ineffective filling method from both a uniformity and mass loading standpoint.

3.2.3.1. Diagnostic Method of Aerosol Loading Uniformity and Characterization

Prior to making an attempt at formulating an aerosol introduction technique, the method by which the droplet loading non-uniformity was to be measured and characterized had to be decided upon. As previously mentioned, Hanson et al. and Davisdon et al. [34, 74] both used a light sheet method with image analysis to measure planar non-uniformity in a vertical slice at the center of the shock tube. Haylett et al. and Haylett [35, 88], respectively, found this method to be less accurate than using a laser extinction Mie scattering diagnostic, however. Although the flow fields for this study were unlikely to be the same as the Gen. II plug flow method of Haylett et al., it was decided that the Mie scattering diagnostic would provide the best method of measuring droplet loading uniformity without the significant increase in complexity required with other potential methods of uniformity visualization. Although a Mie scattering diagnostic like that of Haylett et al. was used for a plug flow and not a flow with induced vorticity and/or turbulence, it was deemed as the most appropriate diagnostic for this new facility. Subsequent facility iterations would benefit from improving this technique which is discussed later in suggestions for future work.

Mie scattering is a process by which droplets with sufficiently small size (generally less than 50 μm, [43]) may be probed and their size determined based upon the scattering

angle of the light off of the particle, provided the wavelength of light is the same size or smaller than the particle size. Additionally, multiple wavelengths of light may be used to estimate the distribution of sizes for non-monotonic size distributions of droplets or particles. This was a facet investigated in the study by Hanson et al. [74]. They used a 5-color laser diagnostic to validate the size distribution of aerosol from an ultrasonic nebulizer and compared the results to a turnkey sizing diagnostic (Malvern Insitec). If the size distribution is already known, however, Mie scattering relations may be used to estimate a droplet volume fraction using a single wavelength. Lasers are often used to measure gaseous absorption, but similar relations of incident and transmitted signals may also be used to define laser extinction and calculate the volume fraction of droplets present within an aerosol. Extinction is defined in Eq (3.5), where I is the laser intensity incident upon the probed medium (signal without droplets), and I_0 is the signal measured after the beam has passed through the medium (signal with droplets), respectively.

$$\epsilon = -\ln\left(\frac{I}{I_0}\right) \tag{3.5}$$

The measure of laser extinction (analog of absorbance in a gaseous measurement system) can now be related to the square of the diameter of the distribution of droplets and the wavelength of light if the droplet distribution parameters are known (as was the case with the ultrasonic nebulizer). This definition of extinction is given in Eq. (3.6), where n is the droplet index of refraction, λ is the wavelength of light, d is droplet diameter, $Q_{ext}(d, n(\lambda))$ is the Mie scattering coefficient, $f(d)$ is the droplet size distribution

probability distribution, L is the pathlength over which light traverses the medium, and F_v is the droplet volume fraction in ppmv, respectively.

$$\epsilon = -\ln\left(\frac{I}{I_0}\right) = F_v \frac{\int_0^\infty Q_{ext}\big(d, n(\lambda)\big) f(d) \frac{\pi}{4}\, d^2 L\, dd}{\int_0^\infty f(d) \frac{4\pi}{3}\, d^3\, dd} \tag{3.6}$$

This relation can be simplified using the known input parameters of the distribution and wavelength to yield Eq. (3.7), where C is a constant with an approximate value of $C = 0.31 \pm 0.01$ in units of m^{-1}, and L has units of m. More information regarding the theory of Mie scattering is given by Hinds and van de Hulst, respectively [43, 121].

$$\epsilon = CLF_v \tag{3.7}$$

Thus, with the known scattering parameters and measured extinction through an aerosol, the mass loading at a given pre-shock condition can be calculated. Although the method of Mie scattering droplet loading estimation provides an estimate for how much liquid is in the shock tube in the form of droplets, the value was not relied upon to calculate the equivalence ratio behind the incident shock wave. Instead, a gaseous laser absorption technique (mentioned previously and detailed in a following section) was used to calculate the fuel concentration behind the incident shock wave. Additionally, it may not be immediately clear as to why the calculations of droplet loading were directly applied to the analysis of measuring aerosol loading uniformity if a method like that of Haylett et al. was used (wherein uniformity was measured with relative extinction signals at various locations in the tube, not absolute concentrations of aerosol volume fraction). However, the estimation of droplet loading by calculation of the volume fraction via laser extinction was an invaluable tool used to verify that the aerosol concentration was at sufficient levels

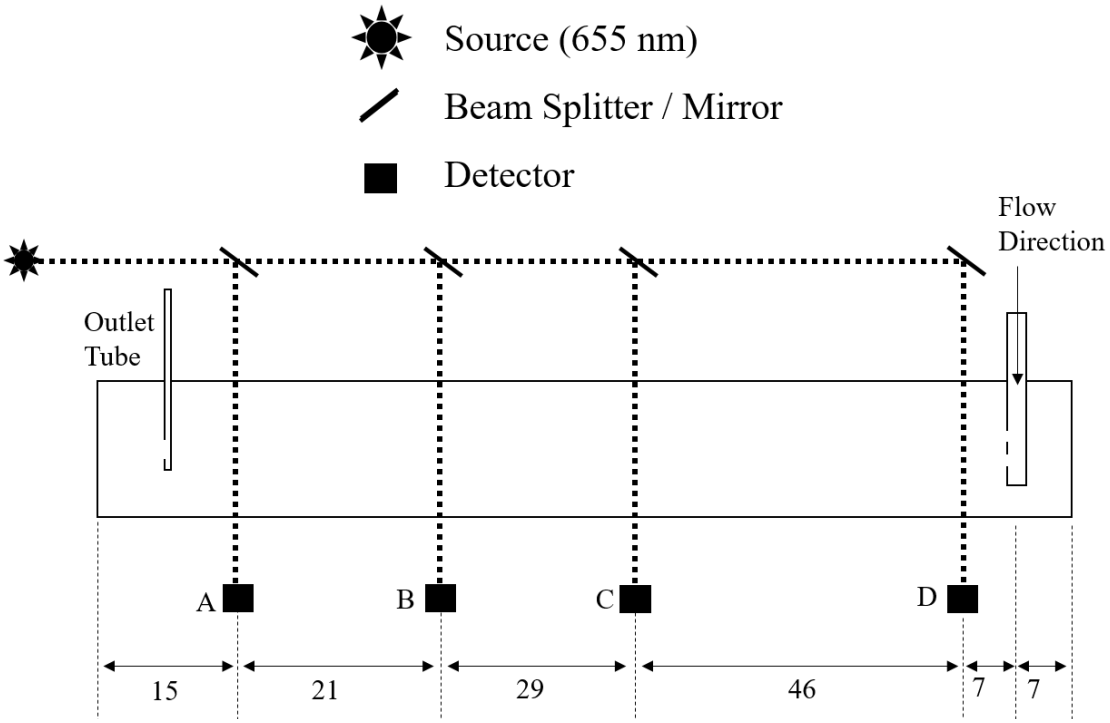

Figure 3.21 Top view of Mie scattering laser diagnostic setup for measuring aerosol loading uniformity in the mock shock-tube test section. Length units are in cm.

to conduct shock-tube experiments. Otherwise, had the volume fractions not been calculated then the final design may have provided high uniformity with an insufficient amount of aerosol loading needed to perform experiments at higher pressures.

During the process of designing the aerosol inlet to the shock tube, a mock version of the aerosol test section between the gate valve and the endwall was constructed to visualize the droplet loading during filling. The mock aerosol test section was made of acrylic tubing. As discussed previously, the chosen diagnostic for determining aerosol loading uniformity and droplet concentrations within the shock tube was similar to that of Haylett et al. [35]. The setup discussed herein used four measurement stations as opposed to three, however. An example diagram showing the diagnostic setup is displayed in

Figure 3.21. To detect relative concentrations of aerosol droplet loading, a laser beam was split into four legs and each beam was sent through the mock test section in the horizontal plane parallel to the tube axis at various locations along the axis of the tube. The filling process was then commenced, and the signals from each detector were used to determine the uniformity within the volume as a function of time using the coefficient of variation (standard deviation of the four signals divided by their mean, expressed as a percentage). With the diagnostic method chosen for determining the aerosol uniformity in the shock tube, the design of the aerosol introduction process was finalized.

3.2.3.2. Aerosol Entrainment Design: The Injector

Computational fluid dynamics simulation packages are an oft-used tool which aid in the design process of fluid flow hardware. Such methods are able to simulate complex geometries and flow conditions without the need for experimentation. These methods, however, were beyond the scope of this work and were not used. Instead, various geometries used to direct the flow within the aerosol test section of the shock tube were investigated experimentally.

When considering various methods for directing the flow of aerosol within the aerosol test section, two variables were available by which to define the nature of the flow. First, the flow rate during filling could be controlled by way of a needle valve located between the aerosol test section and the dump tank. Second, the geometry of the inlet to the shock tube itself controlled the directionality of the flow as it entered the aerosol test section. The combination of these variables led to a somewhat daunting number of possible experiments. This situation was because an optimum geometry for directing the

flow was still undetermined, and therefore a large number of geometries could theoretically be defined with each operated over a theoretically wide range of flow conditions, as defined by the needle valve.

Through an iterative design process, however, it was determined that certain basic combinations of geometries and flow conditions resulted in generally poor uniformity, while others resulted with more acceptable levels of aerosol loading uniformity. Furthermore, the uniformity of the dispersed droplets was found to be influenced by the geometry of the aerosol inlet in the test section to a greater degree than the flow velocity controlled by the needle valve. Thus, the focus of this undertaking was on an iterative process wherein the inlet geometry was defined such that it provided both maximized loading uniformity and maximized mass loading within the aerosol test section of the shock tube.

The relatively high number of geometries and flow conditions investigated over the course of this design iteration process resulted in more than 400 filling experiments wherein the loading uniformity in the mock test section was measured and characterized. These experiments took place over the course of a couple of months and are not discussed here individually. The focus of this analysis will instead be centered on a more generalized approach where key aspects of the flow and aerosol loading will be discussed based on the geometry of the injector head itself. Lastly, as filling experiments were being conducted a requirement based upon the measured uniformity within the test section was set such that if a given inlet geometry resulted in a nonuniformity (coefficient of variation) of 10% or better then the given configuration would be given further consideration. Once

a configuration displayed such levels of nonuniformity, it was further investigated and optimized, if possible.

3.2.3.2.1. Attempts at Achieving a Plug Flow

While characterizing the aerosol distribution using the mock aerosol test section, it was at first theorized that it may be possible to introduce the aerosol such that it expanded into the aerosol test section in somewhat of a uniform flow field. Effectively, if the filling process at the inlet could be configured appropriately, it was believed a plug flow may result. While this theory was ultimately proved false, its investigation did provide insight into the nature of the flow within the test section and into various aspects of the design of the inlet geometry itself. The first attempt at achieving a plug flow was to use an inlet geometry with a wide-open tube from the AGT to the shock tube. This simple geometry is shown in Figure 3.22a. Utilizing such a geometry resulted in a large amount of aerosol within the shock tube but concentrated in a region near the inlet, resulting in a low degree of uniformity along the rest of the test section. Subsequent iterations of the aerosol inlet used a different geometry.

To achieve a higher degree of loading uniformity within the shock tube, it was decided that aerosol inlet needed to be located within the shock tube itself and not at a sidewall location. With this in mind, an injector configuration was conceptualized in a way such that the aerosol tubing between the AGT and shock tube could be inserted into the shock tube for a filling event and retracted prior to initiation of a shock wave. This concept is shown in Figure 3.22b. Efforts were then made to construct a series of 3D-printed injector head geometries such that different versions could be installed and

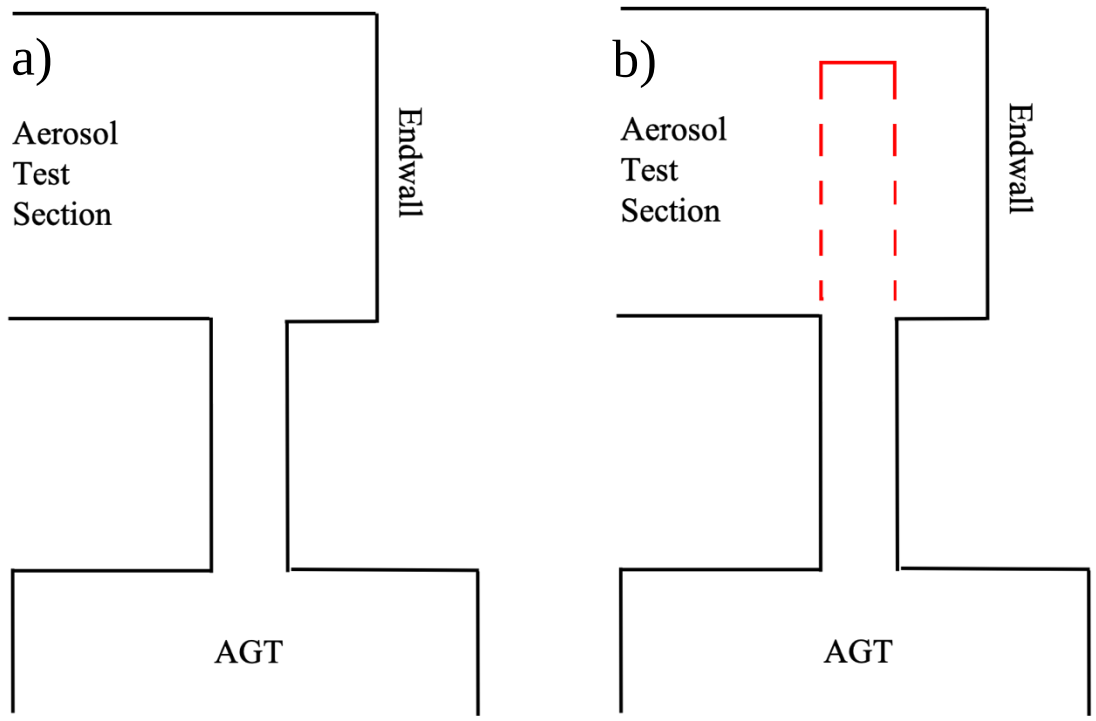

Figure 3.22 Diagram of close-up view of aerosol inlet geometry (not to scale). a) Open-tube geometry; b) Injector head geometry (of an arbitrary configuration) whereby the injector is inserted into the shock tube during the filling process and removed prior to propagation of the shock wave.

removed easily between filling tests. Such a use of 3D printing enabled highly customizable designs and novel, complex geometries without the need for expensive machining for each new version of an injector head. An example injector with a showerhead configuration is shown in Figure 3.23.

Although a wide variety of showerhead injector configurations were used, many were ultimately ineffective at producing a uniform droplet loading within the aerosol test section. This result was in part because the flow field within the injectors themselves did not disperse the aerosol in a uniform manner along the length of the injector. Unsurprisingly, the dynamic pressure resultant at the end of the injector during filling

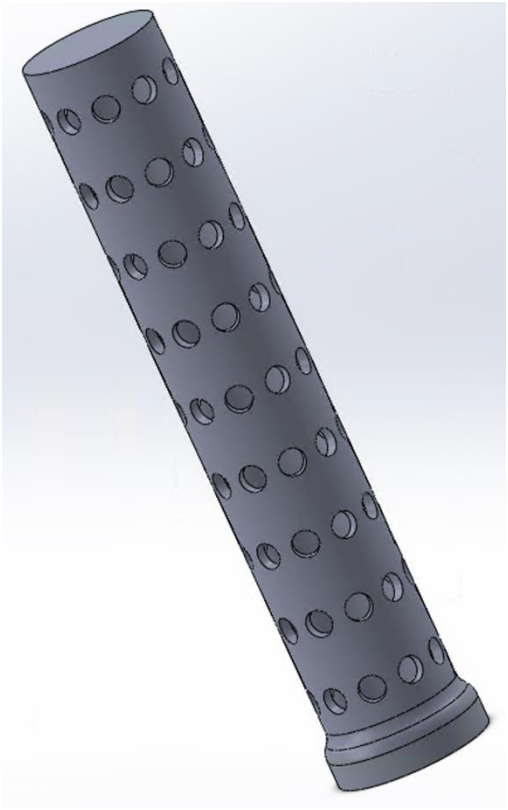

Figure 3.23 Example injector head with showerhead configuration. The outer diameter of the injector is 1.5” and the overall length is approximately 5.00”.

caused most of the flow to exit out of the holes nearest to the end of the injector due to higher flow rates at these locations. This concept is visualized in Figure 3.24a where the internal pressure gradient along the length of the injector increases to a maximum at the end of the injector. In an effort to modify the injector such that the internal dynamic pressure increase was more evenly distributed within the injector itself, the injector geometry was modified with an internal insert. This insert is depicted in Figure 3.24b. While modified injector geometries displayed an improvement in overall loading uniformity within the shock-tube test section, the aerosol was still generally confined to regions nearest the shock-tube endwall. Also, even though the dispersion of the aerosol

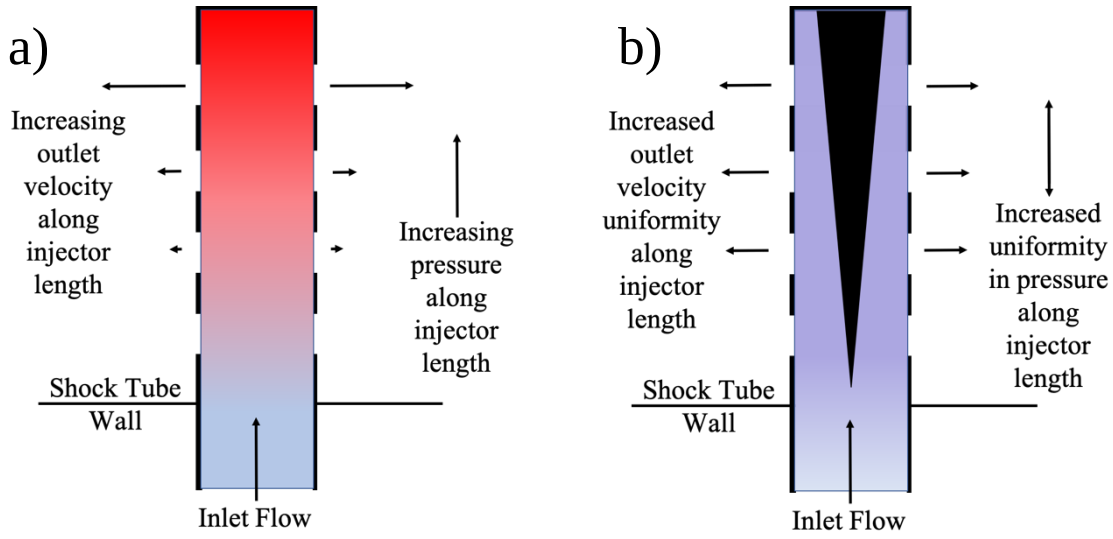

Figure 3.24 Cross-section representation of flow exiting aerosol injector. The flow energy is converted to dynamic pressure along the length of the injector. a) Exit velocities at holes near the end of the injector are greater than those at the base of the injector, b) Exit velocities are more even along the length of the injector with a conical internal insert.

was more uniform using the internal inserts in the injectors, the inserts resulted in too much aerosol loss within the injectors themselves due to smaller, confined spaces and tighter turns in the resultant streamlines. Additionally, the measured non-uniformities in the aerosol test section were above the 10% cutoff considered viable for a given injector geometry.

During the course of the injector design process, attempts at creating a plug flow within the aerosol test section were ultimately unfruitful. A reason for this may have been the design of the injectors themselves, but another source was the more likely culprit behind the lack of uniformity. Up to this point, all injectors were designed in an attempt at forming a plug flow within the aerosol test section. The intent was for the aerosol to expand into the test section around the injector and propagate in a semi-uniform manner

towards the outlet. This technique of forming a well-mixed region of aerosol which is then sent down the length of the tube may have been more effective for a continuous flow filling method, but the duration of filling for the transient method did not provide sufficient time for any kind of equilibrium and/or steady state to be achieved. The flow field could not fully develop due to the relatively short filling time and constant change in the pressure driving the filling process. Thus, when the aerosol was sent into the shock tube and vorticity was induced to cause mixing, recirculation zones and various eddies were formed in the flow.

Additionally, even if a continuous flow introduction method were utilized it is likely that transient eddies would still have been present in the flow. These zones of recirculation resulted in droplets being trapped in regions near to the injector and the endwall, preventing the majority of droplets from propagating further downstream. Although the flow experiments which attempted to form plug flows of aerosol resulted in low levels of aerosol loading uniformity, they did provide insight into important aspects of the transient flow and droplet loss mechanisms.

3.2.3.2.2. Aerosol Dispersion via Jets and Eddies

While the attempts at inducing a plug flow in the aerosol test section did result in such a flow field, they were not unfruitful. A couple of key failings of the injector designs from the attempts at dispersing the aerosol in a plug flow form were still useful for informing subsequent injector designs and aerosol introduction methods. First, aerosol uniformity within the aerosol test section was generally low because the flow was introduced in such a way so as to form large eddies which controlled the behavior of many

of the droplets, preventing them from propagating downstream and evenly filling the test section with aerosol. Second, the dynamic pressure gradient resultant within the injector itself prevented the aerosol from being disbursed in a uniform manner over the length of the injector head, although it did provide reasonable droplet volume fraction concentrations necessary for experiments.

Subsequent attempts to even the dynamic pressure buildup within the injector were somewhat successful at disbursing the aerosol in a more-uniform manner but caused the loss of too many droplets because of the smaller passageways through which the aerosol had to pass. Thus, a successful aerosol injector design should likely not incorporate small internal passageways and/or cavities, but rather remain open internally so as to enable the maximum achievable mass loading. Furthermore, the method of aerosol introduction should not be designed in an attempt at first creating a plug flow near the inlet which is then intended to move towards the outlet (at least not for injector diameters which are significantly smaller than the shock-tube diameter). Instead, the flow should be introduced into the shock tube such that intended order of events in the mixing and entrainment processed are reversed.

When considering the reason for a lack of uniformity within the aerosol test section for the early injector designs, a detailed examination of the phenomena governing the flow should be considered. The primary reason for the failure in achieving aerosol loading uniformity by forming a plug flow within the aerosol test section was not due to a lack of mixing within the flow; the eddies mixed the aerosol quite well in the local region nearest the injector. It was the propensity of the eddies to extract linear momentum from the flow

and transfer it to vortical motion, thereby trapping droplets in the eddies, which was ultimately underestimated. Thus, any subsequent design of the aerosol injector would require that eddies still be used to disburse the aerosol within the test section (as would likely be the case with any filling method using an injector), but not extract too great an amount of linear momentum from the flow and prevent the aerosol from filling the full length of the aerosol test section.

After the unsuccessful efforts aimed at inducing a plug flow of aerosol in the test section, the injector head for the aerosol inlet was redesigned with a focus on propelling the aerosol down the length of the tube. In essence, the function of the injector was changed from that of maximizing mixing with little emphasis on direction, to greater emphasis on directing the flow. This modification of the primary function of the injector was made with the knowledge that the flow would ultimately mix itself via the formation of eddies by shearing at the interface of stationary and non-stationary fluid during the filling process. Another modification to the setup was that the needle valve between the test section and the dump tank was also removed and replaced with a ball valve to maximize the velocity within the test section. Lastly, the injector needed to be able to provide adequate mass loadings within the aerosol test section, requiring that losses within the injector itself also be minimized.

In its final configuration, the design of the aerosol injector head was significantly simpler in geometry than earlier versions. Initial designs of the injector sought to disburse the flow in a uniform manner with a showerhead design and internal inserts meant to aid in disbursing the flow evenly amongst the various holes over the length of the injector

itself. These inserts were more of a hindrance than a help, however, as they forced the flow to make overly sharp turns. This effect caused the local Stokes numbers for the droplets to be quite high, signifying that many droplets lacked the ability to relax to the high degree of curvature in the streamlines caused by the smaller passageways within the injector. Although the injector geometry with no internal insert resulted in higher droplet output than that with an insert, the controlling mechanics may not be obvious and warrant further explanation.

Whether or not the flow proceeding from the injectors encountered an internal insert or not, it still had to make a 90-degree turn to exit the injector. So why, if both injector designs turned the flow regardless of their geometry, did one result in less droplet loss than the other? The answer is twofold and lies in how the dynamic pressure within the injector was utilized and also in the total inner surface area of the injectors. These processes can be visualized with a re-examination of Figure 3.24. In the injector design without inserts, the conversion of fluid momentum to dynamic pressure was concentrated in one region near the end of the injector and not spread out in a more uniform manner as in the injectors with inserts. This local concentration of dynamic pressure resulted in a greater overall deceleration of the flow in the injectors without inserts compared to the injectors with inserts. Additionally, the surface area-to-volume ratio within the injectors with inserts was much higher than in the injectors without inserts, which resulted in a greater likelihood that a droplet would contact a wall.

The inserts also caused streamwise increases in flow velocity. That is, although the insert indeed contributed to an increase in dynamic pressure along the direction of the

injector axis, a decrease in flow area in the plane perpendicular to the incoming flow was also present. This flow area contraction resulted in a competition between acceleration due to area change and deceleration due to dynamic pressure buildup, whereby the dynamic pressure buildup was not maximized. Basically, the injectors without inserts were able to fully utilize the dynamic pressure buildup as an air brake for the droplets by increasing the drag on the droplets and decreasing their momentum in the direction of the injector axis. Thus, the deceleration process in the axial direction was somewhat decoupled from the acceleration process of the droplet as it changed directions and exited the injector.

Injectors with inserts, on the other hand, did not sufficiently slow the flow prior to directing it out of the tube, and this lack of acceleration-deceleration decoupling resulted in relatively fast curvilinear motion to which the droplets were not able to relax. In conclusion, the injectors without inserts acted in a twofold fashion to decelerate the droplets in the direction of the injector axis and then accelerate them again on their way out of the injector using the built-up dynamic pressure. For injectors with inserts, however, the inserts acted in a way so as to turn the flow without decelerating and then accelerating it again, which led to greater droplet losses.

The final design of the aerosol injector geometry is shown in Figure 3.25. The two holes are separated by 20 mm (center-to-center) and are faced towards the gate valve to direct the flow down the length of the aerosol test section. The flow is then disbursed by resultant eddies which are created by the interaction of the jet with stationary or slow-moving fluid. The reason two holes were chosen as opposed to a single hole is because the insertion process into the shock tube was smoother with two holes as opposed to one,

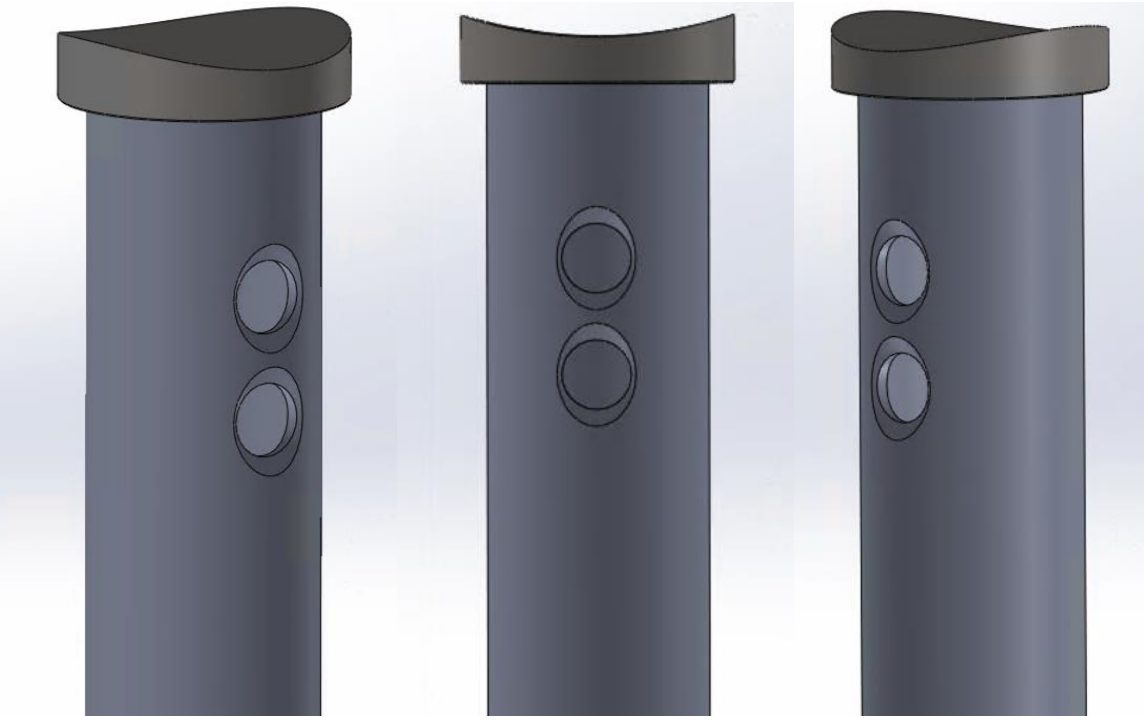

Figure 3.25 Front and isometric views of final aerosol injector design in CAD software. The outlet holes have 12-mm diameter with 20-mm center-to-center spacing and beveled edges for easy passage over sealing o-rings. The top portion of the injector is curved to match the inner diameter of the shock tube when retracted and is made to mount to a custom port for attachment to the sidewall of the shock tube.

and the machining was somewhat simpler with the smaller holes. Also, the uniformity results using two outlet holes seemed best using diameters in the range of 10-15 mm where the total area was roughly equivalent to two holes with diameter of 12 mm (there seemed to be little difference in uniformity for holes in this range). Improvements regarding the aerosol injector are discussed at the conclusion of this study regarding future work. Finally, the uniformity from the final injector design and a characteristic mass loading from this injector are shown in Figure 3.26. The value of non-uniformity achieved in this filling experiment is approximately 5%. In general, the measurements made using the Mie

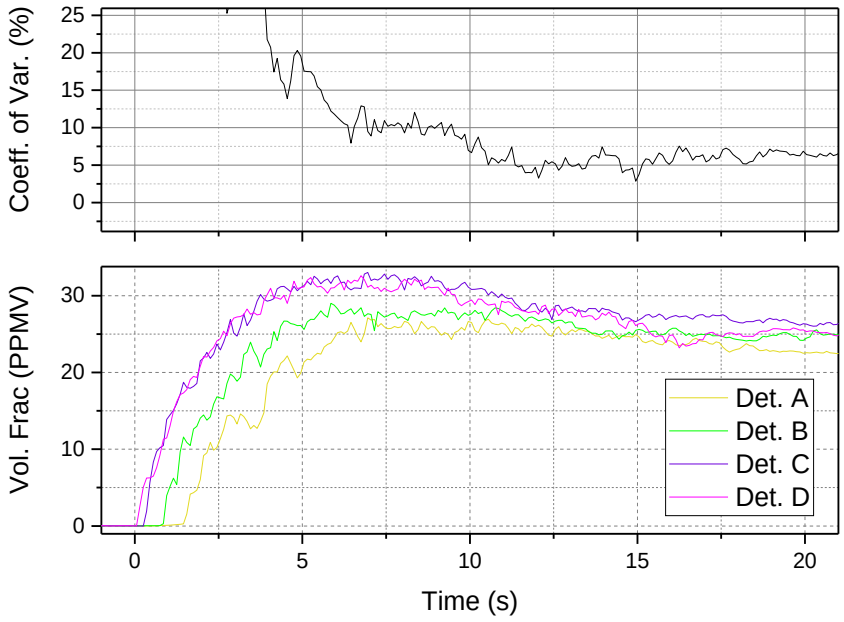

Figure 3.26 Results of aerosol loading and uniformity measurements from the Mie-scattering extinction diagnostic using the final two-holed injector geometry. Non-uniformity is measured at 5% at the completion of the filling process. Detector A corresponds to a Mie scattering measurement location near the aerosol test section outlet tube, and Detector D corresponds to a measurement location nearest to the injector, as shown in Figure 3.21.

scattering diagnostic for droplet loading uniformity yielded results that were greater in nonuniformity of Haylett et al [35]. The values of nonuniformity were generally within the range of 3-8%, and most often in the range of 4-6%, well within an order of magnitude of the nonuniformity resultant from the Gen. II method of aerosol introduction.

3.3. **Shock-Tube and Aerosol-Generation Assembly Construction**

With the design process for the aerosol injectors completed, final construction and assembly of the aerosol generation and entrainment facility could be commenced. Various

aspects of machining are not focused upon here, but a brief discussion of some of the various hardware components is given. First, although the mock aerosol test section was essentially an open tube connecting the AGT and aerosol test section for the injector uniformity characterization trials, the final design incorporated a ball valve such that the AGT could be fully isolated, even with the injector inserted into the shock tube. Although the injector is only intended to be within the shock tube during the aerosol filling process, the ball valve was included to prevent a shock wave from propagating into the AGT in the event that the injector was accidentally left inserted during a shock wave experiment.

Additionally, the injector tube was equipped with a limit switch which controls the operation of the gate valve. If the injector was inserted into the shock tube, the limit switch ensured that the gate valve remained closed and only allowed the gate valve to open if the injector was in the retracted position and in contact with the limit switch. Lastly, the gate valve, injector, and various valves involved in the filling process were fit with pneumatic actuators controlled by solenoid valves and could be actuated remotely from behind a safety barrier. This remote-control operation was configured such that when the gate valve switch was set to open, all other devices associated with aerosol filling would automatically close, if they were not already. Pictures of the final setup at various stages of construction are given in Figure 3.27-Figure 3.32.

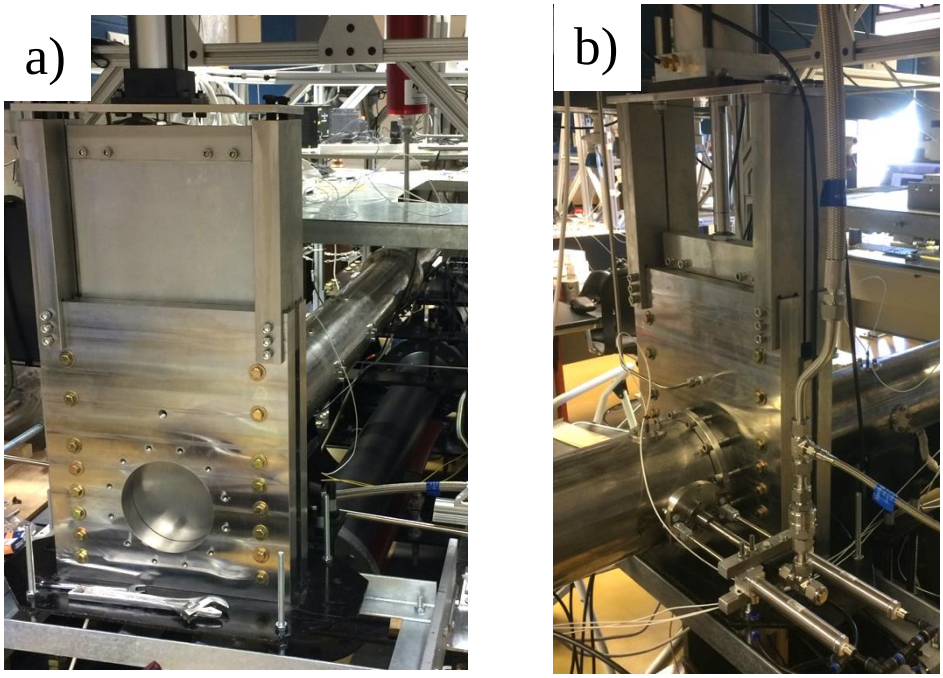

Figure 3.28 View of the final construction of the shock-tube gate valve. a) Gate valve in closed position without aerosol test section attached; b) Gate valve assembled in the open position with aerosol test section and outlet tube connecting to the dump tank.

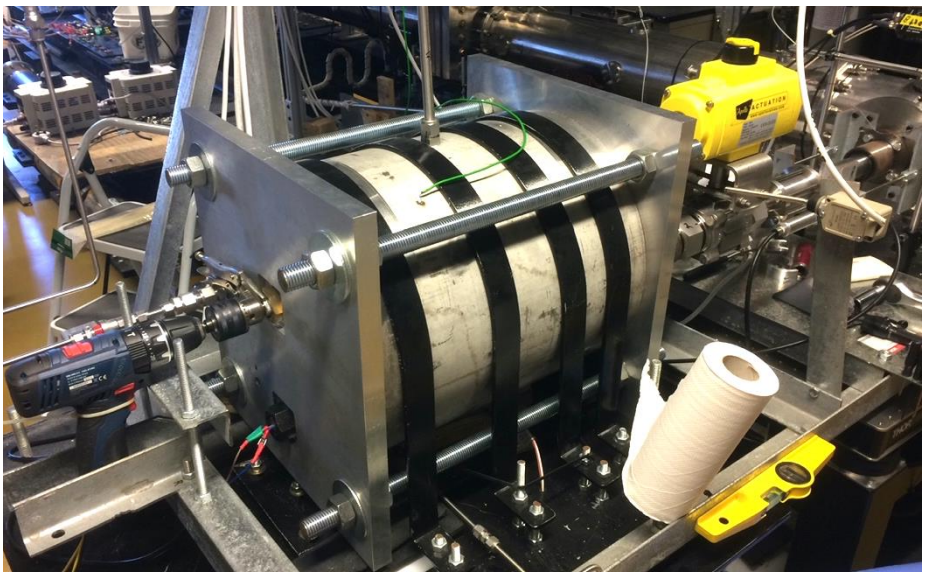

Figure 3.27 Aerosol generation tank (AGT) assembled with mixing fan motor (blue power drill modified for remote operation).

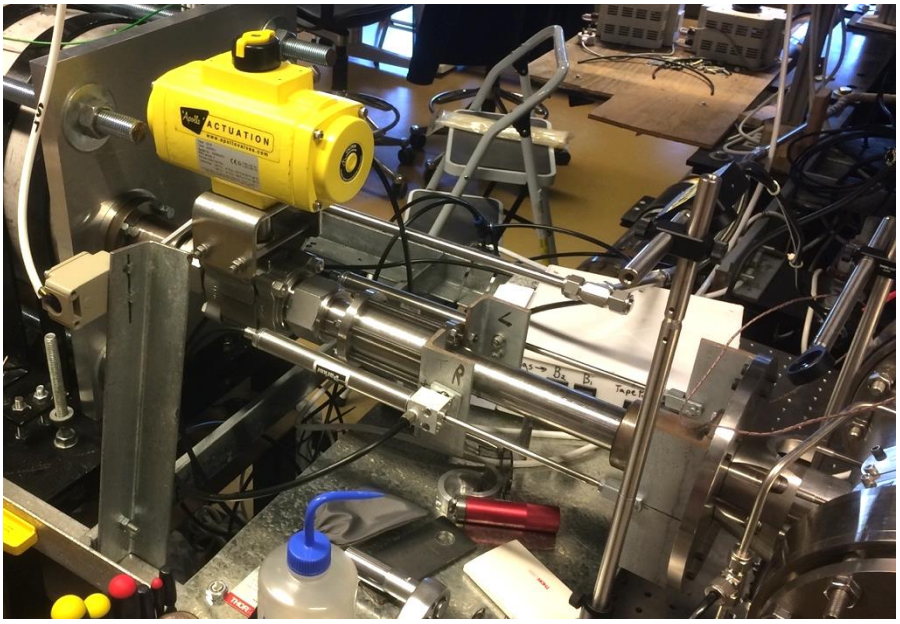

Figure 3.30 Aerosol injector attached to AGT and shock tube with accompanying pneumatic ball valve.

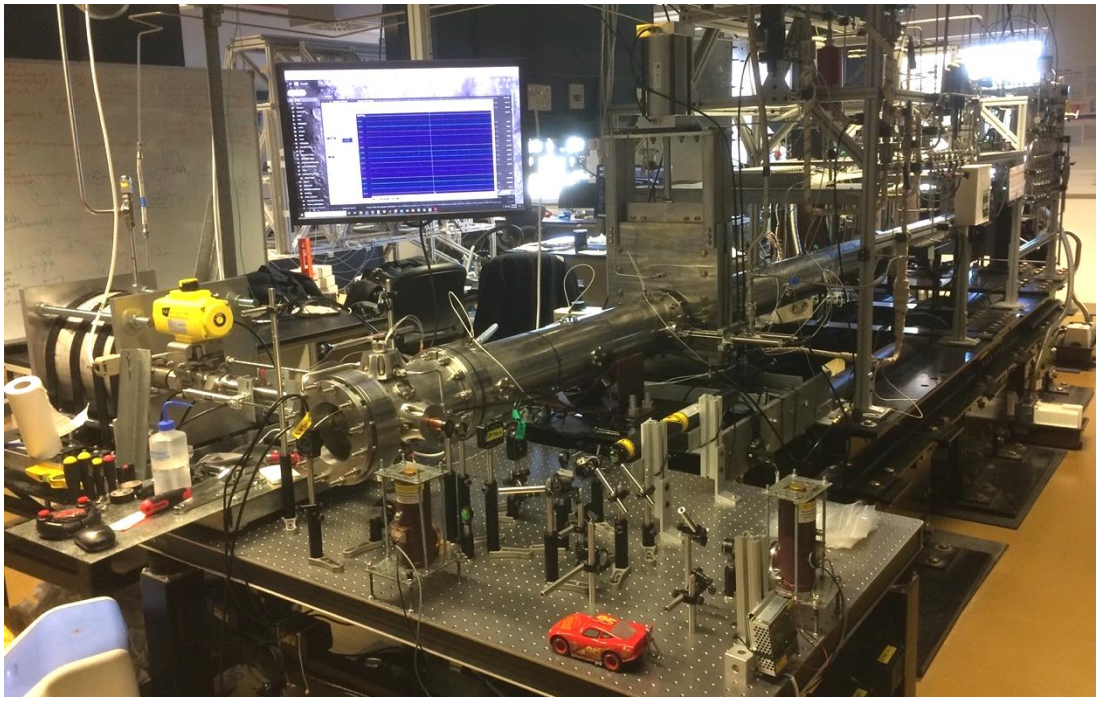

Figure 3.29 View of shock-tube assembly from driven endwall with optical table and associate laser diagnostics.

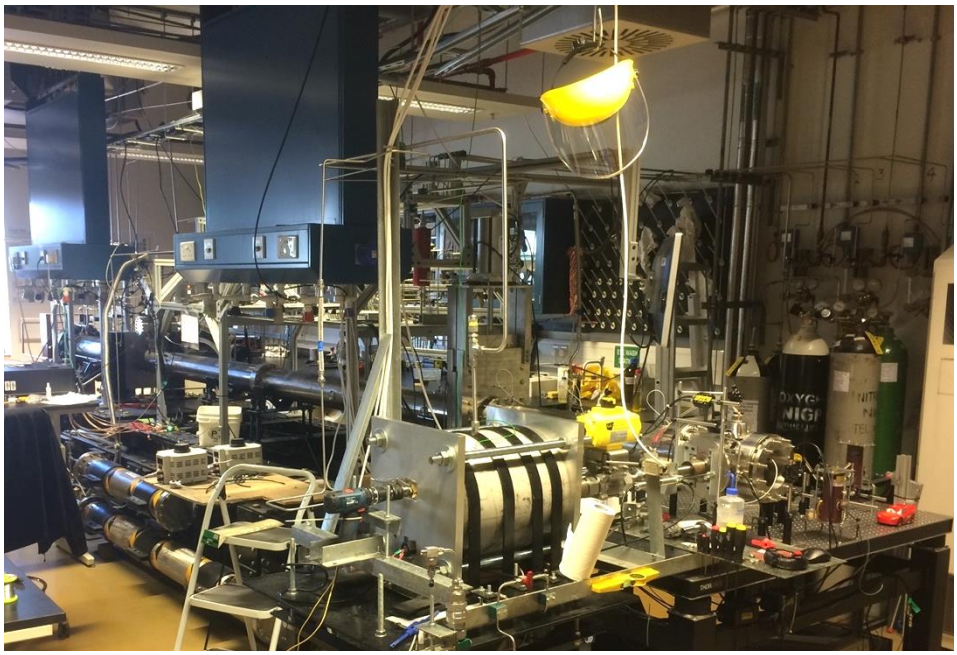

Figure 3.32 Alternate view of the facility from endwall of driven section.

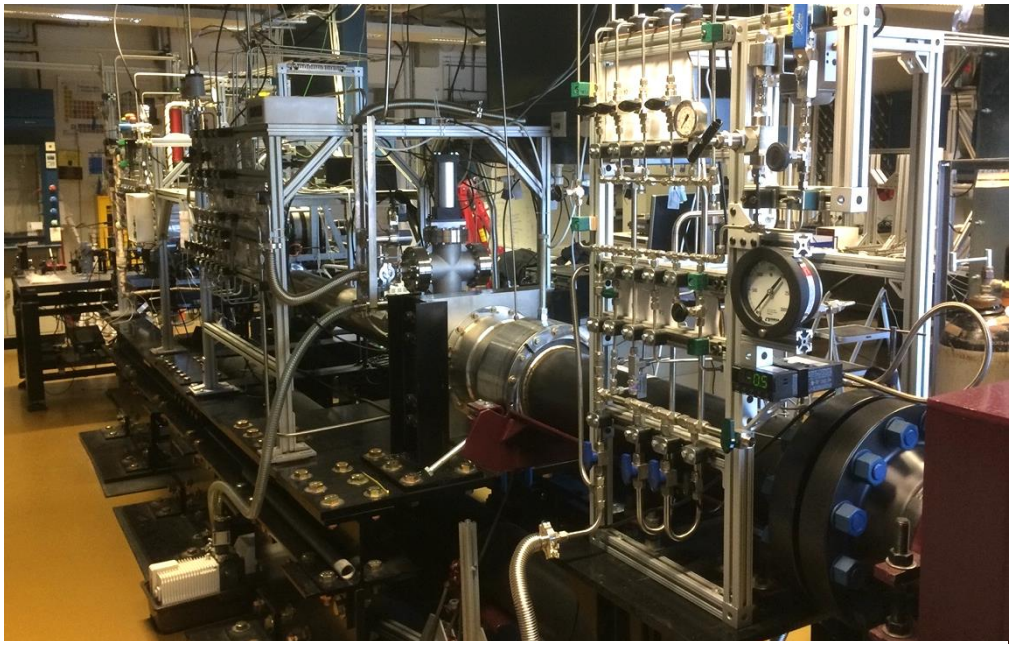

Figure 3.31 View from driver manifold looking toward the driven endwall.

4. CHARACTERIZATION AND EXPERIMENTAL CONSIDERATIONS

Upon completion of the aerosol generation and entrainment design process, the shock-tube facility was prepared for performance characterization trials. Such tests included validation of all diagnostic methods and characterization of elementary shock wave and gas-dynamic behavior within the shock tube. Diagnostic methods included shock velocity detection, measurement of pressure time histories, and optical diagnostics related to aerosol evaporation and gaseous fuel absorption via laser spectroscopy. Nonideal effects were also examined briefly and found to behave similarly to those observed in other facilities [114-116]. Global effects from shock wave interaction with the aerosol were also examined and determined to be present but were not significant enough to inhibit collection of ignition data.

4.1. **Shock Velocity Decay**

When calculating thermodynamic conditions behind shock waves (with or without aerosols), the normal shock relations [38] are coupled with the mass, momentum, and energy conservation equations, respectively, and the system is solved in an iterative fashion [122]. The method for calculation using aerosols requires some slight modification, but the overall procedure for calculating the conditions is similar [123]. A key input parameter, regardless of the presence of liquid droplets, for calculating post-incident and post-reflected-shock conditions is the incident velocity of the shock wave. Piezoelectric pressure transducers are used to record pressure time histories at various locations along the shock tube. These time histories indicate when the shock wave passes over the pressure transducers and the subsequent trigger times (when the shock crosses

the mid-point of the transducer), with the known positions of the transducers, are used to calculate an average shock wave velocity between adjacent transducers. The velocities at several strategically placed transducer intervals are then cataloged and plotted as a function of position along the shock tube.

Because of various non-ideal effects such as diaphragm opening mechanics and boundary-layer growth, the shock wave is attenuated slightly as it propagates towards the driven endwall of the shock tube [124]. This shock attenuation is the reason for using several velocity intervals as opposed to a single interval: the shock velocity at each interval is plotted, and the velocity behavior of the linear decay as a function of distance is extrapolated to the endwall. The result of the linear velocity extrapolation at the endwall is the input parameter used for calculating the thermodynamic conditions behind the shock waves. Due to uncertainty in the measured velocities, however, the extrapolated velocity is the largest source of uncertainty in calculating post-reflected-shock conditions.

When calculating shock velocities at the endwall of the shock tube, uncertainties in extrapolated endwall velocity of the shock wave are traditionally on the order of 1-2%. This velocity uncertainty leads to a 1-2% uncertainty in calculated temperature behind the reflected shock wave, which may at first appear relatively small. Since chemical systems are extremely sensitive to uncertainties in temperature, though, even small perturbations can have a significant effect on chemical reaction rates, and 1-2% variations in temperature at 1000 K can result in significant uncertainty of measured rate constants. This strong temperature dependence makes the task of minimizing shock velocity uncertainty and thereby providing more accuracy in the calculation of post-shock

thermodynamic conditions a critical one. Because of its importance for any shock-tube experiment conducted in this study, the shock velocity measurement was the first diagnostic to be characterized in the new shock-tube facility.

4.1.1. Gaseous Velocity Decay

As many of the features of the driven section of this facility are like those of similar facilities [114-116], the shock velocity attenuation characteristics in traditional gaseous mixtures were not expected to differ significantly from behaviors commonly seen in other shock tubes. This expectation was indeed the case as observed from velocity decay profiles for shock waves in a variety of gaseous mixtures. Some aspects of this facility and the nature of conducting experiments in aerosols, however, did require a closer examination of the velocity decay profiles to verify these differences did not impact performance.

The first aspect that could have potential impact on shock velocity decay in the new facility was the gate valve. No effect on shock velocity behavior was observed due to the gate valve hardware itself, however. This negligible gate valve effect is shown in Figure 4.1. Each velocity point represents a velocity interval between two adjacent pressure transducers. The first three velocity intervals are upstream of the gate valve, the third interval straddles the gate valve, and the last two intervals are downstream of the gate valve. This behavior shown in the plot is typical compared to shocks without the gate valve; that is, there is no observable difference with or without the gate valve when examining the velocity decay behavior of the incident shock wave. Shock velocity decay behaviors using aerosols, on the other hand, were not always linear during shock wave propagation through the driven section and warranted a more rigorous examination.

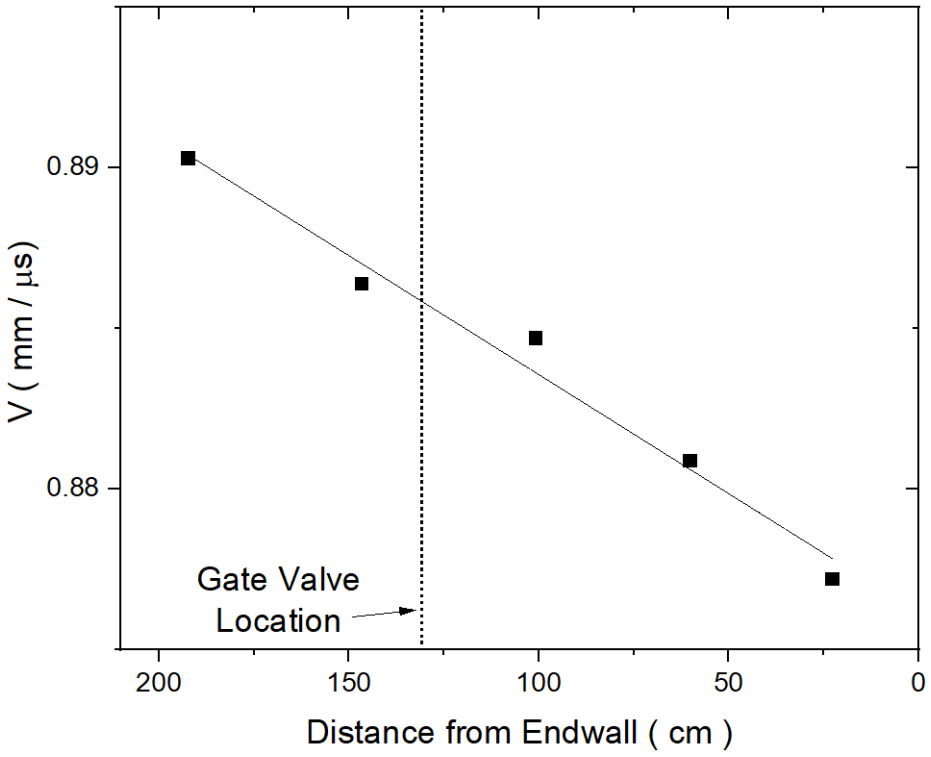

Figure 4.1 Velocity decay plot of a shock wave passing through the driven section in air. T_5=1013 K, P_5=7.04 atm. The extrapolated endwall velocity is 0.876 mm/μs.

4.1.2. Impact of Aerosols and Changing Acoustic Impedance on Velocity Decay

As a shock wave propagates through the (open) gate valve in the shock tube, its velocity over this roughly 10-cm length remains nearly constant. However, were the driven buffer gas to be significantly different than the gas in the test section between the gate valve and driven endwall, the shock wave would experience a step change in composition and properties within the gas and the velocity of the shock wave would be significantly affected by this corresponding change in properties. An analogy to this would be the transition of light from one medium to another where the indices of refraction are different. The indices of refraction are different because the speed of light in the two

mediums is different and the light therefor changes speed when it crosses this interface. Similarly, when the shock wave experiences a step change in properties like gas density, molecular weight, sound speed, etc., the shock wave behavior responds to these new conditions and its velocity changes.

A property which governs this change in velocity from one gas to another is referred to as acoustic or gas-dynamic impedance, Z, and is defined as the density of the gas, ρ, multiplied by its speed of sound, a, or $Z = \rho a$. Although the pressure across the gate valve may be the same on both sides, if the acoustic impedance is different across this interface then the shock wave will send back an expansion or compression wave as it traverses the interface between the gases and the speed of the shock wave will change. This global pressure effect is discussed in a following section. The change in sound speed across the interface may be small, but it should be taken into account for the purposes of calculating the properties of the gas behind the shock waves. To correct for this change in shock speed and avoid formation of reflected compression/expansion waves at the interface of different gases at the gate valve, gas tailoring can be used such that the shock wave experiences no change in acoustic impedance as it passes through the gate valve [86, 87]. It is also advisable that the density of the gases be matched as well their impedances [125].

For the present work, buffer gas tailoring was not conducted because the aerosol was mostly composed of air and the differences in properties between air and the aerosol were slight. The differences in properties of the buffer gas and aerosol, although small, did result in a change in velocity decay behavior of the shock wave across the gate valve

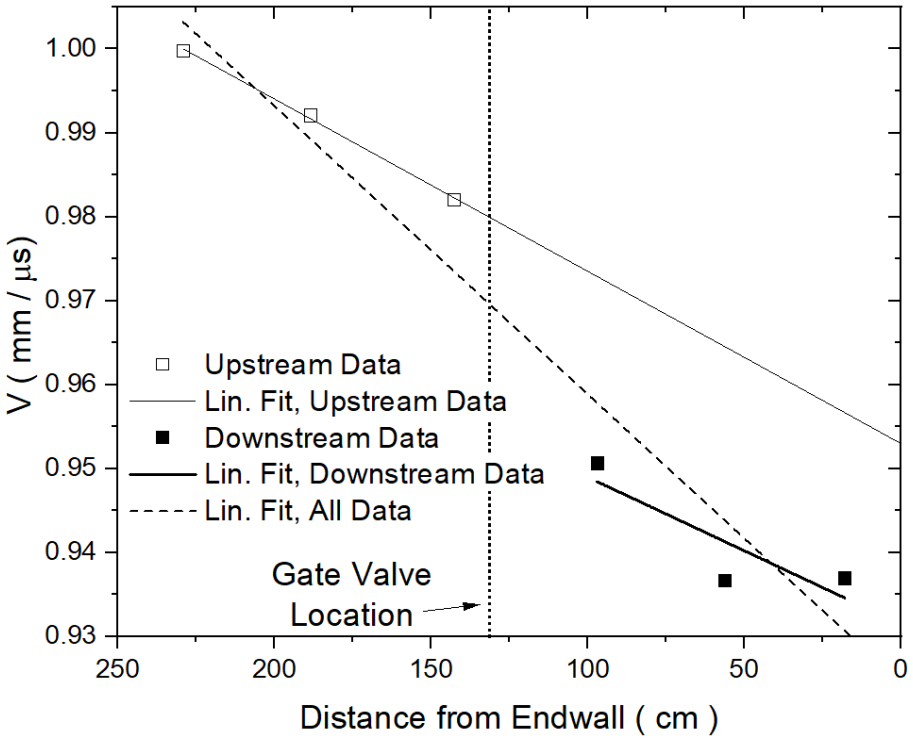

Figure 4.2 Velocity decay plot for a shock wave in an aerosol experiment. The buffer gas is air and the aerosol is air with Jet-A fuel droplets. The mixture is a fuel-air mixture of Jet-A at ϕ=0.95 with T_5=1025 K, P_5=12.80 atm. Linear decay profiles are fit to the velocity data upstream and downstream of the gate valve, respectively, as well as all of the velocity data together. The fit through the downstream data results in V=0.932 mm/μs, whereas the fit thorugh all of the data results in 0.925 mm/μs, a difference of 0.6%, or a difference of approximately 7 K when calculating T_5.

in some cases. An example of this behavior is shown in Figure 4.2. Each velocity point represents a velocity interval between two adjacent pressure transducers. The first two velocity intervals are upstream of the gate valve, the third interval straddles the gate valve (with most of it lying upstream of the gate valve), and the last three intervals are downstream of the gate valve. As the shock wave crosses the gate valve, the velocity decay shows a significant shift downward as the shock crosses into the heavier aerosol. This phenomenon is significant for the purposes of defining the value of the shock velocity

when extrapolated to the endwall. When plotting a linear decay through all of the velocity points, the resultant value when extrapolated to the endwall is significantly lower than the value when only the last 3 locations (all located within the aerosol test section) are used to fit the velocity decay plot. Thus, if the slower velocity is used in calculated thermodynamic properties then the calculated temperature will be lower than if the faster velocity were used. This difference may not seem like much in this example, but it can lead to greater uncertainties than that shown in this example.

When conducting shocks in aerosols, the discontinuity in the velocity decay behavior across the gate valve was not always observed. In particular, when the colder temperatures were investigated this behavior was not as observable. At higher temperatures, though, it was almost always present. Thus, for the experiments where the velocity decay change was observable across the gate valve, only the velocity intervals downstream of the gate valve were used to calculate the extrapolated endwall velocity. Otherwise, all of the velocity intervals were used to calculate the extrapolated endwall velocity (i.e., the velocity of the incident shock wave when it reaches the endwall).

Another aspect of the facility that may affect the velocity decay behavior of the incident shock wave is that introduced by the window heaters. Localized heating of the gases near the endwall may cause the shock wave to accelerate in the region closest to the endwall if the gases in this portion of the tube are significantly warmer (~5 K) than the rest of the gas in the shock tube. It is not believed that the window heaters increased the Region 1 temperature of the shock tube in any significant manner, however. Consider the velocity decay trace of Figure 4.3 (the positions of the intervals are the same as those in

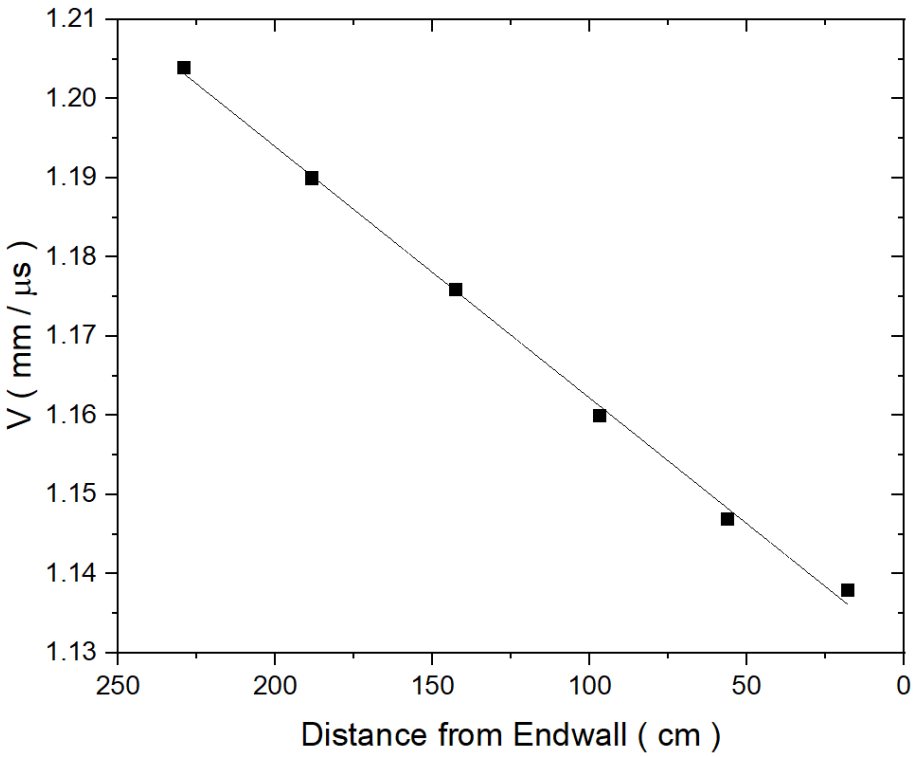

Figure 4.3 Shock wave velocity decay with linear fit extrapolation for an experiment where aerosol was allowed to settle, showing that heaters have little or no effect on the velocity decay behavior of the shock wave near the endwall. T_5~1300 K. The sidewall window port heaters are approximately 5.5 cm from the endwall.

Figure 4.2). This experiment was intended to be conducted in aerosol. However, during the filling process the aerosol was allowed to settle almost completely. It can be seen that there is no apparent discontinuity at the gate valve from the velocity decay plot. Also, the velocity decay behavior of the shock wave at the interval nearest the endwall is in line with the velocity decay behavior from all other intervals. Were the heaters affecting the velocity decay behavior, the last velocity interval would display a greater velocity than the second-to-last interval, showing that the shock accelerated near the endwall as the Region 1 gas in this area would be warmer than the intended T_1~300 K (room temperature).

4.2. Pressure Time Histories

Another use for piezoelectric pressure transducers, in addition to their use in velocity detection schemes, is for the recording of pressure time histories during the course of a shock-tube experiment. These time histories provide a diagnostic for multiple phenomena and equip experimenters with a means of looking inside the shock tube without using optical diagnostics. Although pressure transducers are used solely to measure pressure profiles, any significant event that occurs in an experiment with real fuel-air mixtures will be detectable by using such a transducer. Thus, if the pressure profiles behind a shock wave are not flat (indicating that the pressure is not constant), then an event is taking place which is causing the pressure to change. A pressure change signals that a temperature change is occurring as well. Events which cause the pressure to change during the course of an experiment are generally a result of non-idealities in the shock tube.

4.2.1. Traditional Non-Idealities

As discussed previously, reflected-shock bifurcation occurs under conditions where the boundary-layer fluid in the post-incident-shock flow has insufficient momentum to pass through the reflected shock wave. This event is usually observed in experiments with significant amounts of diatomic and triatomic gases (and larger-sized molecules as well). It was previously discussed that the bulk of the flow in the center portion of the reflected-shock region is believed to be largely unaffected by post-reflected shock waves and is not a significant concern for mixtures composed largely of air, as is the case with

this work. Another boundary-layer effect on the pressure profiles that can be observed is that of non-ideal pressure rise, or dP*/dt.

When conducting shock-tube experiments wherein the driven test gas is air and not a mixture diluted in Argon, the dP*/dt behavior of the mixture will be more pronounced than the Argon-based mixtures. Therefore, dP*/dt behavior observed during experiments which do not employ Argon as a diluent must be accounted for in the analysis of any kinetics data. In fact, it is advisable that when significant dP*/dt is present that test times not be longer than approximately 2 ms. This way, the temperature change within the post-reflected shock region will be limited and the assumption of constant internal energy and volume will be better maintained. To prevent this effect, driver inserts can be used [29]. Such a technique was not used in this study, however, because test times were limited to approximately 2 ms.

It has previously been the case that various researchers have conducted ignition studies up to test times of 10 ms using real fuels (see Chapter 1 and references therein). These investigators reported their measured values of dP*/dt, as they should, and appropriately incorporated these values into their kinetics solvers when comparing ignition data to mechanisms. However, some researchers often go on to compare ignition data to those of other researchers without considering the dP*/dt behavior of their own facility, or that of the facilities which they reference, for comparison. Because dP*/dt behavior can vary significantly between shock tubes of differing diameters, the temperature rise after the reflected shock wave will be different in facilities with differing

internal diameters [126]. This dependence on shock-tube inner diameter is a key reason why it is important to minimize dP*/dt behavior at long test times.

Although the test times in this study did not last much beyond 2 ms, the experimental dP*/dt behavior still required characterization. It was observed that when the driver gas was composed of a single component (He), the dP*/dt behavior from this facility was generally greater than that of the shock-tube facilities in College Station with nearly identical driven-section geometries. When driver gas tailoring was performed, however, the dP*/dt behavior of the facility was less pronounced and levels of dP*/dt were similar to those of the College Station shock tubes. Such differences in dP*/dt behavior between facilities of near-identical driven-section geometries warrants further investigation and will be discussed in a proceeding chapter.

4.2.2. Other Facility Effects on Pressure Time Histories

In addition to the presence of reflected-shock bifurcation and dP*/dt being observed in this facility, as is the case with any shock-tube facility studying real fuel-air mixtures, the effects of the aerosol features of this shock tube were also observed, but did not affect the global pressure traces in a significant manner. That is, the presence of the gate valve exhibited no effect on the time-dependent pressure behavior observed behind the reflected shock wave, and the same was true of the presence of the aerosol itself. In the work of Jourdan et al. [54], the presence of larger droplets (120 μm and larger) in a shock tube was observed to affect the behavior of pressure profiles at locations (particularly) upstream and downstream of the interface of the aerosol and buffer gas.

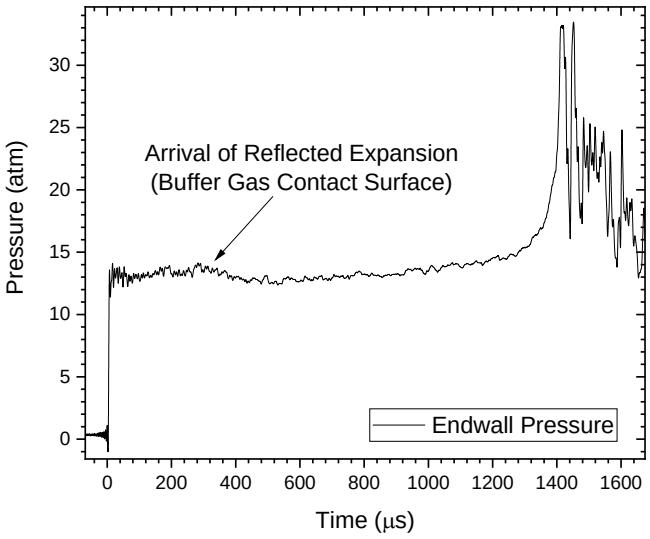

Figure 4.4 Pressure time history from endwall-mounted pressure transducer after passage of shock wave in an experiment using aerosol. Driven Buffer-air, Driven Aerosol- Jet-A in air, Driver gas-16% N_2/He , T_5=1025 K, P_5=12.8 atm, $\phi = 0.95$.

The presence of droplets in the work of Jourdan et al. [54] was shown to have a significant effect on pressure time histories within the shock tube as the shock wave traversed the interface between the droplets and the buffer gas. This pressure disturbance is because the droplets acted as a porous wall and reflected some of the shock wave back toward the driver section and thereby further increasing the pressure upstream of the interface and limiting the effect the shock wave would have on increasing the pressure downstream of the interface. For droplets with diameters around 120 μm, however, the pressure profiles were almost identical to the results of the shock wave propagating through a pure gas. Pressure profiles near the region of aerosol contact surface in this study (wherein the aerosol droplets ranged in size from 1-10 μm) are in good agreement with the results from Jourdan et al., i.e. no abnormal behavior was observed in the pressure time

histories due to the interaction of the incident shock wave with the aerosol interface at the gate valve. Although the presence of aerosol droplets themselves were not observed to impact pressure time history behavior, the interaction of the reflected shock wave with the buffer gas contact surface was minimally apparent in post-reflected shock pressure traces.

One reason for implementing buffer-gas tailoring is to achieve uniform velocity decay of the incident shock wave through Region 1 of the driven section. However, the primary reason to employ this technique is to avoid any consequences from the interaction of the reflected shock with the aerosol contact surface. Because of the differences in gas composition between the Region 2 buffer gas and the evaporated fuel-air mixture in Region 2 formed from the evaporation of the aerosol droplets, the reflected shock interaction with this interface can send back an expansion wave into Region 5. If the properties across this interface are similar, the effect of the reflected expansion will be relatively small, as was generally the case in this work. Figure 4.4 shows an endwall pressure time history after the shock wave has propagated through the aerosol and reflected back towards the diaphragm. The slight pressure depression roughly 250 μs after shock reflection indicates arrival of a slight expansion reflected from the interaction of the reflected shock wave with the contact region between the buffer gas and aerosol. This behavior is not seen so early for the case of a pure nitrogen driven gas. Figure 4.5 shows an endwall pressure time history after passage of the reflected shock wave which does not exhibit an expansion so early after the reflected shock as in Figure 4.4. Instead, an expansion is seen due to the interaction of the reflected shock wave with the driver-driven gas contact surface at a significantly later time. A limited degree of driver gas tailoring

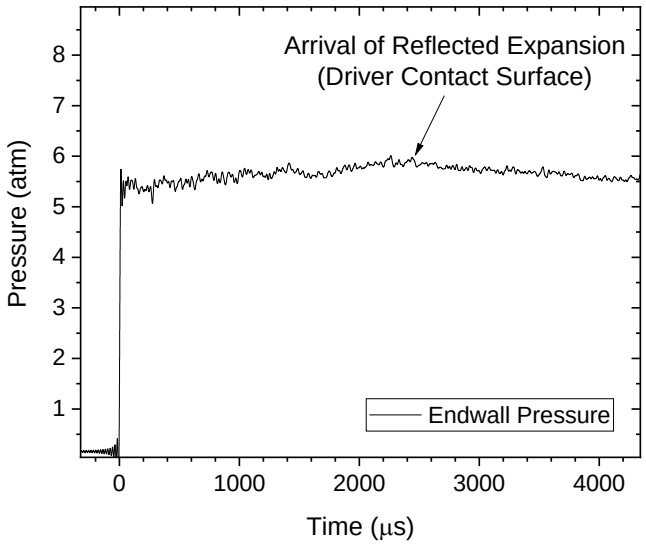

Figure 4.5 Pressure time history from endwall-mounted pressure transducer after passage of shock wave. Driven gas-N_2, Driver gas-16%N_2/He, T_5= 1086 K, P_5= 5.35 atm.

was employed so this interaction was not completely eliminated, as can be done using information provided by Amadio et al. [127] and Hong et al. [128].

4.2.3. Effects of the U-Bend Driver Section

Another feature that could produce a pronounced effect on the appearance of pressure time histories is that of the U-bend in the tubing of the driver section (as seen in Figure 3.6 and in Figure 3.8). This feature had the potential to produce significant pressure perturbations due to the sharp bend in the flow. Although previous researchers have implemented such a feature with no mentioned noticeable effect [86, 117], the U-bend in those works was further from the diaphragm interface than in this facility. Thus, it was deemed necessary to ensure that no significant pressure perturbations were present due to

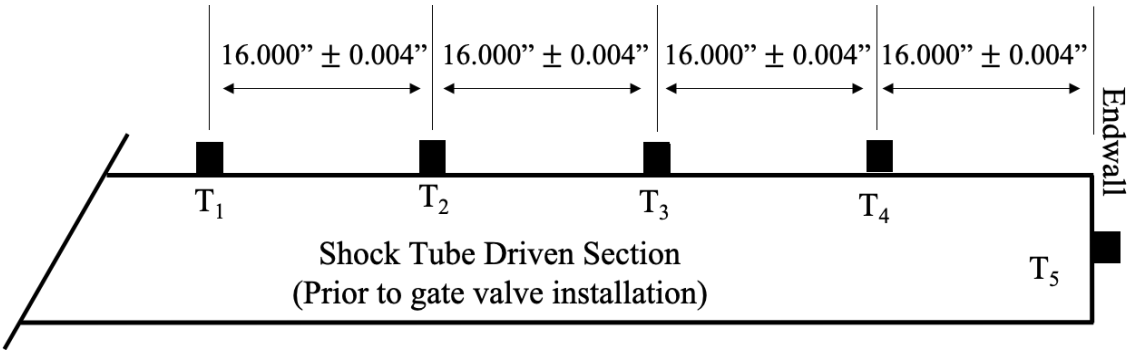

Figure 4.6 Shock-tube driven section pressure transducer spacings and arrangement prior to installation of gate valve.

the presence of the U-bend by way of investigating pressure time histories at various locations along the driven section of the tube.

Pressure time histories were recorded from the pressure transducers used for shock velocity detection and were used to show the relative behaviors of the pressure traces with and without the U-bend, respectively. Figure 4.6 shows the setup of the pressure transducers on the driven section of the shock tube prior to installation of the gate valve. Prior to attaching the U-bend to the driver section and driver extension, the driver end cap was placed on the straight section of tubing which attached directly to the diaphragm breech canister. In this configuration, the driver section was approximately 1.35 m in length. A shock experiment with helium as the driver gas and argon as the driven gas was conducted. The pressure time histories of this experiment are shown in Figure 4.7. The shock wave first arrives at location T_1 at time $t = 0$, and is seen to reach all other transducers (T_2-T_5) in subsequent fashion. After the arrival of the shock wave at each location, the pressure remains constant for no more than a few hundred microseconds prior to the arrival of the expansion wave from the driver endwall. In particular, the Region 5

pressure at transducer location T_5 (the driven endwall transducer), is shown to remain near a constant pressure for approximately 350-450 μs prior to arrival of the expansion fan head. This timing shows that the test time for this particular experiment is no greater than roughly 500 μs. Additionally, the reflected expansion head reaches each sidewall pressure transducer location before the arrival of the reflected shock wave.

After the investigation of the pressure time history behavior using the short driver section, the U-bend was installed with an additional straight extension section of driver tubing after the U-bend. The total length of the driver with the U-bend and a single extension section was approximately 6.6 m. This setup made the total length of the driver section roughly five times that of the driver without the U-bend portion. Figure 4.8 shows pressure time histories of an experiment using the elongated driver configuration. As with the previous experiment, the shock wave passes all transducer locations, increasing the pressure at each location, but in this case the reflected expansion from the driver endwall takes much longer to arrive at each pressure transducer. In fact, the reflected shock wave arrives at each transducer location prior to the arrival of the expansion head. Additionally, the total test time as seen from the endwall pressure transducer is significantly longer than that of the experiment shown in Figure 4.7 with the shortened driver configuration. Furthermore, the purpose of this exercise was to ensure no significant pressure anomalies were produced by the U-bend section. From further examination of the first pressure trace in Figure 4.7 it is seen that the expansion fan arrives within roughly 1 ms after passage of the incident shock wave over the first transducer, T_1. In the elongated driver section, were a significant pressure phenomenon to be produced by the U-bend, its timing would be

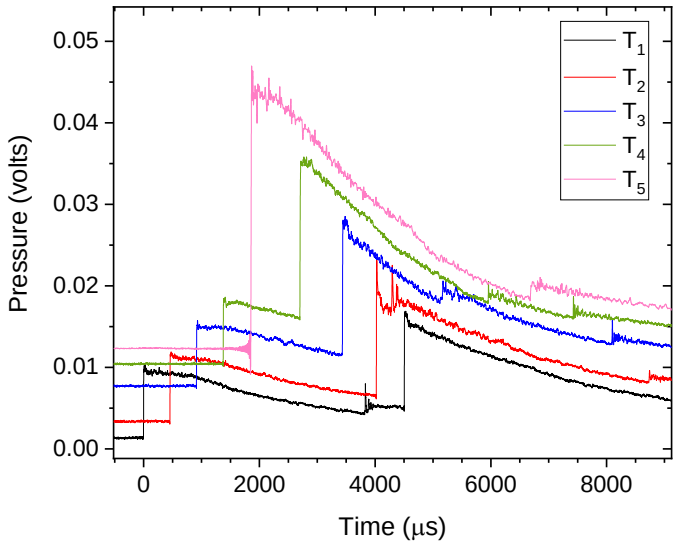

Figure 4.7 Pressure time histories from pressure transducers as shown in Figure 4.6 with a shortened driver section without the U-bend. The Arrival of the incident shockwave occurs first at transducer T_1 and last at the endwall transducer T_5. Individual pressure traces are offset vertically for easier viewing. Experimental conditions: Driver gas-He, Driven gas-Ar, T_5=1785 K, P_5=2.02 atm.

similar to that of the arrival of the expansion fan in Figure 4.7. As can be seen from the first pressure trace in Figure 4.8, this is not the case and there is, in fact, no occurrence of a significant pressure event between the arrival of the incident shock wave and passage of the reflected shock wave over T_1. Further examination of the pressure traces in Figure 4.8 reveals that the expansion wave does not arrive at the driven endwall until approximately 9 ms after the shock wave arrival at the endwall. The first decrease in pressure seen in the endwall transducer (and $T_{3,4}$ as well) is due to the interaction of the reflected shock wave with the driver-driven gas contact surface. Because the T_1 transducer pressure is shown to be constant during the arrival of the expansion event at $T_{3\text{-}5}$, it can be concluded that this expansion originated downstream of T_1 and is not due to the expansion head from the

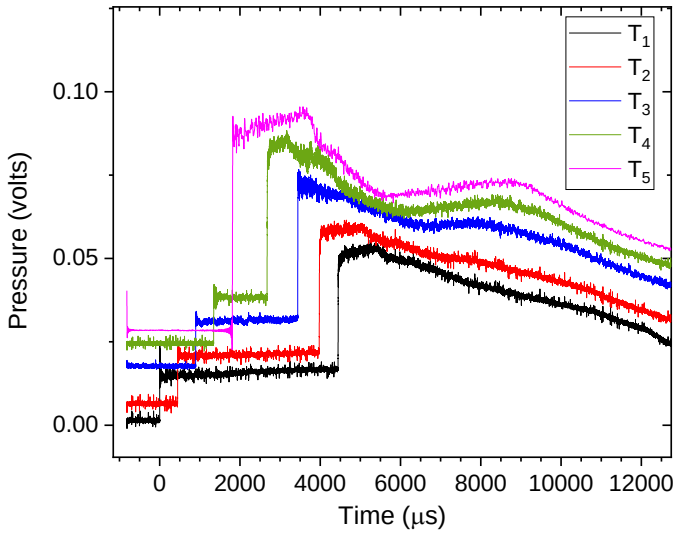

Figure 4.8 Pressure time histories from pressure transducers with an elongated driver section including the U-bend. The Arrival of the incident shock wave occurs first at transducer T_1 and last at the endwall transducer T_5. Individual pressure traces are offset vertically for easier viewing. Experimental conditions: Driver gas-He, Driven gas-Ar, T_5=1879 K, P_5=3.77 atm.

driver endwall. It should also be noted that although the pressures of the experiments in Figure 4.7 and Figure 4.8, respectively, are different, the propagation of pressure waves (dependent on the gas speed of sound, $a = \sqrt{\gamma RT}$) are decoupled from the magnitude of the experimental pressure within the shock tube under the ideal gas assumption for the pressures of the respective experiments. This brief analysis, although rudimentary, provides good confidence that the U-bend portion of the driver did not introduce significant pressure fluctuations in the flow. If such perturbations from the U-bend were present they were on the scale of perturbations associated with non-ideal pressure rise, dP*/dt, from boundary-layer growth in the flow behind the incident shock wave (notice the slight pressure rise in T_1 of Figure 4.8 prior to arrival of the reflected shock wave).

Furthermore, if any perturbations from the U-bend are present, they are small and would only present themselves in any significant fashion during experiments with elongated test times, wherein driver inserts would likely be used to mitigate such small pressure rise effects.

4.3. **Gaseous Ignition Delay Times with Methane**

Following the examination of various gas-dynamic effects within the aerosol shock-tube facility, gaseous ignition delay time experiments were performed to ensure such data recorded in the new shock tube were comparable to those of other facilities. A simple mixture of lean methane in air was used as the driven test gas, and ignition delay time data were recorded over a range of pressures of approximately 1.5-4.5 atm and temperatures from 1100-1600 K, respectively. The results of the gaseous ignition delay time experiments are shown in Figure 4.9 and show good agreement with both models and data from the literature. Although these results are not novel, they do provide confirmation that the shock-tube facility is capable of recording high-quality, gaseous ignition delay time data . Furthermore, the gate valve was attached to the shock tube for these experiments and thus it can be reasoned that the gate valve had no effect upon the results of the ignition delay time experiments in any overly significant way.

4.4. **Fuel Concentration Diagnostic and Thermodynamic Calculations**

After characterizing the basic operations and diagnostic behaviors of the new shock tube, aerosol behavior behind the incident shock wave was characterized. This phase included verifying correct operation of aerosol diagnostics and the aerosol

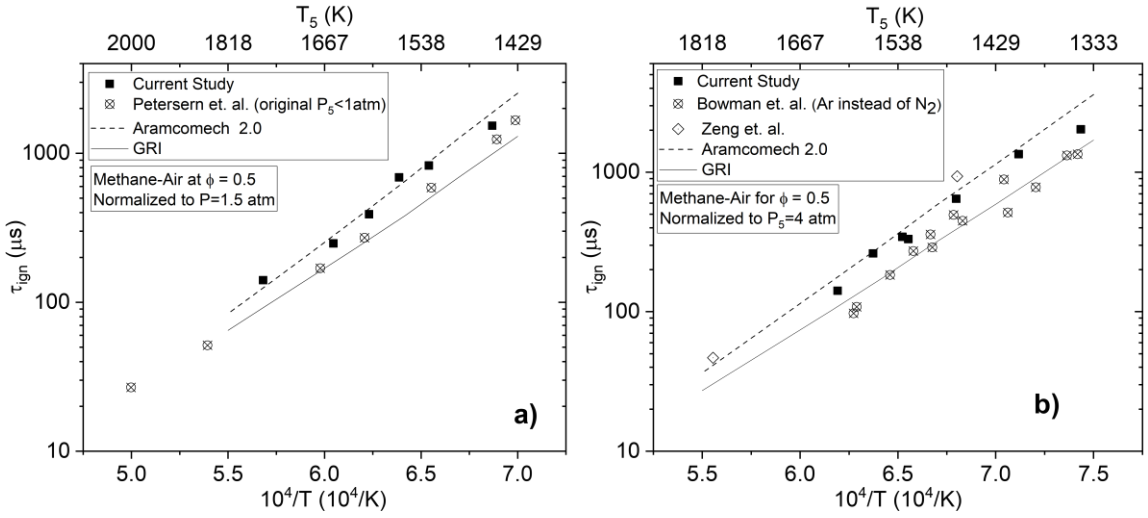

Figure 4.9 Ignition delay time plots for methane in air with an equivalence ratio of $\phi = 0.5$. a) Experimental pressure, P_5, normalized to 1.5 atm. The data from Petersen et al. were recorded for $P_5 < 1$ atm. b) Experimental pressure, P_5, normalized to 4 atm. Data from Bowman et al. used Ar instead of N_2 as a surrogate for air.

functionality of the shock tube itself, while also characterizing the behaviors of the aerosol during the course of a shock tube experiment. Prior to detailing the aerosol function of the new facility, however, some consideration is given here to the motivation behind the fuel concentration diagnostic: calculation of the thermodynamic properties behind the shock waves and associated modifications due to the presence of aerosols.

4.4.1. Thermodynamic Property Calculations

In conventional gas-phase shock tubes, the calculation of thermodynamic properties behind the incident and reflected shock waves is a fairly straightforward process. Combining the known mixture composition, Region 1 state variables, and incident-shock velocity, the thermodynamic calculation is accomplished iteratively using the normal-shock equations coupled to the thermodynamic conservation equations. A

program developed by the Hanson group at Stanford called FROSH was employed to perform such thermodynamic calculations when conducting gas-phase experiments in the shock tube [117, 122]. The calculation of thermodynamic conditions behind shock waves when conducting experiments in aerosols can be performed with a similar technique, but the process for such calculations is more involved and has stricter limits of applicability.

When calculating the thermodynamic conditions behind incident and reflected shock waves using mixtures with aerosols, the nature of both the liquid and the droplet size distribution must be taken into consideration to achieve accurate calculation results. A program called AEROFROSH was developed by Campbell and coworkers [123] for use with aerosols as an extension to Davidson's FROSH program for calculating thermodynamic properties behind shock waves. This program incorporates the additional variables needed for considering the aerosol in the post-shock thermodynamic calculations. In addition to the properties of the carrier gas of the aerosol, the properties of the liquid in the droplets must also be considered. These include the liquid vapor pressure and also the density of the liquid, as well as the chemical formula of the liquid mixture itself.

As is often the case when studying crude-derived fuel mixtures in shock tubes, averaged chemical formulas, or surrogate mixtures, are employed for calculating thermodynamic properties of mixtures associated with combustion. This use of a surrogate is because the chemical formulas for real mixtures of liquid hydrocarbons, such as the jet fuel and diesel fuel investigated in this study, are not easily obtained due to the large numbers of constituents in the fuel. Average chemical formulas can be measured using

complex analysis tools for real fuels such as gas chromatography and nuclear magnetic resonance, or NMR [77].

The precise gas-phase thermodynamic properties of a wide range of crude-derived fuel blends are not cataloged, that is, unless the thermodynamic data for a specific fuel blend have been recorded over a wide range of temperatures and pressures and fit to match the form of the commonly used NASA polynomials [129]. Such a task is a highly impractical, if not an impossible, process to perform on every liquid fuel formulation. Thus, surrogate formulations for real liquid fuels must be used as an estimate for calculating gas-phase thermodynamic properties of real liquid fuels. In addition to using gas-phase thermodynamic data for liquid fuels in thermodynamic calculations, the vapor pressure of the liquid fuels is also required. Although the liquid fuel is primarily in the liquid phase, a non-zero amount is also present in vapor form since few substances have a truly near-zero vapor pressure.

Similar to the liquid fuel mixture composition, the vapor pressure of the real liquid fuel must also be estimated. This need for the vapor pressure is because the low volatility of the components in real liquid fuels makes accurate measurement of the vapor pressures very difficult at room-temperature (the temperature of the shock-tube contents prior to passage of the shock wave), often yielding relatively inaccurate results. However, the approximate formula from analysis of the average fuel composition can provide a reference point from which the vapor pressure may be estimated using the vapor pressure of a compound resembling the average chemical formula of the mixture. Such techniques were employed in the calculation of thermodynamic properties for this work: an

approximate vapor pressure was chosen based on a compound with a formula near that of the average chemical compound obtained for each fuel, and a surrogate formulation was chosen such that it mimicked the thermodynamic behavior of the real fuel during the evaporation and heating processes behind the shock waves.

In addition to thermodynamic properties, spectroscopic properties of the liquid components must also be entered into the numerical AEROFROSH solver for post-shock state calculations. Specifically, the post-evaporation spectroscopic absorption coefficient of the liquid components must be entered to provide closure to the system of equations used to calculate thermodynamic properties behind the shock waves. The reason the system of equations used in traditional gas-phase solvers (mass, momentum, energy) is inadequate is because these solvers are used when the gas-phase composition is known throughout the shock propagation and reflection process. This situation is not the case in aerosol mixtures. Thus, the Beer-Lambert relation is used to provide closure to the system of equations by incorporating the post-incident-shock absorbance of the fuel. Only then can the gas-phase fuel mixture composition calculation be coupled to the mass, momentum, and energy equations by iteratively solving for the conditions behind the shock waves. Although the fuel concentration is measured after evaporation of all aerosol droplets during each experiment, evaporation cannot be assumed without the appropriate diagnostic. Evaporation must be measured to ensure that no droplets remain during the course of the fuel absorption measurement.

Although an absorption diagnostic is required to directly determine gas-phase fuel mole fractions and subsequent thermodynamic conditions, the fuel cannot be assumed to

be completely in the gas phase without an additional diagnostic recording the presence (or eventual vaporization) of droplets. To ensure complete evaporation of liquid droplets, a Mie scattering diagnostic must be employed to record the evaporation process. The reason such a diagnostic is necessary is because the gas-phase thermodynamic calculations can only be performed if the assumption of complete evaporation and uniform diffusion of the gas-phase fuel is correct. This complete evaporation is the primary reason why choosing the correct aerosol size distribution is such a critical portion of the design of an aerosol shock tube: if the post-incident-shock region cannot be assumed to be homogeneous from fast droplet evaporation and diffusion, then calculated gas-phase thermodynamic conditions cannot be considered to display adequate accuracy. Thus, ensuring rapid droplet vaporization via an in-situ optical diagnostic is a key component of performing gas-phase fuel concentration measurements behind incident shock waves in shock-tube aerosol mixtures. More information regarding the calculation of thermodynamic variables behind shock waves with aerosols is provided in Appendix B.

4.4.2. Fuel Concentration Measurement

Because the fuel in an aerosol shock tube experiment is introduced into the shock tube in liquid form, its concentration cannot be measured manometrically as in traditional gas-phase mixtures. Therefore, the equivalence ratio of the aerosol cannot be measured prior to the beginning of an experiment. To accurately measure the concentration of fuel for a given experiment, the fuel concentration must be measured directly in the shock tube prior to each experiment. Because the fuel will exist in one of two states prior to the

beginning of an experiment (that is, prior to the shock wave arriving at the endwall), two methods are available with which the concentration of the fuel can be measured.

The most commonly used method of fuel concentration measurement in conventional shock tubes is accomplished by using a gas-phase absorption spectroscopy diagnostic. Such a diagnostic requires that the fuel not be in the liquid phase but in the gaseous phase. Alternately, volume fractions of liquid fuel droplets could also be measured using a Mie scattering diagnostic using the relations of Eq. (3.6) and Eq. (3.7), respectively, since the droplet size distribution parameters and wavelength of light are known. This volume fraction could then be converted to a density using the known liquid-phase fuel density. Although this method of measuring fuel concentration is possible, the parameters of the droplet distribution are modified by virtually any event which induces significant motion of the aerosol, such as transporting the aerosol from one volume to another during the filling process. A more involved Mie scattering diagnostic, like that of Hanson et al. [74], could also be employed to measure the droplet distribution directly within the shock tube prior to the start of the experiment. Such a diagnostic adds significant complexity compared to a gas-phase absorption spectroscopy technique, however, and provides little, if any, added benefit compared to the simpler gas-phase measurement technique. Thus, it was decided that the most practical way of measuring the fuel concentration within the shock tube was to vaporize the aerosol droplets and measure the fuel concentration of the mixture using gas-phase absorption spectroscopy.

After deciding on the specific method of measuring fuel concentration, the timing of the measurement required another decision to be made. One method for timing the fuel

concentration measurement could be conducted such that concentration was measured behind the reflected shock wave where evaporation of the aerosol is all but guaranteed. Because the fuel immediately begins to break down behind the reflected shock wave, however, the fuel absorption measurement is performed behind the incident shock wave to ensure that the fuel is in a state where decomposition has not yet begun. This choice of timing for measuring fuel concentration in the post-incident shock region provides sufficient time for a measurement to be made and avoids large uncertainties with shorter measurement time periods and possible fuel breakdown. Before spectroscopic measurements can be taken, though, the evaporation of the fuel behind the incident shock wave needed to be verified.

Mie scattering has been discussed previously in this work in relation to the measurement of size distributions of small particles. It can also be used in a simpler form wherein the presence of small droplets or particles in a gas can be detected down to very small number densities. Such was the case in this work: a single-wavelength Mie scattering diagnostic was employed to verify evaporation of nebulized fuel droplets behind the incident shock wave. Once the evaporation process was complete, only then could fuel concentration be measured using gas-phase absorption spectroscopy. This method of verifying evaporation to measure gaseous fuel concentration was also used by Davidson et al. in their Gen. I aerosol shock tube [34] (and employed by Haylett et al. as well [35]). To avoid droplet fouling on the windows, the window heating technique used by Davidson et al. was also employed. The hardware for the heated windows is discussed in Chapter

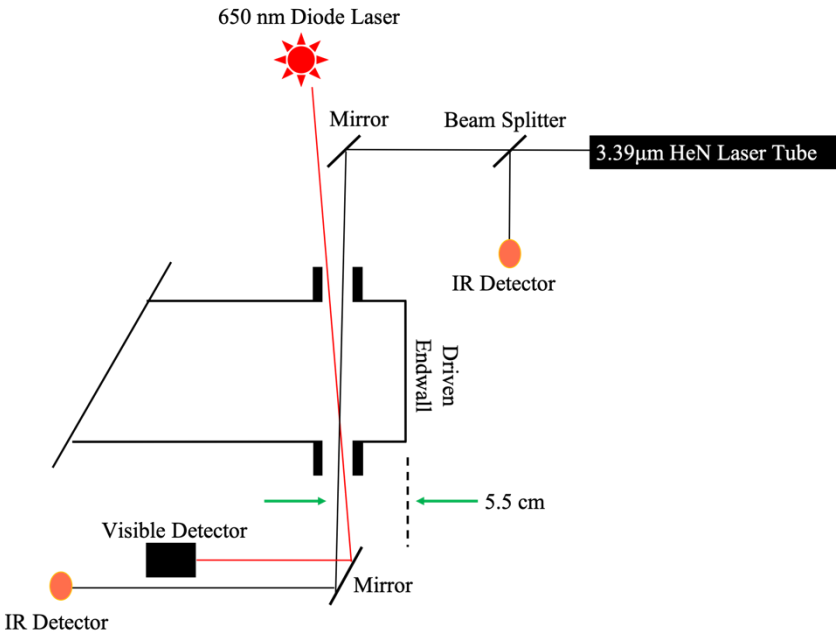

Figure 4.10 Laser diagnostic setup for verifying aerosol vaporization and subsequent measurement of fuel concentration using a Mie scattering and absorption spectroscopy diagnostic, respectively.

Error! Reference source not found. of this work. A schematic showing both the droplet e vaporation diagnostic and the fuel concentration diagnostic is given in Figure 4.10.

The Mie scattering diagnostic was performed with a 650-nm diode laser incident on a Thor Labs PDA36A2 detector after passing through the shock tube. The fuel absorption diagnostic was performed using two InSb IR detectors from Electro-Optical Systems and a 3.39-μm HeNe laser from REO Inc. For the gas-phase absorption diagnostic, common mode rejection was used to eliminate power fluctuations from the HeNe laser signal. This mode cancellation was accomplished by splitting the beam into two legs before it passed through the shock tube. The first leg, referred to as the incident signal, was sent into a detector without being passed through the shock tube. The second

leg from the HeNe laser, referred to as the transmitted signal, was sent through the shock tube and then to a detector.

The formulation used for measuring the fuel concentration within the shock tube employs the oft-used Beer-Lambert relation, which is given by Eq. (4.1). In this equation, I_0 is laser intensity (irradiance) from the incident signal, I is the laser intensity from the transmitted signal, α is a function of the two intensities and termed the absorbance, k_ν is the absorption cross section in units of [atm^{-1} cm^{-1}], P is the total pressure in units of atm, X_{abs} is the mole fraction of the absorbing species present in the volume, and L is the path length in cm over which the laser traverses the volume containing the absorbing species.

$$-\ln\left(\frac{I}{I_0}\right) = \alpha = k_\nu P X_{abs} L \tag{4.1}$$

To implement common mode rejection, Eq. (4.1) can be recast as a function of the difference between the I_0 and I signals. This implementation is shown in Eq. (4.2).

$$1 - \frac{(I_0 - I)_{true}}{I_{0,true}} = \exp(-k_\nu P X_{abs} L) \tag{4.2}$$

The subscript "true" in Eq. (4.2) represents the true values of the intensity measured by the laser detectors when background radiation and detector offsets have been taken into consideration. More information regarding the formulation of Eq. (4.2) can be found in Appendix A.

When conducting experiments in aerosols, it was observed that the aerosol was evaporated in sufficient time so as to provide useful gas-phase absorption measurements for determining the fuel concentration behind the incident shock wave. Furthermore,

fouling of the windows was also not observed to occur in any significant fashion. Example time histories from the Mie scattering diagnostic and the fuel absorption diagnostic in different fuels are shown in Figure 4.11, with sub-figure a) being recreated from Hargis et al. [130]. Prior to arrival of the shock wave, both signals are constant at a non-zero value due to the presence of aerosol in the tube. As the incident shock wave passes through the laser beams, the schlieren spike is observed, which signifies that the plane of the measurement station is transitioning from Region 1 to Region 2 of the experiment (pre-shocked to post-incident-shocked regions).

Immediately after passage of the incident shock wave, the signal from the visible Mie scattering diagnostic at 650 nm quickly decays to zero, indicating total evaporation of the fuel, and also signifying no fouling of the windows due to the presence of droplets on the inner window surface. Simultaneously, as the visible laser signal decays the signal from the resonant absorption laser rises to a steady value. The complete vaporization of the droplets as indicated by the visible laser signifies the beginning of the time period over which the fuel concentration diagnostic is performed. The end of the period over which the fuel concentration is measured is signified by the arrival of the aerosol contact surface or the reflected shock wave at the measurement station, whichever comes first. An average value of the absorbance from the resonant absorption signal is calculated from the gas-phase absorption trace. This absorbance is the value used to determine the gaseous mole fraction of the evaporated fuel in the gaseous mixture behind the incident shock wave. The uncertainty of the fuel concentration measurement shown in Figure 4.11 varies from

±2.5% to ±4.5%, representing the approximate range of uncertainty in the fuel measurement diagnostic from all experiments.

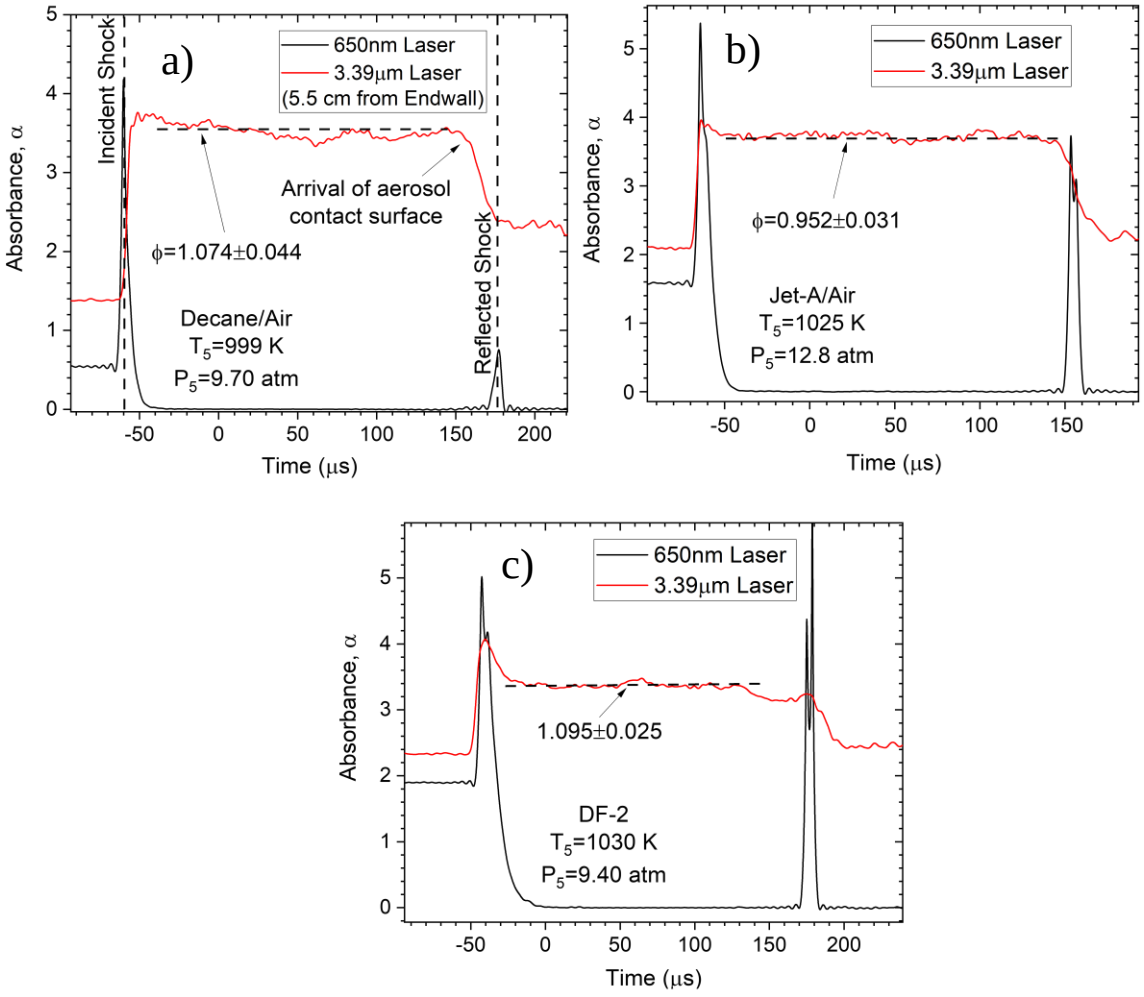

Figure 4.11 Evaporation and fuel concentration measurement of aerosols composed of fuel droplets in air after passage of the incident shock wave. The black trace represents scattering of the 650-nm laser by aerosol droplets, while the red line represents gas-phase absorption of the vaporized fuel at an IR wavelength of 3.39 microns. Time zero on the plots correspond to the arrival of the shock wave at the endwall of the driven section. The temperature of each experiment is around 1000 K and the pressure is in the range of 9.4-12.8 atm. a) Decane/Air, b) Jet-A/Air, c) DF-2/Air.

4.5. **Defining Ignition Delay Time and Sample Ignition Traces**

Upon validation all diagnostic and operational aspects of the new aerosol shock tube facility, preliminary ignition experiments were performed to investigate the quality of ignition data from nebulized liquid fuels in air. Prior to providing examples of ignition behavior in the new facility, though, it is necessary to discuss the metric by which ignition is defined. In shock-tube experiments employing real fuel mixtures, the ignition event is recorded from an endwall diagnostic location [39]. This procedure is because the measurements taken at sidewall measurement locations, especially at higher temperatures, can yield artificially fast values of ignition delay time. Since the ignition event will occur first at a location nearest the endwall, the event will be experienced by endwall diagnostics before it is detected by other diagnostics.

When defining the onset of the ignition event, the zero-referenced intersection of the steepest slope in the rise of a pressure or emission time history trace as observed from an endwall measurement location was used as the method for defining ignition timing. Pressure time histories are occasionally used to measure ignition timings, but emission diagnostics are more sensitive to such events and provide better accuracy of the precise timing of the occurrence of ignition. Thus, for this work the primary diagnostic used to measure the occurrence of ignition was that of an emission diagnostic placed such that it could collect light passing through a window port in the endwall of the shock tube. An example emission trace defining ignition with an example schematic depicting the

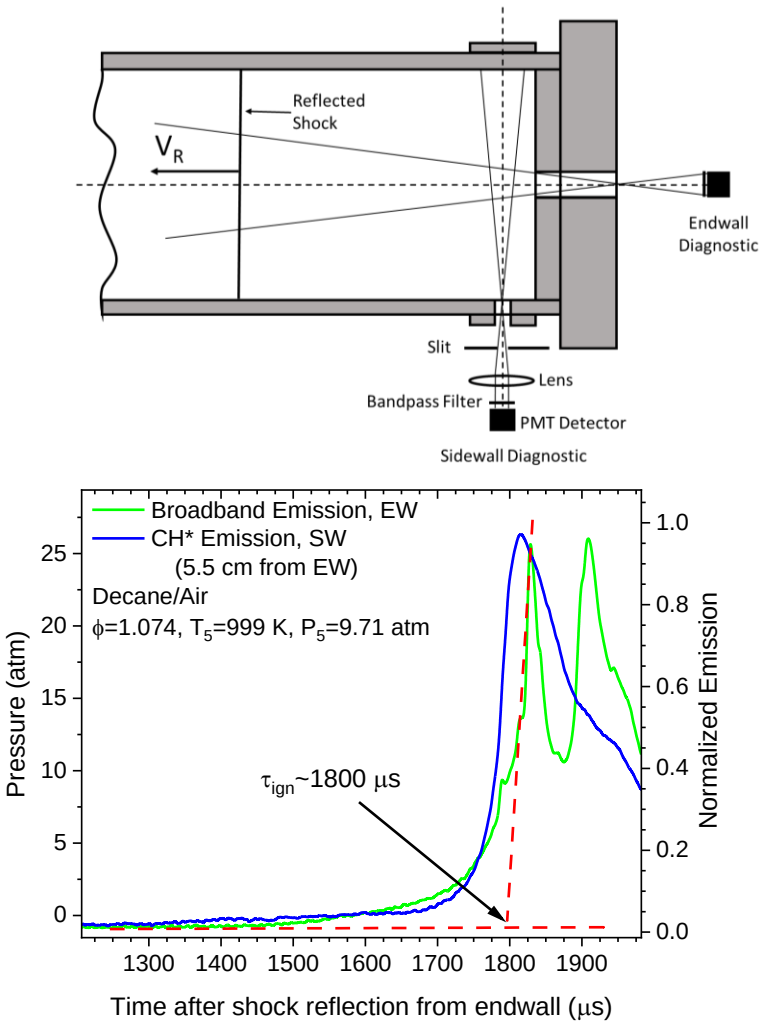

Figure 4.12 a) Schematic setup of example emission diagnostic configuration, b) Emission traces from sidewall and endwall detector locations with ignition delay time defined as the zero-intersection of the steepest slope of the endwall detector.

associated optical diagnostics is shown in Figure 4.12. The emission detector can be fit with a filter to measure the presence of excited-state radical species like OH* or CH* since these species indicate the buildup of the radical pool within the reaction region, more-accurately signifying the onset of ignition.

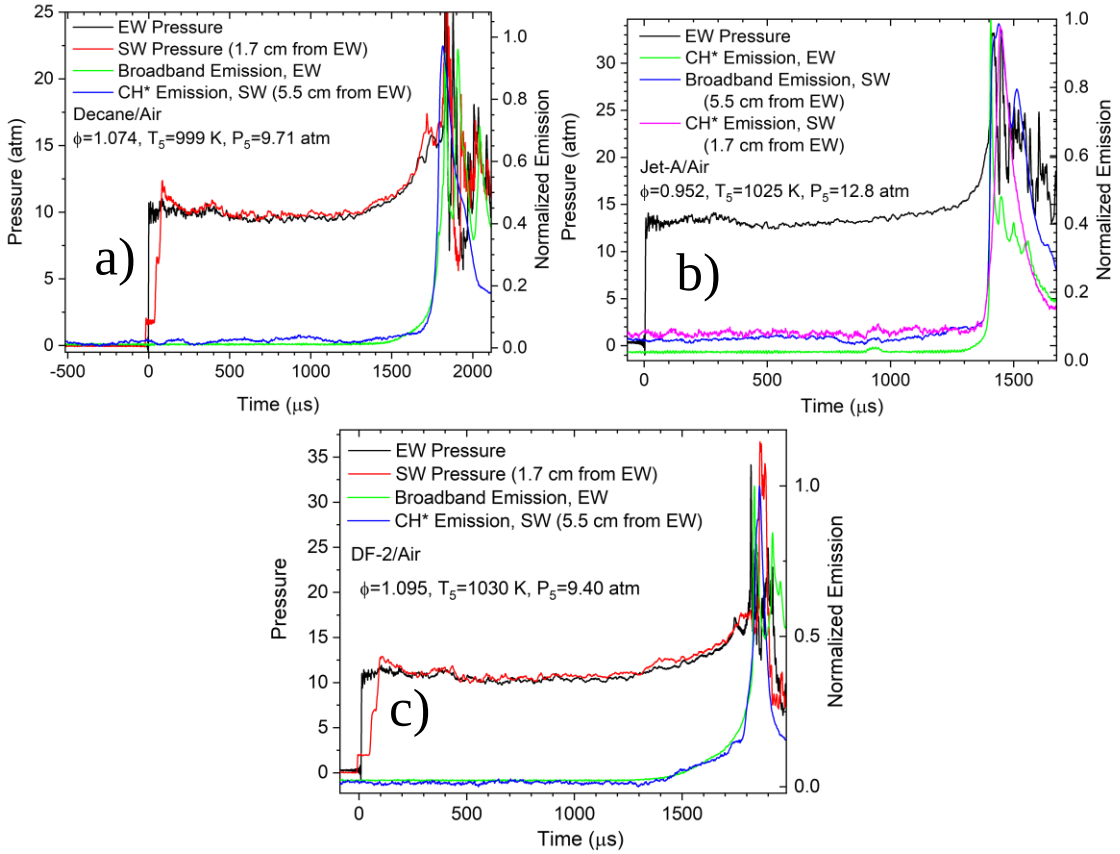

Figure 4.13 Pressure and emission time histories behind reflected shock waves for sidewall and endwall measurement diagnostics in the aerosol shock tube from various aerosol fuel experiments near 1000 K and 10 atm. a) Decane/Air, b) DF-2/Air, c) Jet-A/Air.

Sample traces of the primary fuels investigated in this study are shown in Figure 4.13, with sub-figure a) being recreated from Hargis et al. [130]. The pressure traces for endwall and sidewall pressure transducers are shown as black and red lines, respectively, with the sidewall transducer being placed at a measurement station 1.7 cm from the endwall. Some experiments did not employ a sidewall time history diagnostic after it was ensured that the general ignition behavior of the fuel had been well-characterized. Green traces represent endwall emission (either broadband emission or 431-nm emission from

the decay of electronically excited CH* radicals). Blue traces are from emission detectors (either broadband or CH* emission) placed at a sidewall measurement location 5.5 cm upstream of the endwall; and magenta traces represent emission (broadband/CH*) from sidewall measurement locations 1.5 cm upstream from the endwall. From each of the traces, it can be observed that the pressure traces at different locations show good agreement with one another, as do the emission traces. This level of agreement gives confidence that the ignition event is occurring in a global manner and not a localized manner followed by a detonation propagating throughout the volume to other locations. Furthermore, the uniform ignition of the fuel in Region 5 proves encouraging in that the fuel within the post-reflected shock region is reasonably well-mixed with the carrier gas after being evaporated behind the incident shock wave. Were the gaseous fuel not relatively homogeneous within the post-reflected-shock region, localized pockets with high concentrations of fuel would dominate the global ignition behavior. These pockets of inhomogeneity would present themselves as localized sources of ignition, leading to disagreement in the behavior of pressure and emission time histories and also leading to greater potential for the observation of detonation-like ignition behavior.

4.6. **Conclusions**

At the conclusion of the design phase, all aspects of the new aerosol shock tube facility required characterization. Thus, a campaign was undertaken to characterize all operational aspects of the new aerosol shock tube facility. Velocity decay behavior in gaseous mixtures behaved as expected, but the velocity decay behavior of the shock wave through the aerosol behaved somewhat differently, primarily because impedance

matching was not performed at the interface between the aerosol and buffer gas. Nonetheless, the extrapolated value of the shock wave velocity at the endwall was still able to be reliably calculated, adding little additional uncertainty in the incident shock velocity value compared to that measured in gaseous mixtures.

Pressure time histories were also recorded and shown to be similar when comparing gaseous experiments to aerosol shock experiments. Slight differences were seen due to the reflected shock wave interaction with the contact region between the buffer gas and aerosol. These differences were minor, however, and did not affect the overall performance of the facility. Additionally, the U-bend portion of the driver section tubing was not shown to dramatically affect the overall behavior of the post-reflected-shock pressure time histories. After characterizing the pressure time history behavior of the new facility, the optical diagnostics used to detect aerosol evaporation and subsequent fuel concentration via gas-phase spectroscopy were shown to work as expected.

In the final stage of characterizing the new aerosol shock tube facility, sample ignition experiments were conducted with pressure and emission diagnostics. These traces showed the ignition events using nebulized fuels to be homogeneous, providing confidence that the fuel was well-diffused after evaporation. Thus, it can be concluded that the facility is well-characterized, and all diagnostics and operational aspects of the new aerosol shock tube facility are operating within acceptable limits. After confirmation of the operability of the new facility, new aerosol shock tube data for several fuel-air mixtures were collected for the purposes of validating the ignition delay time behavior of

the aerosol shock tube compared to that collected in heated shock tubes. These experiments are the subject of the next chapter.

5. IGNITION DELAY TIMES OF LIQUID FUELS IN THE AEROSOL SHOCK TUBE

Note: Figs. 5.1-5.4 of this chapter contain data that has been reprinted with permission from the literature. Citations for the sources are given near the plots.

After complete characterization of the new shock tube and aerosol entrainment setup, a campaign was undertaken to acquire ignition delay time data from liquid fuels in mixtures of air from the new aerosol shock tube facility. The data presented herein were acquired for two reasons. First, although the gaseous ignition behavior of the new shock tube was characterized and shown to agree with that of other facilities, the ignition behavior of the facility when using aerosols had yet to be validated against other data. Thus, the aerosol ignition behavior of the facility required validation against liquid hydrocarbon ignition data from other facilities. Second, should they agree with other such ignition data from the literature, the data collected in the aerosol shock tube can be considered as a validated part of the collection of shock-tube ignition data for heavy hydrocarbon fuels.

All experiments were conducted with air as the carrier gas for the aerosol in the aerosol test section and also with air as the driven buffer gas. No buffer-gas tailoring was performed for the experiments herein. Additionally, driver gas tailoring was performed to a limited extent, however. Although the intent of the experiments conducted herein was not to obtain long test times beyond the 2-ms experimental time, driver-gas tailoring was employed in modest amounts (10-20% N_2 with the balance being He) to avoid the most severe effects of un-tailored interactions of the reflected shock wave with the driver-buffer

gas contact surface. Furthermore, driven-gas tailoring also aided in mitigating dP*/dt behavior compared to that observed in untailored mixtures.

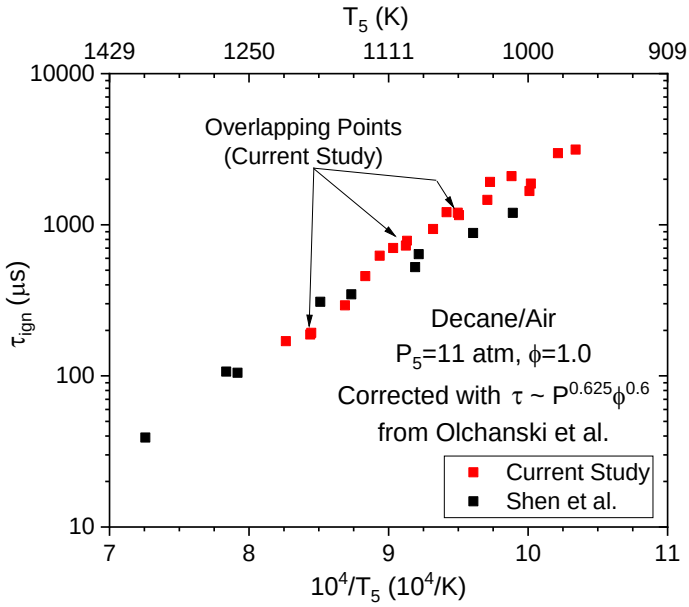

Figure 5.1 Ignition delay time data collected in the aerosol shock tube for mixtures of decane in air at ϕ=1.0 and P_5=11 atm and corrected using correlations from Olchanski and Burcat [131]. The data from the aerosol shock tube are compared to those of Shen et al. [9], with permission.

5.1. **Decane**

The first fuel to be investigated for validating the ignition behavior of the new aerosol shock tube facility was decane. The decane was sourced from Fisher Scientific and was graciously provided by Dr. Nayef Alyafei, Assistant Professor of Petroleum Engineering in the Texas A&M Qatar Petroleum Engineering Department. Ignition data for decane are plotted in Figure 5.1. The data were corrected to a common pressure and

equivalence ratio of P_5=11 atm and ϕ=1.0 using $P^{0.625}$ and $\phi^{0.6}$ dependences, respectively, from Haylett et al. and Olchanski and Burcat, respectively [15, 131]. The range of temperatures investigated were in the high-temperature ignition region from 960-1201 K. Data from the new aerosol shock tube facility are compared to those of Shen et al. [9]. When comparing the two datasets, it can be seen that the agreement between the two facilities is quite good at higher temperatures above 1100 K. Additionally, the agreement between the data sets is not as good below 1100 K, but still within 30-40%.

5.2. **DF-2**

Prior to collecting data on DF-2 in mixtures of air, it was determined that the liquid level height above the ultrasonic nebulizer when using DF-2 caused issues with operating the nebulizer if the liquid depth was too great. When operating in water (as they are originally designed to do), ultrasonic nebulizers are submerged roughly 3-5 cm below the surface of the water. Such a depth in DF-2, however, inhibits the nebulizer from outputting adequate amounts of aerosol because of the increased viscosity of DF-2 compared to water. Since decane viscosity at room temperature is significantly nearer to water than that of DF-2, these issues were not seen when operating the nebulizer in decane at liquid depths of 3-5 cm above the nebulizer surface. Because of the increased viscosity of the DF-2, the liquid level depth above the nebulizer surface was set in the range of 1-2 cm. With this decreased liquid depth, the ultrasonic nebulizer operated less efficiently (in terms of total output) compared to decane, but still output enough aerosol to conduct the 10-atm experiments (although the decrease in efficiency still required a longer time for the

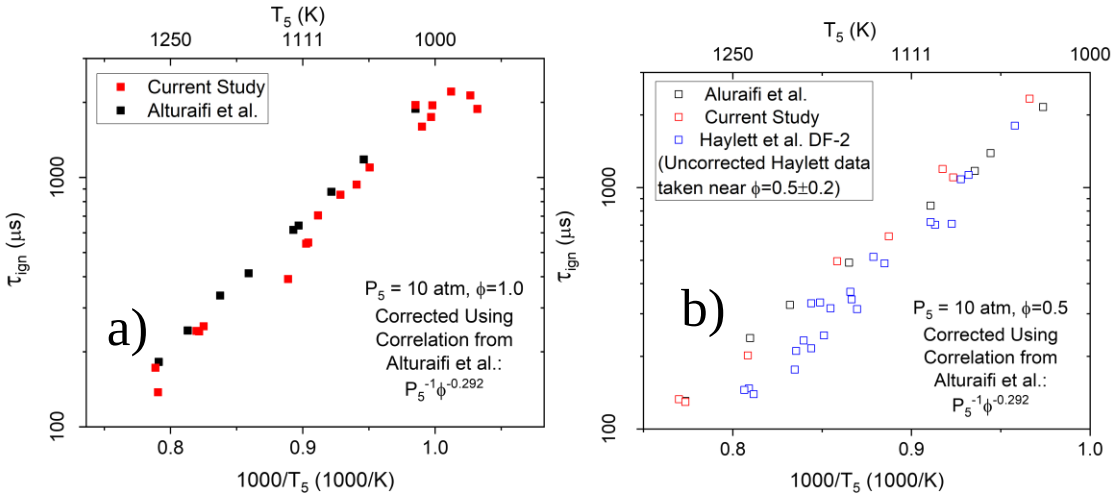

Figure 5.2 Ignition delay times collected in the aerosol shock tube with DF-2/air mixtures compared to data with permission from Alturaifi et al. [23] a) Stoichiometic equivalence ratio, b) lean equivalence ratio, also including data with permission from Haylett et al. [15]. All data are corrected using the DF-2 correlation from Alturaifi et al.

nebulizer to be turned on by a factor of 5-7 compared to that in decane). After this operational issue with the DF-2 was resolved, ignition experiments with aerosols composed of DF-2 droplets in air were conducted.

In addition to investigating the ability of the new facility to acquire ignition delay time data from single-component fuels like decane, an investigation of the ignition behavior of multi-component fuels was also required for validating the facility against other shock tubes. Diesel fuel No. 2, or DF-2, was obtained from the United States Air Force (batch number POSF 12758) courtesy of Dr. J. T. Edwards of the Air Force Research Laboratory (AFRL). Ignition data were collected at pressure conditions of P_5=10 atm, temperature conditions in the range of 960-1260 K, and equivalence ratios of 0.5 and

1.0, respectively. To perform thermodynamic calculations using the AEROFROSH thermodynamic calculator, a surrogate formulation for the fuel was required. A single-component surrogate of dodecane was chosen because it has been used as a single-component surrogate in the past by other researchers [132] and its chemical formula is similar to that of the DF-2 used in this study ($C_{13.1}H_{24.0}$). Additionally, the vapor pressure of the mixture was also estimated by using the vapor pressure of dodecane.

Ignition delay time data from shock-tube experiments conducted in aerosols composed of DF-2 in air are given in Figure 5.2. Sub-figure a) shows stoichiometric equivalence ratios, and sub-figure b) shows lean equivalence ratios, respectively. Ignition data from Alturaifi et al. were plotted against the ignition data of DF-2 collected from this study for purposes of comparison [23]. From examination of both data sets, the comparison between the data collected in the new aerosol shock tube show excellent agreement with the data of Alturaifi et al. for DF-2 fuel. Additionally, DF-2 data from Haylett et al. collected in their Gen. II aerosol shock tube facility are given in sub-figure b) of Figure 5.2 [15]. Further discussion is given in a following section on the data from this study and those from other facilities to which they are compared in the plots.

5.3. **Jet-A**

In addition to the DF-2 supplied by the AFRL, the Jet-A used in this study was also generously provided by Dr. J. T. Edwards (batch number POSF 10325). The Jet-A is a nominal version of Jet-A produced at the Shell Mobile refinery and was acquired by AFRL in June 2013 [77]. Prior to collecting ignition data using the Jet-A fuel, it was again

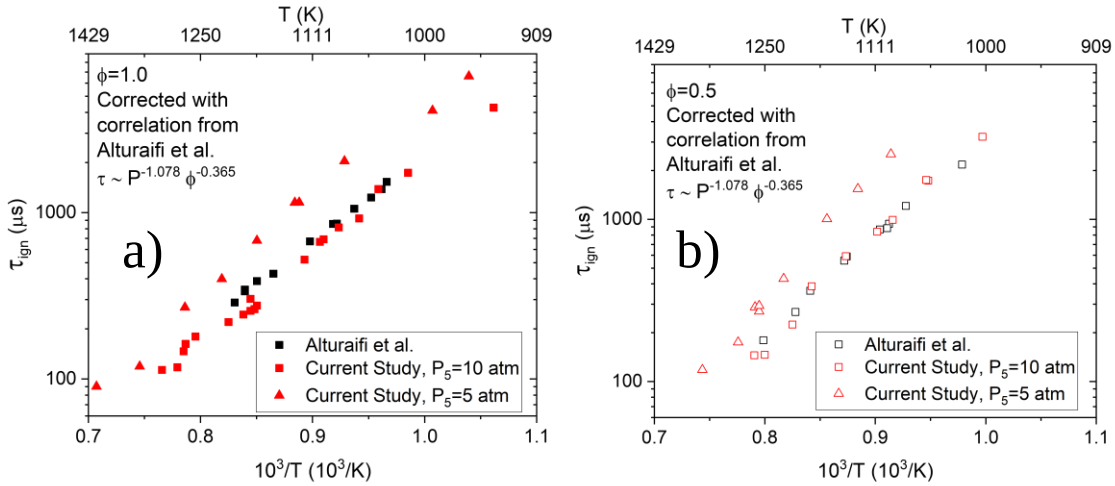

Figure 5.3 Ignition delay times collected in the aerosol shock tube with Jet-A/air mixtures compared to ignition delay time data with permission from Alturaifi et al. [23]. a) Stoichiometric equivalence ratio, b) Lean equivalence ratio. All data are corrected using

necessary to examine the nebulizer behavior to ensure adequate aerosol loading could be achieved by optimizing the liquid level depth above the nebulizer surface, similar to what was done using the DF-2 fuel. It was observed that the Jet-A was significantly less viscous than the DF-2 and behaved in a similar manner to decane in terms of nebulization. The optimum liquid level depth was still on the order of 1-2 cm above the nebulizer, however.

After the brief examination to ensure proper nebulizer operation, a series of ignition delay time experiments were conducted with the aerosol shock tube Jet-A/air mixtures. The pressures examined ranged from P_5=5-10 atm, and the temperatures ranged from approximately T_5=960-1250 K. For the purposes of calculating the post-shock thermodynamic state conditions, a single-component surrogate formulation was used. Although Jet-A is of course a mixture with hundreds of constituents, its mixture-averaged,

gas-phase thermodynamics data have been tabulated such that it can be treated as single component for the purposes of gas-phase thermodynamic calculations. The 7-term polynomials (from the NASA formulation [129]) used for this surrogate came from the Burcat thermodynamic database [133]. Lastly, the vapor pressure of the mixture used as the input to AEROFROSH was estimated by using the vapor pressure of dodecane.

Ignition delay time data for Jet-A/air mixtures at both P_5=5 and P_5=10 atm, respectively, are given in Figure 5.3. Data from Alturaifi et al. at P_5=10 atm are also displayed on the graphs for the purpose of comparison. From the plots, it can be seen that the agreement between the two data sets is quite good at 10 atm for equivalence ratios of both ϕ=0.5 and ϕ=1.0, respectively. This was also the case for the DF-2 ignition delay data. More discussion is provided in a following section.

5.4. **GTL Diesel**

Following ignition delay time experiments conducted in the aerosol shock tube with conventional fuels derived from crude oil stock, a Fisher-Tropsch fuel was investigated. This gas-to-liquid (GTL) fuel was produced in Qatar and was generously provided by the TEES Gas and Fuels research center under the direction of Dr. Nimir Elbashir, Professor in the Petroleum Engineering Department at Texas A&M Universty Qatar. Although the class of fuel was known, the chemical analysis of the composition was not known as completely as either the Jet-A or DF-2 provided by AFRL.

Prior to outlining the properties of the fuel used for calculations, it should be underscored again here that analyzing the composition of a given fuel is an expensive

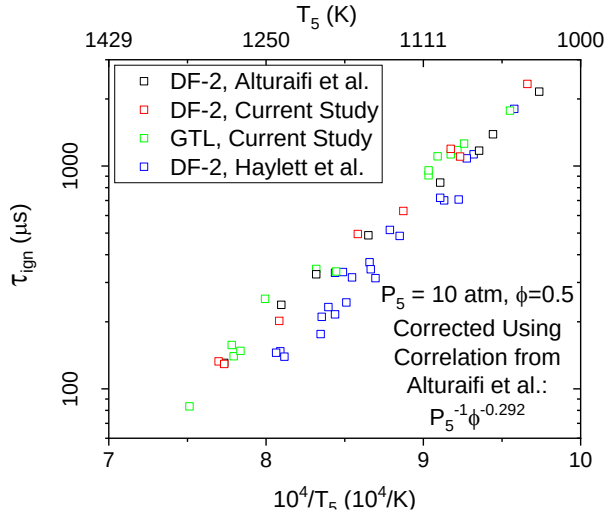

Figure 5.4 Ignition delay times collected in the aerosol shock tube with GTL-Diesel/air mixtures compared to DF-2 ignition delay time data (with permission) from Alturaifi et al. [23], DF-2 ignition delay time data from this study, and DF-2 data (with permission) from Haylett et al. [15], all at lean equivalence ratios. All data are corrected using the correlation from Alturaifi et al.

process and requires the use of several techniques including FTIR spectroscopy, gas chromatography mass spectroscopy (GCMS), and NMR techniques, among others. Because of this, a thorough analysis of the provided GTL fuel was not conducted beyond the analysis of basic properties such as density and viscosity. Thus, knowledge of the precise composition (0.1% C_6 paraffins, 0.04% C_6 aromatics, etc), was not known and therefore the approximate chemical formula of the fuel was not known.

Because the precise composition of the GTL fuel investigated in this study was unknown, the chemical formula was estimated to be the same as that of the DF-2 used in this study, as were the surrogate and vapor pressure of the fuel. Although the composition of the fuel is not known precisely, its properties were not anticipated to differ significantly

from that of DF-2 since GTL fuels are manufactured to be sufficient as drop-in replacements of the crude-derived counterparts. Although it has been shown that lubricity of GTL fuels does not match that of their crude-derived counterparts, this was not anticipated to affect the results of the ignition behavior of the fuel in a major way [134]. Such an assumption was proved correct by the subsequent ignition delay times.

Similar to the other fuels investigated in this study, ignition delay time experiments were conducted with the GTL fuel at conditions of P_5=10 atm, and ϕ=0.5 over a range of temperatures from approximately 1000 K – 1250 K. The results of the ignition delay time experiments of the GTL fuel are shown in Figure 5.4. It can be observed from the plot that the ignition delay time behavior of this GTL fuel is similar to that of the DF-2 fuel used in this study and also shows good agreement to the ignition delay time results obtained from DF-2 fuels in the experiments by Alturaifi et al. [23]. The DF-2 results of Haylett et al. are also displayed on the plot for comparison [15]. All data are corrected for pressure and equivalence ratio to P_5=10 atm and ϕ=0.5, respectively.

5.5. **Discussion**

Although all ignition-delay time data display some uncertainty which results in scatter of the plotted data, lessening the scatter can be achieved by investigating post-reflected-shock conditions in a repeatable manner, i.e. maintaining a constant P_5 and equivalence ratio, ϕ, over the range of experiments. When these two variables are varied within an experimental dataset, however, scaling relations are necessary to correct the data to common values of pressure and equivalence ratio. This adjustment is because it is

desirable to plot ignition delay times as a function of temperature, ensuring that T_5 is the only parameter that varies between experiments for a given P_5/ϕ condition. To aid in lowering the scatter of ignition delay time data, it was necessary to attempt to minimize variations in the equivalence ratio between experiments.

Prior to conducting the ignition delay time experiments for this study, the DF-2 ignition delay time data from the work of Haylett et al. [15] were observed to display significantly more scatter than their ignition delay time data for single-component fuels. Also, the DF-2 ignition data were more scattered than data obtained by other researchers for similar mixtures in heated shock tubes [23]. This increased scatter may be due to multiple factors. First, perhaps the data acquired in aerosol shock tubes display generally greater scatter than those collected in heated shock tubes. While still relatively new, the aerosol shock tube method itself being the cause of increased scatter seems unlikely because the low scatter in the ignition plots of the single-component data from Haylett et al. contradict this hypothesis and shows the ability of their Gen. II aerosol shock tube to produce data which display excellent quality and low amounts of scatter.

A more-likely reason for the higher scatter in the DF-2 ignition data compared to the single-component ignition delay times from Haylett et al. stems from the range of equivalence ratios used [15]. The equivalence ratios from the data of Haylett et al. were collected over a considerably wide range ϕ=0.2-1.4. The number of data points for a given equivalence ratio was relatively low, however: not many of the experiments they present from the DF-2 ignition-delay data are near ϕ=1.0, and those near $\phi = 0.5$ also have a

considerable spread. It is also noted in Figure 5.2b that the data of Haylett et al. were collected at ϕ=0.5 $\pm$ 0.2 and then scaled to ϕ=0.5. Thus, even though the data are scaled to a common equivalence ratio and pressure, their initial equivalence ratio spread is still $\pm$40% of the final, scaled equivalence ratio. Such scatter does not indicate that the data points themselves are poor quality, but rather that more data at equivalence ratios closer to a specifically desired value are necessary to minimize the scatter in subsequent ignition delay time plots at a specific equivalence ratio. Thus, the significant scatter observed in the Haylett et al. ignition data in DF-2 provided motivation for ensuring that all ignition data collected in this dissertation be near specific equivalence ratios as opposed to being dispersed over a wide range. More specifically, this approach was desired since the motivation for the present study was not to determine specific ignition delay time correlations.

To achieve consistent equivalence ratios in the aerosol shock tube over a wide range of temperature conditions, the nebulizer was turned on for varying amounts of time depending on the initial pressure in the AGT prior to introducing the aerosol into the shock tube. Although this method was empirical in nature, it proved effective at lessening the test-to-test variations in measured equivalence ratios.

5.5.1. Decane

When examining the ignition delay time data in decane/air mixtures collected in this facility, it is observed that the data from this study and those of Shen et al. [9] are in good agreement at higher temperatures. But when examining the comparison at lower

temperatures, the data from the present study display longer ignition times than those of Shen et al. below temperatures of approximately 1100 K. Given the $\pm$20 K uncertainty in T_5 stated by Shen et al., however, the agreement of the aerosol shock tube ignition data with those taken in the heated shock tube of Shen et al. can be considered quite good for decane-air mixtures at ϕ=1.0. Due to the smaller diameter of the tube used by Shen et al., it is possible that a greater dP/dt effect was present compared to the shock tube used herein, resulting in somewhat greater temperature changes behind the reflected shock wave and shorter ignition times at longer experiment times.

5.5.2. Direct Comparison of Heated and Aerosol Shock

The primary goal of this study on the behavior of ignition delay time properties of various fuels was to compare the known ignition delay time characteristics of fuels for which data are available in the literature to the ignition delay time behavior of the same fuels in the new aerosol shock tube. After comparing the ignition delay time results using the single-component fuel of decane with results from the literature, a more rigorous comparison was sought which would validate the overall operation of the new facility with that of a heated shock tube.

For the validation of the new aerosol shock tube facility, it was desirable to mimic the exact experimental conditions achieved in a different heated shock-tube facility to provide a direct comparison between heated facilities and the aerosol shock tube. Such direct comparison includes not only the experimental test conditions of T_5, P_5, and ϕ, but also of the fuel blend itself. Although ignition delay time data from the same class of fuel

may be investigated, the ignition delay time results may not always align due to compositional variations between batches. This variation is evidenced by the ignition delay time comparison of different batches of DF-2 in Figure 5.2b from Haylett et al. [15]. Limiting differences in ignition delay time behavior between various batches of fuel was therefore the motivation for direct comparison of the ignition delay time behavior of the new aerosol shock tube with that of a heated shock tube. This comparison is achieved by using not only identical experimental conditions for validating the new aerosol shock tube, but also identical batches of fuel. Thus, the respective DF-2 and Jet-A fuels used in the study by Alturaifi et al. were not only the same class of diesel and jet fuels as those used in this study, they were also from the same exact batches acquired from AFRL, which were provided directly from refineries [23, 77].

In addition to using the same batch of fuel for validating the new aerosol shock tube, the heated shock-tube facility of Alturaifi et al. possessed nearly identical driven section dimensions as those of the aerosol shock tube used in this study [23]. Using shock tubes of similar geometries was another aspect intended to minimize variations in ignition behavior between the two facilities, further enabling direct comparisons. Thus, the validation of the new aerosol shock tube was performed by using similar shock tubes, identical fuels, and identical experimental conditions with which a thorough comparison could be made to confirm the operability of the new facility.

As is observed in Figure 5.2 and Figure 5.3, the plots of the DF-2 and Jet-A data collected in the new aerosol shock tube from this study show excellent agreement with

that of the heated shock tube ignition data from Alturaifi et al. Such close agreement between the different facilities using identical fuels provides validation that the new shock-tube facility is able to replicate the ignition data collected from heated shock tubes. Such good agreement between the data sets also shows that the new facility is able to replicate data recorded in heated shock tubes by using the aerosol shock tube method.

An additional point of emphasis necessitates discussion in regard to the DF-2 data referenced in this study. Although the DF-2 data from Haylett et al. displayed in Figure 5.2 exhibit shorter ignition delay times at higher temperatures than the data from this study, this may not be solely due to the fact that the fuels investigated herein and by Haylett et al. come from different sources. Another source of variation between the data sets is the fact that the Haylett et al. data were collected in an aerosol carrier/buffer gas composed of 21% O_2 / 79% Ar. Such a difference in the oxidizer was not shown to cause much variation when investigating Jet fuel ignition delay times in a heated shock tube from the work of Davidson et al. [20]. Perhaps, though, the effect is more pronounced in DF-2 as opposed to Jet fuels. This point does not change the overall nature or quality of any of the data sets from this work, or references herein, but is rather introduced to point out differences which may be of interest to future researchers.

In general, the substitution of Ar for N_2 in air leads to a lengthening of the decomposition step prior to ignition, but a shortening of the oxidation step in non-dilute mixtures. Thus, it could be the case that the shortening of the oxidation step is more significant as temperature is increased in diesel fuel mixtures like DF-2 than in fuel

mixtures like the Jet fuels investigated by Davidson et al. Such a conclusion is not likely the case, however. Work from previous researchers has shown for single-component, gaseous fuels that substitution of Ar for N_2 leads to an increase in ignition delay times [135, 136]. This discrepancy in ignition behavior of the diesel fuels from this study and that of Haylett et al. warrants further investigation before any firm conclusions are drawn was not investigated further in this thesis work.

5.5.3. GTL Diesel

After validation of the new aerosol shock tube was conducted by comparing data in the new facility to those from heated shock tubes, a fuel not yet studied in aerosol shock tubes was selected for investigation. Ignition delay time data from a GTL diesel fuel produced in Qatar was collected and is displayed in Figure 5.4. In fact, to the author's knowledge, these are the first such ignition delay time data from a GTL diesel fuel recorded in a shock tube, let alone an aerosol shock tube. The results of the recorded ignition data for the GTL fuel are similar to those of the recorded data for the DF-2 from this study; that is, the GTL diesel displays similar ignition characteristics to the DF-2 diesel supplied by AFRL. Such a result is relatively unsurprising as GTL fuels are composed primarily of n-paraffin molecules. As discussed in Chapter 1, mixtures with differing amounts of n-paraffins behave similarly in regard to the kinetics of the high-temperature ignition regime because the presence of significant amounts of n-paraffins results in similar rates of production of C_1-C_4 radicals. As such, these short carbon chains generally control the combustion behavior of hydrocarbons in the high-temperature

ignition regime due to their influence on the buildup of radical pool with species such as OH* and CH* during the pre-ignition reaction process.

5.5.4. Evaporation and Uniformity Validation by Ignition Delay Time Data

Although much of the discussion on the various validation aspects of the new aerosol shock tube methods was presented in Chapters 3 and 4, respectively, the final discussion of the overall validation of the facility is given here. This discussion has been left until now because the primary metric for determining the reliability of the aerosol generation and introduction apparatus is the quality of the corresponding ignition delay time data and comparisons made thereof to ignition data collected in other facilities. Thus, a presentation of all ignition delay time data, which demonstrate the ability of the facility to acquire reliable data, was necessary prior to discussing the overall validation of the new aerosol introduction methods developed for this shock tube.

5.5.4.1. Facility Validation by Ignition Delay Time Comparison

From the work characterizing the new aerosol shock tube conducted for this study, the capability of the new aerosol shock tube facility to generate homogeneous aerosols and subsequent homogenous, gas-phase mixtures behind reflected shock waves has been demonstrated. This conclusion is borne out in part by the validation of the fuel evaporation and absorption diagnostic discussed in Chapter 4. From that analysis, it was shown that the evaporated fuel behind the incident shock wave was axially uniform within 2-5% over the duration of the measurement. More importantly, the aerosol loading diagnostic discussed in Chapter 3 for the mock version of the aerosol test section was shown to

produce high levels of aerosol loading uniformity along the axis of the aerosol test section with nonuniformities ranging from 3-8%. This aerosol loading uniformity diagnostic further validated the homogeneity of the pre-shocked aerosol. Most importantly, however, the results of ignition delay time experiments presented herein are the truest indicator of whether or not the aerosol generation and entrainment method is adequate for producing homogenous fuel-oxidizer mixtures behind reflected shock waves when investigating liquid fuel ignition behavior.

Upon examination of all ignition delay time data collected using the new aerosol shock tube facility, it can be concluded that the aerosol and entrainment method developed for this facility is able to reliably produce a homogenous aerosol in the driven section of the shock tube. Additionally, the ignition delay times presented herein also validate the resultant homogeneity of the post-reflected shock region by comparing ignition delay time data collected in this new facility to those of both heated shock tubes and another rigorously validated aerosol shock tube facility. In particular, the excellent agreement in ignition delay time behavior between this facility and a heated shock-tube facility using identical fuel blends confirms that the aerosol generation and entrainment method developed in this work is capable of producing aerosols of adequate homogeneity for studying the ignition behavior of heavy hydrocarbon fuel components and mixtures. Although the Region 5 conditions in the shock tube have been shown to be sufficiently uniform as evidenced by ignition delay time results, among others, a final point of

discussion regarding the nature of the aerosol filling process and resultant loading uniformity is necessary.

5.5.4.2. Aerosol Contact Surface

As mentioned previously, the gas-phase fuel absorption measurement of liquid droplets can be used to serve as a rudimentary method for measuring the aerosol loading uniformity within the aerosol test section of the shock tube prior to the experiment (and the subsequent gas-phase homogeneity after evaporation and diffusion of the droplets). Although the Mie scattering diagnostic discussed in Chapter 3 is more appropriate to estimate relative uniformity of the pre-shocked aerosol, the gas-phase absorption method provides some qualitative confirmation of the uniformity. From the post-incident shock time histories displayed in Figure 4.11, it can be seen that the gas displays relatively good uniformity after evaporation over the time span which the concentration measurement is performed. However, it is also shown in the traces that the aerosol contact surface arrives at the measurement location (5.5 cm upstream of the endwall) around the same time as the arrival of the reflected shock wave. The arrival time of the aerosol contact surface at the measurement station coinciding with that of the reflected shock wave is merely a coincidence and is of little interest, but the arrival of the aerosol contact surface itself is a significant event and merits further analysis.

The arrival of the aerosol contact surface at the fuel absorption measurement station indicates that the interface between the aerosol and the buffer gas has been moved from its starting position to a position nearer to the driven section endwall (as does all

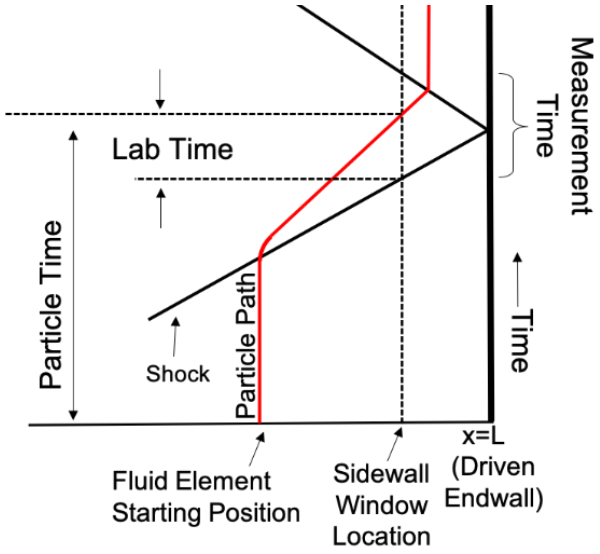

Figure 5.5 x-t diagram of the time experienced by a fluid element at an arbitrary location upstream from a sidewall measurement station compared to the time

gas/aerosol through which the shock wave passes). This shift downstream is significant because the approximate position of this contact surface can be measured by calculating the time that the fluid element spends behind the incident shock wave and the time between the passage of the incident shock wave and the arrival of the fluid element at the measurement station. That is, the amount of time that a fluid element, when observed from a sidewall measurement station, has spent in Region 2 behind the incident shock wave is greater than the time between passage of the incident shock and the arrival of the element at the measurement location. This concept is referred to in the present discussion as fluid time (or particle time) versus lab time.

Consider the simplified x-t diagram in Figure 5.5 which illustrates the concept of particle time versus lab time. The shock wave passes over the fluid particle at some time

prior to its arrival at the measurement station. The shock wave then arrives at the measurement station, followed by the arrival of the fluid element. This time difference is the lab time as experienced by observing the events within the shock tube at the sidewall measurement station. Using the known properties of the gases in Region 1 and Region 2 (which are calculated as outputs from FROSH or AEROFROSH), the duration of the particle time can be derived and calculated from Eq. (5.1), where FT is fluid time, LT is lab time, and ρ_1 and ρ_2 are the gas densities in Region 1 and Region 2, respectively.

$$FT = \frac{\rho_2}{\rho_1} LT \tag{5.1}$$

If we consider the lab time with respect to the arrival of the aerosol contact surface, we can then use the calculated fluid time, FT=Δt, to calculate the distance traveled by the aerosol contact surface after its interaction with the incident shock, Δx. Using the post-incident gas velocity (also from FROSH/AEROFROSH) with the fluid time and the definition of velocity, this gives $\Delta x = v\,\Delta t$. Thus, the original starting location of the aerosol contact surface at a distance Δx upstream of the measurement station can be calculated. For the conditions produced by shock waves in this study and considering the location of the measurement station in the shock tube (5.5 cm upstream from the endwall), the aerosol contact surface should likely not reach the measurement station prior to arrival of the incident shock wave. However, as observed from Figure 4.11, this is not the case, which indicates that the aerosol contact surface does not begin at the gate valve as expected. To be more specific, two distinct regions with differing aerosol loadings are present in the aerosol test section at the end of the aerosol filling process.

When considering the analysis in the previous paragraphs, the density ratio, ρ_2/ρ_1, across the incident shock wave for the experiment in Figure 4.11b was calculated as approximately 4.16. Using this density ratio and the lab time of roughly 230 μs from the arrival of the incident shock to the arrival of the aerosol contact surface, the initial starting location of the aerosol contact surface is estimated at approximately 72 cm upstream of the driven section endwall. The length of the aerosol test section is approximately 130 cm, nearly twice that of the aerosol contact surface distance from the endwall as calculated for this example. What then is the conclusion from this brief analysis? The conclusion is that the aerosol injection process does not fill the entirety of the aerosol test section with a uniform aerosol but instead fills the shock tube with an aerosol displaying more of a stratified loading along the tube axis. If the aerosol were uniform along the entire shock tube axis, then no aerosol contact surface would be observed at the measurement location.

Although the aerosol loading has been shown not to be uniform along the entire axis of the aerosol test section, it should be re-emphasized that the aerosol is believed to be sufficiently uniform in the region nearest the endwall for two reasons. First, the diagnostics developed for this work indicate that the aerosol is uniform prior to arrival of the aerosol contact surface at the sidewall measurement location (Mie scattering from Chapter 3 and concentration measurement from Chapter 4). Second, as discussed in section 5.5.4.1, the ignition delay time results obtained in this dissertation agree well with those of identical conditions investigated in the literature. More specifically, data collected using identical fuels and shock tubes with similar driven-section geometries yielded

ignition delay times which display excellent agreement between the new aerosol shock tube and a heated shock tube with DF-2 and Jet-A fuels.

A couple of final points of emphasis should also be made regarding the suitability of the current aerosol introduction method for generating uniform aerosols in shock tubes. First, from the diagram of the aerosol filling scheme in Figure 3.22 it can be seen that a finite volume exists between the aerosol injector and the endwall of the driven section. It may be suspected that since the final design of the aerosol injector is one that directs the aerosol from the endwall and toward the gate valve that the region between the injector and the endwall is not sufficiently filled with aerosol. This is not the case and it was shown with Mie scattering detectors placed on either side of the injector (upstream and downstream) that the region between the endwall and injector display nearly identical loadings during the filling process. Second, some discrepancy exists between the Mie scattering concentration diagnostic in Chapter 3 and the fuel concentration diagnostic in Chapter 4.

When considering the discrepancy between the Mie scattering diagnostic presented in Chapter 3 and the fuel concentration diagnostic presented in Chapter 4, the nature of the jet flow from the injector was likely the cause of disagreement between the two diagnostics. It was observed by visual inspection during the aerosol filling experiments in the mock aerosol test section that the jet from the injector dissipated roughly halfway between the injector inlet and the outlet near the gate valve, or 60-70 cm from the shock-tube endwall. This jet dissipation was likely the main reason for the lack

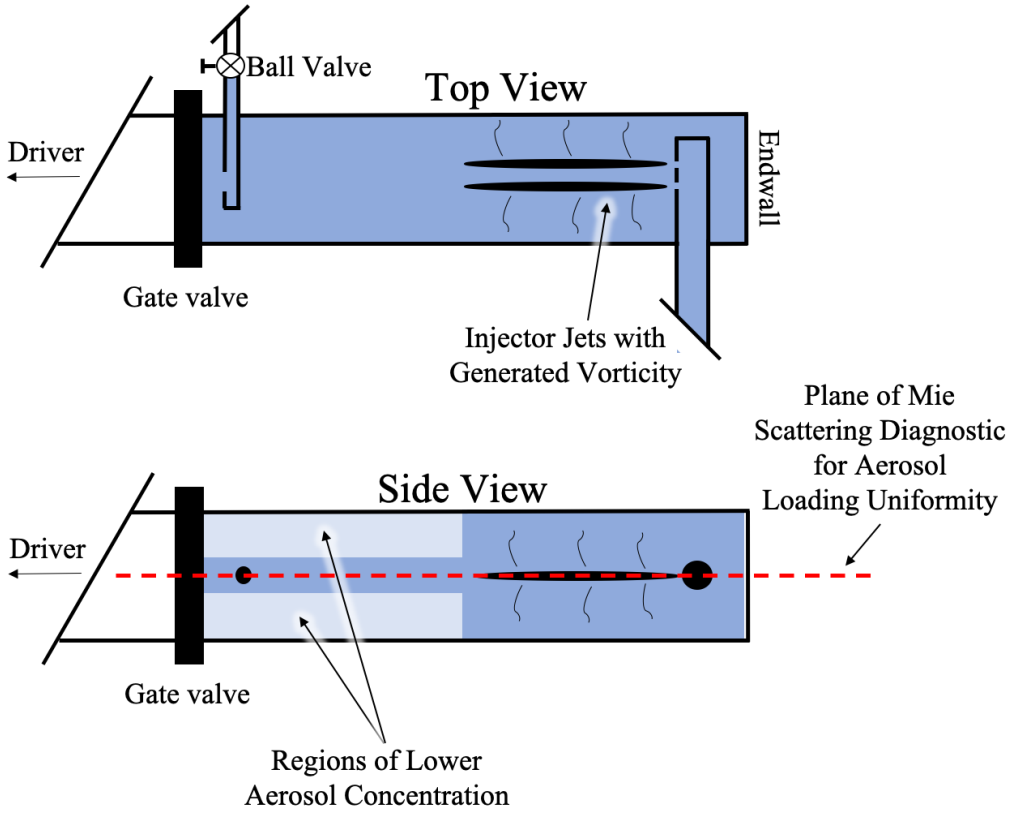

Figure 5.6 Illustration of sources of discrepancy between Mie scattering uniformity diagnostic and fuel concentration diagnostic. The jet causes induced vorticity which disperses the aerosol. Once the jet is attenuated, however, the flow is slower and less likely to have regions of high vorticity where mixing happens.

of aerosol in the half of the aerosol test section furthest upstream of the aerosol injector as observed by arrival of the aerosol contact surface at the fuel absorption diagnostic sidewall measurement station. Aerosol still travels toward the flow outlet near the gate valve, but most of it is believed to be dispersed in the half of the test section nearest to the injector. This concept is illustrated in Figure 5.6. After the jet is dissipated in the plane of the injector (also the measurement plane for the Mie scattering loading uniformity diagnostic),

the aerosol is thought to remain concentrated around the central axis of the shock tube. This central concentration is believed to be the reason why the Mie scattering uniformity diagnostic showed uniform concentration along the entire length of the aerosol test section axis. Additionally, it should be noted that the gaseous absorption diagnostic for measuring the fuel concentration is performed using a vertical beam through the top/bottom of the shock tube, which is why the supposed planar uniformity in the horizontal plane was not observed.

To conclude discussion on the validity of the aerosol filling method, it is seen from the analysis presented in this chapter and previous chapters that the aerosol loading is adequate for ignition delay time experiments in real fuels but may only produce a uniform aerosol in the half of the aerosol test section nearest to the endwall. This region is believed to be sufficiently uniform for generating a homogenous mixture of fuel and oxidizer in Region 5 of a shock-tube experiment, however, because the ignition event occurs nearest the endwall in the region of greatest aerosol uniformity. Also, the ignition data collected in this study show excellent agreement to those collected in other shock-tube facilities. Additionally, the discrepancies observed in the aerosol loading uniformity from various diagnostics provide avenues for further study, but the aerosol generation and entrainment method discussed in this work should still be considered adequate for generating homogenous aerosols required for shock-tube ignition delay time experiments. Although the facility is now fully validated and characterized, opportunities for developing the

facility further are possible and warrant added discussion. These suggestions and future work are discussed in the following chapter.

5.5.5. Estimation of Experimental Temperature Uncertainty

As a final point of validation, the experimental uncertainty of the shock-tube facility requires attention. For any shock-tube experiment, the largest source of uncertainty when calculating post-reflected-shock temperatures is the uncertainty of the incident-shock velocity extrapolation at the endwall. The shock velocity extrapolation commonly yields an uncertainty below 1%. Thus, using 1% as the shock velocity uncertainty is a conservative over-estimate, but it is used here to establish upper limits of T_5 uncertainty. Such treatment is particularly necessary in this case because the extrapolated shock wave velocity at the endwall has greater uncertainty than typically observed due to the lack of buffer-gas tailoring. That is, the shock wave shows a change in velocity decay behavior as it passes through the gate valve into the aerosol, making the linear velocity decay fit less accurate than those from either gaseous shock-tube experiments or aerosol experiments with a tailored buffer gas.

Using the experiment from Figure 4.13b as an example, a brief analysis of experimental uncertainty for the shock-tube facility using various variables from the inputs to the AEROFROSH program yielded an estimated experimental uncertainty in T_5 of $\delta_{T_5} \approx 16.5$ K. Upon further examination, it was seen that the extrapolated shock velocity uncertainty dominated the T_5 uncertainty when assuming a 1% uncertainty in shock velocity; this yielded a 15-K uncertainty in T_5 as a conservative over-estimate.

Furthermore, although the most critical variables were considered in the analysis, not all variables were considered (such as those in the analysis by Campbell et al. [123]), so a conservative over-estimate of δ_{T_5} can be considered as roughly 18-20 K. Were the extrapolated shock velocity uncertainty lower, within 0.5%, for example, then the uncertainty in the contribution to T_5 from the shock velocity would be roughly 8K, reducing the overall uncertainty by a factor of approximately 2. Consequently, this underscores the need for accurate measurement of the incident shock wave velocity.

6. CONCLUSIONS

The design and construction of a new aerosol shock tube facility has been presented in detail. Along with aspects of the facility design and construction, validation data for the new facility regarding its operational capabilities have also been presented to demonstrate the readiness of the new aerosol shock tube facility. Additionally, ignition data from liquid fuels have been collected to characterize the facility and may now be considered, along with other such data of this nature in the literature, as a benchmark to which chemical kinetics mechanisms may be compared to and tuned. Although the work presented herein is thorough and complete as a standalone study, additional work is needed to further both the development of this facility and the understanding of the kinetic behavior of long-chain hydrocarbons.

6.1. **Traditional and Aerosol Shock Tube Methods**

After design and construction of the new aerosol shock tube, various characterizations of the operational aspects of the facility were performed. Aspects considered as brick-and-mortar operations of a shock tube were first characterized. The incident-shock velocity decay behavior in gaseous experiments was characterized and behaved like that observed in the facilities in the College Station labs of the Petersen Research Group. Non-ideal behaviors due to boundary-layer growth were also observed and found to be within acceptable limits relative to those displayed by other facilities when using tailored driver gases. Next, the gaseous ignition delay times of a lean mixture of methane in air were measured and the results agreed with those from the literature and

kinetic mechanisms. An additional behavior of the new facility was examined in relation to gas-dynamic behavior. The presence of the U-bend geometry of the driver section tubing was not shown to affect the global behavior of pressure time histories in any major way.

Moving on from the gaseous behavior of the shock-tube facility, the aerosol generation and entrainment method was characterized. Knowing that small tube diameters and bends in tubing between the aerosol generation tank (AGT) and the aerosol test section of the shock tube would limit the throughput of aerosol mass, the transport mechanism from the AGT to the shock tube was designed to minimize losses. With an aerosol injection mechanism that formed a jet in the aerosol test section, the aerosol filling process was characterized and found to produce good uniformity within the aerosol test section from a Mie scattering diagnostic.

With the aerosol loading method characterized, the operational aspects of the shock tube in regards to aerosol experiments were characterized. Velocity decay behavior of the incident shock wave was shown to behave differently than in gaseous shock waves due to the lack of a tailored buffer gas upstream of the gate valve. This lack of a buffer gas added some uncertainty to the calculation of T_5, but not too great an amount to prevent collection of meaningful data. Another effect of an untailored buffer gas was the interaction of the reflected shock wave with the contact surface between the aerosol and the buffer gas. This interaction produced small compression waves as shown in endwall pressure time histories. These pressure waves were not overly significant, however.

Additionally, the interaction of the incident shock wave with the aerosol interface at the gate valve was not shown to produce any significant global effect on pressure time histories. Finally, the aerosol evaporation and fuel concentration diagnostic was characterized and showed that the post-incident shock conditions are able to evaporate and disperse the fuel in a sufficient amount of time so as to result in reliable measurements of fuel concentration behind the incident shock wave.

6.2. **Ignition Delay Time Results**

Upon completion of the validation of all operational aspects of the new aerosol shock tube facility, ignition delay time data were recorded using mixtures of heavy-hydrocarbon fuels of decane, Jet-A, DF-2, and GTL diesel in synthetic air. The results of the ignition delay time experiments showed good agreement with those of similar data recorded in the literature. Furthermore, ignition delay time data from two of the fuels, Jet-A and DF-2, were compared directly to a heated shock-tube facility in College Station. This series was a direct comparison of not only the experimental conditions, but also of the fuel blends themselves. The excellent agreement between the two facilities using the same fuel blend validates the ability of the new aerosol shock tube facility for collecting ignition delay time data from mixtures of heavy hydrocarbon fuels.

Lastly, some discrepancy was ultimately observed by the arrival of the aerosol contact surface at the fuel absorption measurement location. This discrepancy was observed between the aerosol loading uniformity diagnostic and the fuel absorption diagnostic. While these differences were non-trivial, they are not believed to affect the

overall performance and operation of the new facility. That is, the somewhat stratified nature of the aerosol loading along the test section axis still resulted in homogenous mixtures behind the reflected shock wave in the region nearest to the endwall, thereby allowing for the collection of quality ignition delay times as evidenced by the agreement of the ignition data collected herein when compared to those found in the literature.

6.3. **Future Work**

A new aerosol shock tube facility for the study of long-chain hydrocarbons (and mixtures thereof) has been fully characterized. Furthermore, experimental ignition delay time data from the new facility have been recorded are display good agreement to those found in the literature. Although this work for this dissertation is complete, further work in regard to the development of the facility is suggested. Various aspects of the facility could benefit from refinement. First, the particular aerosol filling process used herein is a novel technique for aerosol introduction, and has not been used previously by other researchers for such experiments. Similar to the progression between the Gen. I and Gen. II aerosol shock tube facilities by Davidson et al. [34] and Haylett et al. [35], respectively, the current facility would benefit from further design iterations. In addition to design iterations, various operational improvements to the process of aerosol shock tube experimentation can be implemented to improve the nature of nonidealities present during an experiment. The modifications to the facility's driver-tube geometry in comparison to those of shock tubes in the College Station laboratory of the Petersen Research Group also

provide additional opportunities for investigation of variation of shock-tube nonidealities with differing facility geometries.

6.3.1. Aerosol Uniformity Measurement

When considering further design iterations on the aerosol generation and entrainment techniques used in the new aerosol shock tube facility, attention must first be given to the diagnostics used in determining the aerosol loading uniformity within the test section itself. Although the diagnostic used in the present work proved useful for determining aerosol loading uniformity (as proved by the ignition delay time data), further refinement is necessary due to disagreement between the Mie scattering diagnostic in Chapter 3 and the fuel absorption diagnostic in Chapter 4. This disagreement showed that an additional aerosol contact surface, an interface between regions of differing aerosol droplet loading, was present within the aerosol test section prior to the propagation of the incident shock wave through the aerosol test section. Thus, it was shown that the aerosol loading uniformity diagnostic was unable to capture the true nature of the aerosol loading within the aerosol test section. Furthermore, even though the Mie scattering diagnostic from Chapter 3 proved adequate for the work of Haylett et al. in their Gen. II aerosol shock tube design [35], it was not fully sufficient for the particular aerosol introduction design discussed herein. This difference is because the introduction method of Haylett et al. used a plug flow, whereas the flow in the current facility's aerosol introduction method was highly vortical and non-uniform. Thus, the current Mie scattering diagnostic used for measuring aerosol loading uniformity, while sufficient for determining aerosol loading

uniformity resultant from a plug flow, was shown not to capture all facets of the spatial loading uniformity from the aerosol introduction method used in this thesis.

6.3.2. Aerosol Introduction Scheme

In addition to improvement of the aerosol uniformity diagnostics, the method of aerosol introduction in the present facility can be improved as well. Of course, several aspects of the introduction process are viable candidates for redesign of the aerosol test introduction method.

6.3.2.1. Short-term Facility Modifications

With the goal of any design modifications being to improve aerosol loading uniformity from that in the current facility, simple modifications to the current design of the facility offer the most effective avenues for providing near-term improvements in the aerosol loading uniformity without the need for a complex redesign process. These suggestions for modification are relatively straightforward and provide cost-effective avenues of pursuit compared to more-rigorous redesign processes. Also, these methods of facility modification are relatively inexpensive as they can be performed in large part with much of existing laboratory hardware present in the aerosol shock tube laboratory at Texas A&M Qatar.

The simplest avenue for potential improvement of aerosol loading uniformity in the shock tube is to increase the speed of the flow from the injector tube jet. This would cause the jet to be longer and protrude further into the aerosol test section, causing more swirling fluid further down the length test section than within just half of the aerosol test

section nearest the endwall. Faster inlet jet velocities could be achieved by increasing the size of the outlet tubing between the aerosol test section and the dump tanks. This is because the flow area in the present system is smallest at the outlet in the aerosol test section. That is, the ½" tubing between the aerosol test section and dump tank represents the smallest area through which the flow passes during the filling process and thus the flow itself is choked at the aerosol test section outlet point during the filling process. Thus, were a larger-diameter tubing utilized (such as ¾" OD tubing), the maximum flow rate in the outlet tubing would be greater (although the maximum velocity in the outlet tubing would remain constant at the choked velocity) and the jet at the injector inlet would produce a longer region with high vorticity and stirring action along the length of the aerosol test section.

Another design modification aimed at improving aerosol loading uniformity would be to enlarge the dump tank volume. This would allow for a longer filling time and greater flow rates in the aerosol test section outlet tubing due to larger differences in initial dump tank and aerosol generation tank pressures, respectively. Increased flow rates within the system would result in an increase in velocity and a larger jet at the aerosol injector inlet within the aerosol test section. With a longer time for aerosol filling and a longer jet due to increased flow velocities, the increased duration of the flow would provide the opportunity for more of the aerosol to be directed down the length of the aerosol test section.

A further design modification of the current facility relates to the overall length of the aerosol test section itself. Given that the aerosol loading uniformity in the aerosol test section has been shown to be adequate (due to ignition data agreeing well with literature data) and also that only roughly ½ to ¾ of the current length of the test section is filled with a homogenous aerosol, there seems to be no need to have an aerosol test section with a length of 1.2-1.3 m. Furthermore, the length of the aerosol test section in this work was modeled after that of Haylett et al. [35] who chose a test section length of approximately 1.2 m, but never provided a reasoning for this length. Presumably, this length was chosen to ensure that the aerosol contact surface, which is actually not a step change but rather a region where buffer gas and aerosol mix during the actuation of the gate valve, was a sufficient distance away from the endwall of the driven section after passage of the reflected shock wave. Should the aerosol test section of this facility be shortened, the overall length of the aerosol test section could be decreased by 40-50 cm from its current 1.3-m length.

Decreasing the length of the aerosol test section would first require a re-characterization of the loading uniformity in a shortened, mock aerosol test section. It is unlikely that there would be much difference in the flow behavior, however, other than that the jet from the aerosol injector would protrude down most of the length of the shortened aerosol test section. This protrusion would likely result in improved loading uniformity within the entirety of the aerosol test section compared to the current geometry. Additionally, since the shortened aerosol test section would require further

characterization, the mock section used for previous characterizations could be shortened and reused prior to purchasing and machining a new length of driven-section tubing for the shock tube itself, thereby saving unneeded expenses should the shortened test section design prove ineffective.

6.3.2.2. Design Aided by Computational Fluid Dynamics (CFD)

An additional avenue available for further improvement of the aerosol shock tube facility is that of computational fluid dynamics. CFD would be especially useful in the design process for a new and/or improved aerosol injection method. New geometries could be conceptualized, modeled, and examined using computer-aided modeling. These computer-generated geometries could then be run in a parallel manner using CFD codes such that several differing geometries could be investigated simultaneously (tens or hundreds if done correctly). Such an approach could greatly reduce the time necessary for completing the design and validation processes by using knowledge of the flow properties within the system and automating the iterative process of experimentally examining different injector geometries.

The particular aspects where CFD could be utilized most critically when improving the aerosol shock tube design are related to the design of the injector head geometry itself. Not only could CFD aid in the design of the positioning of the injector and the nature of the flow within the aerosol test section as it exits the injector, CFD could also aid in understanding the flow pattern within the injector tubing. Furthermore, employing CFD would elucidate the nature of how the aerosol droplets exit the injector

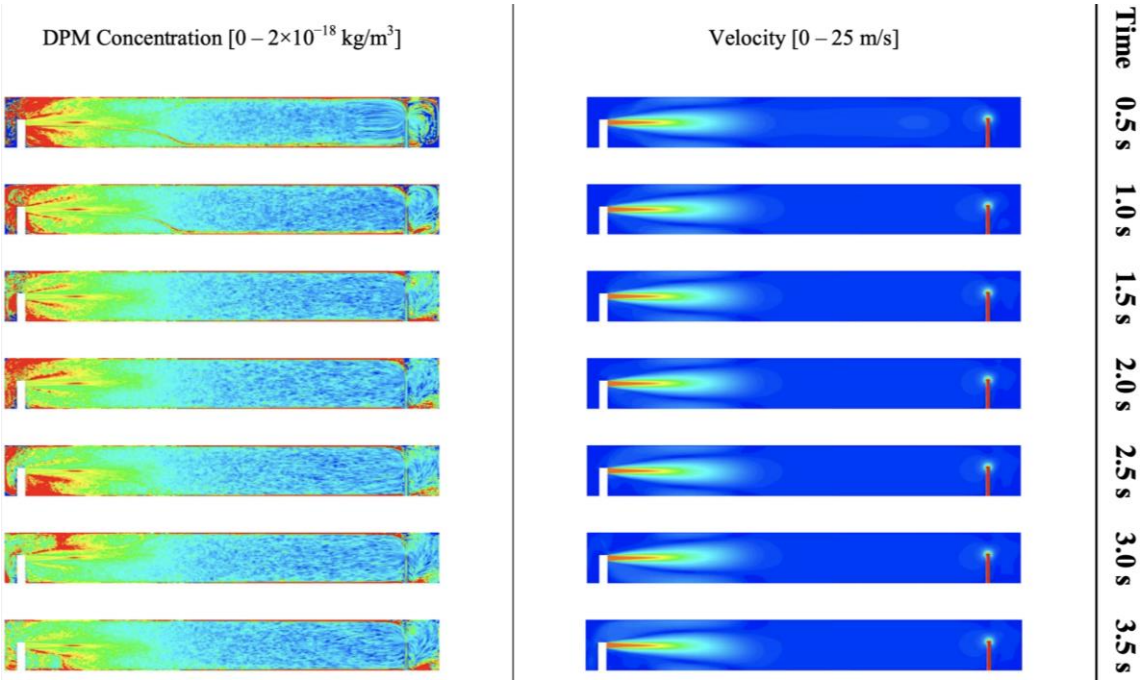

Figure 6.1 Results of CFD simulations of the aerosol injection process in the aerosol test section. The total duration of the simulation is 3.5 s with steps of 0.5 s between each picture (simulation time steps are 0.01s). The top set of pictures displays velocity contours, and the bottom set of figures displays droplet mass concentration, each from a central horizontal slice coincident with the central axis of the shock tube. The injector geometry used is similar to that of the final design of the final aerosol injector geometry used in this study.

and if any areas of improvement are possible to minimize droplet losses. This new opportunity is because the design of the aerosol injector itself was performed primarily on a qualitative and empirical basis, without the more rigorous numerical analysis techniques afforded by CFD. The analysis provided by CFD could display regions of high Stokes number within the flow and inform the design process for minimizing droplet loss.

Prior to finalizing the initial aerosol introduction design process, some preliminary CFD studies were conducted for this work with the assistance of Dr. Way Lee Cheng. Although the flow conditions used in the analysis were not accurate compared to the actual flow conditions within the final design, the CFD can be seen to provide good insight into areas where aerosol is concentrated. Sample results from the calculations are provided in Figure 6.1. These results, while not conclusive, display similar behavior to that previously observed in the aerosol test section of the shock tube. That is, the jet from the injector protruded into the aerosol test section, generating significant vorticity and dispersing the aerosol droplets in a uniform manner. Additionally, however, the aerosol is seen to be primarily concentrated in the region of the shock tube nearest the injector where the jet was shown to influence the flow most significantly.

6.3.3. Nonidealities

Various nonidealities in the new shock-tube facility are present, as they are in all shock-tube facilities. While the understanding of some of the phenomena would be aided by further study, they can all be minimized or altogether eliminated. Non-ideal pressure rise, or dP*/dt, effects due to the boundary-layer growth behind the incident shock wave, can be mitigated with careful construction of driver inserts. Additionally, the dP*/dt of the facility can also be decreased (but not eliminated) by using Ar as a substitute for N_2 in mixtures simulating air. Another boundary-layer effect caused by the presence of N_2 is post-reflected-shock bifurcation. Using Ar instead of N_2 would likely not eliminate this phenomenon, but such a substitution would greatly decrease its effect.

In addition to mitigating non-ideal effects due to boundary layers behind the incident shock wave, global gas-dynamic effects can also be mitigated. In the present study, driver-gas tailoring was not prioritized to ensure precise tailoring of the driver gas/buffer gas contact surface (although it was still used in a less-exact sense). Tailoring of this interface with appropriate driver gas mixtures could completely eliminate reflected pressure/expansion waves due to the driver/buffer gas interface from traveling toward the driven section endwall and limiting experimental test times.

Another tailoring that can be performed is that of the aerosol/buffer gas interface. In this work, such tailoring was not performed. Were it implemented correctly, buffer-gas tailoring would eliminate two nonidealities: interaction of the reflected shock wave with the buffer/aerosol contact surface and subsequent reflection of compression/expansion waves, and non-ideal shock velocity decay behavior as the incident shock wave passes through the gate valve into the aerosol.

An additional aspect of experimental nonidealities is present in this facility compared to that of the facilities in the College Station laboratory of the Petersen Research Group. The difference in driver-tube geometries in this facility and that of the High-Pressure Shock Tube (HPST) in the College Station laboratory can be investigated for furthering the understanding of boundary-layer growth behavior in shock tubes and its contribution to experimental dP*/dt. First, the enlarged diaphragms and associated mechanics of the breaking action during shock initiation may be a source of increased boundary layer growth compared to the smaller diaphragms used in the HPST facility in

College Station. Additionally, the U-bend in the driver tube may contribute to increased boundary-layer growth nonidealities. Although the U-bend does not appear to introduce a major pressure event within the driven section over the course of an experiment, it likely produces additional perturbations in the flow which present themselves as increased contributions to the overall dP*/dt of the shock tube.

Upon re-examination of Figure 4.8, it can be seen that the dP*/dt behavior of the facility is more than double that expected for driven mixtures of Argon and driver mixtures of Helium. The non-ideal pressure rise from Figure 4.8 is in the range of 7-8%/ms, whereas the results from the HPST in the College Station laboratory with nearly-identical driven section geometries (but different driver geometries) has been shown to be on the order of 2-3%/ms at the same Mach number conditions [126, 137]. However, at present it is unknown whether or not the U-bend portion of the driver section is the primary factor in this increased dP*/dt behavior compared to that of the HPST or whether the larger tube diameter is the primary culprit, or there is some other reason to be determined later.

6.3.4. Negative Temperature Coefficient (NTC) and Low-Temperature Ignition Chemistry

For all of the discussions given on improving the aforementioned nonideal behaviors of the new aerosol shock tube facility in the preceding sections, these discussions would lack some degree of significance if they were not put into the context of one of the primary motivations for constructing this facility: obtaining long, constant-pressure test times. The driver-section design of this facility is configurable up to lengths

of over 6.5 m to provide experimenters with the flexibility to increase test times, should they desire to do so, up to and beyond 50 ms. Also, the driver diameter has been enlarged for increasing test times as well. Furthermore, all the efforts aimed at mitigating nonidealities are primarily focused on this end goal.

An additional aspect related to long test times is improved operational control of the facility. In this study, the double-diaphragm chamber of the diaphragm breech canister was not used. For more precise control of T_5 and P_5 conditions, the double-diaphragm chamber is an essential tool available to experimenters. This feature will allow not only precise control of the thermodynamic conditions (making driver-gas tailoring less of an empirical guess-and-check process), but also enable much greater precision of when the diaphragm is ruptured. At present, the diaphragm is pressurized until it ruptures; a process controllable within $\pm$1-2 seconds. With the double-diaphragm operation enabled, diaphragms can be ruptured on-demand within tenths of a second, providing experimenters with significantly greater control of the experimental timing and condition repeatability.

The reason longer test times and improved operational control of the facility are necessary is to enable the study of both the negative temperature coefficient (NCT) and low-temperature ignition chemistry regions of various fuels, respectively. These ignition regions occur at lower temperatures, where ignition delay times can be on the order of several tens of milliseconds, necessitating the shock tube be capable of achieving long test times. For more information on NTC and low-temperature ignition chemistry, the reader

is referred to the discussion from Chapter 1 and references therein. Once the various suggestions for future work outlined in the preceding sections are implemented, the facility will be fully capable of achieving the long test times required to investigate the NTC and low-temperature ignition regions of various long-chain hydrocarbons and mixtures thereof.

REFERENCES

[1] E.I. Administration, Monthly Energy Review: December 2019, United States Energy Information Administration, 2019.

[2] K. Epping, S. Aceves, R. Bechtold, J.E. Dec. 2002 Published. The Potential of HCCI Combustion for High Efficiency and Low Emissions. 2002;

[3] A. de Klerk, Fischer–Tropsch Process, Kirk-Othmer Encyclopedia of Chemical Technology, pp. 1-20.

[4] P.J. Boogaard, J.C. Carrillo, L.G. Roberts, G.F. Whale, Toxicological and ecotoxicological properties of gas-to-liquid (GTL) products. 1. Mammalian toxicology, Critical Reviews in Toxicology 47 (2017) 121-144.

[5] O. Herbinet, W.J. Pitz, C.K. Westbrook, Detailed chemical kinetic oxidation mechanism for a biodiesel surrogate, Combustion and Flame 154 (2008) 507-528.

[6] Y. Pei, M. Mehl, W. Liu, T. Lu, W.J. Pitz, S. Som. 2014 Published. A Multi-Component Blend as a Diesel Fuel Surrogate for Compression Ignition Engine Applications. ASME 2014 Internal Combustion Engine Division Fall Technical Conference; 2014;

[7] A.J. Dean, O.G. Penyazkov, K.L. Sevruk, B. Varatharajan, Autoignition of surrogate fuels at elevated temperatures and pressures, Proceedings of the Combustion Institute 31 (2007) 2481-2488.

[8] D.C. Horning, D.F. Davidson, R.K. Hanson, Study of the High-Temperature Autoignition of n-Alkane/O/Ar Mixtures, Journal of Propulsion and Power 18 (2002) 363-371.

[9] H.-P.S. Shen, J. Steinberg, J. Vanderover, M.A. Oehlschlaeger, A Shock Tube Study of the Ignition of n-Heptane, n-Decane, n-Dodecane, and n-Tetradecane at Elevated Pressures, Energy & Fuels 23 (2009) 2482-2489.

[10] D.F. Davidson, S.C. Ranganath, K.Y. Lam, M. Liaw, Z. Hong, R.K. Hanson, Ignition Delay Time Measurements of Normal Alkanes and Simple Oxygenates, Journal of Propulsion and Power 26 (2010) 280-287.

[11] B. Rotavera, E.L. Petersen, Model predictions of higher-order normal alkane ignition from dilute shock-tube experiments, Shock Waves 23 (2013) 345-359.

[12] G. Flora, J. Balagurunathan, S. Saxena, J.P. Cain, M.S.P. Kahandawala, M.J. DeWitt, S.S. Sidhu, E. Corporan, Chemical ignition delay of candidate drop-in replacement jet fuels under fuel-lean conditions: A shock tube study, Fuel 209 (2017) 457-472.

[13] S.S. Vasu, D.F. Davidson, R.K. Hanson, Jet fuel ignition delay times: Shock tube experiments over wide conditions and surrogate model predictions, Combustion and Flame 152 (2008) 125-143.

[14] H. Wang, M.A. Oehlschlaeger, Autoignition studies of conventional and Fischer–Tropsch jet fuels, Fuel 98 (2012) 249-258.

[15] D.R. Haylett, D.F. Davidson, R.K. Hanson, Ignition delay times of low-vapor-pressure fuels measured using an aerosol shock tube, Combustion and Flame 159 (2012) 552-561.

[16] S. Gowdagiri, W. Wang, M.A. Oehlschlaeger, A shock tube ignition delay study of conventional diesel fuel and hydroprocessed renewable diesel fuel from algal oil, Fuel 128 (2014) 21-29.

[17] V.P. Zhukov, V.A. Sechenov, A.Y. Starikovskiy, Autoignition of kerosene (Jet-A)/air mixtures behind reflected shock waves, Fuel 126 (2014) 169-176.

[18] C. Zhang, B. Li, F. Rao, P. Li, X. Li, A shock tube study of the autoignition characteristics of RP-3 jet fuel, Proceedings of the Combustion Institute 35 (2015) 3151-3158.

[19] Y. Zhu, S. Li, D.F. Davidson, R.K. Hanson, Ignition delay times of conventional and alternative fuels behind reflected shock waves, Proceedings of the Combustion Institute 35 (2015) 241-248.

[20] D.F. Davidson, Y. Zhu, J. Shao, R.K. Hanson, Ignition delay time correlations for distillate fuels, Fuel 187 (2017) 26-32.

[21] A.R. De Toni, M. Werler, R.M. Hartmann, L.R. Cancino, R. Schießl, M. Fikri, C. Schulz, A.A.M. Oliveira, E.J. Oliveira, M.I. Rocha, Ignition delay times of Jet A-1 fuel:

Measurements in a high-pressure shock tube and a rapid compression machine, Proceedings of the Combustion Institute 36 (2017) 3695-3703.

[22] S. Burden, A. Tekawade, M.A. Oehlschlaeger, Ignition delay times for jet and diesel fuels: Constant volume spray and gas-phase shock tube measurements, Fuel 219 (2018) 312-319.

[23] S.A. Alturaifi, R.L. Rebagay, O. Mathieu, B. Guo, E.L. Petersen, A Shock-Tube Autoignition Study of Jet, Rocket, and Diesel Fuels, Energy & Fuels 33 (2019) 2516-2525.

[24] Y. Mao, L. Yu, Z. Wu, W. Tao, S. Wang, C. Ruan, L. Zhu, X. Lu, Experimental and kinetic modeling study of ignition characteristics of RP-3 kerosene over low-to-high temperature ranges in a heated rapid compression machine and a heated shock tube, Combustion and Flame 203 (2019) 157-169.

[25] S. Wang, Y. Mao, M. Raza, L. Yu, X. Lu, Autoignition of diesel/oxygen/nitrogen mixture under elevated temperature in a heated shock tube, Fuel 254 (2019).

[26] P. Dagaut, F. Karsenty, G. Dayma, P. Diévart, K. Hadj-Ali, A. Mzé-Ahmed, M. Braun-Unkhoff, J. Herzler, T. Kathrotia, T. Kick, C. Naumann, U. Riedel, L. Thomas, Experimental and detailed kinetic model for the oxidation of a Gas to Liquid (GtL) jet fuel, Combustion and Flame 161 (2014) 835-847.

[27] S. Wang, L. Yu, Z. Wu, Y. Mao, H. Li, Y. Qian, L. Zhu, X. Lu, Gas-phase autoignition of diesel/gasoline blends over wide temperature and pressure in heated shock tube and rapid compression machine, Combustion and Flame 201 (2019) 264-275.

[28] M.A. Oehlschlaeger, J. Steinberg, C.K. Westbrook, W.J. Pitz, The autoignition of iso-cetane at high to moderate temperatures and elevated pressures: Shock tube experiments and kinetic modeling, Combustion and Flame 156 (2009) 2165-2172.

[29] M.F. Campbell, T. Parise, A.M. Tulgestke, R.M. Spearrin, D.F. Davidson, R.K. Hanson, Strategies for obtaining long constant-pressure test times in shock tubes, Shock Waves 25 (2015) 651-665.

[30] K. Kumar, C.-J. Sung, An experimental study of the autoignition characteristics of conventional jet fuel/oxidizer mixtures: Jet-A and JP-8, Combustion and Flame 157 (2010) 676-685.

[31] C.J. Hayes, D.R. Burgess, J.A. Manion, Combustion Pathways of Biofuel Model Compounds, 2015, pp. 103-187.

[32] M. Assad, V.V. Leschevich, O.G. Penyazkov, K.L. Sevrouk, V.E. Tangirala, N.D. Joshi. Autoignitions of n-hexadecane and heptamethylnonane at high temperatures. In: G.D. Roy, S.M. Frolov, A.M. Starik. Nonequilibrium Processes: Plasma, Combustion, Atmospheric Phenomena; 2009: Torus Press Ltd. p.

[33] A. Osmont, L. Catoire, P. Dagaut, Thermodynamic Data for the Modeling of the Thermal Decomposition of Biodiesel. 1. Saturated and Monounsaturated FAMEs, The Journal of Physical Chemistry A 114 (2010) 3788-3795.

[34] D.F. Davidson, D.R. Haylett, R.K. Hanson, Development of an aerosol shock tube for kinetic studies of low-vapor-pressure fuels, Combustion and Flame 155 (2008) 108-117.

[35] D.R. Haylett, D.F. Davidson, R.K. Hanson, Second-generation aerosol shock tube: an improved design, Shock Waves 22 (2012) 483-493.

[36] S.R. Turns, An Introduction to Combustion : Concepts and Applications, 3rd ed., McGraw-Hill, New York, 2012.

[37] C.K. Law, Combustion Physics, Cambridge University Press, Cambridge, 2006.

[38] A.G. Gaydon, I.R. Hurle, The shock tube in high-temperature chemical physics. [by] A. G. Gaydon and I. R. Hurle, New York : Reinhold Pub. Corp., 1963.1963.

[39] E.L. Petersen, Interpreting Endwall and Sidewall Measurements in Shock-Tube Ignition Studies, Combustion Science and Technology 181 (2009) 1123-1144.

[40] D.F. Davidson, R.K. Hanson, Recent advances in shock tube/laser diagnostic methods for improved chemical kinetics measurements, Shock Waves 19 (2009) 12.

[41] B. Rotavera, E.L. Petersen. 2012. Shock-Wave Induced Ignition of Normal Undecane (n-$C_{11}H_{24}$) and Comparison to Other High-Molecular-Weight n-Alkanes. In. 28th International Symposium on Shock Waves. 2012; Berlin, Heidelberg: Springer Berlin Heidelberg. p. 783-788.

[42] B. Rotavera, N. Polley, E.L. Petersen, K. Scheu, M. Crofton, G. Bourque. Ignition and Combustion of Heavy Hydrocarbons Using an Aerosol Shock-Tube Approach. In. Proceedings of ASME Turbo Expo 2010: Power for Land, Sea and Air; 2010; Glasgow, UK. p.

[43] W.C. Hinds, Aerosol technology : properties, behavior, and measurement of airborne particles. 2nd ed. William C. Hinds, New York : Wiley, [1999], 2nd ed.1999.

[44] E. Petersen, S. Smith, Interaction of Reflected Shock Waves with Solid or Liquid Particulates, doi:10.2514/6.2004-973(2004).

[45] R.K. Hanson, Shock-tube study of vibrational relaxation in carbon monoxide using pressure measurements, AIAA Journal 9 (1971) 1811-1819.

[46] K.G. Owen, D.F. Davidson, R.K. Hanson, Oxygen Vibrational Relaxation Times: Shock Tube/Laser Absorption Measurements, Journal of Thermophysics and Heat Transfer 30 (2016) 791-798.

[47] C.J.S.M. Simpson, T.R.D. Candler, A Shock Tube Study of Vibrational Relaxation in Pure CO2 and Mixtures of CO2 with The Inert Gases, Nitrogen, Deuterium and Hydrogen, Proceedings of the Royal Society of London 317 (1970) 265-277.

[48] D.R. White, R.C. Millikan, Vibrational Relaxation in Air, AIAA Journal 2 (1964) 1844-1846.

[49] B.E. Gelfand, S.A. Gubin, S.M. Kogarko, Main Modes of Droplet Breakup in Shock Wves and Their Characteristics, Journal of Engineering Physics 27 (1974) 119-126.

[50] M. Pilch, C.A. Erdman, Use of breakup time data and velocity history data to predict the maximum size of stable fragments for acceleration-induced breakup of a liquid drop, International Journal of Multiphase Flow 13 (1987) 741-757.

[51] E.L. Petersen. 2000 Published. Shock Tube Measurements of Heterogeneous Combustion Phenomena. Western States Section of The Combustion Institute; 2000;

[52] M.A. Nettleton, Shock-wave chemistry in dusty gases and fogs: A review, Combustion and Flame 28 (1977) 3-16.

[53] H. Liu, Science and Engineering of Droplets - Fundamentals and Applications, William Andrew Publishing/Noyes2000.

[54] G. Jourdan, L. Biamino, C. Mariani, C. Blanchot, E. Daniel, J. Massoni, L. Houas, R. Tosello, D. Praguine, Attenuation of a shock wave passing through a cloud of water droplets, Shock Waves 20 (2010) 285-296.

[55] E.J. Chang, K. Kailasanath, Shock wave interactions with particles and liquid fuel droplets, Shock Waves 12 (2003) 333-341.

[56] J. Kersey, E. Loth, D. Lankford, Effect of Evaporating Droplets on Shock Waves, AIAA Journal 48 (2010) 1975-1986.

[57] G. Gai, O. Thomine, A. Hadjadj, S. Kudriakov, Modeling of particle cloud dispersion in compressible gas flows with shock waves, Physics of Fluids 32 (2020).

[58] B.E. Gelfand, Droplet breakup phenomena in flows with velocity lag, Progress in Energy and Combustion Science 22 (1996) 201-265.

[59] T.G. Theofanous, G.J. Li, On the physics of aerobreakup, Physics of Fluids 20 (2008).

[60] Y. Kim, J.C. Hermanson, Breakup and vaporization of droplets under locally supersonic conditions, Physics of Fluids 24 (2012).

[61] G.-S. Yeom, K.-S. Chang, Dissipation of shock wave in a gas-droplet mixture by droplet fragmentation, International Journal of Heat and Mass Transfer 55 (2012) 941-957.

[62] J.C. Meng, T. Colonius, Numerical simulations of the early stages of high-speed droplet breakup, Shock Waves 25 (2014) 399-414.

[63] S.V. Poplavski, A.V. Minakov, A.A. Shebeleva, V.M. Boyko, On the interaction of water droplet with a shock wave: Experiment and numerical simulation, International Journal of Multiphase Flow 127 (2020).

[64] M. Paudel, J. Dahal, J. McFarland, Particle evaporation and hydrodynamics in a shock driven multiphase instability, International Journal of Multiphase Flow 101 (2018) 137-151.

[65] Y. Zhang, Z. Huang, J. Wang, S. Xu, Shock tube study on auto-ignition characteristics of kerosene/air mixtures, Chinese Science Bulletin 56 (2011) 1399-1406.

[66] H.W.J. Goossens, J.W. Cleijne, H.J. Smolders, M.E.H. van Dongen, Shock wave induced evaporation of water droplets in a gas-droplet mixture, Experiments in Fluids 6 (1988) 561-568.

[67] H. Hirahara, M. Kawahashi. Shock wave reflection in a gas-vapor mixture with condensation. In: K. Takayama. Shock Waves; 1992; Berlin, Heidelberg: Springer Berlin Heidelberg. p. 547-552.

[68] F. Peters, B. Paikert. Shock Tube Study of Droplet-Vapor Phase Transition of Hexane in Argon. In: R. Brun, L.Z. Dumitrescu. Shock Waves @ Marseille III; 1995; Berlin, Heidelberg: Springer Berlin Heidelberg. p. 101-106.

[69] P. Roth, The shock tube technique applied to aerosol rate processes, Shock Waves, (1991) 73-82.

[70] P. Roth, R.d. Fischer, An experimental shock wave study of aerosol droplet evaporation in the transition regime, Physics of Fluids 28 (1985) 1665.

[71] H.J. Smolders, M.E.H. van Dongen, Shock wave structure in a mixture of gas, vapour and droplets, Shock Waves 2 (1992) 255-267.

[72] J. Timmler, P. Roth, Measurements of High-Temperature Evaporation Rates of solid and Liquid Aerosol Particles, International Journal of Heat and Mass Transfer 32 (1989) 1887-1895.

[73] H. Goossens, M. Berkelmans, M. van-Dongen. Experimental Investigation of Weak Shock Waves Propagating in a Fog. In: D. Bershader, R.K. Hanson. Shock Waves and Shock Tubes, Proceedings of the Fifteenth International Symposium on Shock Tubes and Shock Waves; 1986; Berkeley, CA, USA: Stanford University Press. p. 721-725.

[74] T.C. Hanson, D.F. Davidson, R.K. Hanson, Shock-induced behavior in micron-sized water aerosols, Physics of Fluids 19 (2007).

[75] P. Cadman, Shock tube combustion of liquid hydrocarbon sprays of toluene, Physical Chemistry Chemical Physics 3 (2001) 4301-4309.

[76] B. Rotavera, A. Amadio, V. Antonovski, E.L. Petersen. 2006 Published. New Approaches for Fundamental Rocket Injector Studies Using a Shock Tube. 42nd AIAA/ASME/SAE/ASEE Joint Propulsion Conference & Exhibit; 2006;

[77] J.T. Edwards. 2017 Published. Reference Jet Fuels for Combustion Testing. 55th AIAA Aerospace Sciences Meeting; 2017; AIAA Paper 2017-0146.

[78] C. Jiang, M.C. Parker, A. Spencer, G. Wigley, C.P. Garner, J. Helie. Droplet Size Development in a DISI Injector Fuel Spray. In. 18th International Symposium on the Application of Laser and Imaging Techniques to Fluid Mechanics; 2016; Lisbon, Portugal. p.

[79] A. Urbán, M. Zaremba, M. Malý, V. Józsa, J. Jedelský, Droplet dynamics and size characterization of high-velocity airblast atomization, International Journal of Multiphase Flow 95 (2017) 1-11.

[80] S.D. Sovani, P.E. Sojka, A.H. Lefebvre, Effervescent atomization, Progress in Energy and Combustion Science 27 (2001) 483-521.

[81] M. Mezhericher, I. Ladizhensky, I. Etlin, Atomization of liquids by disintegrating thin liquid films using gas jets, International Journal of Multiphase Flow 88 (2017) 99-115.

[82] D.P.H. Smith, The Electroyhydrodynamic Atomization of Liquids, IEEE Transactions on Industry Applications 1A (1986) 527-535.

[83] A. Lawley, Atomization, in: K.H.J. Buschow, R.W. Cahn, M.C. Flemings, B. Ilschner, E.J. Kramer, S. Mahajan, P. Veyssière (Eds.), Encyclopedia of Materials: Science and Technology, Elsevier, Oxford, 2001, pp. 387-392.

[84] R.J. Lang, Ultrasonic Atomization of Liquids, The Journal of the Acoustical Society of America 34 (1962) 6-8.

[85] D.R. Haylett, P.P. Lappas, D.F. Davidson, R.K. Hanson, Application of an aerosol shock tube to the measurement of diesel ignition delay times, Proceedings of the Combustion Institute 32 (2009) 477-484.

[86] M.F. Campbell, A.M. Tulgestke, D.F. Davidson, R.K. Hanson, A Second-Generation Constrained Reaction Volume Shock Tube, Review of Scientific Instruments 85 (2014) 055108.

[87] R.K. Hanson, G.A. Pang, S. Chakraborty, W. Ren, S. Wang, D.F. Davidson, Constrained reaction volume approach for studying chemical kinetics behind reflected shock waves, Combustion and Flame 160 (2013) 1550-1558.

[88] D.R. Haylett, The Deveolpment and Application of Aerosol Shock Tube Methods for the Study of Low-Vapor-Pressure Fuels, Mechanical Engineering, Stanford University, Stanford, CA, 2011.

[89] C. Frazier, M. Lamnaouer, E. Divo, A. Kassab, E. Petersen, Effect of wall heat transfer on shock-tube test temperature at long times, Shock Waves 21 (2010) 1-17.

[90] H. Mirels, Boundary Layer Behind Shock or Thin Expansion Wave Moving into Stationary Fluid, in: NACA (Ed.), Cleveland, Ohio, 1956.

[91] H. Mirels. Boundary layer growth effects in shock tubes. In: J.L. Stollery, A.G. Gaydon, P.R. Owen. Shock Tube Research. Proceedings of the Eighth International Shock Tube Symposium; 1972: Chapman and Hall, London. p. 6/2-6/30.

[92] G. Rudinger, Effect of Boundary-Layer Growth in a Shock Tube on Shock Reflection from a Closed End, Physics of Fluids 4 (1961) 1463.

[93] H. Mirels, Laminar Boundary Layer Behind Shock Advancing into Stationary Fluid, in: NACA (Ed.), Cleveland, Ohio, 1955.

[94] E.L. Petersen, R.K. Hanson, Nonideal Effects Behind Reflected Shock Waves in a High-Pressure Shock Tube, Shock Waves 10 (2001) 16.

[95] H. Mark, The Interaction of a Reflected Shock Wave With the Boundary Layer in a Shock Tube, in: N.A.C.A. 1418 (Ed.), NACA, Washington D.C., March 1958.

[96] J.W. Hargis, E.L. Petersen, Methane Ignition in a Shock Tube with High Levels of CO2 Dilution: Consideration of the Reflected-Shock Bifurcation, Energy & Fuels 29 (2015) 7712-7726.

[97] H. Kleine, V.N. Lyakhov, L.G. Gvozdeva, H. Gronig. Bifurcation of a Reflected Shock Wave in a Shock Tube. In: K. Takayama. 18th International Symposium on Shock Waves; 1992: Springer. p. 261-266.

[98] H.B. Dyner, Density Variation due to Reflected Shock-Boundary-Layer Interaction, Physics of Fluids 9 (1966) 879-892.

[99] L. Dumitrescu, C. Popescu, R. Brun. Experimental Studies of the Shock Reflection and Interaction in a Shock Tube. In: I. Glass. Shock Tubes. Proceedings of the 7th International Shock Tube Symposium; 1970 1970: University of Toronto Press, Toronto. p. 751-770.

[100] L. Davies, J. Wilson, Influence of Reflected Shock and Boundary-Layer Interaction on Shock-Tube Flows, Physics of Fluids 12 (1969) 37-43.

[101] D.C. Bull, D.H. Edwards, An Investigation of the Reflected Shock Interaction Process in a Shock Tube, AIAA Journal 6 (1968) 1549-1555.

[102] E.L. Petersen, R.K. Hanson, Measurement of Reflected-shock Bifurcation Over a Wide Range of Gas Composition and Pressure, Shock Waves 15 (2006) 333-340.

[103] S. Byron, N. Rott. On the Interaction of the Reflected Shock Wave with the Laminar Boundary Layer on the Shock Tube Walls. In: R. Binder, M. Epstein, R. Mannes, H. Yang. Proceedings of the Heat Transfer and Fluid Mechanics Institute; 1958: Stanford University Press, Stanford. p. 38-54.

[104] R.E. Center, Reflected Shock Interaction with Shock Tube Boundary Layers, Physics of Fluids 6 (1963) 307-308.

[105] M. Nishida, M. Lee. Reflected Shock/Side Boundary Layer Interaction in a Shock Tube. In: J.S. B. Sturtevant, H. Hornung. Proceedings of the 20th International Symposium on ShockWaves; 1996: World Scientific. p. 705-710.

[106] V.P. Fokeev, L.G. Gvozdeva, Study of Bifurcation of Reflected Shock Waves in Channels of Various Cross-Sections, 208 (1990) 862-866.

[107] H. Yamashita, J. Kasahara, Y. Sugiyama, A. Matsuo, Visualization Study of Ignition Modes Behind Bifurcated-Reflected Shock Waves, Combustion and Flame 159 (2012) 2954-2966.

[108] M. Lamnaouer, A. Kassab, E. Divo, N. Polley, R. Garza-Urquiza, E. Petersen, A Conjugate Axisymmetric Model of a High-Pressure Shock-Tube facility, International Journal of Numerical Methods for Heat & Fluid Flow 24 (2014) 873-890.

[109] M. Ihme, Y. Sun, R. Deiterding. 2013 Published. Detailed Simulations of Shock-Bifurcation and Ignition of an Argon-diluted Hydrogen/Oxygen Mixture in a Shock Tube. 51st AIAA Aerospace Sciences Meeting; 2013;

[110] Y.S. Weber, E.S. Oran, J.P. Boris, J.D. Anderson Jr., The Numerical Simulation of Shock Bifurcation Near the End Wall of a Shock Tube, Physics of Fluids 7 (1995) 2475-2488.

[111] A. Khokhlov, J. Austin, C. Bacon, S. Aithal, K. Riley. 2011 Published. Reflected Shock Bifurcation in a Square Channel. 49th AIAA Aerospace Sciences Meeting; 2011;

[112] Y. Takano. 1987 Published. Simulations for Effects of Side-Wall Boundary-Layer on Reflected-Shock Flow Fields in Shock Tubes. Shock Tubes and Waves: Proceedings of the Sixteenth International Symposium on Shock Tubes and Waves; 1987;

[113] G.J. Wilson, S.P. Sharma, W.D. Gillespie. 1992 Published. Time-Dependent Simulation of Reflected-Shock/Boundary Layer Interaction in Shock Tubes. Shockwaves at Marseille; 1992;

[114] C.J. Aul, W.K. Metcalfe, S.M. Burke, H.J. Curran, E.L. Petersen, Ignition and Kinetic Modeling of Methane and Ethane Fuel Blends With Oxygen: A Design of Experiments Approach, Combustion and Flame 160 (2013) 1153-1167.

[115] E.L. Petersen, M.J.A. Rickard, M.W. Crofton, E.D. Abbey, M.J. Traum, D.M. Kalitan, A Facility for Gas- and Condensed-Phase Measurements Behind Shock Waves, Measurement Science and Technology 16 (2005) 1716-1729.

[116] J.E. Vivanco, A New Shock Tube Facility for the Study of High Temperature Chemical Kinetics, Mechanical Engineering, Texas A&M University, College Station, TX, 2014.

[117] M.F. Campbell, Studies of Biodiesel Surrogates using Novel Shock Tube Techniques, Mechanical Engineering, Stanford University, Stanford, CA, 2014.

[118] A.E. Klingbeil, J.B. Jeffries, R.K. Hanson, Temperature- and pressure-dependent absorption cross sections of gaseous hydrocarbons at 3.39 μm, Measurement Science and Technology 17 (2006) 1950-1957.

[119] N.K. Anand, A.R. McFarland, F.S. Wong, C.J. Kocmoud, DEPOSITION: Software to calculate particle penetration through aerosol transport systems. Final report, United States, 1993-04-01, 1993.

[120] S.-L.v.d. Weiden;, F. Drewnick, S. Borrmann, Particle Loss Calculator – A New Software tool for the Assessment of the Performance of Aerosol Inlet Systems, Atmospheric Measurement Techniques 2 (2009) 479-494.

[121] H.C.v.d. Hulst, Light scattering by small particles, Dover Publications, Inc., Mineola, NY, USA, 1981.

[122] D.F. Davidson, RGFROSH: A Real gas frozen shock equation solver, Stanford University, Stanford, CA, 94305, October, 1995.

[123] M.F. Campbell, D.R. Haylett, D.F. Davidson, R.K. Hanson, AEROFROSH: a shock condition calculator for multi-component fuel aerosol-laden flows, Shock Waves 26 (2016) 429-447.

[124] D.R. White, Influence of diaphragm opening time on shock-tube flows, Journal of Fluid Mechanics 4 (1958) 15.

[125] A.J. Susa, D.F. Davidson, R.K. Hanson, Gravity-current-induced test gas stratification and its prevention in constrained reaction volume shock-tube experiments, Shock Waves 29 (2019) 969-984.

[126] D. Nativel, S.P. Cooper, T. Lipkowicz, M. Fikri, E.L. Petersen, C. Schulz, Impact of shock-tube facility-dependent effects on incident- and reflected-shock conditions over a wide range of pressures and Mach numbers, Combustion and Flame 217 (2020) 200-211.

[127] A.R. Amadio, M.W. Crofton, E.L. Petersen, Test-Time Extension Behind Reflected Shock Waves Using CO2–He and C3H8–He Driver Mixtures, Shock Waves 16 (2006) 157-165.

[128] Z. Hong, D.F. Davidson, R.K. Hanson, Contact surface tailoring condition for shock tubes with different driver and driven section diameters, Shock Waves 19 (2009) 331-336.

[129] B.J. McBride, S. Gordon, M.A. Reno, Coefficients for Calculating Thermodynamic and Transport Properties of Individual Species, Report No. 4513, NASA, 1993.

[130] J. Hargis, S. Cooper, O. Mathieu, B. Guo, E.L. Petersen. 2020 Published. Ignition-Delay Time Measurements of Heavy Hydrocarbons in an Aerosol Shock Tube. AIAA Scitech 2020 Forum; 2020; AIAA Paper 2020-2144.

[131] E. Olchanski, A. Burcat, Decane oxidation in a shock tube, International Journal of Chemical Kinetics 38 (2006) 703-713.

[132] T. Yao, Y. Pei, B.-J. Zhong, S. Som, T. Lu, K.H. Luo, A compact skeletal mechanism for n-dodecane with optimized semi-global low-temperature chemistry for diesel engine simulations, Fuel 191 (2017) 339-349.

[133] A. Burcat, B. Ruscic, Third Millenium Ideal Gas and Condensed Phase Thermochemical Database for Combustion (with Update from Active Thermochemical Tables), Report No. ANL-05/20; TAE 960; TRN: US200809%%737 United States 10.2172/925269, Argonne National Lab. (ANL),, Argonne, IL (United States), 2005.

[134] I.A. Al-Nuaimi, M. Bohra, M. Selam, H.A. Choudhury, M.M. El-Halwagi, N.O. Elbashir, Optimization of the Aromatic/Paraffinic Composition of Synthetic Jet Fuels, Chemical Engineering & Technology 39 (2016) 2217-2228.

[135] A.G. Mclain, C.J. Jachimowski, R.C. Rogers, Ignition of Mixtures of SiH4, CH4, O2, and Ar or N2 Behind Reflected Shock Waves, Report No. 2415, NASA, 1985.

[136] H.-P.S. Shen, J. Vanderover, M.A. Oehlschlaeger, A shock tube study of iso-octane ignition at elevated pressures: The influence of diluent gases, Combustion and Flame 155 (2008) 739-755.

[137] J.W. Hargis, E.L. Petersen, Shock-Tube Boundary-Layer Effects on Reflected-Shock Conditions with and Without CO2, AIAA Journal 55 (2017) 902-912.

APPENDIX A

PARAMETERS IN THE SPECTROSCOPIC FUEL ABSORPTION MEASUREMENT

In this appendix, consideration is given to details involving the measurement of fuel concentration behind the incident shock wave, as discussed in Chapter 4. The measurement was made using the well-known Beer-Lambert law from which the calculation of gaseous fuel mole fractions was performed in an iterative manner by coupling the Beer-Lambert law to the normal shock relations and mass, momentum, and energy conservation equations to calculate the experimental temperature and pressure behind the incident and reflected shock waves, respectively. The two inputs for the Beer-Lambert law, which is given by Equation (4.1), that have the most uncertainty are the value of the absorption coefficient of the fuel and the value of absorbance measured directly within the shock tube, respectively.

A.1 Absorbance Formulation

Although the absorbance is measured directly for each shock-tube experiment. The final value used requires a different form than taking the direct ratio of the incident and transmitted signals, I and I_0, respectively. This different form is because, although other absorbing species of the 3.39-μm wavelength are not present within the laboratory to affect the signal outside of the shock tube, there are other sources of radiation which can affect the accurate measurement of the absorbance. Background radiation present within the lab itself from room-temperature infrared emission of various surfaces is incident upon the detectors and contributes finite, albeit small, amounts of radiation to the values of both the

I and I_0 signals. Thus, this background emission must be accounted for in the formulation of the measured absorbance. In addition to these background sources, the detectors themselves have a small bias (although this is effectively lumped in with the background radiation).

As briefly mentioned in Chapter 4, when calculating the value of the absorbance from the incident and transmitted laser signals it is helpful to perform a technique known as common mode rejection. Using this technique, the absorbance is defined as shown in Equation (A1).

$$-\ln\left(\frac{I}{I_0}\right) = \alpha = -\ln\left(1 - \frac{I_0 - I}{I_0}\right) \tag{A1}$$

This method enables the cancelation of the laser power fluctuations within the signals, decreasing the uncertainty of the measurement. Although absorption levels were relatively high for the measurement performed in this study, common mode rejection was still employed (its usefulness becomes less significant as absorption levels are increased). When calculating absorbance using incident and transmitted detector signals, the measured signal values recorded from the oscilloscope software are not the true values of intensity from the laser. This difference is because background emission from various surfaces within the laboratory contribute to the laser signal. These background sources are generally assumed to be constant over the course of an experiment but must still be measured prior to each experiment and subtracted out of the values in Equation (A1).

In addition to background radiation being present in the I and I_0 detectors (symbolized as either $\Delta_{(I_0-I)_{offset}}$ or $\Delta_{(I_0)_{offset}}$ in this analysis, and assumed constant over the course of several minutes), another source of bias in the laser signals must be subtracted from the (I_0-I) term in Equation (A1). To split the laser beam into two legs, a 50:50 beam splitter is used. While the ideal ratio of transmitted-to-reflected intensity of the beam splitter is 1.00, this is often not the true ratio of the split intensities in the two legs. Thus, the intensity of the two legs will vary by a small but nontrivial amount (symbolized as $\delta_{(I_0-I)_{imbalance}}$). To remedy this imbalance, the intensity of the two beams can be balanced using a polarizer after the beam splitter on one of the legs (presumably the leg with the greater initial intensity). Oftentimes, however, there still exists some amount of imbalance between the two legs of the absorption signal at the beginning of an experiment (where, presumptively, no absorbing species are present). Such an imbalance needs to be subtracted out of the value of (I_0-I) during postprocessing. The corrected version of Equation (A1) with these adjustments is shown in Equation (A2). Challenges in balancing the two beams specific to the aerosol shock tube experiment were also present, however, and resulted in some further complications when postprocessing the absorption signal data.

$$\frac{I}{I_0} = 1 - \frac{(I_0 - I)_{meas} - \Delta_{(I_0-I)_{offset}} - \left(\delta_{(I_0-I)_{imbalance}} - \Delta_{(I_0-I)_{offset}}\right)}{I_{0,meas} - \Delta_{(I_0)_{offset}}\left(\delta_{(I_0-I)_{imbalance}} - \Delta_{(I_0-I)_{offset}}\right)} \qquad \text{(A2)}$$

When considering the imbalance in the intensity of two beams of a Beer-Lambert absorption diagnostic, the reason the beams become imbalanced over time is due to

fluctuations in the laser power. Were laser power constant for all time, there would be no need for a detector to measure the light intensity prior to entry into the shock tube. The value of I_0 could be measured prior to the start of aerosol filling, and then the aerosol could be filled, and the experiment conducted while measuring only the transmitted signal, I, of the laser. Because there are low-amplitude power fluctuations (with frequencies in the kHz-MHz range) in the laser, I_0 must be measured constantly and used to achieve cancelation of this noise due to power fluctuations. With the aerosol shock tube, this issue of balancing is further complicated because it is not possible to measure the degree to which the lasers are imbalanced at the beginning of an experiment. This situation speaks to an additional aspect of laser instability: low-frequency baseline shift of the laser power output. Not only can short-term power fluctuations be present within the laser, but the average power can fluctuate by tens of millivolts over the course of several minutes, complicating interpretation of the $\delta_{(I_0-I)_{imbalance}}$ in Equation (A2).

In traditional gas-phase absorption measurements, the value of $\delta_{(I_0-I)_{imbalance}}$ is easily measured prior to the start of an experiment because no absorbing species which absorb the diagnostic wavelength have yet been formed. For example, when measuring the formation of CO during a combustion reaction in a shock tube, CO is not present within the initial pre-shocked mixture. Because aerosol and trace amounts of fuel vapor are present within the shock tube prior to the experiment in the aerosol shock tube, however, measurement of the value of $\delta_{(I_0-I)_{imbalance}}$ in Equation A1 at the beginning of an experiment is not possible. Furthermore, since the relatively inexpensive HeNe laser

exhibits significant shifts in baseline power output over the course of several minutes, this value of $\delta_{(I_0-I)_{imbalance}}$ cannot be assumed constant.

Due to the fluctuation in laser power, the value of $\delta_{(I_0-I)_{imbalance}}$ required estimation since it could not be determined precisely. But by what manner should $\delta_{(I_0-I)_{imbalance}}$ be determined if the laser power fluctuations are random? It was hypothesized that perhaps the change in the incident signal, I_0, over a given time period could be used to estimate the change in the transmitted signal, I, (or similarly I_0-I) over the same time period if the ratio of the two were relatively constant. While this hypothesis did not prove to be exactly true, there was an approximate value around which the ratio of the difference between the two signals at differing times could be correlated.

Equation (A3) was used after measuring signal fluctuations from multiple tests over 10-20 minute durations (the approximate time required for filling various volumes and running the experiment, during which the true value of $\delta_{(I_0-I)_{imbalance}}$ cannot be measured due to the presence of fuel vapors within the aerosol test section). In this way, the value of $(I_0 - I)_{meas,t_2}$ could be estimated at the beginning of a shock-tube experiment since it could not be measured directly. In this equation, t_1 represents some time prior to the introduction of aerosol into the shock tube, and t_2 represents the time at the start of an experiment where the value of $(I_0 - I)$ is unknown

$$\frac{I_0(t_1)_{meas} - I_0(t_2)_{meas}}{(I_0 - I)_{meas,t_1} - (I_0 - I)_{meas,t_2}} \approx 0.70 \qquad \text{(A3)}$$

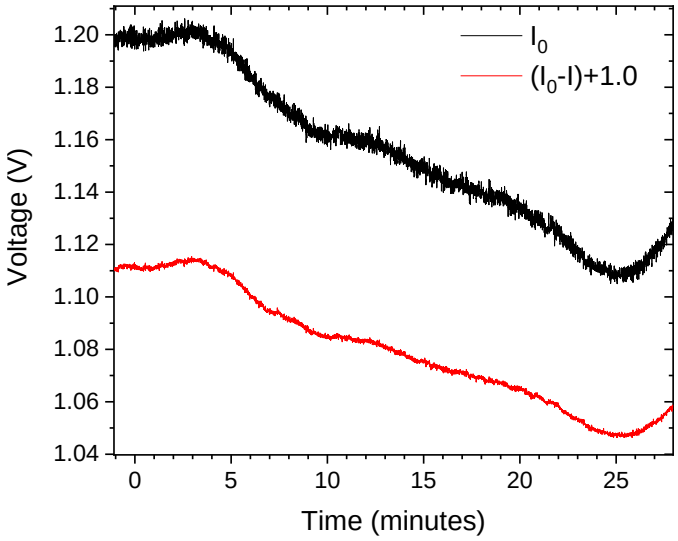

Figure A.1 Time-varying behavior of laser signals over the course of approximately 30 minutes. The (I_0-I) signal is offset by +1.0 V for easier comparison to the I_0 signal.

Knowing that the value of $\{(I_0 - I)_{meas,t_1} - (I_0 - I)_{meas,t_2}\}$ from Equation (A3) is equivalent to the change in the value of $\delta_{(I_0-I)_{imbalance,}}$ over the measured time span, the value for $\delta_{(I_0-I)_{imbalance}}$ can be estimated and used in Equation (A2). An example of the signals from the I_0 and I_0-I signals in the 3.39-μm laser absorption setup are shown in Figure A.1. From the figure, it can be seen that the laser power fluctuates by a significant amount (~10-15%) over the course of 25 minutes. This random drift in signal due to changing laser power is what causes difficulty in estimating the pre-shock value of the difference between the I and I_0 signals. Such fluctuations necessitate the use of a more stable laser for future experiments, but the above method for estimating $\delta_{(I_0-I)_{imbalance}}$ was shown to be satisfactory in terms uncertainty added to T_5. While the estimation of $\delta_{(I_0-I)_{imbalance}}$ is accompanied by a relatively significant amount of uncertainty, the

change in the amount of absorption due to this uncertainty is relatively small since the $\delta_{(I_0-I)_{imbalance}}$ term is included in both the numerator and denominator of Equation (A2). The addition of any uncertainty added by this method of estimating $\delta_{(I_0-I)_{imbalance}}$ in the analysis performed in Chapter 5 will add significantly less than 0.5 K to the overall uncertainty of T_5 and at most 1% to the uncertainty in calculating ϕ, but often much less.

A.2 Absorption Coefficients

Another important input parameter in the Beer-Lambert relation is the absorption coefficient, k_ν. The absorption coefficient must be specified based upon the particular wavelength used for the diagnostic and on the species of interest. This absorption coefficient dependence on wavelength is because it is a measure of the propensity for a specific species to absorb radiation at a specific wavelength of light. Since some of the fuels investigated in this study were mixtures, their mixture-averaged absorption coefficients were required. Absorption coefficients for Jet-A were taken from the work of Klingbeil et al. [118]. The absorption coefficient for decane came from the work of Campbell et al. [123]. The absorption coefficients for DF-2 were taken from Haylett et al. [85]. Absorption coefficients for the GTL diesel were estimated to be the same as those from the DF-2 fuel.

APPENDIX B

CALCULATION OF THERMODYNAMIC PROPERTIES IN SHOCK-INDUCED FLOWS WITH AEROSOLS

For calculations of thermodynamic conditions behind incident and reflected shock waves, respectively, the program AEROFROSH was used due to the presence of aerosols in the pre-shocked mixture within the aerosol test section [123]. This appendix discusses some of the parameters which were input into AEROFROSH for thermodynamic calculations and assumptions associated with the calculations (specifically, the surrogate mixture for the fuel and the vapor pressure of the surrogate). More information regarding AEROFROSH is given in the works of Campbell and Campbell et al., respectively [117, 123].

Compared to the gas version of FROSH [122], additional inputs are required by AEROFROSH to complete thermodynamic calculations. These additional inputs are related to the properties of the room-temperature liquid being used. The inputs are not limited to properties of the droplets in the liquid phase, however. The gas-phase absorption coefficients of the fuel and the vapor pressure of the liquid (albeit small) are also critical input parameters to AEROFROSH. Other properties of the liquid are the density of the liquid itself, the mole fractions of the various components in the liquid mixture, and the enthalpy of vaporization of the liquid. For mixtures with large numbers of components, a surrogate formulation for the mixture is required. As mentioned previously, a multi-

component surrogate was not used in this study but could be implemented easily in the future.

The calculation of the thermodynamic properties behind the incident and reflected shock waves is performed in AEROFRSOH with two key assumptions regarding the nature of the aerosol in the pre-shocked region. First, because the aerosol is brought into the shock tube from a mixing tank which houses the nebulizer in an open pool of liquid, each component in the liquid mixture is assumed to be at its liquid-vapor equilibrium. This assumption means that each component in the liquid fuel has a corresponding amount of vapor in the gas phase with a partial pressure equal to its vapor pressure. These vapor pressures are inputs to AEROFROSH, which account for this additional fuel in the calculation. The second key assumption, which was discussed in detail in previous chapters, is that the aerosol evaporates quickly and disperses in a uniform manner within the shock-tube volume. The second assumption is not discussed in detail here because it has already been shown to hold true for the droplet distribution used herein.

Although the fuels used in conjunction with aerosol shock tubes generally have low vapor pressures, these pressures are still significant enough to cause moderate amounts of gaseous fuel to be suspended in the carrier gas, along with the pre-shocked aerosol droplets. Depending on the fuel of interest, the pre-shock amounts of fuel vapor can be significant compared to the final fuel loading after evaporation behind the incident shock wave. For example, decane has a vapor pressure near 1.4 torr. For experiments in air with a P_1 of 100 torr, the vapor pressure of decane is a significant factor in the total

amount of fuel used to achieve the equivalence ratios investigated in this study (in mixtures of air). Thus, ensuring accurate values of the liquid-vapor equilibrium pressure is a critical part of utilizing AEROFROSH, particularly with more volatile components.

One challenge which accompanies the use of AEROFROSH when calculating thermodynamic conditions in real fuels is the uncertainty associated with the vapor pressure of the fuel itself in relation to a surrogate formulation. When using a surrogate formulation, the chosen species are intended to accurately mimic the combustion behavior of the real fuel. The vapor pressure of the surrogate mixture, however, may not mimic the that of the real fuel. For example, were the jet fuel surrogate formulation from the work Narayanaswamy et al. to be used, the vapor pressure of the surrogate would be far too high compared to that of a realistic jet fuel. This higher vapor pressure is because one of the components of the surrogate, methylcyclohexane, has a vapor pressure around 45 torr at room temperature (values of P_1 in this study ranged from ~70-250 torr). Thus, although a surrogate may be a good candidate to mimic combustion properties (the primary goal in using heated facilities), it must also mimic physical properties when used with the AEROFROSH thermodynamic calculator in aerosol shock tubes.

Although current surrogates may not mimic the physical properties of the mixtures accurately, these properties of the real fuels can still be estimated while keeping the surrogate constituents the same for the purposes of combustion modeling. This estimate can be done by keeping the same surrogate constituents but modifying the vapor pressures in the AEROFROSH inputs to more closely match that of the real liquid fuel mixture. Care

must be taken in the estimation of the vapor pressure, however, to ensure that the calculation results make sense and provide convergence of a solution within the program. In fact, incorrect vapor pressure inputs will lead to a lack of convergence of the solution. This difficulty was the motivation behind decoupling the room-temperature physical properties of the surrogate from its chemical formulation. If the vapor pressure was too high, AEROFROSH was unable to converge to a solution. It should also be noted here that if the liquid fuel being investigated were actually a true mixture of, say, 3-10 different components, then decoupling the vapor pressures from the fuel mixture in favor of different vapor pressures would not be appropriate.

Prior to achieving convergence in AEROFROSH, it was observed that the measured values of droplet loading in the Mie scattering diagnostic were significantly higher than the calculated values output by AEROFROSH. This disagreement between calculated and observed droplet volume fractions was the primary motivation in decoupling the AEROFROSH fuel vapor pressure input values from the surrogate vapor pressure. While some error is expected when using the Mie scattering diagnostic for estimating droplet loading within the shock tube, the observed difference between the calculated values of droplet loading from AEROFROSH versus those measured from the Mie scattering diagnostic were well beyond typical uncertainties. Thus, the vapor pressure input into the AEROFROSH code was modified to that of a species with a similar chemical formula as that measured from the fuel composition. For example, the chemical formula for the Jet-A used in this study as measured by J.T. Edwards [77] was approximately

$C_{11.4}H_{22.1}$, which is close to that of dodecane. Thus, the vapor pressure of dodecane was used as the vapor pressure input for AEROFROSH when performing calculations with the Jet-A fuel.

Although the droplet loading estimate performed within the aerosol shock tube was accompanied by some level of uncertainty since the diagnostic was merely intended for confirming evaporation, it provided a rough means why which to gauge the vapor pressure of the fuel mixture within the shock tube. This rough estimate, however, suggests that perhaps with a more rigorous diagnostic, the true room temperature vapor pressure of the real liquid fuel could be measured more accurately. With an accurate Mie scattering diagnostic (like that of Hanson et al. [74]), the droplet loading volume fraction can be measured prior to performing a shock experiment. In conjunction with the gas-phase fuel-absorption diagnostic, a shock-tube experiment can be performed and the conditions calculated in AEROFROSH (as was done for the calculations in this study) with the resultant droplet loading output of AEROFROSH compared to the measured value from the Mie scattering diagnostic. The vapor pressure of the liquid mixture can then be changed in an iterative manner until the droplet loading output from AEROFROSH aligns with that of the measured Mie scattering diagnostic. Additionally, a temperature sensing diagnostic can also be employed to verify the accuracy of the AEROFROSH calculation (use the existing 3.39-μm HeNe and another wavelength applicable to C-H stretch). Such a method of calculating vapor pressures is certainly not a practical one. This advanced Mie-scattering diagnostic would, however, provide increased accuracy in calculating the

vapor pressures for complex multi-component mixtures compared to results provided by benchtop measurement methods conducted at room temperature. Such turn-key methods are of course preferable, but often these devices measure vapor pressures at elevated temperatures, and not room temperature, where it is critical to know the accuracy of the fuel mixture vapor pressure within 5-10% for the purposes of accurate calculations related to shock-tube experimentation.

APPENDIX C

LIST OF EXPERIMENTAL CONDITIONS AND IGNITION DELAY TIMES

Fuel	T_5 (K)	P_5 (atm)	ϕ	τ_{ign} (μs)	Fuel	T_5 (K)	P_5 (atm)	ϕ	τ_{ign} (μs)
DF-2	1015	10.29	0.99	1890	DF-2	1077	9.25	0.93	931
DF-2	988	9.60	1.01	2309	DF-2	1212	10.96	0.92	235
DF-2	974	9.69	1.03	2144	DF-2	1083	9.69	0.48	1150
DF-2	1003	10.09	1.00	1668	DF-2	1035	9.62	0.71	2192
DF-2	969	8.76	1.03	2080	DF-2	1127	9.26	0.67	620
DF-2	1010	8.60	0.99	1820	DF-2	1165	9.84	0.60	477
DF-2	1002	8.78	1.00	2222	DF-2	1237	9.70	0.48	210
DF-2	1052	8.97	0.95	1225	DF-2	1299	10.58	0.51	125
DF-2	1097	8.94	0.91	790	DF-2	1293	10.78	0.53	118
DF-2	1125	8.31	0.89	464	DF-2	1090	10.08	0.47	1210
DF-2	1265	9.0	0.79	156	Jet-A	1193	11.12	1.06	213
DF-2	1268	10.82	0.79	164	Jet-A	1271	12.32	1.04	128
DF-2	1217	10.96	0.82	225	Jet-A	1184	11.38	1.04	220
DF-2	1106	9.38	0.90	582	Jet-A	1274	10.7	1.07	133
DF-2	1063	9.27	0.94	1000	Jet-A	1306	10.77	0.99	105
DF-2	1220	11.17	0.82	220	Jet-A	1283	10.37	0.95	115

Fuel	T_5 (K)	P_5 (atm)	ϕ	τ_{ign} (μs)	Fuel	T_5 (K)	P_5 (atm)	ϕ	τ_{ign} (μs)
Jet-A	1257	12.95	0.89	142	Jet-A	1232	11.56	0.59	186
Jet-A	1108	11.37	0.97	610	Jet-A	1273	12.63	0.59	111
Jet-A	1103	11.29	0.95	595	Jet-A	1115	12.87	0.52	783
Jet-A	1102	12.44	0.94	683	Jet-A	1075	12.94	0.50	1374
Jet-A	1053	13.63	0.86	1072	Jet-A	1187	10.9	0.57	336
Jet-A	1034	12.86	0.95	1403	Jet-A	1131	6.80	0.96	837
Jet-A	1179	11.6	0.95	228	Jet-A	1126	6.80	1.01	823
Jet-A	1184	11.88	1.00	252	Jet-A	962	4.31	1.03	7660
Jet-A	1176	12.53	0.99	217	Jet-A	1176	6.54	0.91	526
Jet-A	1212	12.85	0.93	172	Jet-A	993	4.27	1.15	4629
Jet-A	958	8.90	1.08	4900	Jet-A	1221	6.42	1.02	303
Jet-A	1084	11.50	1.04	817	Jet-A	1272	6.05	1.14	209
Jet-A	1120	12.18	1.01	421	Jet-A	1414	5.95	0.99	75
Jet-A	1145	11.50	0.74	443	Jet-A	1341	5.9	1.21	93
Jet-A	1118	12.76	0.63	609	Jet-A	1077	6.52	0.83	1638
Jet-A	1060	12.69	0.55	1316	Jet-A	1131	6.78	0.69	985
Jet-A	1003	12.56	0.54	2531	Jet-A	1094	6.69	0.61	1712
Jet-A	1265	11.88	0.624	111	Jet-A	1168	6.32	0.63	718

Fuel	T_5 (K)	P_5 (atm)	ϕ	τ_{ign} (μs)	Fuel	T_5 (K)	P_5 (atm)	ϕ	τ_{ign} (μs)
Jet-A	1224	6.2	0.62	315	GTL Diesel	1276	14.27	0.51	105
Jet-A	1264	5.74	0.75	214	GTL Diesel	1047	13.24	0.48	1363
Jet-A	1345	5.47	0.59	101					
Jet-A	1289	5.55	0.60	146					
Jet-A	1258	5.89	0.54	220					
Jet-A	1258	6.13	0.47	240					
GTL Diesel	1251	10.82	0.45	240					
GTL Diesel	1285	10.56	0.45	152					
GTL Diesel	1283	12.14	0.44	119					
GTL Diesel	1331	12.95	0.43	67					
GTL Diesel	1100	11.88	0.40	978					
GTL Diesel	1085	12.71	0.48	944					
GTL Diesel	1080	13.65	0.50	936					
GTL Diesel	1107	15.08	0.51	611					
GTL Diesel	1107	11.64	0.62	795					
GTL Diesel	1090	12.78	0.51	890					
GTL Diesel	1184	11.91	0.57	277					
GTL Diesel	1202	12.25	0.57	277					